

**Study of Rydberg blockade and anti-blockade
in rubidium atomic vapor**

By

DUSHMANTA KARA

PHYS11201404002

National Institute of Science Education and Research, Bhubaneswar

*A thesis submitted to the
Board of Studies in Physical Sciences*

In partial fulfillment of requirements

for the Degree of

DOCTOR OF PHILOSOPHY

of

HOMI BHABHA NATIONAL INSTITUTE



February, 2021

Homi Bhaba National Institute

Recommendations of the Viva Voce Committee

As members of the Viva Voce Committee, we certify that we have read the dissertation prepared by **Dushmanta Kara** entitled **Study of Rydberg blockade and anti-blockade in rubidium atomic vapor** and recommend that it may be accepted as fulfilling the thesis requirement for the award of Degree of Doctor of Philosophy.

Chairman - Prof. Bedangadas Mohanty *Bedangadas* Date: 08/02/2021

Guide / Convener - Dr. Ashok K. Mohapatra *Ashok K Mohapatra* Date: 08/02/2021

Co-guide -

Examiner - Dr. Saptarishi Chaudhuri *Saptarishi* Date: 08/02/2021

Member 1 - Dr. Ritwick Das *Ritwick Das* Date: 08/02/2021

Member 2 - Dr. Anamitra Mukherjee *Anamitra* Date: 08/02/2021

Member 3 - Dr. Rajan Jha *Rajan* Date:

Final approval and acceptance of this thesis is contingent upon the candidate's submission of the final copies of the thesis to HBNI.

I/We hereby certify that I/we have read this thesis prepared under my/our direction and recommend that it may be accepted as fulfilling the thesis requirement.

Date : 08/02/2021

Place : NISER Bhubaneswar

Ashok K Mohapatra
Dr. Ashok K. Mohapatra
Guide

STATEMENT BY AUTHOR

This dissertation has been submitted in partial fulfillment of requirements for an advanced degree at Homi Bhabha National Institute (HBNI) and is deposited in the Library to be made available to borrowers under rules of the HBNI.

Brief quotations from this dissertation are allowable without special permission, provided that accurate acknowledgement of source is made. Requests for permission for extended quotation from or reproduction of this manuscript in whole or in part may be granted by the Competent Authority of HBNI when in his or her judgment the proposed use of the material is in the interests of scholarship. In all other instances, however, permission must be obtained from the author.

Dushmanta Kara
(Dushmanta Kara)

DECLARATION

I, hereby declare that the investigation presented in the thesis has been carried out by me. The work is original and has not been submitted earlier as a whole or in part for a degree / diploma at this or any other Institution / University.

Dushmanta Karca
(Dushmanta Kara)

List of Publications arising from the thesis

Journal

1. Rydberg interaction induced enhanced excitation in thermal atomic vapor, D. Kara, A. Bhowmick and A. K. Mohapatra, Scientific Reports, **2018**, 8, 5256, 1-9.
2. High sensitivity measurement of Rydberg population via two photon excitation in atomic vapor using optical heterodyne detection technique, A. Bhowmick, D. Kara and A. K. Mohapatra, Pramana Journal of Physics, **2019**, 92, 5, 0076, 75-81.
3. Study of the effect of super-atom dephasing on Rydberg blockade in thermal vapor, D. Kara and A. K. Mohapatra, J. Phys. B: At. Mol. Opt. Phys., **2020**, 53, 245301.
4. Robust measurement of Rydberg population in thermal vapor using optical heterodyne detection technique, D. Kara, T. Firdoshi and A. K. Mohapatra, [Manuscript communicated].
5. Study of Rydberg blockade in thermal vapor using four-photon excitation process, V. Gupta, D. Kara, T. Firdoshi, S. Garain and A. K. Mohapatra, [Manuscript under preparation].

Conferences

1. Topical meeting on advances in photonics (TMAP-2019), 29th to 30th march 2019, NISER Bhubaneswar, India (Poster presentation).
2. International workshop on strongly interacting open many body system with emphasis on Rydberg atom physics, 30th Sept. to 3rd October 2018, Heraklion, Crete, Greece (Oral Presentation).
3. Frontier in Optics-2018, 17th to 20th Sept. 2018, Washington DC, USA (participation).
4. Student leadership conference, OSA 14th to 16th sept. 2018, Maryland USA (Poster presentation).
5. Recent trends on cold and ultra-cold matter, 27th to 29th March 2018, IIT Guwahati, India (Poster-presentation).

6. Annual Condensed matter physics meet, 26th to 27th February 2018, NISER Bhubaneswar India, (poster presentation).
7. National Laser Symposium (NLS-26) 20th to 23rd December 2017, BARC Mumba, India (poster presentation).
8. SERB school on frontiers in quantum optics, 1st to 19th December, 2017, IIT Guwahati, India (Participation).
9. International workshop on complex photonics, 22nd to 24th January 2017, TIFR Mumbai, India (Poster presentation).
10. COPT-2016, NISER Bhubaneswar, 25th Nov 2016 (Participation).
11. Recent trends in cold atom physics, 16th to 17th may 2016, IISER Pune, India (poster presentation).
12. International school and conference on quantum information, 9th to 18th February 2016, Institute of Physics Bhubaneswar, India (Poster presentation).
13. Frontiers in light matter interaction-2016, Department of Physics, 29th -30th March 2016, IIT Ropar, India (Poster presentation).

Others

1. Study of electromagnetically induced transparency in strong blockade regime using four-photon excitation process in thermal rubidium vapor, T. Firdoshi, S. Garain, V. Gupta, D. Kara and A. K. Mohapatra, (Manuscript communicated).


(Dushmanta Kara)

DEDICATIONS

This thesis is dedicated to my mother late Mrs. Sanjulata Kara and to my parents Mr. Mangulu Kara and Mrs. Sarojini Kara.

ACKNOWLEDGEMENTS

First of all, I would like to thank my thesis supervisor Dr. Ashok K. Mohapatra for giving me the opportunity to do research with his invaluable guidance and support. Without his constant encouragement, stimulating discussions on fundamental concepts, guidance in performing the experiment and constructive criticism, this thesis would not have been completed. His enthusiasm and scientific intuition has deeply inspired me throughout the research work.

Besides my supervisor, I am also thankful to my thesis monitoring committee members, Prof. Bedangadas Mohanty, Dr. Anamitra Mukherjee, Dr. Ritwick Das and Dr. Rajan Jha for guiding me throughout the PhD tenure. My sincere thanks goes to Dr. V. Ravi Chandra and Dr. Anamitra Mukherjee for their insightful discussion on many-body theory. I would also like to thank my teachers from NISER who have helped to shape my foundations for carrying out the research. I am sincerely thankful to Simon Pereira for his help in learning LABVIEW and DAQ programs. I am grateful to the department of atomic energy, Govt. of India for the financial support to carry out this research.

I would like to thank my fellow lab members Arup, Sushree, Snigdha, Tanim, Akshaya, Soumya, Sujit, Vishu, Ananya, Satya and Nikhil. It was a great pleasure working with them and I deeply appreciate their assistance in the experiments and conceptual discussions as well as their effort towards creating a friendly environment in the lab. I wish to specifically mention the initial help and guidance from Arup and Sushree. I would like to express my gratitude to my seniors Mukesh Shukla and Sameer Kumar for their support and guidance. I convey my special thanks to Kishora Nayak for his guidance, motivations and supports. I express my deepest gratitude to Binod Ch. Sahoo Sir for motivating me to continue my career in physics.

I am thankful to my friends from hostel Shakti, Soumya, Vidya, Akshaya, Abhilash, Bikash, sujit and Chandi for the beautiful memories of hostel parties and celebrations, as well as in badminton, cricket and kho-kho matches. My whole-hearted thanks goes to Sushree for her emotional support and care during the difficult situations of my PhD life. I am thankful to Dr. Brundaban Sahu and Manjushree Sahoo for providing me a homely experience in many festive occasions. I am also thankful to my younger brother Tekadhara Kara, my sister Nitu Kara and my mother Sorojini Kara for their emotional support throughout. Last but not least I would like to thank my father Mr. Mangalu Kara for being the backbone of my progress and for providing me with all the required facilities without ever mentioning his difficulties.

Contents

Summary	1
List of Figures	2
List of Tables	14
1 Introduction	16
1.1 Developments in the study of Rydberg blockade and anti-blockade in atomic vapor	18
1.1.1 Rydberg blockade	18
1.1.2 Rydberg anti-blockade	19
1.2 Developments in the study of coherent Rydberg excitation in thermal atomic vapor	20
1.3 Contribution of the thesis in the field of coherent Rydberg excitation in atomic vapor	21
1.4 Layout of the thesis	22
2 Basic atom-light interactions and Rydberg atoms	24
2.1 Two-level system	24
2.2 Dressed state picture of two-level system	27
2.2.1 Energy level spacing between the dressed states	29
2.2.2 Steady state population of the dressed states	30
2.3 Three-level system	31
2.4 Effective two-level system using adiabatic elimination	34
2.5 Rubidium energy levels	36
2.6 Doppler broadening	37
2.7 Saturation absorption spectroscopy and frequency locking of laser	38

2.8	Rydberg atoms	41
2.8.1	Properties of Rydberg atoms	42
2.8.2	Interaction of Rydberg atoms	43
2.8.3	Interaction induced Rydberg blockade	46
2.8.4	Interaction induced Rydberg anti-blockade	48
3	Robust measurement of Rydberg population in thermal vapor using OHDT	50
3.1	Overview of the OHDT	51
3.2	Modified OHDT	53
3.2.1	Experimental set-up	53
3.2.2	Experimental observations and analysis	56
3.3	Conclusion	58
4	Study of Rydberg interaction induced enhanced excitation in thermal atomic vapor	59
4.1	Theory of Rydberg anti-blockade	61
4.1.1	Dressed state picture of a three-level atomic system	61
4.1.2	Two-atom model	64
4.1.3	Interaction induced enhanced excitation	72
4.1.4	Non-interacting two-atom model for thermal vapor	74
4.1.5	Interacting two-atom model for thermal vapor	75
4.2	Experimental observation	82
4.3	Analysis	84
4.4	Conclusion	88
5	Study of the effect of super-atom dephasing on Rydberg blockade in thermal vapor	90
5.1	Two-atom model	92
5.1.1	Two-atom system in thermal vapor	92
5.1.2	Simplified two-atom system with super-atom dephasing	96
5.1.3	Approximate two-atom model	100
5.1.4	Empirical formula based on the super-atom model	101
5.1.5	Effect of dephasing mechanisms in the two-atom model	106
5.2	Three-atom model	111

5.2.1	Effect of dephasing mechanisms in three-atom model	116
5.3	Four-atom model	118
5.4	N-atom model	121
5.4.1	Effect of laser frequency noise and super-atom dephasing in the model .	123
5.5	Conclusion	124
6	Theoretical study of Rydberg blockade using four-photon excitation	126
6.1	Five-level system	127
6.1.1	Doppler averaging	130
6.2	Effective two-level system using adiabatic elimination	131
6.3	Theory of Rydberg blockade using four-photon excitation	135
6.3.1	Effect of Super atom dephasing	139
6.4	Experimental proposal using four-photon excitation	140
6.5	Conclusion	141
7	Summary and Future plans	142
	Bibliography	143
	Appendix A Data table	155
	Appendix B Monte-Carlo simulation	157
B.1	Fortran code for monte carlo simulation	158
	Appendix C LabVIEW Program for computer control	174
	Appendix D Cold atom set-up developments	176
D.1	Anti-helmholtz coil arrangements	176
D.2	Low cost mechanical shutter	178
D.3	Computer Controlled AOM Driver	179
D.4	NI-DAQMx programming	180

List of Figures

- 2.1 Energy level diagram of two-level atomic system. $|g\rangle$ and $|e\rangle$ represents the ground and the excited energy levels. Ω is the Rabi frequency, Γ_{eg} is the population decay rate from $|e\rangle$ to $|g\rangle$ and Δ is the laser detuning. 25
- 2.2 (a) The dressed state picture of two-level system. $|g_1\rangle$ and $|g_2\rangle$ represents the two dressed states. (b) Energy of bare levels (black and cyan) and the dressed states (red and blue) with laser detuning showing anti-crossing due to the dressed states. 28
- 2.3 Energy level diagram for a three-level system. $|g\rangle$, $|e\rangle$ and $|r\rangle$ represents the three energy levels. $\Omega_P = \frac{2\mu_{eg}\mathbf{E}_P}{\hbar}$ and $\Omega_C = \frac{2\mu_{re}\mathbf{E}_C}{\hbar}$ represents the probe and coupling rabi frequency respectively. The laser detuning of the probe and coupling laser is given by Δ_P and Δ_C respectively. 31
- 2.4 Energy level diagram for a three-level system. $|g\rangle$, $|e\rangle$ and $|r\rangle$ represents the three energy levels. $\Omega_P = \frac{2\mu_{eg}\mathbf{E}_P}{\hbar}$ and $\Omega_C = \frac{2\mu_{re}\mathbf{E}_C}{\hbar}$ represents the probe and coupling Rabi frequencies respectively. Here $\Delta_P \gg \Omega_P, \Gamma_{eg}$. (b) Energy level diagram for an effective two-level system. Ω_{eff} and Δ_{eff} represents the effective Rabi frequency and effective laser detuning respectively. 34
- 2.5 Energy level diagram of rubidium atoms. a) ^{87}Rb with hyperfine states and showing the excitation from $5S_{1/2}$ to $5P_{3/2}$ and $5P_{1/2}$. b) ^{85}Rb with hyperfine states and showing the excitation from $5S_{1/2}$ to $5P_{3/2}$ and $5P_{1/2}$ 37

2.6	<i>The optical set-up for the saturated absorption spectroscopy. $\lambda/4$: quarter wave-plate, ND: Neutral density filter, PBS: Polarizing beam splitter and PD: Photo-detector.</i>	38
2.7	<i>Saturated absorption spectroscopy signal for of rubidium for D1 transitions.</i>	39
2.8	<i>Saturated absorption spectroscopy signal for of rubidium for D2 transitions. The inset shows the hyperfine lines and the cross-over line of $F=3$ to F' transition of ^{85}Rb.</i>	39
2.9	<i>A screenshot of digilock110 software. The yellow dot shows the lock point where the laser is frequency locked.</i>	41
2.10	<i>A system of two Rydberg atoms with inter nuclear separation \mathbf{R}. \mathbf{a} and \mathbf{b} are the most probable radius of the electron from the atomic nucleus.</i>	43
2.11	<i>The phenomena of Rydberg blockade a) Two-level system driven with a laser field of Rabi frequency Ω to the Rydberg state, b) a two-atom system where the interaction is zero and c) Two-atom system satisfying the blockade condition where a defines the blockade radius.</i>	46
2.12	<i>a) Energy level diagram for two non-interacting atomic system excited to Rydberg state in a cold atomic ensemble. b) Interacting two-atom system excited to the Rydberg state depicting the energy level shift of $rr\rangle$ state due to Rydberg-Rydberg interaction satisfying the resonance to the applied laser.</i>	48
2.13	<i>a) Energy level diagram for non-interacting two-atom system in thermal atomic vapour each moving with different velocity. b) Interacting two-atom system in thermal vapor depicting the energy level shift of $rr\rangle$ state due to interaction satisfying resonance to the applied laser.</i>	49

3.1	(a) Experimental Set-up to measure the dispersion of the probe beam using OHDT due to the two photon excitation to the Rydberg state. $\lambda/2$: Half wave plate, $\lambda/4$: Quarter wave plate, PBS: Polarizing beam splitter, AOM: Aucostoptic modulator, DM: Dichroic mirror, PD: Photo detector, WM: Waveform mixer OPS: optical phase shifter, SAS: Saturated absorption spectroscopy and LP: Low pass filter. (b) Energy level diagram presenting two-photon excitation to the Rydberg state.	51
3.2	The modified experimental set up for the optical heterodyne detection technique. PBS: polarizing beam splitter, NPBS: non-polarizing beam splitter. . . .	53
3.3	(a) Energy level diagram of the two photon excitation to the Rydberg state. (b) Observed dispersion signal with the variation of the coupling laser frequency for S_{LX} (\square) and S_{LY} (\bullet) with $\phi_X = \pi/2$ and $\phi_Y = 0$ and (c) with $\phi_X = \frac{\pi}{4}$ and $\phi_Y = \frac{\pi}{4}$	56
3.4	The dispersion peak height for anti-blockade peak as a function of ϕ_X for S_{LX} (\circ), S_{LY} (\square) and R (\triangle). The error bar represents the statistical error. The dotted and the dashed lines are the fitting of the data S_{LX} and S_{LY} . The dotted dash straight line is the linear fitting of the measured R values and the solid line is the fitting of with $\sqrt{(\sin(\phi_X - \phi_{c1}))^2 + (\cos(\phi_X - \phi_{c2}))^2}$	57
4.1	Energy level diagram of a three-level system. $ g\rangle$, $ e\rangle$ and $ r\rangle$ represents the ground state, excited state and the Rydberg state, respectively. The probe laser with Rabi frequency Ω_P couples the state $ g\rangle \rightarrow e\rangle$ and coupling laser with Rabi frequency Ω_C couples the states $ e\rangle \rightarrow r\rangle$ satisfying $\Omega_P \gg \Omega_C$. $\Delta_{LS} = \frac{\Omega_P^2}{4\Delta_P}$, which represents the light shift factor. $ g_1\rangle$ and $ g_2\rangle$ are the two dressed states with separated in frequency by $\Delta_P + \Omega_P^2/2\Delta_P$	61

- 4.2 *Population of the Rydberg state $|r\rangle$ i.e. ρ_{rr} as a function of Δ_C . The optical parameters used are $\Delta_P = 1250$ MHz and $\Omega_P = 400$ MHz and $\Omega_C = 10$ MHz. (a) For a cold atomic ensemble with the inset showing the magnified view of peak due to the transition $|g_1\rangle \rightarrow |r\rangle$. The main peak is due to $|g_2\rangle \rightarrow |r\rangle$. (b) For a thermal vapor ensemble where ρ_{rr} is Doppler averaged over the Maxwell-Boltzmann distribution. The inset shows the magnified view of peak due to $|g_1\rangle \rightarrow |r\rangle$ 63*
- 4.3 *(a) Energy level diagram for single atom with $\delta = \Delta_P + \frac{\Omega_P^2}{2\Delta_P}$ representing the energy difference between the states $|g_1\rangle$ and $|g_2\rangle$. The laser is detuned by Δ_C to the transition $|g_2\rangle \rightarrow |r\rangle$. (b) Composite two-atom model with laser close to the resonance of the transition $|g_1\rangle \rightarrow |r\rangle$. $\Omega_1 = \Omega_C$ and $\Omega_2 = \frac{\Omega_P\Omega_C}{2\Delta_P}$ are the Rabi frequencies for the transitions $|g_1\rangle \rightarrow |r\rangle$ and $|g_2\rangle \rightarrow |r\rangle$ respectively. (c) Simplified two-atom model by eliminating the states not contributing to the Rydberg excitation processes. 65*
- 4.4 *(a) Energy level diagram for single atom with $\delta = \Delta_P + \frac{\Omega_P^2}{2\Delta_P}$ representing the energy difference between the states $|g_1\rangle$ and $|g_2\rangle$. The laser is detuned by Δ_C to the transition $|g_2\rangle \rightarrow |r\rangle$. (b) Composite two-atom model with laser close to the resonance of the transition $|g_2\rangle \rightarrow |r\rangle$. $\Omega_{eff} = \frac{\Omega_P\Omega_C}{2\Delta_P}$ is the Rabi frequency for the transitions $|g_2\rangle \rightarrow |r\rangle$ respectively. 66*
- 4.5 *Energy level diagram of the two-atom system with laser satisfying resonance condition to $|g_1\rangle \rightarrow |r\rangle$ when (a) the atoms are not-interacting and (b) for interacting system with $2V_{rr} = \Delta_1 + \Delta_2$ i.e. the anti-blockade condition when the system satisfies the resonance $|rg_2\rangle \rightarrow |rr\rangle$. The states are $|1\rangle \equiv |g_1g_2\rangle$, $|2\rangle \equiv |rg_2\rangle$, $|3\rangle \equiv |g_1r\rangle$ and $|4\rangle \equiv |rr\rangle$. The Rabi frequencies are $\Omega_1 = \Omega_C$, $\Omega_2 = \Omega_{eff}$ and interaction $V_{rr} = \frac{C_6}{r^6}$ 67*

- 4.6 (a) Rydberg population ρ_{rr} as a function of Δ_C for non-interacting two-atomic system (\circ) and for a single atom three-level exact calculation (—) in a cold atomic ensemble. The parameters used are $\Omega_P = 20$ MHz, $\Delta_P = 200$ MHz and $\Omega_C = 1$ MHz. The inset shows the magnified view of the peak corresponding to the transition $|g_1\rangle \rightarrow |r\rangle$ at $\Delta_C = 0$. (b) The residual plot of the non-interacting two-atom model and the three-level system with the variation of Δ_C . The inset shows the magnified view of the residual plot of the peak corresponding to the transition $|g_1\rangle \rightarrow |r\rangle$ at $\Delta_C = 0$ 70
- 4.7 Energy level diagram of the two-atom system with laser satisfying resonance condition to $|g_1\rangle \rightarrow |r\rangle$ when (a) the atoms are not-interacting and (b) the atoms are interacting such that the energy level shift due to interaction satisfies $2V_{rr} = \Delta'$ i.e. the anti-blockade condition where the system satisfies the resonance $|rg_2\rangle \rightarrow |rr\rangle$. The states are $|1\rangle \equiv |g_1g_2\rangle$, $|2\rangle \equiv |rg_2\rangle$, $|3\rangle \equiv |g_1r\rangle$ and $|4\rangle \equiv |rr\rangle$. The Rabi frequencies are $\Omega_1 = \Omega_C$, $\Omega_2 = \Omega_{eff}$ 72
- 4.8 Rydberg population of the two-atomic system ρ_{rr} as a function of Δ_C for an ultracold atomic ensemble for a non-interacting two-atom system (\circ) and two-atom system satisfying the anti-blockade condition $2V_{rr} = \Delta'$ is presented by (—). The inset shows the magnified peak corresponding to $\Delta_C = 0$. The parameters used are $\Delta_P = 100$ MHz, $\Omega_P = 20$ MHz and $\Omega_C = 1$ MHz. 73
- 4.9 (a) Rydberg population calculated using exact three-level single atomic system (—) and two-atoms non-interacting model (\circ) for a thermal atomic ensemble. Inset shows the magnified view of the peak near $\Delta_C = 0$. Laser parameters used in the calculation are $\Omega_P = 400$ MHz, $\Omega_C = 5$ MHz and $\Delta_P = 1.5$ GHz. (b) The residual plot of the non-interacting two-atom model and the three-level system with the variation of Δ_C . The inset shows the magnified view of the residual plot of the peak corresponding to the transition $|g_1\rangle \rightarrow |r\rangle$ at $\Delta_C = 0$. 74

4.10	<i>(a) Energy level diagram to model Rydberg anti-blockade. Δ_1 and $\Delta_2 (= \Delta_1 + \Delta')$ are the coupling laser detuning of atom 1 and 2 respectively. (b) Schematic of the interaction sphere of radius r_b. The atom in the dressed state $g_2\rangle$ is placed at the centre of the sphere. The atoms in the spherical shell of radius r and thickness dr can compensate for the two-photon resonance to the $rr\rangle$ state due to van der Waals type Rydberg-Rydberg interaction ($V_{rr} = C_6/r^6$) with the atom at the center.</i>	76
4.11	<i>(a) Dispersion spectrum of the probe laser calculated using non-interacting model (solid line) and two-atom interacting model (\circ). (b) Calculated dispersion peak height of the anti-blockade peak using two-atom interacting model (\circ) showing the quadratic dependence (solid line) on density.</i>	81
4.12	<i>Experimental Set-up to measure the dispersion of the probe beam using OHDT due to the two photon excitation to the Rydberg state. $\lambda/2$: Half wave plate, $\lambda/4$: Quarter wave plate, PBS: Polarizing beam splitter, AOM: Acousto-optic modulator, DM: Dichroic mirror, PD: Photo detector, WM: Waveform mixer, OPS: Optical phase shifter, SAS: saturated absorption spectroscopy and LP: Low pass filter.</i>	82
4.13	<i>(a) Energy level diagram of the two-photon atomic excitation to the Rydberg state. (b) Observed dispersion signal of the probe beam while scanning the coupling laser frequency Δ_C.</i>	84
4.14	<i>Dispersion spectrum measured from the experiment (black triangle) and calculated from the interacting two-atom model (\circ) for the Rydberg state with principal quantum numbers (a) $n = 35$ (b) $n = 40$ (c) $n = 45$ and (d) $n = 53$. For comparison, dispersion calculated from the non-interacting model is depicted as solid lines for all the n states. P.H represents the Peak height of the anti-blockade peak.</i>	85

4.15	<p><i>Anti-blockade peak height (●) and the usual two-photon resonant peak height for $^{85}\text{Rb } 5S_{1/2} F=3 \rightarrow nS_{1/2}$ (○) and $^{85}\text{Rb } 5S_{1/2} F=2 \rightarrow nS_{1/2}$ transition (◇) for $n = 35$ Rydberg state as a function of the density of the atomic vapor. The peak heights are normalized to the dispersion peak height corresponding to the highest density. Dotted lines are the straight line fitting of usual two-photon resonant peaks showing the linear dependence of density whereas the solid line is fitting of the anti-blockade peak height showing quadratic dependence of density.</i></p>	86
4.16	<p><i>The dispersion peak height for anti-blockade peak as a function of the density of the atomic vapor. The dots are the experimental observation and red line represents the quadratic fitting.</i></p>	87
5.1	<p><i>(a) The energy level diagram of the two-atom system with levels $1\rangle \equiv gg\rangle$, $2\rangle \equiv gr\rangle$, $3\rangle \equiv rg\rangle$ and $4\rangle \equiv rr\rangle$. The applied laser is detuned by Δ_1 from one atomic resonance and Δ_2 from the other atomic resonance and the Rabi frequencies are Ω_1 and Ω_2.</i></p>	92
5.2	<p><i>Rydberg state population as a function of Δ_1 for non-interacting (—) and interacting (○) two-atom system with (a) $\Delta_1 - \Delta_2 = 0$, (b) $\Delta_1 - \Delta_2 = \Omega$ and (c) $\Delta_1 - \Delta_2 = 3\Omega$. The parameters used for these plots are $\Omega_1 = \Omega_2 = 2 \text{ MHz}$, $\Gamma = 0.1 \text{ MHz}$, $\gamma_{rel} = 0$ and $V_{rr} = 10 \text{ MHz}$.</i></p>	97
5.3	<p><i>(a) A two-level atomic system with ground state $g\rangle$ and Rydberg state $r\rangle$. Ω (Δ) is the Rabi frequency (laser detuning) of the the applied laser and Γ is the population decay rate. (b) The energy level diagram of an identical two-atom system with levels $1\rangle \equiv gg\rangle$, $2\rangle \equiv gr\rangle$, $3\rangle \equiv rg\rangle$ and $4\rangle \equiv rr\rangle$. Γ_S is the super-atom dephasing introduced between the states $2\rangle$ and $3\rangle$.</i></p>	98

- 5.4 (a) The population of the Rydberg state as a function of Δ with $\Omega = 1$ MHz, $\Gamma = 0.1$ MHz, $\gamma_{rel} = 0$ and $\Gamma_S = 0$ for the single atom two-level system (\bullet) and exact two-atom calculation with $V_{rr} = 0$ (\square) and with $V_{rr} = 20$ MHz (—). (b) The residual plot of the exact two-atom calculation with $V_{rr} = 0$ and the single atom two-level system. 102
- 5.5 (a) ρ_{rr} as a function of Δ for two-atom exact numerical calculation (\square) and approximate model (\bullet) with $V_{rr} = 20$ MHz and for the empirical formula (—). (b) The residual plot of empirical formula (blue dotted line) and approximate model (red dashed line) with the exact numerical calculation. 103
- 5.6 Dispersion of the probe beam due to single photon excitation to the Rydberg state as a function of Δ with $\Omega = 1$ MHz and $\Gamma = 0.1$ MHz for (a) exact two-atom calculation (\square) with $V_{rr} = 0$ and for single atom picture (\bullet). (b) The residual plot for the non-interacting two-atom model and the single atom calculation. (c) ρ_{rr} as a function of Δ for empirical formula (—), approximate model (\bullet) and exact calculation (\square) with $V_{rr} = 20$ MHz. The inset of the figure represents a magnified view of a small section of the graph.(d) the residual plot for empirical formula (blue dashed line) and approximate calculation (red dotted line) with the exact calculation. 105
- 5.7 (a) Rydberg population with the variation of Δ using $\Gamma = 1.5$ MHz for exact numerical calculation (\square), approximate two-atom model (\bullet) and the empirical formula (—). (b) The residual plot of the empirical formula (red dotted line) and approximate model (blue dashed line) with the exact calculation with the variation of Δ . (c) ρ_{rr} as a function of Γ at $\Delta = 0$ for exact numerical calculation (\square), approximate two-atom model (\bullet) and the empirical formula (—). (d) The residual plot of the empirical formula (red dotted line) and approximate model (blue dashed line) with the exact calculation by varying Γ . In both the plots $\Omega = 1$ MHz, $\gamma_{rel} = 0$ and $\Gamma_S = 0$ 107

- 5.8 (a) Rydberg population as a function of Δ with $\Gamma = 1.5$ MHz, $\gamma_{rel} = 0.3$ MHz and $\Gamma_S = 0$ for exact numerical calculation (\square), approximate model (\bullet) and the empirical formula (---). The residual plot of exact numerical calculation with the (b) empirical formula (blue dotted line) and (c) the approximate calculation (red dashed line) with the variation of frequency. 108
- 5.9 (a) $\rho_{rr}^{(b)}$ as a function of γ_{rel}/Ω at $\Delta = 0$ with $\Gamma = 1.5$ MHz for exact numerical calculation (\square), approximate model (\bullet) and the empirical formula (\circ). The residual plot of the exact numerical calculation with (b) the empirical formula (blue dashed line) and (c) the approximate calculation (red dotted line) with the variation of γ_{rel} 109
- 5.10 (a) ρ_{rr} as a function of Δ with $\Gamma_S = 50$ MHz for exact numerical calculation (\square), approximate model (\bullet) and the empirical formula (---). The residual plot of the exact calculation with (b) the empirical formula (blue dotted line) and (c) the approximate calculation (red dashed line) with the variation of frequency. (d) ρ_{rr}^b at $\Delta = 0$ with Γ_S/Ω using $\gamma_{rel} = 0.3$ MHz for exact numerical calculation (\square) and for the approximate model (---). $\Gamma = 1.5$ MHz and $\gamma_{rel} = 0.3$ MHz are used for both the plots. (e) Residual plot of the approximate model and the empirical formula with the variation of Γ_S 110
- 5.11 (a) The energy level diagram for three interacting atoms. The applied laser is detuned by Δ from the atomic resonance and Rabi frequency of the transition is Ω . $|ggg\rangle \equiv |1\rangle$, $|rgg\rangle \equiv |2\rangle$, $|grg\rangle \equiv |3\rangle$, $|ggr\rangle \equiv |5\rangle$, $|rrg\rangle \equiv |4\rangle$, $|rgr\rangle \equiv |6\rangle$, $|grr\rangle \equiv |7\rangle$ and $|rrr\rangle \equiv |8\rangle$. (b) ρ_{rr} as a function of Δ for non-interacting three-atom calculation (\square), two-level system (\bullet) and interacting three-atom model (---). 112

- 5.12 (a) The population of the Rydberg state as a function of Δ with $\Omega = 1$ MHz, $\Gamma = 0.1$ MHz and $V_{rr} = 50$ MHz for exact three-atom calculation (\square), approximate model (\bullet) and for empirical formula (---). The residual plot of (b) approximate model (blue dotted line) and (c) empirical formula (red dashed line) with exact calculation. (d) ρ_{rr} at $\Delta = 0$ is plotted as a function of Γ for exact calculation (\square), empirical formula (---) and approximate model (\bullet). (e) The residual plot of empirical formula (red dotted line) and approximate model (blue dashed line) with exact calculation by varying Γ 115
- 5.13 (a) Rydberg population as a function of Δ with $\Gamma = 1.5$ MHz, $\gamma_{rel} = 0.3$ MHz and $\Gamma_S = 0$ for exact numerical calculation (\square), approximate model (\bullet) and the empirical formula (---). The residual plot of (b) the empirical formula (blue dotted line) and (c) approximate model (red dashed line) with the exact calculation by varying Δ . (d) ρ_{rr}^b as a function of γ_{rel}/Ω at $\Delta = 0$ with $\Gamma = 1.5$ MHz for approximate model (\square), the exact numerical calculation (\bullet) and empirical formula (\circ). The residual plot of (e) the empirical formula (red dashed line) and (f) approximate model (blue dotted line) with the exact calculation by varying γ_{rel} 116
- 5.14 (a) ρ_{rr} as a function of Δ with $\Gamma_S = 50$ MHz, $\gamma_{rel} = 0.3$ MHz and $\Gamma_S = 1.5$ MHz for exact three-atom calculation (\square), approximate model (\bullet) and the empirical formula (---). (b) ρ_{rr}^b at $\Delta = 0$ with Γ_S/Ω for approximate model (\bullet) and the exact calculation (\square). The inset shows the residual plot of the graph. 117
- 5.15 (a) The energy level diagram for 4 interacting atoms with states $|1\rangle = |gggg\rangle$, $|2\rangle = |rggg\rangle$ and $|4\rangle = |rrgg\rangle$. (b) The population of the Rydberg state as a function of laser detuning Δ with $\Omega = 1$ MHz, $\Gamma = 0.1$ MHz and $V_{rr} = 200$ MHz for the empirical formula (\circ) and the approximate model (---). The inset shows the variation of ρ_{rr} as a function of Γ/Ω . (c) The residual plot of the approximate model and the empirical formula with the variation of frequency. 118

- 5.16 (a) The energy level diagram for N interacting atoms with states $|1\rangle \equiv |ggg \cdots g\rangle$, $|2\rangle \equiv |rgg \cdots g\rangle$ and $|3\rangle \equiv |rrg \cdots g\rangle$. (b) The population of the Rydberg state as a function of laser detuning Δ with $\Omega = 1$ MHz, $\Gamma = 0.1$ MHz and $V_{rr} = 200$ MHz for approximate model (\circ) and for the empirical formula (---). The inset shows the variation of Rydberg population as a function of Γ/Ω 120
- 5.17 $\rho_{rg}^{(re)}$ as a function of Δ for the approximate model (\circ) and the empirical formula (\times) with $\Omega = 1$ MHz and $\Gamma = 0.1$ MHz and $\Gamma_S = \gamma_{rel} = 0$ 123
- 5.18 Normalized Rydberg blockaded population as a function of (a) γ_{rel}/Ω for the approximate model (\square) and the empirical formula (\circ) and (b) Γ_S/Ω for approximate model (\circ) for 10 interacting atoms with $\Delta = 0$, $\Gamma = 1.5$ MHz. The inset of (a) represents the residual plot of the empirical formula and the approximate model with the variation of γ_{rel} 124
- 6.1 (a) Five-level atomic system with levels $|g\rangle$, $|e\rangle$, $|e'\rangle$, $|e''\rangle$ and $|r\rangle$ coupled by four laser sources with Rabi frequencies (laser detunings) Ω_1 (Δ_1), Ω_2 (Δ_2), Ω_3 (Δ_3) and Ω_4 (Δ_4). Γ_{if} is the population decay rate from initial state $|i\rangle$ to $|f\rangle$. (b) Four-photon excitation to the Rydberg state with beams in counter-propagating configuration. 127
- 6.2 Rydberg population as a function of Δ_4 with $\Omega_1 = 150$ MHz, $\Omega_2 = 300$ MHz, $\Omega_3 = 180$ MHz, $\Omega_4 = 180$ MHz, $\Delta_1 = 1200$ MHz, $\Delta_2 = -800$ MHz and $\Delta_3 = 800$ MHz for (a) cold atom and (b) thermal vapor. The decay terms are $\Gamma_{re''} = 0.01$ MHz, $\Gamma_{e''e'} = 0.1$ MHz, $\Gamma_{e'e} = 1$ MHz, $\Gamma_{eg} = 6$ MHz, $\Gamma_{re} = 0.01$ MHz, $\Gamma_{rg} = \Gamma_{e''g} = \Gamma_{e'g} = 0.1$ MHz. 129
- 6.3 (a) Five-level atomic system $|g\rangle$, $|e\rangle$, $|e'\rangle$, $|e''\rangle$ and $|r\rangle$ coupled by four laser sources with Rabi frequencies (laser detunings) Ω_1 (Δ_1), Ω_2 (Δ_2), Ω_3 (Δ_3) and Ω_4 (Δ_4). Γ_{if} is the population decay rate from initial state $|i\rangle$ to $|f\rangle$. (b) Effective two-level system by adiabatically eliminating the intermediate state with levels $|g\rangle$ and $|r\rangle$ coupled by lasers with effective Rabi frequency Ω_{eff} , effective detuning Δ_{eff} and effective decay rate Γ_{eff} 131

6.4	(a) Rydberg state population as a function of Δ_4 calculated using the five-level system (\square) and the effective two-level system (\bullet) for parameters $\Omega_1 = 150$ MHz, $\Omega_2 = 300$ MHz, $\Omega_3 = 180$ MHz, $\Omega_4 = 180$ MHz, $\Delta_1 = 1200$ MHz, $\Delta_2 = -800$ MHz and $\Delta_3 = 800$ MHz. The decay terms are $\Gamma_{re''} = 0.01$ MHz, $\Gamma_{e''e'} = 0.1$ MHz, $\Gamma_{e'e} = 1$ MHz, $\Gamma_{eg} = 6$ MHz, $\Gamma_{re} = 0.01$ MHz, $\Gamma_{rg} = \Gamma_{e''g} = \Gamma_{e'g} = 0.1$ MHz and $\Gamma_{eff} = 0.17$ MHz. (b) The residual plot with the variation of frequency.	135
6.5	(a) Energy level diagram of the individual atom with effective two-level system with Rabi frequency Ω_i and detuning Δ_i . (b) Energy level diagram of the two-atom system with levels $ 1\rangle \equiv gg\rangle$, $ 2\rangle \equiv rg\rangle$, $ 3\rangle \equiv gr\rangle$ and $ 4\rangle \equiv rr\rangle$. Δ_1 (Ω_1) and Δ_2 (Ω_2) represents the laser detuning (Rabi frequency) of atom 1 and atom 2 respectively. Γ is the effective population decay rate.	136
6.6	Rydberg state population as a function of Δ_4 for single atom five-level system (\bullet), two-atom system with $V_{rr} = 0$ (\square) and $V_{rr} = 20$ MHz (---). The parameters used are $\Omega_1 = 150$ MHz, $\Omega_2 = 300$ MHz, $\Omega_3 = 180$ MHz, $\Omega_4 = 180$ MHz, $\Delta_1 = 1200$ MHz, $\Delta_2 = -800$ MHz, $\Delta_3 = 800$ MHz, $\Gamma = 0.17$ MHz and $\Gamma_S = 0$	137
6.7	Normalized Rydberg blockaded population as a function of Γ_S/Ω for the two-atom interacting system.	139
6.8	Experimental proposal for four-photon excitation. (a) The energy level diagram for rubidium atom excited to a Rydberg state $70S_{1/2}$ by four photon excitation. (b) Experimental set-up with suitable geometry such that residual wave vector $\Delta k = 0$	140
B.1	The Cartesian and polar co-ordinates relation in the unit circle.	157
C.1	Labview program for connecting the oscilloscope DPO5034 to the computer and transfer data.	175
C.2	LabVIEW program for connecting the oscilloscope DPO5034 and Agilent Digital multimeter to the computer and transfer data.	175

D.1	<i>MOT set-up for trapping atoms in a 3D trap. $\lambda/4$: quarter wave plate. I: current applied to the anti-Helmholtz coil.</i>	176
D.2	<i>Plot for magnetic field for current of (a) 5 amp and (b) 3 amp.</i>	177
D.3	<i>Optical setup to block the beam using mechanical shutter. M: Mirror; AWG: Arbitrary waveform generator and PD: Photo detector.</i>	178
D.4	<i>Rise time and fall time plot of the mechanical shutter and the detector signal. (a) Power supply switching on time (red) and detector switching off time (black) and (b) Power supply switching off time (red) and detector switching on time (black).</i>	178
D.5	<i>Electronic circuit for digitally controlled AOM driver.</i>	179
D.6	<i>NI PXIe system and DAQ card to generate digital output.</i>	180
D.7	<i>NI-DAQmx program to acquire signal.</i>	181
D.8	<i>NI-DAQmx program to generate signal.</i>	181

List of Tables

2.1	Hyperfine levels of Rubidium 85 and 87 for the ground state $5S_{1/2}$ and excited states $5P_{1/2}$ and $5P_{3/2}$	36
2.2	Scaling of atomic properties with 'n' for Rydberg state.	43
A.1	Fundamental physical constants used in this thesis. Adapted from: http://physics.nist.gov/cuu/Co	
A.2	Properties of ^{85}Rb	156

Chapter 1

Introduction

Understanding science is a driving force of knowledge about the world we live in. The evolution in realization of the laws governing the physical phenomena happening around us enhances technological developments which in return improves our way of living. From the first ever computer modeled that is nearly the size of a room to a recent one that fits to our pocket and is even more powerful is an example of such scientific progress. The field of light-atom interaction has also contributed enormously to these developments like all other fields of science.

Invention of laser by Maiman in 1960 was one of the greatest contribution to the field of non-linear and quantum optics. The relative phase of the applied laser beam does not change while passing through a linear medium. In non-linear optics, the high optical intensity of the applied laser could modify the properties of the atomic ensemble through which it passes due to its strong electric field. Thus, an intensity dependent refractive index is generated inside the system as a result of the optical Kerr effect. Four wave mixing, self phase modulation, cross phase modulation, optical parametric oscillation and sum or difference frequency generation are some of the examples of non-linear phenomena.^{1,2} This optical non-linearity has applications in material science to study the physical properties of matter and also has technological applications like optical switching and optical signal processing.³

The non-linearity in an ensemble can also be generated when the constituent atoms are strongly interacting. This interaction leads to the generation of a correlated atomic ensemble

where the non-linearity can be observed even at a single photon level. Rydberg atoms serve this purpose of generating the correlated atomic ensemble due to its exaggerated atomic properties.⁴ Since the outermost electron has a very high probability of being far from the atomic nucleus, the dipole moment of the Rydberg atom is large. Apart from that these atoms are very sensitive to external electric field. Thus, a large Kerr non-linearity is generated in the contributing atomic ensemble due to the strong interactions between Rydberg atoms. A strong self phase modulation and cross phase modulation in the applied photons are observed using the phenomenon of Rydberg Electromagnetically induced transparency.⁵⁻²⁹

The discovery of ultra-cold atoms which is awarded with the noble prize in physics started a new era in the field of atomic and molecular physics.³⁰⁻³⁶ Ultra-cold temperature are necessary to study quantum degenerate gas like Bose-Einstein condensate³⁷⁻³⁹ and degenerate Fermi gas.⁴⁰ Several exciting discoveries are emerging with Rydberg atoms at ultra-cold temperature.⁴ Phenomena like Rydberg blockade, Rydberg anti-blockade, RF field sensing and single photon non-linearity in ultra-cold atom opens up the possibility for quantum entanglement of large number of atoms leading to advanced technological applications like quantum information processing and quantum communication.⁴

From the investigator's point of view thermal atomic ensemble has an advantage due to its simplified experimental set-up compared to a cold atomic ensemble. Although the Doppler effect and Maxwell-Boltzmann velocity distribution create a large uncertainty in the system, it has found a lot of appreciations for its results. Phenomena that leads to enhanced optical non-linearity at single photon level in thermal atomic vapor open up the possibility of its application in quantum information processing. The work presented in this thesis focuses on the theoretical study of Rydberg blockade phenomenon as well as theoretical and experimental study of Rydberg anti-blockade phenomenon in thermal atomic vapor.

In this chapter a brief overview of the on going developments in the field of Rydberg atom physics is presented.

1.1 Developments in the study of Rydberg blockade and anti-blockade in atomic vapor

1.1.1 Rydberg blockade

Due to the large dipole moment of Rydberg atoms, they offer long range repulsive and attractive interaction with possibility of tunable interaction strength. The interaction between two Rydberg atoms are several order of magnitude larger as compared to that of the ground state atoms. This interaction leads to the Rydberg blockade which restricts the simultaneous excitation of multiple atoms to the Rydberg state within a critical length scale known as the blockade radius. This excitation is coherently distributed within the atoms contributing to the blockade phenomenon which leads to the generation of a correlated atomic ensemble.⁴¹ A significant suppression in Rydberg excitation within the blockade regime has been observed in ultra-cold atomic ensemble⁴²⁻⁴⁷ and Bose Einstein condensate.⁴⁸⁻⁵³ The blockade phenomena has also been demonstrated between two atoms individually trapped by optical tweezers.^{54,55} Enhancement in Rabi oscillation by a factor of $\sqrt{2}$ due to collective Rydberg excitation of two atoms has been reported in the experiment.⁵⁵ It was realized that a fully blockaded ensemble of N atoms can be represented by a super-atom with dipole moment enhanced by a factor of \sqrt{N} which leads the system to a many-body entangled state.^{56,57} A precise measurement of Van der Waals interaction strength between two individually trapped atoms is also reported.⁵⁸ There have been experimental demonstration of single Rydberg excitation in a string of trapped ions.⁵⁹ Rydberg atoms are also used to describe the Bose-Hubbard model.⁶⁰ Rydberg blockade was also used for quantum non-demolition measurements.⁶¹⁻⁶⁵

Since the blockade interaction generates a large correlated ensemble, the non-linearity in the single photon level is also large. Experimentally there are reports on the evidence of non-linearity at single-photon level.^{10,46,57,66,67} There have been experimental reports on observation of attractive photons in the strong blockade regime.¹¹ Single photon mediated optical non-linearity in the blockade regime is also observed with a phase shift of π .⁶⁸ Rydberg block-

ade in an electromagnetically induced transparency medium results single photon non-linearity for atoms in a cavity ⁶⁹ as well as for individual atoms trapped by optical tweezers.⁷⁰ Optically driven Rydberg interaction induced many body effect due to the blockade phenomenon are also studied in a dissipative system theoretically⁷¹⁻⁷⁵ as well as experimentally in ultra-cold ensemble.⁷⁶ This state dependent non-linearity is essential for technological applications such as quantum information processing and quantum computation.⁷⁷⁻⁸⁷ It has been demonstrated that Rydberg blockade can be used to implement C-NOT gate between atom pairs.^{88,89}

1.1.2 Rydberg anti-blockade

Interaction induced enhancement in Rydberg excitation or the Rydberg anti-blockade is an opposite effect of Rydberg excitation blockade. It was first predicted by Ates et. al. in 2007 who suggested that far detuned laser can be used to overcome the excitation blockade and atom pairs can be selectively excited to the Rydberg state within the blockade radius.⁹⁰ This result was experimentally observed in ultra cold ensemble of atom by fixing the quantum number of the Rydberg state and tuning the interaction strength by choosing specific atomic pair with required separation .⁹¹ The atoms are considered to be attracting via a Van der Waals interaction and Penning ionization is used to study nearest neighbor distribution without performing a spatially resolved measurement.⁹¹ Resonant dipole dipole interaction is observed with non-additive character due to anti-blockade in an ensemble having more than two atoms in the blockade sphere.⁹² In addition to this, the existence of anti-blockade between two Rydberg atoms, interacting with a zero area phase jump pulse is also reported.⁹³ The anti-blockade condition is also achieved by adjusting the laser detuning for a fixed interaction strength.^{94,95} Theoretical study of the anti-blockade effect in a periodically driven array of Rydberg atoms has also been reported.⁹⁶ Due to the co-operative effect anti-blockade phenomenon creates a steady entangled state in the participating atomic ensemble as studied in some recent results.⁹⁷⁻¹⁰⁰ Since the anti-blockade phenomenon also creates a correlated atomic ensemble which leads to a large non-linearity within the system, it can have application in quantum information processing as proposed by some theoretical studies.¹⁰¹⁻¹⁰⁹

1.2 Developments in the study of coherent Rydberg excitation in thermal atomic vapor

Atomic vapor are also widely used to study optical non-linearity. There are early experiments in thermal atomic vapor using alkaline materials to study ionization using Rydberg excitation.^{110,111} Since the first Rydberg EIT observed in thermal atomic vapor cell¹⁶ and atomic beam,¹¹² study started in generation of many-body entangled state using interaction.¹¹³ This results signifies that Rydberg atoms are coherently excited to the Rydberg state and are also probed in order to study many optical phenomena. Coherent dynamics faster than a nanosecond time scale is achieved with a nanosecond pulsed excitation with Rabi coupling strength in GHz regime.¹¹⁴ Rydberg excitations are used to study multi-wave mixing process in thermal atomic vapor.^{115,116}

Experimentally, it has been observed that Rydberg excitation in thermal vapor in the mean field regime shows non-equilibrium phase transition.¹¹⁷⁻¹²⁰ However, there is a controversy in the mechanism behind this observation as the charged particles in hot atomic vapor as well as the Rydberg long range interaction both can lead to the bistability in the system. Non-equilibrium phase transition finds application in tera-hertz detection methods.¹²²⁻¹²⁴ Experimental observation of the stark shift in Rb lines are reported due to the presence of ions.¹²⁰ A recent result also reports the study of non-equilibrium dynamics in a driven dissipative thermal ensemble of interacting Rydberg atoms.¹²¹ Rydberg EIT is combined with the detection of ion using an electrode for thermal Rb vapor.¹²⁵ High optical non-linearity in thermal rubidium vapor has been reported using optical heterodyne detection technique (OHDT) by our group.¹²⁶ Using the OHDT our group has also reported the observation of Rydberg blockade phenomenon in thermal Rubidium vapor using a two-photon excitation scheme.¹²⁷ High sensitive measurement of Rydberg population due to two photon excitation in thermal vapor using the OHDT has been studied by our group.¹²⁸ A single photon source based on strongly interacting Rydberg atoms in room temperature is also reported recently.¹²⁹

1.3 Contribution of the thesis in the field of coherent Rydberg excitation in atomic vapor

Using OHDT the dispersion of the probe beam is measured due to two-photon excitation to the Rydberg state. Enhancement in Rydberg excitation is observed experimentally for higher density of the atomic vapor where the interaction becomes significant.¹³¹ The experimental observations are explained theoretically using a two-atom model with the dressed state picture of a three-level system. A good qualitative agreement is observed between the theory and the experiment indicating the existence of the anti-blockade phenomena in thermal atomic vapor. We also report a modified OHDT, where the output signal is found to be independent of the phase offset variation due to change in density.¹³⁰ The technique is established by measuring the dispersion peak height which is found to be constant with the variation of phase offset.

A theoretical modeling of Rydberg blockade for N atoms inside a blockade sphere in thermal as well as cold atomic ensemble is also presented in this thesis.¹³² The model is useful to explain the blockade phenomenon for atomic ensemble having large dephasing due to relative motion of the atoms as well as dephasing due to laser frequency noise. The theoretical study also clearly indicates the existence of Rydberg blockade phenomenon in thermal atomic vapor where the dephasing due to relative motion of the atoms is very large. In addition to this, a theoretical model for Rydberg blockade in thermal atomic vapor is presented using four-photon excitation where the Doppler broadening due to the residual wave vector mismatch is very small.

The work presented in this thesis opens up the possibility of application of thermal atomic vapor in quantum information processing. The phenomena of Rydberg blockade and anti-blockade can be observed in thermal atomic vapor as predicted in this thesis. The optical non-linearity observed in the experiment is small as the observed spectrum is Doppler broadened due wave vector mismatch of the applied laser in a two-photon excitation process. However, using a four-photon excitation process, the residual wave vector can be reduced to zero with suitable beam geometry. Thus, the system in thermal vapor can produce similar result as the

cold atomic ensemble. This will be useful to generate a correlated atomic ensemble leading to strong optical non-linearity even at single-photon level. This will be helpful to generate CNOT gate using thermal atomic ensemble.

1.4 Layout of the thesis

The work presented in this thesis are organized as follows.

In chapter 2, the basic concepts which are useful for understanding of the thesis work are presented. The basic properties of Rydberg atoms are presented and the scaling of these properties with the principal quantum number of the Rydberg state are explained along with the interactions between the Rydberg atoms. In addition to this, the phenomena of Rydberg blockade and anti-blockade are explained using two interacting atoms. Thereafter, some basic atom-light interaction using two-level system, three-level system and the effective two-level system using adiabatic elimination are described using the optical Bloch equations. In addition, the experimental techniques such as saturated absorption spectroscopy and frequency locking of the laser is presented. The different atomic transition lines of Rubidium atoms are also described here.

A modified optical heterodyne detection technique (OHDT) is described in chapter 3. OHDT is established to study Rydberg excitation in thermal atomic vapor by our group, which will be discussed briefly. Thereafter, the modified OHDT is explained with the experimental set-up. In order to verify the technique, the experimental data are collected for the anti-blockade peak in the dispersion spectrum of the probe beam due to the two photon excitation.

In chapter 4, the theoretical and experimental observation of the Rydberg anti-blockade phenomenon is described. The dressed state picture of the three level system is used to explain the observation. Using a model of two interacting atoms, the anti-blockade phenomenon is explained for a cold atomic ensemble. In order to extend the theory for thermal vapor ensemble, the physical quantities are Doppler averaged over the whole velocity class of the atom. The experimental set-up to observe the anti-blockade phenomenon due to two-photon excitation to the Rydberg state using OHDT is described. The analysis is presented where a comparison of

the theoretical results and the experimental observations is explained.

In chapter 5, the theoretical model of Rydberg blockade for N atoms inside the blockade sphere for cold atom and thermal atomic vapor is presented. The exact calculation for two-atoms inside the blockade sphere is formulated for cold atomic ensemble. The calculation is extended for thermal atomic vapor, and the effect of velocity in the model is also discussed. The exact calculation of the two-atom model are simplified using the symmetry in the system which gives rise to an approximate model. An empirical formula is also formulated for the system considering the atoms within the blockade sphere which are contributing to the Rydberg blockade phenomena behaves as a super-atom. The effect of different dephasing mechanisms arising due to the thermal motion of the atom in the blockade phenomenon are described. The exact numerical calculation, the approximate model and the empirical formula is extended for three and four-atom system. An approximate model for N -atoms inside the blockade sphere is presented using the simplified OBEs of two, three and four-atom system. The super-atom dephasing arising due to the velocity of the atoms and its effect on the blockade phenomenon is also described in details.

In chapter 6, the blockade phenomenon using a four-photon excitation process is described. The advantage of the four-photon process over the usual two-photon scheme is explained. The five-level atomic system is described using the OBEs in steady state. An effective two-level system is described here which is formulated using the adiabatic elimination of the intermediate states of a five level system. The blockade process is explained for the system using a two-atom model and the effect of different dephasing mechanisms are also studied.

In chapter 7, the summary and possible future experimental proposals using the cold atomic ensemble and the thermal atomic vapor are presented.

Chapter 2

Basic atom-light interactions and Rydberg atoms

In this chapter, the basic atom light interactions are explained along with the properties of Rydberg atoms. Starting from a two-level system, the three-level system and the effective two-level system are discussed here. Then, the dressed state picture of the two-level system is explained in details. The energy level diagram of the rubidium atom as well as the saturated absorption spectroscopy (SAS) along with the frequency locking of the LASER using the digilock module is explained. Thereafter, the properties of Rydberg atoms and the scaling of different physical quantities such as dipole moment, lifetime, polarizability etc. with the principal quantum number of the Rydberg state are discussed. Also, the co-operative phenomena like Rydberg blockade and Rydberg anti-blockade arising due to the strong inter-atomic interactions are explained.

2.1 Two-level system

Let us consider a two-level atomic system as shown in figure 2.1 with ground state $|g\rangle$ and excited state $|e\rangle$ with resonant frequency w_0 . A laser with frequency w_L is applied to the system which is detuned by an amount $\Delta = w_L - w_0$ from the atomic resonance. Using the dipole

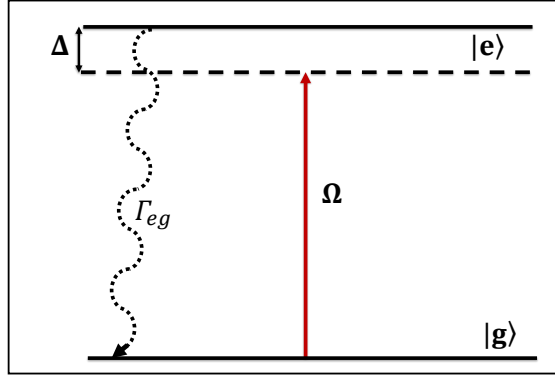


Figure 2.1: Energy level diagram of two-level atomic system. $|g\rangle$ and $|e\rangle$ represents the ground and the excited energy levels. Ω is the Rabi frequency, Γ_{eg} is the population decay rate from $|e\rangle$ to $|g\rangle$ and Δ is the laser detuning.

approximations and the rotating wave approximation,¹⁶⁰ the time independent Hamiltonian of the system is given by

$$H = H_0 + H_I = -\frac{\hbar}{2} \begin{bmatrix} 0 & 0 \\ 0 & 2\Delta \end{bmatrix} - \frac{\hbar}{2} \begin{bmatrix} 0 & \Omega \\ \Omega^* & 0 \end{bmatrix} = -\frac{\hbar}{2} \begin{bmatrix} 0 & \Omega \\ \Omega^* & 2\Delta \end{bmatrix}. \quad (2.1)$$

Here, H_0 is the bare atom Hamiltonian and H_I is the Hamiltonian due to the atom-light interaction. $\Omega = \frac{2\mu_{eg}|\mathbf{E}|}{\hbar}$ is defined as the Rabi frequency of the system. Here, μ_{eg} is the dipole moment due to the coupling between the states $|g\rangle \rightarrow |e\rangle$ and $|\mathbf{E}|$ represents the amplitude of electric field of the applied laser. The density matrix of the 2 level system is given by

$$\rho = \begin{bmatrix} \rho_{gg} & \rho_{ge} \\ \rho_{eg} & \rho_{ee} \end{bmatrix}.$$

ρ_{gg} and ρ_{ee} represent the population of the ground and the excited states. For a closed system, $\rho_{gg} + \rho_{ee} = 1$, which represents the total population of the system is conserved. $\rho_{ge} = \rho_{eg}^*$ (* represents the complex conjugate) represents the coherence between both the states introduced due to the applied laser field. Due to the process of spontaneous emission the atom decays from excited state to the ground state after a certain interval of time. This time is known as the lifetime of the excited state t_d . The population decay rate (Γ_{eg}) of the atom is related to t_d

as $\Gamma_{eg} = \frac{1}{t_d}$. This introduces a decoherence in the system which can be incorporated using a Lindblad operator¹⁶¹ given by

$$L_D = \Gamma_{eg} \begin{bmatrix} \rho_{ee} & -\frac{\rho_{ge}}{2} \\ -\frac{\rho_{eg}}{2} & -\rho_{ee} \end{bmatrix}, \quad (2.2)$$

The dynamics of the system can be studied using the optical Bloch equations (OBEs) given by $\dot{\rho} = \frac{i}{\hbar}[\rho, H] + L_D$. The system is studied using the steady state condition $\dot{\rho} = 0$. On solving, the equations for the population of the excited state (ρ_{ee}) and the coherence (ρ_{eg}) is found to be

$$i((1 - 2\rho_{ee})\frac{\Omega}{2} + \Delta\rho_{ge}) - \Gamma_{eg}\frac{\rho_{ge}}{2} = 0. \quad (2.3)$$

$$i(\rho_{eg}\frac{\Omega}{2} - \frac{\Omega^*}{2}\rho_{ge}) - \Gamma_{eg}\frac{\rho_{ee}}{2} = 0. \quad (2.4)$$

Solving these two equations ρ_{ee} and ρ_{ge} is calculated. The real and imaginary part of ρ_{ge} gives the information about the dispersion and the absorption of the applied laser field respectively. On solving the above equations, these two quantities are found to be

$$\rho_{ee} = \frac{\Omega^2}{2\Omega^2 + 4\Delta^2 + \Gamma_{eg}^2}. \quad (2.5)$$

$$\rho_{ge} = -\frac{2(\Delta - i\frac{\Gamma_{eg}}{2})\Omega}{2\Omega^2 + 4\Delta^2 + \Gamma_{eg}^2}. \quad (2.6)$$

The susceptibility (χ) is a physical quantity of interest which is observed during the experiment. It is related to ρ_{ge} as

$$\chi = \frac{N\mu_{eg}}{\epsilon_0|E|}\rho_{ge}.$$

Where, N is the density of the atomic ensemble, ϵ_0 is the permittivity of vacuum and \hbar is the Planck's constant. The real part of susceptibility (χ^{Re}) gives information about the phase change of the applied laser. The imaginary part (χ^{Im}) explains the absorption or transmission of the laser due to the excitation process. Using the above expression χ^{Re} and χ^{Im} is found to

be

$$\chi^{Re} = -\frac{n\mu_{eg}}{\epsilon_0|E|} \left(\frac{2\Delta\Omega\Gamma_{eg}}{\Gamma_{eg}^2 + 2\Omega^2 + 4\Delta^2} \right). \quad (2.7)$$

$$\chi^{Im} = \frac{n\mu_{eg}\Omega\Gamma_{eg}^2}{\epsilon_0|E|(\Gamma_{eg}^2 + 2\Omega^2 + 4\Delta^2)}. \quad (2.8)$$

The system described above has a dephasing only due to the population decay by the process of spontaneous emission. However, the laser applied for the excitation has a linewidth or frequency noise. This frequency noise of the applied laser also introduces a dephasing in the system. For a stable external cavity diode laser (ECDL) used in the experiment presented here, this noise is 300 KHz. For the two-level system this is included as a decoherence term in the L_D matrix which is written as

$$L_D = \begin{pmatrix} \Gamma_{eg}\rho_{ee} & -\frac{(\Gamma_{eg} + \gamma_{rel})\rho_{ge}}{2} \\ -\frac{(\Gamma_{eg} + \gamma_{rel})\rho_{eg}}{2} & -\Gamma_{eg}\rho_{ee} \end{pmatrix}.$$

Here, γ_{rel} is the dephasing rate arising due to the laser frequency noise. The population of the Rydberg state is calculated for this system by solving the OBEs in the steady state condition as described previously in this section and is given by

$$\rho_{ee} = \frac{\Omega^2(\Gamma_{eg} + \gamma_{rel})}{2\Omega^2(\Gamma_{eg} + \gamma_{rel}) + 4\Delta^2\Gamma_{eg} + \Gamma_{eg}(\Gamma_{eg} + \gamma_{rel})^2}. \quad (2.9)$$

For a Rydberg state, the population decay rate is $\simeq 100$ KHz. Thus, the laser frequency noise is significant compared to Γ in this system. Therefore, the Rydberg population calculated for the system in presence of γ_{rel} is significantly different than a case where it is not included. The calculations presented in this thesis include γ_{rel} in the L_D matrix.

2.2 Dressed state picture of two-level system

Consider an atomic system with ground state $|g\rangle$ and excited state $|e\rangle$ coupled by an applied laser having rabi frequency Ω_P and detuning Δ_P as shown in figure 2.2(a). The most general

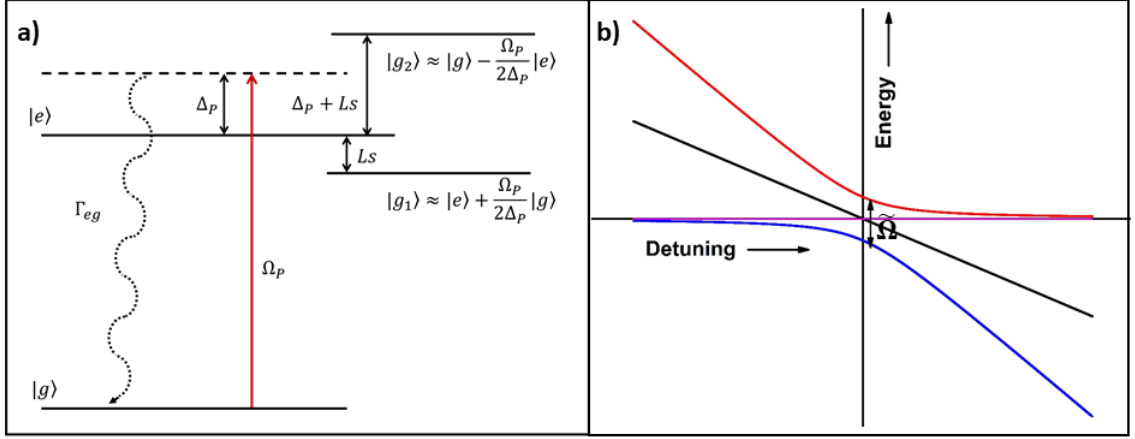


Figure 2.2: (a) The dressed state picture of two-level system. $|g_1\rangle$ and $|g_2\rangle$ represents the two dressed states. (b) Energy of bare levels (black and cyan) and the dressed states (red and blue) with laser detuning showing anti-crossing due to the dressed states.

state of a two-level system is given by $|\Psi\rangle = c_g |g\rangle + c_e |e\rangle$. In presence of a driving field the Schrodinger equation $|\dot{\Psi}\rangle = \frac{1}{i\hbar} H |\Psi\rangle$ for the system is given by

$$\begin{pmatrix} \dot{c}_g \\ \dot{c}_e \end{pmatrix} = -\frac{i}{\hbar} \begin{pmatrix} 0 & \Omega_P/2 \\ \Omega_P/2 & \Delta_P \end{pmatrix} \begin{pmatrix} c_g \\ c_e \end{pmatrix}. \quad (2.10)$$

The Hamiltonian can be diagonalized using the eigenvalue equation in order to change the basis vectors.

$$\begin{pmatrix} g_1 \\ g_2 \end{pmatrix} = -\frac{i}{\hbar} \begin{pmatrix} 0 & \Omega_P/2 \\ \Omega_P/2 & \Delta_P \end{pmatrix} \begin{pmatrix} c_g \\ c_e \end{pmatrix} - \lambda \mathbb{I} \begin{pmatrix} c_g \\ c_e \end{pmatrix} \quad (2.11)$$

For the two-level system, the diagonalization of the Hamiltonian is given by

$$-\frac{i}{\hbar} \begin{vmatrix} 0 - \lambda & \Omega_P/2 \\ \Omega_P/2 & \Delta_P - \lambda \end{vmatrix} = 0. \quad (2.12)$$

$$\Rightarrow \lambda_{\pm} = -\frac{i}{\hbar} \left(\frac{\Delta_P \pm \sqrt{\Delta_P^2 + \Omega_P^2}}{2} \right) = -\frac{i}{\hbar} (\Delta_P \pm \Omega').$$

Here, $\Omega' = \sqrt{\Delta_P^2 + \Omega_P^2}$. This values of λ_{\pm} can be substituted in equation 2.11, which give

the eigenvector of the states as

$$|g_1\rangle = \cos \theta |e\rangle - \sin \theta |g\rangle. \quad (2.13)$$

$$|g_2\rangle = \cos \theta |g\rangle + \sin \theta |e\rangle. \quad (2.14)$$

Here $\tan \theta = \frac{\Omega}{\Omega' - \Delta_P}$. These states are called the dressed states of the atomic system consisting of superposition of bare atomic states. Due to the presence of a coupling laser even if at $\delta = 0$ the two dressed states will have different energy unlike the uncoupled bare states which will have zero energy at $\Delta_P = 0$. This leads to an anti-crossing at resonance which is arising due to the applied laser field as shown in figure 2.2(b).^{1,164} The energy difference of the two dressed states at resonance is given by the rabi frequency $\tilde{\Omega}$ which is calculated to be

$$\tilde{\Omega} = \lambda_+ - \lambda_- = \frac{\Omega_P^2}{2\Delta_P}. \quad (2.15)$$

2.2.1 Energy level spacing between the dressed states

As calculated in the two-level dressed state picture the eigenvalues for a system is given by $\lambda_{\pm} = \frac{\Delta_P \pm \sqrt{\Delta_P^2 + \Omega_P^2}}{2}$. There are two possible conditions. One is when $\Delta_P = 0$, i.e. the resonant case. Here the two dressed states will be equally separated from the unperturbed atomic energy level and in opposite direction with energy $\frac{\Omega_P}{2}$ of each state. The second condition is $\Delta_P \gg \Omega_P$ such that $\frac{\Omega_P^2}{\Delta_P^2} \ll 1$. Therefore, λ_{\pm} can be expanded using the Taylor series expansion which gives

$$\lambda_+ \simeq \Delta_P + \frac{\Omega_P^2}{4\Delta_P},$$

$$\lambda_- \simeq -\frac{\Omega_P^2}{4\Delta_P}.$$

The difference between these two energy eigen values gives the separation between the dressed states. This depends on the laser parameters i.e. the detuning from the atomic resonance and the rabi frequency. The term $\frac{\Omega_P^2}{4\Delta_P}$ is called the light shift that arises due to the presence of the

strong probe laser. We can always tune the separation between the dressed states by changing the laser parameters depending on the requirement of the experiment. The separation is given by $\Delta' = \Delta_P + \frac{\Omega_P^2}{2\Delta_P}$.

2.2.2 Steady state population of the dressed states

The energy of the dressed state are in the diagonal basis of the bare atomic levels, the density matrix of the bare atom system is diagonalized in order to calculate the populations of each of the dressed states. The system reaches a steady state after a time greater than $1/\Gamma_{eg}$. The eigenvalue equation for the two-level density matrix in steady-state is given by

$$\begin{vmatrix} \rho_{gg} - \Lambda & \rho_{ge} \\ \rho_{eg} & \rho_{ee} - \Lambda \end{vmatrix} = 0, \quad (2.16)$$

$$\Rightarrow (\rho_{gg} - \Lambda)(\rho_{ee} - \Lambda) - |\rho_{ge}|^2 = 0.$$

Since, it is a closed atomic system we know $\rho_{gg} + \rho_{ee} = 1$. The eigenvalue equation or the diagonalization of the density matrix gives

$$\Lambda_{\pm} = \frac{1 \pm \sqrt{1 + 4(1 - \rho_{ee})\rho_{ee} - |\rho_{ge}|^2}}{2}. \quad (2.17)$$

Equation 2.5 and 2.6 represents the population of the excited state and the coherence term. The system is considered such that it satisfies the condition $\Delta_P \gg \Omega_P \gg \Gamma_{eg}$. These two expressions are simplified under these condition to

$$\rho_{ee} = \frac{\Omega_P^2}{4\Delta_P^2} \left(1 - \frac{\Omega_P^2}{2\Delta_P^2}\right).$$

$$|\rho_{ge}|^2 = \frac{\Omega_P^2}{4\Delta_P^2} (2\rho_{ee} - 1)^2.$$

On substitution of the density matrix expression on equation 2.17, the eigen value equation

simplifies to

$$\Lambda_{\pm} = \frac{1}{2} \pm \frac{1}{2} \sqrt{1 - \frac{\Omega_P^4}{4\Delta_P^4}}.$$

Since the second term inside the square root is much smaller than 1, then it is expanded using the binomial expansion and neglecting the higher order terms except the first order we get

$$\Lambda_+ \simeq 1 \quad (2.18)$$

and

$$\Lambda_- \simeq \frac{\Omega_P^4}{16\Delta_P^4}. \quad (2.19)$$

Λ_+ and Λ_- represents the population of the state $|g_2\rangle$ and $|g_1\rangle$ respectively. Hence, the population of the upper dressed state is nearly one while the lower one is much more smaller than one. This is due to the high value of laser detuning that we are using here. However, if $\Delta_P = 0$ then the population of both the states are equal.

2.3 Three-level system

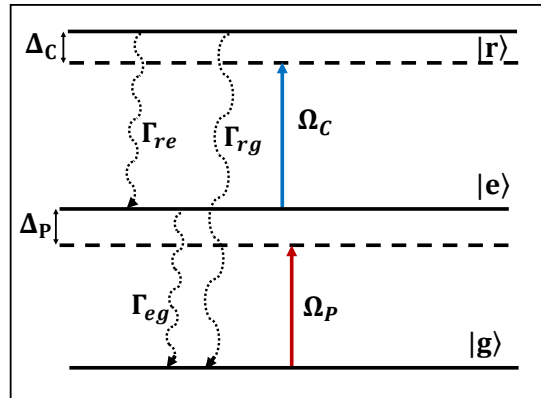


Figure 2.3: Energy level diagram for a three-level system. $|g\rangle$, $|e\rangle$ and $|r\rangle$ represents the three energy levels. $\Omega_P = \frac{2\mu_{eg}\mathbf{E}_P}{\hbar}$ and $\Omega_C = \frac{2\mu_{re}\mathbf{E}_C}{\hbar}$ represents the probe and coupling rabi frequency respectively. The laser detuning of the probe and coupling laser is given by Δ_P and Δ_C respectively.

The atoms can be excited to the desired level using a single photon as explained in the previous section. However, it is difficult to get the laser source in some frequency range. For example consider rubidium atom, where the excitation to the Rydberg state required laser in the ultraviolet region. It is very difficult to have a laser in this frequency range. Therefore, the excitation can be performed using multi-photon process e.g. a 780 nm and a 480 nm laser is used for the excitation. Consider an atomic system with three-levels with ground state $|g\rangle$, excited state $|e\rangle$ and second excited state $|r\rangle$ coupled by two lasers. The first laser excites the atom from $|g\rangle \rightarrow |e\rangle$ known as the probe laser and the second laser excites the atom $|e\rangle \rightarrow |r\rangle$ known as the coupling laser. The rabi frequency (Laser detuning) of the probe is Ω_P (Δ_P) and for the coupling beam it is Ω_C (Δ_C). The energy level diagram is shown in figure 2.3.

Using the similar approach as the two-level system, the time independent Hamiltonian for the three-level system can be written using the rotating wave approximation and dipole approximation which is given by

$$H = \frac{-\hbar}{2} \begin{bmatrix} 0 & \Omega_P & 0 \\ \Omega_P^* & 2\Delta_P & \Omega_C \\ 0 & \Omega_C^* & 2(\Delta_P + \Delta_C) \end{bmatrix}. \quad (2.20)$$

The atom will decay from the excited state to the ground state by the process of spontaneous emission. There are three possible population decay channels. Two direct decays from $|e\rangle \rightarrow |g\rangle$ and $|r\rangle \rightarrow |e\rangle$ which are dipole allowed. An indirect decay arises due to the finite transit time of the atoms across the laser beam profile. When a Rydberg excited atom moves out of the beam profile and a ground state atom comes in, it is considered as a decay from the Rydberg state to the ground state. Thus, an indirect decay which is dipole forbidden considered from $|r\rangle \rightarrow |g\rangle$. These decay processes introduces a decoherence in the system and it is incorporated

using the Lindblad operator which is given by

$$L_D = \begin{bmatrix} \Gamma_{eg}\rho_{ee} + \Gamma_{rg}\rho_{rr} & -(\Gamma_{eg}/2)\rho_{ge} & -(\Gamma_{rg} + \Gamma_{re})\rho_{gr}/2 \\ -(\Gamma_{eg}/2)\rho_{eg} & -\Gamma_{eg}\rho_{ee} + \Gamma_{re}\rho_{rr} & -(\Gamma_{eg} + \Gamma_{rg} + \Gamma_{re})\rho_{er}/2 \\ -(\Gamma_{rg} + \Gamma_{re})\rho_{gr}/2 & -(\Gamma_{eg} + \Gamma_{rg} + \Gamma_{re})\rho_{re}/2 & -(\Gamma_{rg} + \Gamma_{re})\rho_{rr} \end{bmatrix}. \quad (2.21)$$

Γ_{ij} represents the decay rate from excited state i to lower state j . The system can be solved using the OBEs and different physical quantities can be studied. In a steady state the independent set of OBEs for the system are given by

$$Im(\rho_{ge}) + \Gamma_{eg}\rho_{ee}/\Omega_P + \Gamma_{rg}\rho_{rr}/\Omega_P = 0 \quad (2.22)$$

$$\Omega_P(2\rho_{ee} + \rho_{rr} - 1) - (2\Delta_P - i\Gamma_{eg})\rho_{ge} - \rho_{gr}\Omega_C = 0 \quad (2.23)$$

$$\rho_{ge}\Omega_C - \Omega_P\rho_{er} + \rho_{gr}[2(\Delta_P + \Delta_C) - i\Gamma_2] = 0 \quad (2.24)$$

$$\rho_{er}(2\Delta_C - i\Gamma_3) + \Omega_C(\rho_{ee} - \rho_{rr}) - \Omega_P\rho_{gr} = 0 \quad (2.25)$$

$$Im(\rho_{er}) + \Gamma_2\rho_{rr}/\Omega_C = 0 \quad (2.26)$$

Here we have used $\frac{\Gamma_{rg} + \Gamma_{re}}{2} = \Gamma_2$ and $\frac{\Gamma_{eg} + \Gamma_{rg} + \Gamma_{re}}{2} = \Gamma_3$. The real and imaginary part of ρ_{ge} gives the information about the dispersion and absorption of the probe laser respectively. For a low probe approximations ($\Omega_P \ll \Omega_C$) these quantities are calculated to be

$$Re(\rho_{ge}) = \frac{2a\Omega_P\Delta_2 - 2\Omega_P\Gamma_2b}{a^2 + 4b^2}.$$

$$Im(\rho_{ge}) = -\frac{4b\Omega_P\Delta_2 + a\Omega_P\Gamma_2}{a^2 + 4b^2}.$$

Where, $a = \Gamma_{eg}\Gamma_2 - 4\Delta_P\Delta_2 + \Omega_C^2$ and $b = \Gamma_{eg}\Delta_2 - \Delta_P\Gamma_2$ with $\Delta_2 = \Delta_P + \Delta_C$ and $\Gamma_2 = \Gamma_{re} + \Gamma_{rg}$.

Depending on the laser detuning and the rabi frequency the three-level system can show Electromagnetically induced transparency (EIT).¹⁶² EIT is an interesting phenomenon that introduces strong non-linearity in the system. These equations can be solved analytically for the single atom picture. However, when we consider multi-atom system, the mathematical complexity enhances using the three-level system. Therefore, the system can further be simplified to an effective two-level system by using a technique called adiabatic elimination which is explained in the next section.

2.4 Effective two-level system using adiabatic elimination

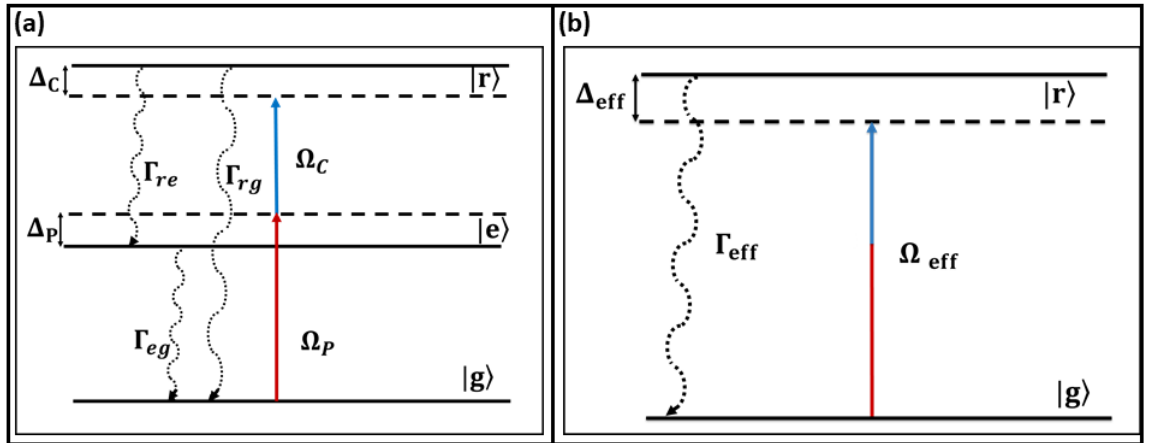


Figure 2.4: Energy level diagram for a three-level system. $|g\rangle$, $|e\rangle$ and $|r\rangle$ represents the three energy levels. $\Omega_P = \frac{2\mu_{eg}E_P}{\hbar}$ and $\Omega_C = \frac{2\mu_{re}E_C}{\hbar}$ represents the probe and coupling Rabi frequencies respectively. Here $\Delta_P \gg \Omega_P, \Gamma_{eg}$. (b) Energy level diagram for an effective two-level system. Ω_{eff} and Δ_{eff} represents the effective Rabi frequency and effective laser detuning respectively.

Adiabatic elimination is a technique used to simplify a complex system. In order to simplify the three-level system the laser parameters can be adjusted. As presented in figure 2.4(a), the probe laser is detuned from the atomic resonance such that $\Delta_P \gg \Omega_P, \Gamma_{21}$. Therefore, the population $\rho_{ee} \simeq 0$. In presence of the coupling laser with Rabi frequency Ω_C , the population is transferred to the state $|r\rangle$. Using these conditions the Hamiltonian of the system can be reduced to an effective two-level Hamiltonian given by¹⁶³

$$H_{eff} = -\hbar \begin{bmatrix} \frac{\delta}{2} + \frac{\Omega_P^2}{2(2\Delta_P - \delta)} & \frac{\Omega_P \Omega_C}{2(2\Delta_P - \delta)} \\ \frac{\Omega_P \Omega_C}{2(2\Delta_P - \delta)} & \frac{\Omega_C^2}{2(2\Delta_P - \delta)} - \frac{\delta}{2} \end{bmatrix}. \quad (2.27)$$

Here, $\delta = \Delta_P + \Delta_C$ is the total detuning of the system which satisfies the condition $\delta \ll \Delta_P$. Thus the above Hamiltonian simplifies to

$$H_{eff} = -\frac{\hbar}{2} \begin{bmatrix} 0 & \frac{\Omega_P \Omega_C}{2\Delta_P} \\ \frac{\Omega_P \Omega_C}{2\Delta_P} & \frac{\Omega_C^2}{2\Delta_P} - 2\delta \end{bmatrix}. \quad (2.28)$$

This is equivalent to a two-level Hamiltonian. The rabi frequency for the effective system is given by $\frac{\Omega_P \Omega_C}{4\Delta} = \Omega_{eff}$. Similarly the effective detuning is given by $\Delta_{eff} = \frac{\Omega_C^2}{2\Delta_P} - 2\delta$. Therefore, the system can be represented by an effective two-level system as shown in figure 2.4(b). The density matrix and the Lindblad operator for the system is found to be

$$\rho = \begin{bmatrix} \rho_{gg} & \rho_{gr} \\ \rho_{rg} & \rho_{rr} \end{bmatrix}. \quad (2.29)$$

$$L_D = \begin{bmatrix} \Gamma_{31}\rho_{rr} & \frac{-\Gamma_{31}\rho_{gr}}{2} \\ \frac{-\Gamma_{rg}\rho_{13}}{2} & -\Gamma_{31}\rho_{rr} \end{bmatrix}. \quad (2.30)$$

Now putting all this terms in the OBE we have

$$\dot{\rho}_{gr} = \frac{i}{2} [\rho_{gr}(2\delta + \frac{|\Omega_p|^2 - |\Omega_c|^2}{2\Delta}) + \Omega_{eff}(2\rho_{rr} - 1)] - \frac{\Gamma_{31}\rho_{gr}}{2}. \quad (2.31)$$

$$\dot{\rho}_{rr} = \frac{i}{2} (\Omega_{eff}^* \rho_{gr} - \rho_{rg} \Omega_{eff}) - \Gamma_{31}\rho_{rr}. \quad (2.32)$$

The equations can be solved for a steady state and the population of the second excited state as well as the coherence can be calculated. As we can see this two equations are similar to the two level equations with the rabi frequency replaced by the Ω_{eff} and the detuning by Δ_{eff} . Details regarding the effective two-level system can be found in .¹⁶⁵

2.5 Rubidium energy levels

Rubidium atomic vapor is used for all the experiments reported in the thesis. It is a suitable candidate for the Rydberg excitation as it has a single valence electron. Natural Rubidium has a combination of two isotopes. ^{87}Rb with natural abundance of 28% and ^{85}Rb with 72%. The ground state of Rubidium is $5^2S_{1/2}$ and the first excited state have two fine structure levels $5^2P_{1/2}$ and $5^2P_{3/2}$. The hyperfine levels of both the isotopes will depend on the total electron angular momentum (**J**) and nuclear angular momentum (**I**) which is 3/2 for ^{87}Rb and 5/2 for ^{85}Rb . The total angular momentum is given by $\mathbf{F} = \mathbf{J} + \mathbf{I}$ and it varies from $\mathbf{J} + \mathbf{I}$ to $\mathbf{J} - \mathbf{I}$ by one unit. The **F** for ground state and first excited state of Rb is tabulated in table 2.1.^{166,167}

SL. no.	Rb Isotope	Energy level	J	I	F
1	^{85}Rb	$5S_{1/2}$	1/2	5/2	2,3
2	^{85}Rb	$5P_{1/2}$	1/2	5/2	2,3
3	^{85}Rb	$5P_{3/2}$	3/2	5/2	1,2,3,4
4	^{87}Rb	$5S_{1/2}$	1/2	3/2	1,2
5	^{87}Rb	$5P_{1/2}$	1/2	3/2	1,2
6	^{87}Rb	$5P_{3/2}$	3/2	3/2	0,1,2,3

Table 2.1: Hyperfine levels of Rubidium 85 and 87 for the ground state $5S_{1/2}$ and excited states $5P_{1/2}$ and $5P_{3/2}$.

^{85}Rb has two hyperfine ground state with $F=2$ and $F=3$. Similarly ^{87}Rb has two hyperfine ground state with $F=1$ and $F=2$. The transitions from $5S_{1/2}$ to both $5P_{1/2}$ and $5P_{3/2}$ are dipole allowed and are known as D1 and D2 transitions respectively. The energy level diagram for both D1 and D2 transitions are shown in figure 2.5. The transitions that satisfy the conditions $\Delta F = 0, \pm 1$ are only allowed, where $\Delta F = |F_2 - F_1|$. The possible transitions can be observed

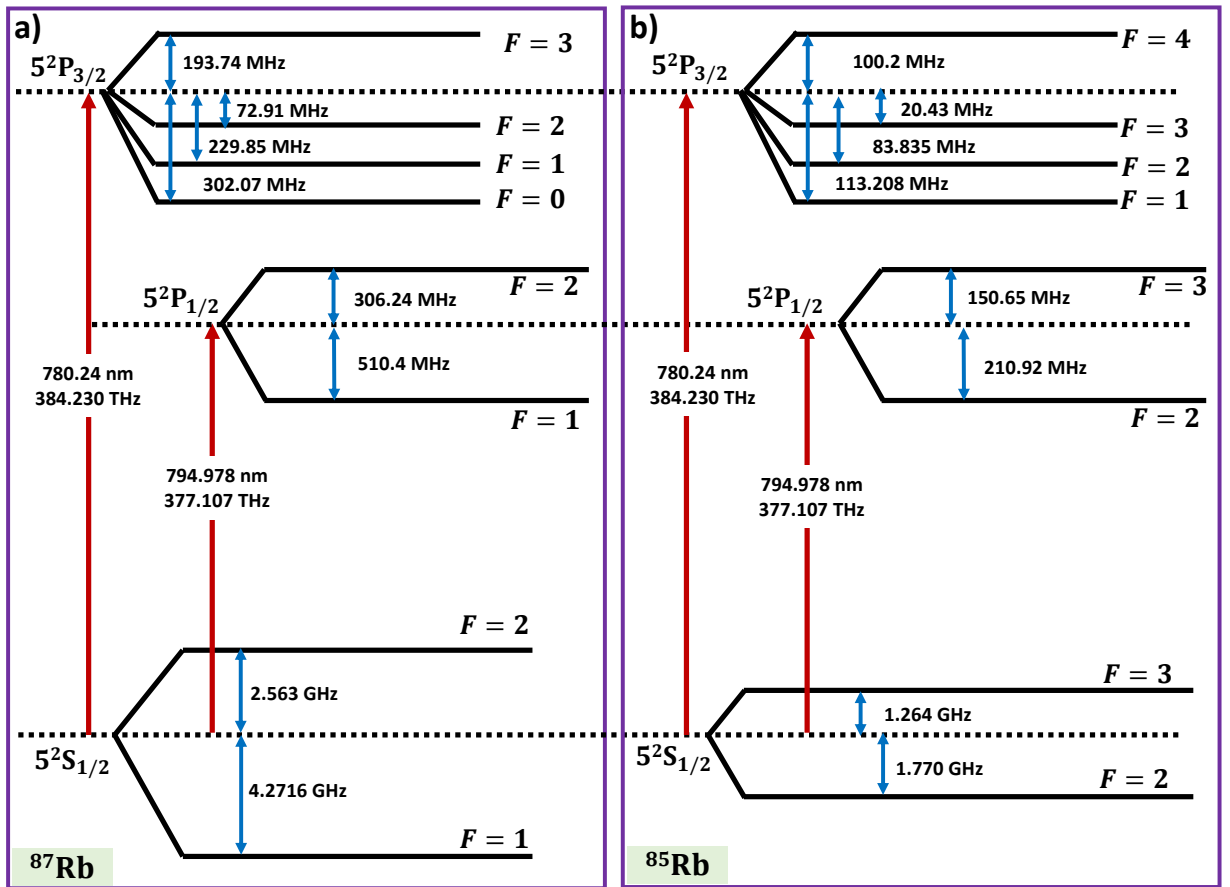


Figure 2.5: Energy level diagram of rubidium atoms. a) ^{87}Rb with hyperfine states and showing the excitation from $5S_{1/2}$ to $5P_{3/2}$ and $5P_{1/2}$. b) ^{85}Rb with hyperfine states and showing the excitation from $5S_{1/2}$ to $5P_{3/2}$ and $5P_{1/2}$.

when the atom is excited to the excited state using a coherent laser beam.

2.6 Doppler broadening

The broadening of spectral lines arising due to Doppler effect as a result of the motion of atoms are known as Doppler broadening. Due to difference in velocities of the atoms, the frequency shift will be different for each atom. The collective effect due to all these atoms is observed as the line broadening. When the particle move towards the light source, the radiation will be blue shifted and when it is moving away from the particle it will be red shifted. Mathematically it can be written as $\omega = \omega_0 \pm \vec{k} \cdot \vec{v}$, where ω is the frequency of the light observed by the atom and

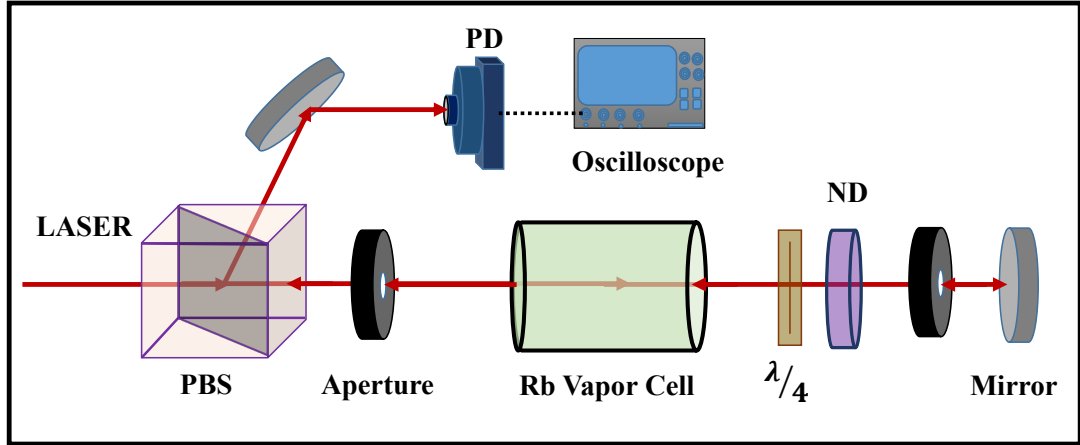


Figure 2.6: The optical set-up for the saturated absorption spectroscopy. $\lambda/4$: quarter wave-plate, ND: Neutral density filter, PBS: Polarizing beam splitter and PD: Photo-detector.

ω_0 is the frequency when the atom is at rest. \vec{k} is the wave vector of the laser and \vec{v} represents the velocity of the atom.

In a thermal atomic ensemble, the velocities of the atoms follow a Maxwell-Boltzmann distribution. This distribution function for an atom moving in one dimension is given by

$$f(v)dv = \frac{1}{\sqrt{\pi}v_p} e^{-v^2/v_p^2} dv. \quad (2.33)$$

Here, $v_p = \sqrt{(2k_b T)/m}$ represents the most probable velocity of the atom. T is the average temperature of the atomic sample, m is the mass of the atom and k_b is the Boltzmann constant. In order to calculate a physical quantity for a thermal ensemble of atom, it is Doppler averaged by integrating over the whole velocity class using equation 2.33.

2.7 Saturation absorption spectroscopy and frequency locking of laser

Saturation absorption spectroscopy (SAS) is a useful tool to precisely determine atomic transition frequencies. This technique is also known as Doppler free spectroscopy and is used for precise determination of the frequency of atomic transitions without cooling the sample. With

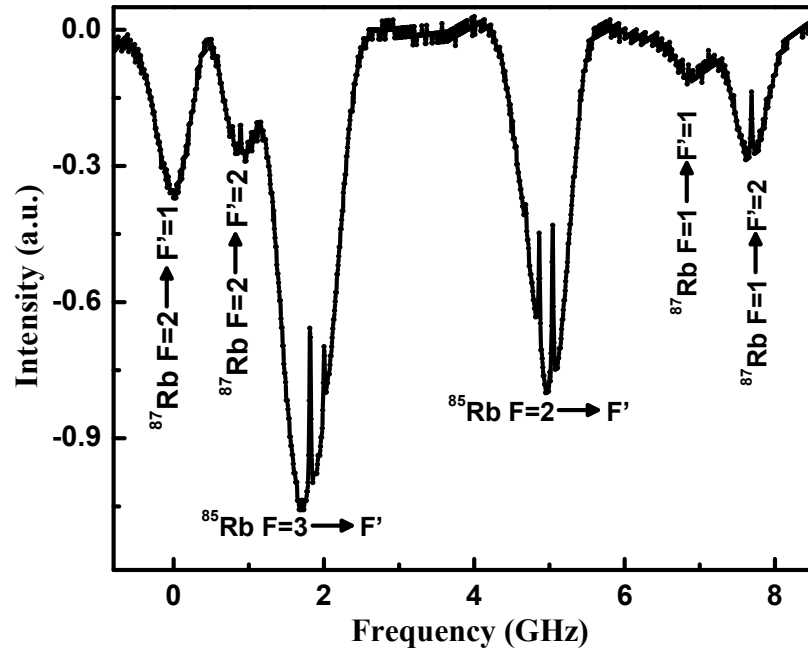


Figure 2.7: Saturated absorption spectroscopy signal for of rubidium for D1 transitions.

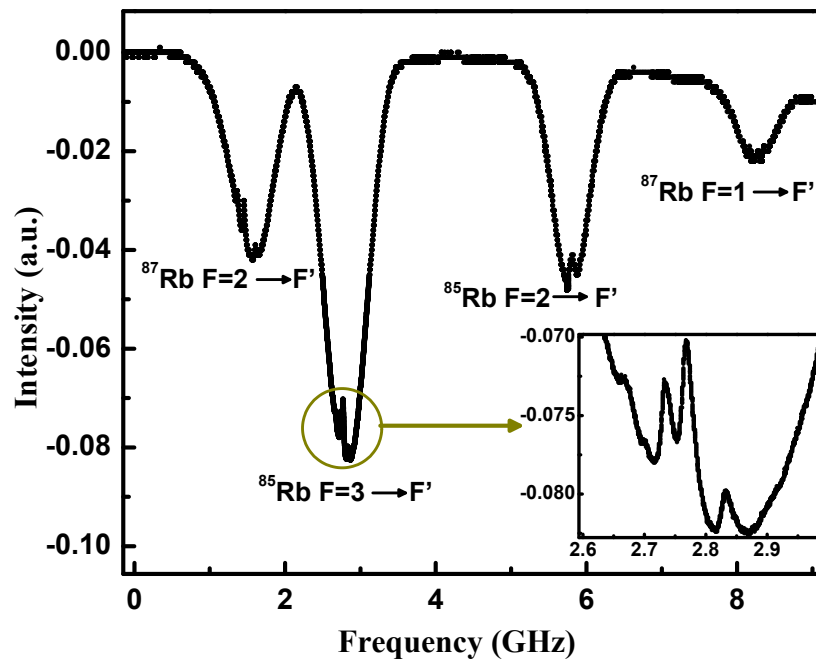


Figure 2.8: Saturated absorption spectroscopy signal for of rubidium for D2 transitions. The inset shows the hyperfine lines and the cross-over line of $F=3$ to F' transition of ^{85}Rb .

a single laser beam resonating to the atomic excitation in a vapor cell at room temperature the absorption line-width is nearly 500 MHz. This is due to the atom's velocity distribution that satisfies the Maxwell-Boltzmann statistics. Hence, a single beam cannot be used to observe the hyperfine transitions. Therefore, SAS technique uses two counter propagating beams satisfying the excitation frequency. As shown in figure 2.6, the laser beam is passed through a polarizing beam splitter (PBS) and then the vapor cell. The power of the beam is $\simeq 100\mu\text{W}$ and is known as the pump beam. It is passed through a neutral density filter (ND) to reduce the power. It is then retro-reflected using a mirror through a $\lambda/4$ plate in order to filter it out through the PBS. This is known as the probe beam and is observed at the photo-detector (PD). The pump beam excites atoms such that the system goes to a saturated state with half of the atoms in the excited state and the other half in the ground state. When the probe beam is applied it sees both the atoms and will be absorbed by the ground state atoms. This intensity profile is observed in the photo-detector.

The sas signal for rubidium D1 and D2 transitions are shown in figure 2.7 and figure 2.8 respectively. The atomic sample has both ^{87}Rb and ^{85}Rb , and hence, there are 4 transitions lines in D2 spectroscopy and similarly there are 6 transition lines in D1. Inside each transitions there are hyperfine levels depending on the atomic states. Along with that there are cross-over lines which arises due the atoms having velocity such that the Doppler shift due to the probe and pump will be equal and opposite. This hyperfine transitions and the cross-over lines are used to precisely frequency lock the laser at the required point.

In order to perform the experiment, the frequency of the laser is stabilized. The LASER is frequency locked using the SAS signal via a digilock-110 module from Toptica. The digilock module uses the SAS and depending on the lock point it supplies a feedback voltage to the piezo that drives the cavity length of the laser.¹⁸⁶ This also supplies a fixed current to the laser diode which is connected internally via a jumper. When the piezo voltage is kept fixed the laser cavity length remains constant and the frequency stabilizes. A screenshot of the software controlling the digilock module is shown in figure 2.9. A lock point is shown in the figure where the laser frequency is locked.

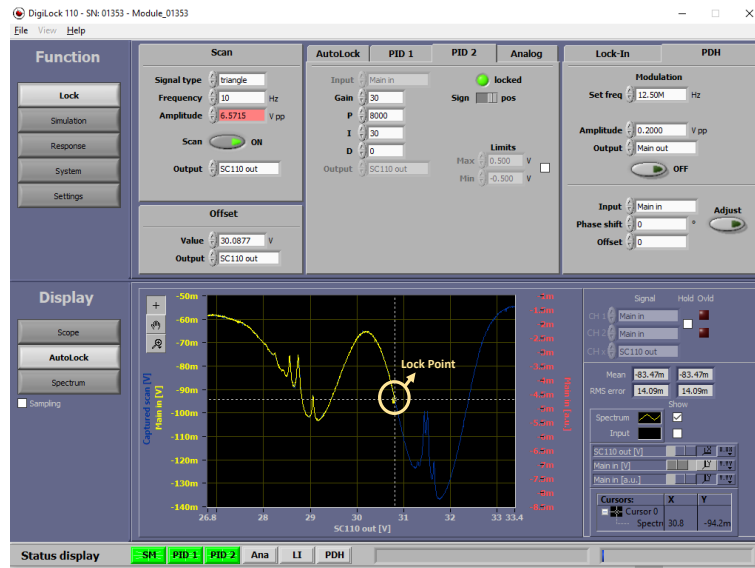


Figure 2.9: A screenshot of digilock110 software. The yellow dot shows the lock point where the laser is frequency locked.

The stabilization of the lock-point depends on the signal strength. When the signal is good enough the lock point remains stable. However, some experiments requires frequency locking using some peaks having very small signal strength. Also, the frequency locking not stable at the top of a peak. In those cases the signal strenght is improved using the PDH technique where a derivative of the absorption signal is generated.¹⁸⁷ Thus, the stability of the lock point at the top of the absorption signal increases in this case.

2.8 Rydberg atoms

Atoms with one or more electrons excited to a state with very high principal quantum number are known as Rydberg atoms. The first indication of Rydberg excitations came from the spectral lines studied by Balmer in 1885. J. R. Rydberg in 1890 began to classify the different spectral transitions and he grouped them into different series.¹³⁴ The significance of Rydberg state became clear after the model of H-atom was proposed by Bohr on 1913.¹³⁵ Since the electron in Rydberg atoms are excited to a very high principal quantum number state, for $l \neq 0$, they remains very far from the atomic nucleus. Thus, these atoms exhibit some exaggerated proper-

ties as compared to the ground state atoms. With gradual development in scientific equipments and theoretical understandings, these properties were uncovered one by one which is explained in details in the next section.^{136, 137, 139–143}

2.8.1 Properties of Rydberg atoms

Heavy alkali metal atoms are most suitable for many experiments as they have a single valence electron in the outermost cell. This electron when excited to a high principal quantum number (n) state known as the Rydberg state, their atomic structure becomes similar to a Hydrogen atom with the nucleus and the surrounding electron shield behaving as a positive charge due to the screening effect. The energy of the excited state for Hydrogen atom is proportional to $1/n^2$. The difference arises for heavy alkali atoms when the Rydberg state electron orbits in a state with low orbital angular momentum quantum number (l), where the electron's orbit is highly elliptical. There it has a significant probability to penetrate the electron cloud and interact with the nucleus. Hence, the binding energy of the system increases and thus decreasing the total energy. To accommodate this action of the core at small distances, the quantum defect δ is included in the system. The quantum defect is a dimensionless state-dependent quantity that depends on n and l of the atomic state. So the binding energy of the Rydberg atom is given by $E = -\frac{R_y}{(n - \delta)^2} = -\frac{R_y}{(n^*)^2}$. Here R_y is the Rydberg constant which is $109736.605 \text{ cm}^{-1}$ and $n^* = (n - \delta)$.¹³⁴

Some of the properties of Rydberg atoms and their scaling with n is tabulated in table 2.2. These atoms are huge in size as the radius r varies with n^2 . So, the dipole moment $\mu = e\langle r \rangle$ varies as n^2 and is large in magnitude. These atoms are long lived and the radiative decay lifetime goes as n^3 . For a state with $n = 100$ the size of the atom is of the order of $1 \mu\text{m}$ i.e. the typical size of a bacteria and the lifetime is around $200 \mu\text{s}$. The energy difference between two adjacent Rydberg states goes as $\Delta_n = n^{-3}$. Thus, the separation between the states keeps on decreasing for higher Rydberg states. Since the electron is very loosely bound to the atomic nucleus, Rydberg atoms are very sensitive to external electric fields. The dependence of ionization energy due to externally applied electric field (E) for Rydberg atoms is of the order

of n^{-4} . So the polarizability of the system is given by $\alpha = \frac{\mu^2}{\Delta_n}$ which varies as n^7 ,¹⁴⁴⁻¹⁴⁷ where, μ is the dipole moment between the coupling states. Similarly the Rabi frequency ($\Omega \propto \frac{\mu|E|}{\hbar}$) of the Rydberg state varies as $n^{-3/2}$.¹³⁷ Here, E is the electric field due to the applied laser.

SL. No.	Atomic properties	Scaling with 'n'	Typical Values for $n = 60D$ of Rb
1	Binding Energy	n^{-2}	3.96 meV
2	Energy Level Spacing	n^{-3}	33.5 GHz
3	Dipole Moment	n^2	138.3 ea_0
4	Orbital Radius	n^2	5156 a_0
5	Radiative Lifetime	n^3	215 μs
6	Electric field	n^{-4}	44 V/cm
7	Polarizability	n^7	191 MHz/(V/cm) ²

Table 2.2: Scaling of atomic properties with 'n' for Rydberg state.

2.8.2 Interaction of Rydberg atoms

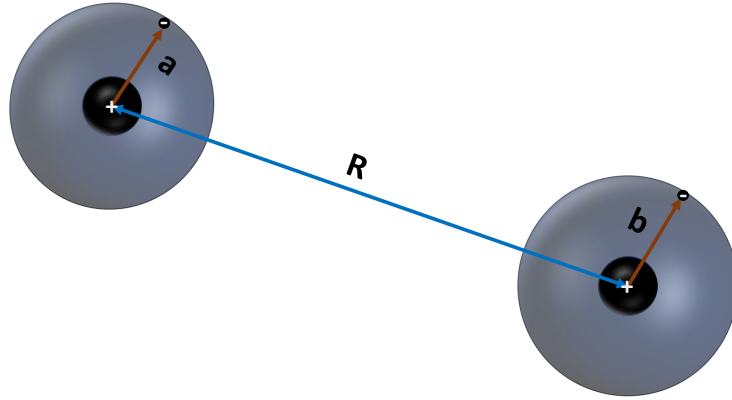


Figure 2.10: A system of two Rydberg atoms with inter nuclear separation R . a and b are the most probable radius of the electron from the atomic nucleus.

Rydberg electrons being far from atomic nucleus and having large dipole moments are considered to be a good candidate to study inter-atomic interaction. Rydberg atoms interact strongly with each other depending on their inter-particle separation. For two Rydberg atoms separated by a distance $R \gg n^2 a_0$, where a_0 is the Bohr's radius, the leading electrostatic

interaction is the dipole-dipole interaction. The overlap between the atoms can be neglected at such large separation. For a two-atom system shown in figure 2.10 this interaction is given by⁴

$$V(R) = \frac{e^2}{\mathbf{R}^3} \left(\mathbf{a} \cdot \mathbf{b} - 3 \frac{(\mathbf{a} \cdot \mathbf{R}) \times (\mathbf{R} \cdot \mathbf{b})}{\mathbf{R}^2} \right). \quad (2.34)$$

Where \mathbf{a} and \mathbf{b} are the positions of the two Rydberg electrons from their respective nuclei and e represents the charge of the electron. In absence of externally applied electric field, the atomic state has a degeneracy of $2J+1$, where J is the total angular momentum quantum number. Long range interaction between the Rydberg atoms are considered to be arising from two predominantly coupled channels. The contribution of the nearest energy level will be the dominating in this case. Contribution of interaction of atoms in the same Rydberg state $|rr\rangle$ or in a nearby Rydberg state $|r'r''\rangle$ with energy defect $\delta = E(r') + E(r'') - 2E(r)$ arises due to the fluctuation in energy. This energy defect arises as the electron is far from the atomic nucleus and is fluctuating with large dipole moment.⁴ From the time independent Schrodinger's equation we have

$$(H_0 + H_I) \begin{pmatrix} |rr\rangle \\ |r'r''\rangle \end{pmatrix} = \Delta \begin{pmatrix} |rr\rangle \\ |r'r''\rangle \end{pmatrix}.$$

Here Δ is the energy eigenvalue for the dipole-dipole interaction. H_0 and H_I are the unperturbed Hamiltonian and the interaction Hamiltonian respectively.

$$\begin{pmatrix} 0 & V(R) \\ V(R)^\dagger & \delta \end{pmatrix} \begin{pmatrix} |rr\rangle \\ |r'r''\rangle \end{pmatrix} = \Delta \begin{pmatrix} |rr\rangle \\ |r'r''\rangle \end{pmatrix}. \quad (2.35)$$

The LHS of the above equations is diagonalized in order to calculate the eigenvalues which gives

$$\Delta = \frac{\delta \pm \sqrt{\delta^2 + 4V(R)^2}}{2}. \quad (2.36)$$

Depending on the interaction strength as compared to the energy defect there are two kinds

of interactions arise between the atoms, Van der Waals interaction and dipole-dipole interaction.

Van der Waals interaction

Consider the case of fluctuating dipoles. Here, interaction strength is small compared to quantum defect i.e. $V \ll \delta$, equation 2.36 can be expanded using Taylor's expansion to have

$$\Delta \simeq -\frac{V(R)^2}{\delta} = -\frac{C_6}{R^6}. \quad (2.37)$$

This kind of interaction is called the Van der Waals interaction and it has a $\frac{1}{R^6}$ dependence. The sign of the interaction depends on δ . For Rydberg atoms, $C_6 = \frac{(e^2 \langle a \rangle \langle b \rangle)^2}{\delta}$ defines the strength of interaction. Using the scaling presented in table 2.2, $C_6 \propto n^{11}$. Thus, it can take a very large value depending on the principal quantum number state to which the atom is excited. In the case of two rubidium atoms the Van der Waals coefficient for Rydberg state (50s) is nearly 11 order of magnitude greater than that of the ground state (5s).¹⁴⁸ The contribution of the nearest neighbor is significantly large as compared to other atoms for this kind of interaction. The results presented in this thesis are in thermal atomic vapor where the interaction between the atoms is of Van der Waals kind.

Dipole-dipole interaction

The other kind of interaction is the Dipole-Dipole interaction which arises for permanent dipoles. To study this interaction, the dipoles are aligned using an external electric field. Here the interaction strength is much larger than the quantum defect i.e. $V \gg \delta$ where,

$$\Delta \approx \pm V(R) \approx \pm \frac{C_3}{R^3}. \quad (2.38)$$

The quantity $C_3 = e^2 \langle a \rangle \langle b \rangle$ defines the interaction coefficient and it depends on the principal quantum number as $C_3 \propto n^4$. This interaction occurs at short range where the interaction strength is very high. The contribution of the other surrounding atoms along with the nearest neighbor is also significant for this kind of interaction.¹⁴⁸

2.8.3 Interaction induced Rydberg blockade

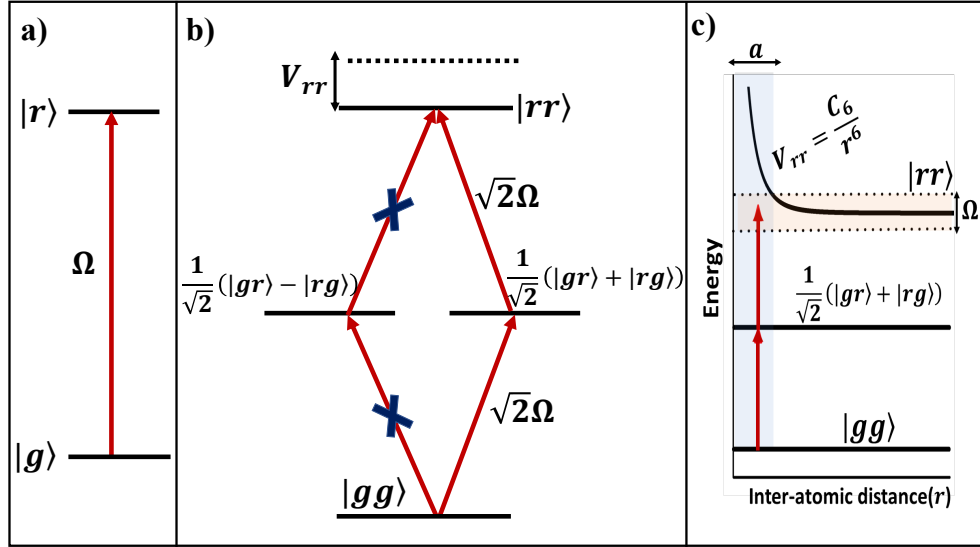


Figure 2.11: The phenomena of Rydberg blockade a) Two-level system driven with a laser field of Rabi frequency Ω to the Rydberg state, b) a two-atom system where the interaction is zero and c) Two-atom system satisfying the blockade condition where a defines the blockade radius.

Rydberg blockade is one of the most interesting effect that arises between two interacting Rydberg atoms.^{4,77,81,149–154} It creates a correlated ensemble of atoms that are observed in various systems and have a variety of applications. Consider a two-level system as shown in figure 2.11(a) with ground state $|g\rangle$ and excited state $|r\rangle$ coupled by an applied laser with Rabi frequency Ω . If we consider two such atoms, the energy level diagram for the composite system can be presented as given in figure 2.11(b). When both the atoms are in ground state it is represented by $|gg\rangle$, when one of them is excited it is represented by $|+\rangle = \frac{1}{\sqrt{2}}(|gr\rangle + |rg\rangle)$ or $|-\rangle = \frac{1}{\sqrt{2}}(|gr\rangle - |rg\rangle)$ and when both are in Rydberg it is $|rr\rangle$ state. The rabi frequency of the coupling of the transition $|gg\rangle \rightarrow |+\rangle$ is $\sqrt{2}\Omega$ and for the transition $|gg\rangle \rightarrow |-\rangle$ it is 0. Similarly, the rabi frequency of the coupling of the transition $|+\rangle \rightarrow |rr\rangle$ is $\sqrt{2}\Omega$ and for the transition $|-\rangle \rightarrow |rr\rangle$ it is 0. The atoms are considered to be non-interacting in this case with $V_{rr} = 0$ and hence both the atoms are excited to the Rydberg state. However, when the system is considered to be interacting following the Van der Waals interaction, the inter-atomic interaction strength will change depending on their separation. As shown in figure 2.11(c), for

two atoms within the length scale a , the interaction energy shift will be larger than the line width of the Rydberg state. Therefore, the probability of simultaneous excitation of both the atoms to the Rydberg state is significantly small. In other words, the excitation of the other atoms present within a separation of a from the Rydberg excited atom is blockaded. This phenomenon is known as Rydberg blockade and a is known as blockade radius.

The interaction Hamiltonian for the energy level diagram shown in figure 2.11(c) is given by

$$H = \Omega (|gg\rangle \langle gr| + |gg\rangle \langle rg| + |rg\rangle \langle rr| + |gr\rangle \langle rr| + H.C.) \pm 2V_{rr} |rr\rangle \langle rr|. \quad (2.39)$$

Here \pm sign depends on whether the interaction is attractive or repulsive. When the interaction is weak compared to the Rabi frequency, the system behaves as non-interacting. However, when the interaction is strong such that $V_{rr} > \hbar\Omega$, the applied laser cannot be coupled to the state $|rr\rangle$. Thus, the system will remain in the entangled state $|+\rangle = \frac{1}{\sqrt{2}}(|gr\rangle + |rg\rangle)$. The Hamiltonian of the laser coupling between the state $|gg\rangle$ and $|+\rangle$ is given by

$$H = \sqrt{2}\Omega (|gg\rangle \langle +| + H.C.).$$

From the above expression, it can be observed that the Rabi frequency of the system enhances by a factor of $\sqrt{2}$. Also as the atoms cannot be excited to the state $|rr\rangle$, the population of the Rydberg state will reduce to half compared to the non-interacting two-atom system. Similarly if there are N atoms inside the length scale a , the Rabi frequency of the system will be $\sqrt{N}\Omega$ and population of the Rydberg state will be $\frac{\rho_{rr}}{N}$. This blockade phenomenon creates an entanglement between the participating atoms and therefore it is very useful in quantum information processing.⁷⁷⁻⁸⁹

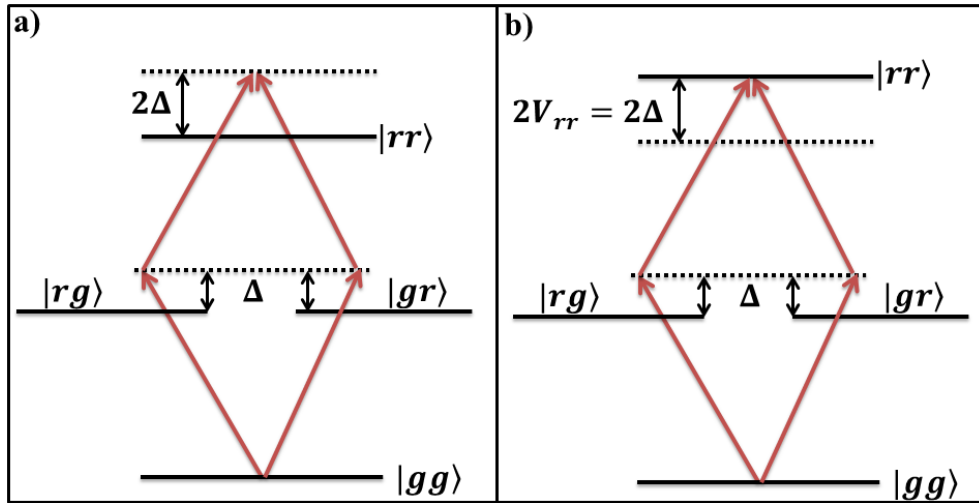


Figure 2.12: *a) Energy level diagram for two non-interacting atomic system excited to Rydberg state in a cold atomic ensemble. b) Interacting two-atom system excited to the Rydberg state depicting the energy level shift of $|rr\rangle$ state due to Rydberg-Rydberg interaction satisfying the resonance to the applied laser.*

2.8.4 Interaction induced Rydberg anti-blockade

Strong Rydberg-Rydberg interaction also introduces another effect known as Rydberg anti-blockade. This is also an interesting phenomenon observed in various atomic systems and has application in quantum information processing as studied by various groups.^{90–93,103–105} This can be understood in a similar way as that of the blockade phenomenon. Consider a two-atom system as shown in figure 2.12(a). The applied laser is detuned by Δ from the atomic resonance. Therefore, individual atom excitation as well as the simultaneous two-atom excitation are not possible as shown in figure 2.12(a) for a non-interacting system. However, if the atoms are interacting and are separated in such a way that, the energy level shift due to interaction is equal to the laser detuning i.e. $V_{rr} = 2\Delta$. In that case even if the atoms are not satisfying resonance condition individually they satisfy simultaneous two-atom resonance and are excited to the Rydberg state due to interaction as shown in figure 2.12(b). This phenomenon is known as Rydberg anti-blockade.

In a cold atomic ensemble, the atoms are considered to be frozen and effect of velocity is negligible. However, this effect can also be observed in thermal atomic vapor where atoms move with broad range of velocities. Suppose two atoms are moving with two different veloc-

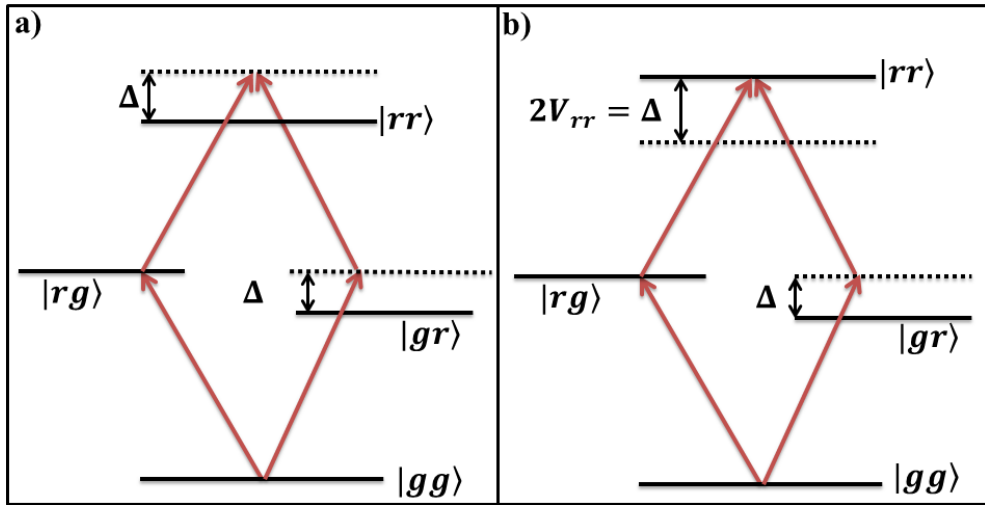


Figure 2.13: *a) Energy level diagram for non-interacting two-atom system in thermal atomic vapour each moving with different velocity. b) Interacting two-atom system in thermal vapor depicting the energy level shift of $|rr\rangle$ state due to interaction satisfying resonance to the applied laser.*

ities. Thus, the laser detunings will be different for both due to Doppler shift. One of them is resonant to the applied laser while the other one is out of resonance as shown in figure 2.13(a). When the atoms are non-interacting the resonant atom will be excited, but the off-resonant atom cannot be excited. However, if the atoms are interacting with suitable inter-particle separation such that $V_{rr} = \Delta$, the off-resonant atom is also excited to the Rydberg state as shown in figure 2.13 (b). This is due to the Rydberg anti-blockade effect in thermal atomic vapor. This phenomenon also leads to generation of correlated atomic ensemble which has applications in quantum information processing.^{90–93, 103–105}

Chapter 3

Robust measurement of Rydberg population in thermal vapor using OHDT

Rydberg atoms are enriched with strong dipolar interaction which make them suitable for a variety of applications.⁴ These dipolar interaction lead to phenomena like rydberg blockade^{42–47,54,55} and anti-blockade^{90–93,168,169} in cold atomic ensemble. Rydberg population is measured using the absorption of the probe beam in a two photon excitation scheme.¹⁷⁰ However, the precision of the measurement of population in this experiment is found to be 10^{-2} . In ultra cold atomic ensemble, Rydberg blockade is imaged using Rydberg tomography technique.¹⁷¹ Micro-channel plates are also used in cold atomic ensemble to detect Rydberg atoms by ionizing them with an external DC electric field. However, these techniques cannot be used for thermal atomic vapor as the system contains some initial ions sticking to the dielectric surface of the vapor cell. Various interferometric techniques have been used in different experiments to improve the measurement and the data quality.^{24–26,28,172} Optical heterodyne detection technique (OHDT) is extensively used for phase sensitive measurements in various systems.^{173–175} OHDT has been developed in our group to observe the dispersion of the probe beam and to measure the Rydberg population.^{126,128,131} The sensitivity of the OHDT is found to be very high which can measure a Rydberg population of the order of 10^{-7} .¹²⁸ However, while performing the experiment, the system is stabilized in order to reduce error in the experiment due

to the density fluctuation.

In this chapter, we have presented a modified OHDT which is independent of any initial phase offset between the beat signals. Therefore the data can be collected in a faster way and is also reliable. This technique has been used to study the Rydberg anti-blockade in thermal atomic vapor. The dispersion peak height of the anti-blockade peak is found to be independent of the phase offset.¹³¹

3.1 Overview of the OHDT

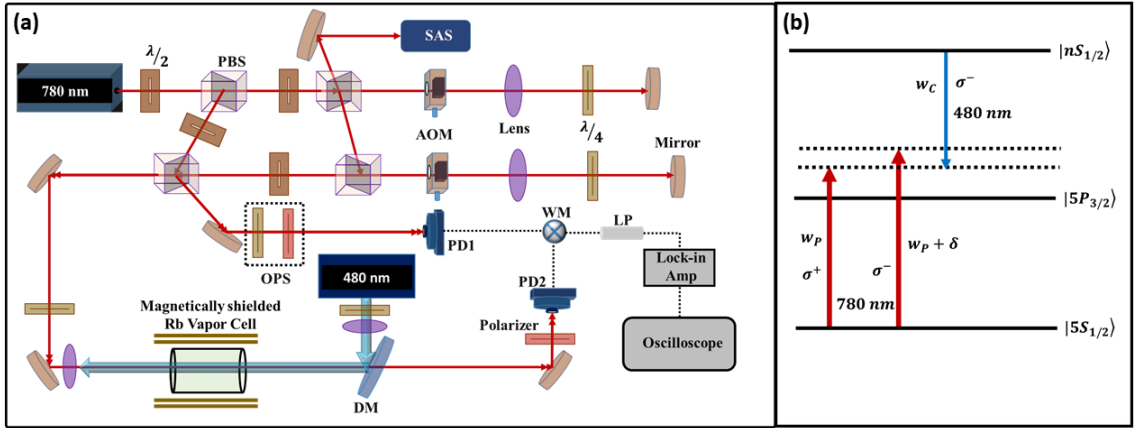


Figure 3.1: (a) Experimental Set-up to measure the dispersion of the probe beam using OHDT due to the two photon excitation to the Rydberg state. $\lambda/2$: Half wave plate, $\lambda/4$: Quarter wave plate, PBS: Polarizing beam splitter, AOM: Acousto-optic modulator, DM: Dichroic mirror, PD: Photo detector, WM: Waveform mixer OPS: optical phase shifter, SAS: Saturated absorption spectroscopy and LP: Low pass filter. (b) Energy level diagram presenting two-photon excitation to the Rydberg state.

Optical Heterodyne Detection Technique (OHDT) is an useful tool for phase sensitive measurements. The details about the OHDT is presented in the references .^{126, 128} In both the reported works, the dispersion of the probe beam is measured during two-photon excitation of the rubidium atom to the Rydberg state. The optical set-up for the OHDT is depicted in figure 3.1(a). The technique uses two probe beams which are frequency separated using acousto-optic modulators (AOMs). Both the beams are then interfered using a polarizing beam splitter (PBS). Two interference signals are generated at both output faces of the PBS. Probe beams coming out

from one face of the PBS is detected in a detector directly and is taken as the reference beat. Beams from the other output face of the PBS is passed through the medium and is detected in another detector which is considered as the signal beat. The phase difference between the reference and the signal beat (ϕ_0) can be varied using a combination of $\lambda/4$ plate and a polarizer known as the optical phase shifter (OPS).¹²⁶ When the coupling beam is applied the signal beat will undergo a phase shift (ϕ) satisfying two-photon excitation to the Rydberg state as depicted in figure 3.1(b). This phase shift is measured by comparing the reference beat with the signal beat. These two beats are multiplied using a waveform mixer and is passed through a low pass filter. Output of the low pass filter is given by

$$S_L \approx 2A_r A_s e^{-\frac{kl}{2} \text{Im}[\chi_{3L}]} \cos(\phi + \phi_0). \quad (3.1)$$

Here, l is the length of the vapor cell and k is the wave vector of the applied laser. A_r and A_s represent the amplitudes of the reference and the signal beat respectively. $\chi_{3L} = \chi - \chi_{2L}$ represents the susceptibility of the probe beam due to two-photon excitation process only, where χ is the total susceptibility of the system and χ_{2L} is the susceptibility of the probe in absence of the coupling beam. Depending on the value of ϕ_0 , the absorption ($\phi_0 = 0$) or the dispersion ($\phi_0 = \pi/2$) of the probe beam can be measured. The signal observed at the output of the low pass filter setting $\phi_0 = \pi/2$ is found to be

$$S_L \approx 2A_r A_s e^{-\frac{kl}{2} \text{Im}[\chi_{3L}]} \phi. \quad (3.2)$$

The susceptibility $\text{Re}[\chi_{3L}]$, can be calculated from ϕ using the lock-in amplifier parameters and the sensitivity of the waveform mixer.¹²⁸ As presented in the reference,¹²⁸ $\text{Re}[\chi_{3L}]$ gives a measure of the population of the Rydberg state ρ_{rr} . Therefore, the dispersion observed using OHDT can be used to calculate ρ_{rr} .

Since the experiments presented in the references^{128,131} are in thermal vapor ensemble, the vapor density of the system is varied in order to change the inter-particle separation. However,

this changes the phase offset ϕ_0 of the system which ultimately changes the observed signal strength. Therefore, before taking a measurement the density of the system is stabilized and the OPS is adjusted in order to maximize the signal strength. Some experiments¹³¹ require a larger number of data in order to have a better statistics. Thus, experiments with current technique is time consuming. Hence, the technique is modified in order to avoid any variation in signal strength due to change in phase offset.

3.2 Modified OHDT

3.2.1 Experimental set-up

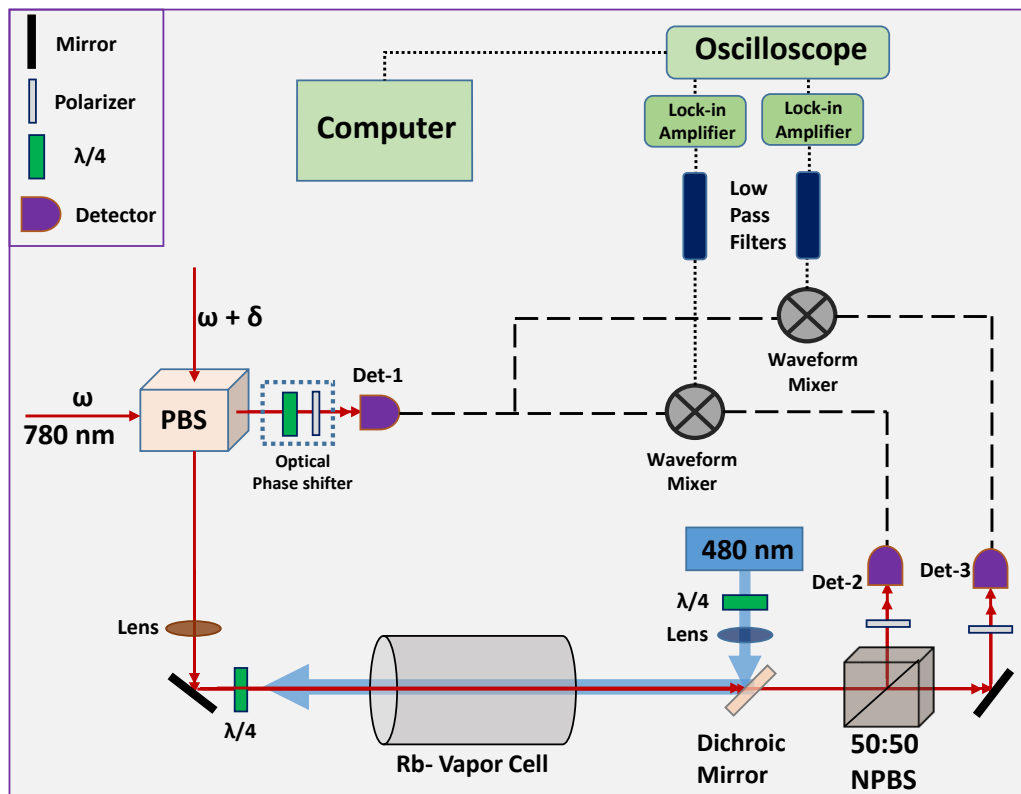


Figure 3.2: The modified experimental set up for the optical heterodyne detection technique. PBS: polarizing beam splitter, NPBS: non-polarizing beam splitter.

The modified experimental set-up of the OHDT is shown in figure 3.2. Two probe beams with frequency offset of $\delta = 800$ MHz is prepared using AOMs. Both the beams are interfered

using PBS. Interference from one face of the PBS is fed to a fast detector Det-1, which is consider as the reference. Probe beams from other face of the PBS is passed through the experimental vapor cell. A 50:50 non-polarizing beam splitter (NPBS) is placed in this path of the probes after the experimental vapor cell as shown in figure 3.2. Interference signal from both output faces of the NPBS is fed to two fast detectors Det-2 and Det-3 which are considered as signal beats. The phase difference between the two signal beats is adjusted using the OPS placed before the detectors. Apart from that, the phase difference between the reference and the signal beats are adjusted using the optical phase shifter. The two signal beats were individually multiplied with the reference beat using two waveform mixers and are passed through low pass filters. The output signals from the two low pass filters were fed to lock-in amplifiers to improve the signal to noise ratio. The coupling beam is intensity modulated by using an optical chopper and the chopper frequency is used as a reference signal for the lock-in amplifier. The output signal is observed in an oscilloscope. The signal beats will undergo a phase change due to the presence of a counter-propagating coupling beam satisfying two photon resonance to the Rydberg state. This phase change can be observed as a dispersion signal from both the outputs. The data are collected in a computer by interfacing the oscilloscope using LABView program.

Let us consider that the output signal from the Det-1 is $D_r = A_r \cos(\phi_r + \delta t)$, where A_r and ϕ_r are the amplitude and phase of the reference beat and δ is the beat frequency. The output signals from the det-2 and det-3 are $D_{s1} = A_s e^{-\frac{kl}{2} \text{Im}(\chi_{3L})} \cos(\phi_s + \phi_X + \delta t)$ and $D_{s2} = A_s e^{-\frac{kl}{2} \text{Im}(\chi_{3L})} \cos(\phi_s + \phi_Y + \delta t)$ respectively. A_s and ϕ_s represent the amplitude and phase of the signal beat due to two photon excitation. ϕ_X and ϕ_Y represent the phase difference of the reference and signal beat in absence of the coupling beam for Det-2 and Det-3 respectively. The outputs of the low pass filters after multiplication of the signal beats with reference beat are given by

$$S_{LX} = 2A_r A_s e^{-\frac{kl}{2} \text{Im}(\chi_{3L})} \cos(\phi_s + \phi_X) \quad (3.3)$$

$$S_{LY} = 2A_r A_s e^{-\frac{kl}{2} \text{Im}(\chi_{3L})} \cos(\phi_s + \phi_Y). \quad (3.4)$$

$\phi_X \simeq \frac{\pi}{4}$ and $\phi_Y = \phi_X + \frac{\pi}{2}$ is the experimental regime. ϕ_X is varied from $\frac{\pi}{4}$ to $\frac{\pi}{2}$, which is the range where this technique works well. In this regime, $\phi_s \ll \phi_X, \phi_Y$, the above two expressions are expanded using Taylor's series. Neglecting second or higher order terms of ϕ_s the expressions are simplified to

$$S_{LX} = 2A_r A_s e^{-\frac{kl}{2} \text{Im}(\chi_{3L})} [\cos(\phi_X) - \phi_s \sin(\phi_X)] \quad (3.5)$$

$$S_{LY} = 2A_r A_s e^{-\frac{kl}{2} \text{Im}(\chi_{3L})} [\cos(\phi_Y) - \phi_s \sin(\phi_Y)]. \quad (3.6)$$

These two signals are passed through the lock-in amplifiers to filter out the first two terms which gives a constant DC value. The remaining phase dependent signals are given by

$$S_{LX} = 2A_r A_s e^{-\frac{kl}{2} \text{Im}(\chi_{3L})} [\phi_s \sin(\phi_X)]$$

$$S_{LY} = 2A_r A_s e^{-\frac{kl}{2} \text{Im}(\chi_{3L})} [\phi_s \sin(\phi_Y)]$$

Using these two expressions we calculated the quantity

$$R = \sqrt{S_{LX}^2 + S_{LY}^2} = 2A_r A_s e^{-\frac{kl}{2} \text{Im}(\chi_{3L})} \phi_s \sqrt{(\sin(\phi_X))^2 + (\sin(\phi_Y))^2}.$$

The phase difference between the signal beats is varied using optical phase shifter placed before the detectors. When we set $\phi_X - \phi_Y = \frac{\pi}{2}$,

$$R = \sqrt{S_{LX}^2 + S_{LY}^2} = 2A_r A_s e^{-\frac{kl}{2} \text{Im}(\chi_{3L})} \phi_s. \quad (3.7)$$

Thus, R will be independent of the phase offset variation between the signal and reference beat for $\phi_X - \phi_Y = \frac{\pi}{2}$. In this condition any variation of density which changes the phase offset will not change the signal strength of the experiment. However, when $\phi_X - \phi_Y \neq \frac{\pi}{2}$, the signal will vary depending on the phase offset.

3.2.2 Experimental observations and analysis

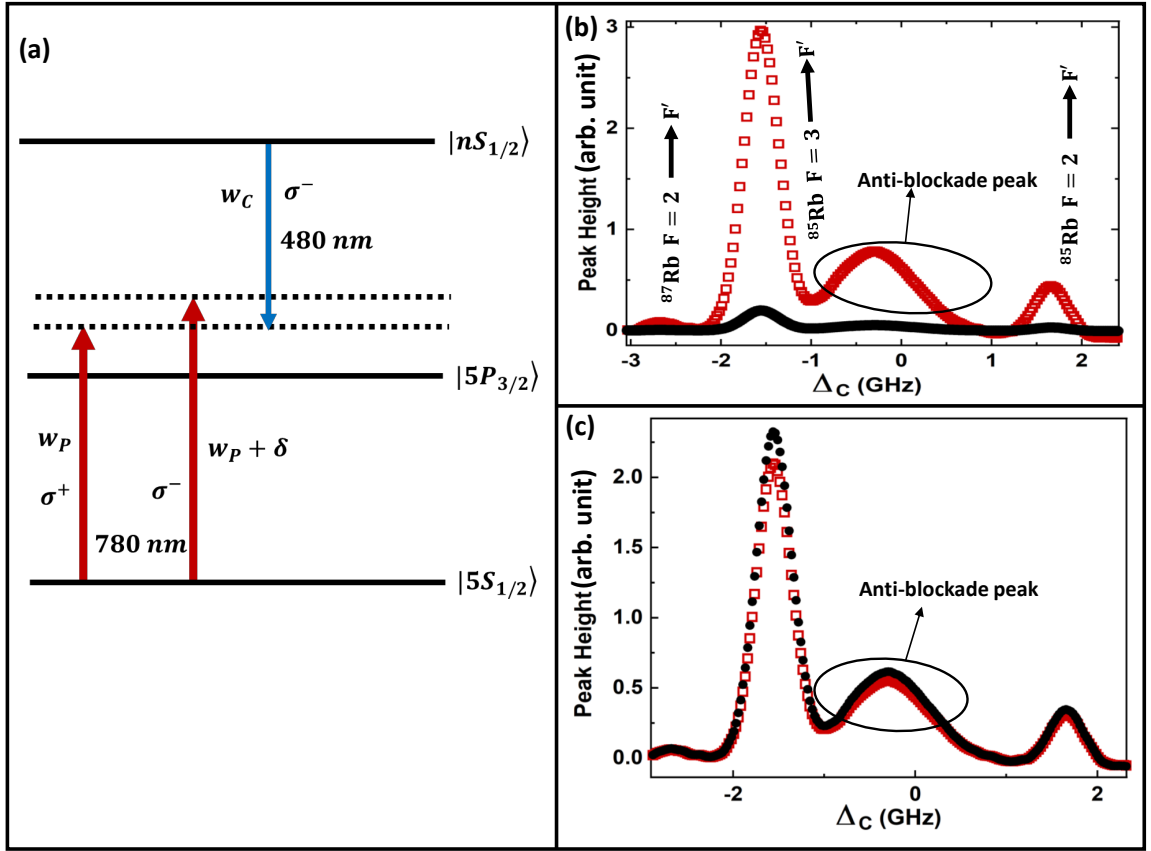


Figure 3.3: (a) Energy level diagram of the two photon excitation to the Rydberg state. (b) Observed dispersion signal with the variation of the coupling laser frequency for S_{LX} (\square) and S_{LY} (\bullet) with $\phi_X = \pi/2$ and $\phi_Y = 0$ and (c) with $\phi_X = \frac{\pi}{4}$ and $\phi_Y = \frac{\pi}{4}$.

In order to verify the efficiency of the modified technique, we performed an experiment in thermal rubidium vapor. We observed the dispersion of the probe beam during the two photon excitation to the Rydberg state $33S_{1/2}$. The energy level diagram for the excitation is shown in figure 3.3(a). The dispersion of the probe beam is observed at both signal beat detectors. The signals observed at the oscilloscope are depicted in figure 3.3 (b) where $\phi_X = \pi/2$ and $\phi_Y = 0$. In this case the dispersion observed at DET-2 is maximum while that of DET-3 is minimum. When $\phi_X = \frac{\pi}{4}$ and $\phi_Y = \frac{\pi}{4}$ the observed signal is depicted in figure 3.3(c). There are four peaks observed in the dispersion spectrum when the coupling laser is scanned over few GHz. Out of them, three of the peaks correspond to the hyperfine lines of rubidium as

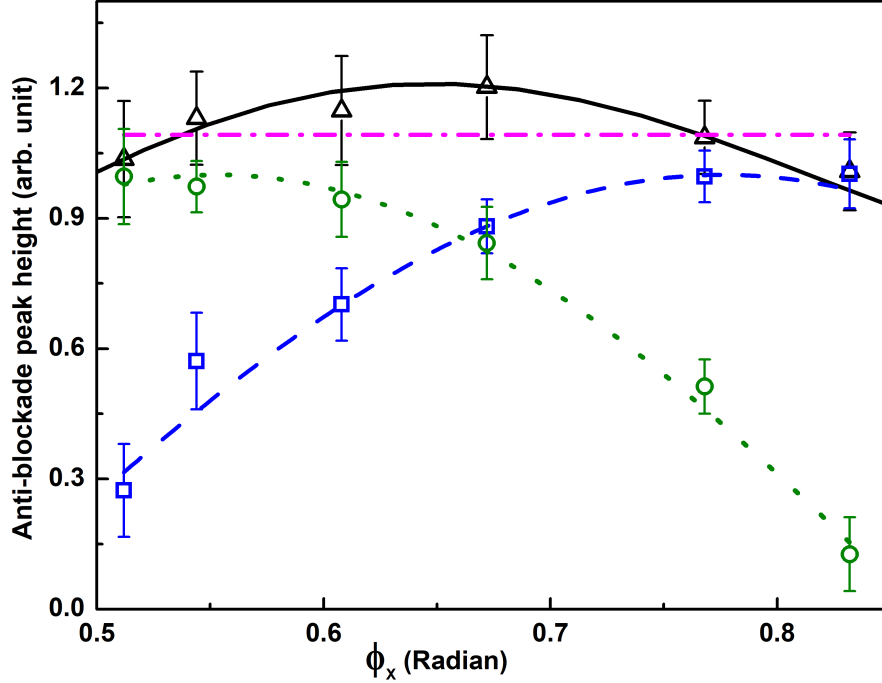


Figure 3.4: The dispersion peak height for anti-blockade peak as a function of ϕ_X for S_{LX} (\circ), S_{LY} (\square) and R (\triangle). The error bar represents the statistical error. The dotted and the dashed lines are the fitting of the data S_{LX} and S_{LY} . The dotted dash straight line is the linear fitting of the measured R values and the solid line is the fitting of with $\sqrt{(\sin(\phi_X - \phi_{c1}))^2 + (\cos(\phi_X - \phi_{c2}))^2}$.

depicted in figure 3.3(b). However, a fourth peak that doesnot satisfy two-photon excitation also appears in the signal. The details of the anti-blockade peak is explained in section 4.3. In order to varify the technique, the anti-blockade peak height is measured by varying the phase difference between the reference and the signal beats.¹³¹ The dispersion signal after both the lock in amplifiers were observed using an oscilloscope. The data is collected for S_{LX} and S_{LY} using a LABView program by varying the phase offset between the reference and signal beats.

As shown in figure 3.4, when ϕ_X is varied the signal in both S_{LX} and S_{LY} changes. The phase difference of the beats observed in DET-2 and DET-3 is set at $\phi_X - \phi_Y = \frac{\pi}{2}$. Thus, when the signal in S_{LX} becomes maximum, S_{LY} goes to minimum and vice versa. The dotted and the dashed line show the fitting of these two data to the functions $a_1 \sin(\phi_X - \phi_{c1})$ and $a_2 \cos(\phi_X - \phi_{c2})$ respectively. Here a_1 (a_2) and ϕ_{c1} (ϕ_{c2}) represents the amplitude and phase of the data S_{LX} (S_{LY}). The reduced χ^2 of the fitting of the S_{LX} and S_{LY} data to the theoretical

model is found to be 0.21 and 0.39 respectively. As the number of data point is less, the reduced χ^2 is smaller than expected. This also indicates the fact that the variation is similar to that presented in theory. Both the data set were normalized to the amplitudes (a_1, a_2) of the fitting. $\phi_{XY} = \phi_{c1} - \phi_{c2}$, is found to be 0.2263 ± 0.0134 rad. This is arising as the phase difference between the two signal beats was not $\pi/2$. This could be due to the electronics used in the experiment or the cable length used for propagation of beat signal. R is calculated using the formula presented above and is expected to have a constant value. R is found to be fitting to a straight line with slope 0 and an intercept of $C = 1.0925 \pm 0.028$. However, there is a small variation of R from the straight line fitting as presented in the figure. This is due to the fact that $\phi_{c1} - \phi_{c2} \neq 0$. As presented in fig 3.4, when the measured R values were fit to a function $\sqrt{(\sin(\phi_X - \phi_{c1}))^2 + (\cos(\phi_X - \phi_{c2}))^2}$, the reduced χ^2 is observed to be 0.09. This could be due to less number of data in the experimental observation. Here ϕ_{c1} and ϕ_{c2} are the phases calculated using the fitting of the data S_{LX} and S_{LY} respectively. Even if we neglect the small phase variation arising in the system and consider the straight line fitting, the technique provides a phase offset independent measurement with an error of 3% as observed for the value of C .

3.3 Conclusion

We have presented a modified OHDT which is independent of any phase offset variation between the reference and the signal beat. This technique have been verified by performing an experiment in thermal atomic vapor where the anti-blockade peak height for two photon Rydberg excitation has been observed. With the variation of phase offset the anti-blockade peak height is found to be constant. This technique will be useful for experiments that require a larger number of data to have higher statistics.

Chapter 4

Study of Rydberg interaction induced enhanced excitation in thermal atomic vapor

Long-range many-body interactions in Rydberg atoms give rise to many interesting phenomena. The suppression in the Rydberg population or the excitation blockade is the most striking one giving rise to a variety of applications.⁴ The opposite effect of Rydberg blockade where enhancement in Rydberg population arising due to interaction has also been observed.⁹¹ This phenomenon is also known as Rydberg anti-blockade. Using detuned excitation, Rydberg pair distribution can be manipulated, and thus atomic pairs with separation less than the blockade radius can be excited to Rydberg state. This phenomenon has been proposed in the ultracold atomic ensemble using a two-photon excitation scheme to Rydberg state.⁹⁰ Here, the ensemble is considered in an optical lattice with fixed lattice constant and the interaction strength is tuned by changing the principal quantum number. An experiment performed in the ultra-cold atomic ensemble verifies the existence of Rydberg anti-blockade phenomenon predicted in the above theoretical model.⁹¹ In this experiment, quantum number of the Rydberg state was kept fixed and the interaction was tuned by selecting specific pairs with required inter-atomic separation. Resonant dipole dipole interaction is observed showing non-additive character due to

anti-blockade for ensemble having more than two atoms in the blockade sphere.⁹² The existence of anti-blockade between two Rydberg atoms interacting with a zero area phase jump pulse is also reported.⁹³

The energy shift due to Rydberg interaction can also be compensated by adjusting the laser detuning from the atomic transition frequency such that it satisfies resonance.^{94,95} Steady entanglement between two Rydberg atoms can be achieved in the anti-blockade regime using dissipative dynamics.¹⁰¹ A study has reported Coulomb anti-blockade in a dense cold Rydberg gas.¹⁰² Several theoretical studies also proposed the implementation of quantum logic gate using Rydberg anti-blockade phenomenon.^{103–106} Three-dimensional entanglement between two Rydberg atoms using the anti-blockade effect can also be achieved.¹⁰⁷

Some recent experiments with thermal vapor have drawn the attention for the study of Rydberg interaction induced many-body effects.^{21,155,156} Rydberg electromagnetically induced transparency in thermal vapor cell as well as in micron size vapor cell has also been studied.^{16,157} In addition, four-wave mixing for a Rydberg state¹¹⁵ and optical Kerr non-linearity in Rydberg EIT has been reported in thermal Rubidium vapor.¹²⁶ A study of population suppression due to Rydberg blockade in thermal atomic vapor has also been reported.¹⁵⁸ Anomalous excitation facilitated by Rydberg interaction has been proposed in thermal atomic vapor.¹⁵⁹

In this chapter, we present strong evidence of Rydberg excitation enhancement due to interaction in thermal atomic vapor. Using the dressed state picture of a three-level system, an interacting two-atom model is formulated for a cold atomic ensemble. The model is further extended to thermal atomic vapor by Doppler averaging it over the Maxwell-Boltzmann velocity distribution. An experiment is performed in thermal rubidium vapor using a technique based on optical heterodyne detection¹²⁸ to observe the Rydberg anti-blockade effect. A good agreement is found between the theoretical model and the experimental observation as evidence of the existence of Rydberg anti-blockade in thermal atomic vapor.

4.1 Theory of Rydberg anti-blockade

As explained in the section 2.8, the strong interaction between Rydberg atoms lead to the phenomenon of Rydberg anti-blockade. The experiment presented in this thesis uses a two-photon process for Rydberg excitation. Therefore, each atom is considered to be a three-level system in the calculation. In order to study the anti-blockade effect, a two-atom model is formulated considering the dressed state picture of the three-level system.

4.1.1 Dressed state picture of a three-level atomic system

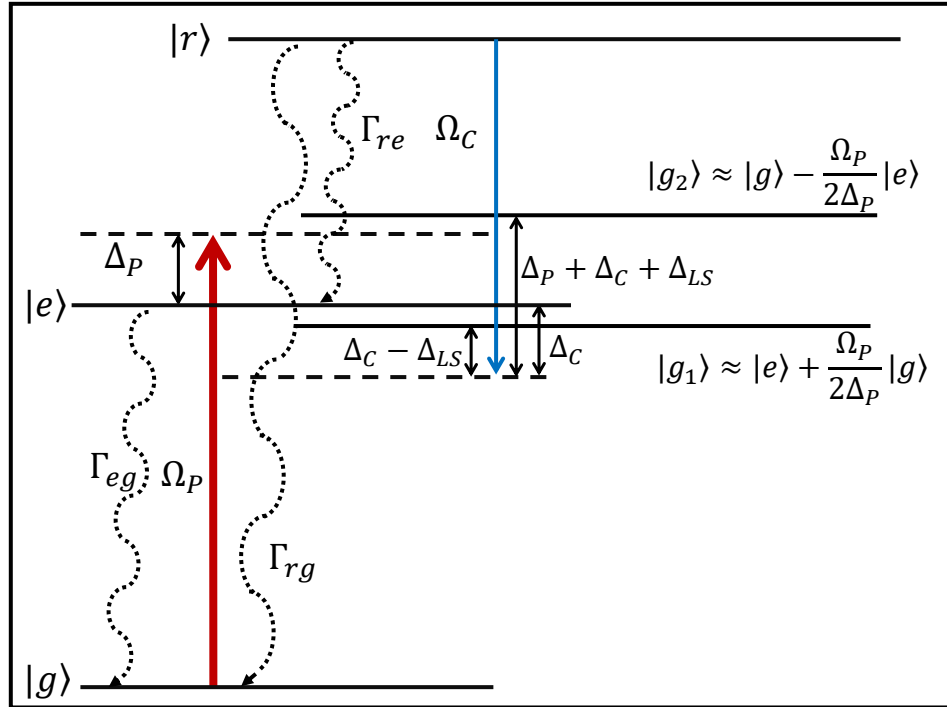


Figure 4.1: Energy level diagram of a three-level system. $|g\rangle$, $|e\rangle$ and $|r\rangle$ represents the ground state, excited state and the Rydberg state, respectively. The probe laser with Rabi frequency Ω_P couples the state $|g\rangle \rightarrow |e\rangle$ and coupling laser with Rabi frequency Ω_C couples the states $|e\rangle \rightarrow |r\rangle$ satisfying $\Omega_P \gg \Omega_C$. $\Delta_{LS} = \frac{\Omega_P^2}{4\Delta_P}$, which represents the light shift factor. $|g_1\rangle$ and $|g_2\rangle$ are the two dressed states with separated in frequency by $\Delta_P + \Omega_P^2/2\Delta_P$.

Let us consider a three-level atomic system with energy levels $|g\rangle$, $|e\rangle$ and $|r\rangle$ coupled by two monochromatic laser sources. As explained in chapter-2, the energy levels are dressed

when a probe laser beam is applied in order to couple a two-level system. The separation between the dressed states and population of each state changes depending on the laser detuning and magnitude of the probe Rabi frequency. For a three-level system, another coupling laser is applied in order to perform a two photon excitation to the Rydberg state. Here, the Rabi frequency of coupling laser is much smaller compared to the Rabi frequency of the probe. Hence, the effect of coupling on the dressed states can be neglected. Therefore, the coupling laser interacts with both the dressed states generated due to the first laser and hence excites the atom from both these states.

As presented in figure 4.1, the probe laser couples the transition $|g\rangle \rightarrow |e\rangle$ with Rabi frequency Ω_P and detuning Δ_P satisfying the condition $\Delta_P \gg \Omega_P$ and Γ_{eg} . Here, Γ_{eg} represents the population decay rate from $|e\rangle$ to $|g\rangle$. Thus, there are two dressed states $|g_1\rangle \approx \frac{\Omega_P}{2\Delta_P} |g\rangle + |e\rangle$ and $|g_2\rangle \approx |g\rangle - \frac{\Omega_P}{2\Delta_P} |e\rangle$. When the coupling laser with Rabi frequency Ω_C is applied such that $\Omega_P \gg \Omega_C$, it can be treated as a small perturbation to the dressed states. Also, $\Omega_C \ll \Gamma_{eg}$ such that the coherence between the two dressed states introduced by the coupling laser can be neglected. Therefore, both these states can be treated independently. When the coupling laser frequency is scanned over the dressed states, it excites the populations from both $|g_1\rangle$ and $|g_2\rangle$ to $|r\rangle$. The coupling laser satisfies the dipole allowed transition $|e\rangle \rightarrow |r\rangle$. Thus, the Rabi frequency for $|g_1\rangle \rightarrow |r\rangle$ is Ω_C and for $|g_2\rangle \rightarrow |r\rangle$, it is $\Omega_{eff} = \frac{\Omega_P \Omega_C}{2\Delta_P}$. Depending on the population of the two dressed states, the coupling laser excites the population to the state $|r\rangle$. As discussed in chapter-2, population of the state $|g_1\rangle$ is $\simeq \frac{\Omega_P^4}{16\Delta_P^4}$ and state $|g_2\rangle$ is $\simeq 1$. The population decay from the state $|r\rangle$ has two pathways. One direct population decay from $|r\rangle \rightarrow |e\rangle$, Γ_{re} which is dipole allowed. The second one is an indirect decay from $|r\rangle \rightarrow |g\rangle$, Γ_{rg} which arises due to the finite transit time of the atom through the beam profile. Thus, the population decay rates for the transition $|r\rangle \rightarrow |g_1\rangle$ and $|r\rangle \rightarrow |g_2\rangle$ are given by $\Gamma_{rg_1} \simeq \Gamma_{re} + \frac{\Omega_P}{2\Delta_P} \Gamma_{rg}$ and $\Gamma_{rg_2} \simeq \Gamma_{rg} + \frac{\Omega_P}{2\Delta_P} \Gamma_{re}$. However, the two dressed states have population in the state $|e\rangle$ which decay to the ground state $|g\rangle$ with decay rate Γ_{eg} . Therefore, the dipole dephasing rates for the two dressed states are given by $\Gamma_1 = \Gamma_{rg_1}/2 + \Gamma_{eg}$ and $\Gamma_2 = \Gamma_{rg_2}/2 + (\Omega_P/2\Delta_P)\Gamma_{eg}$.

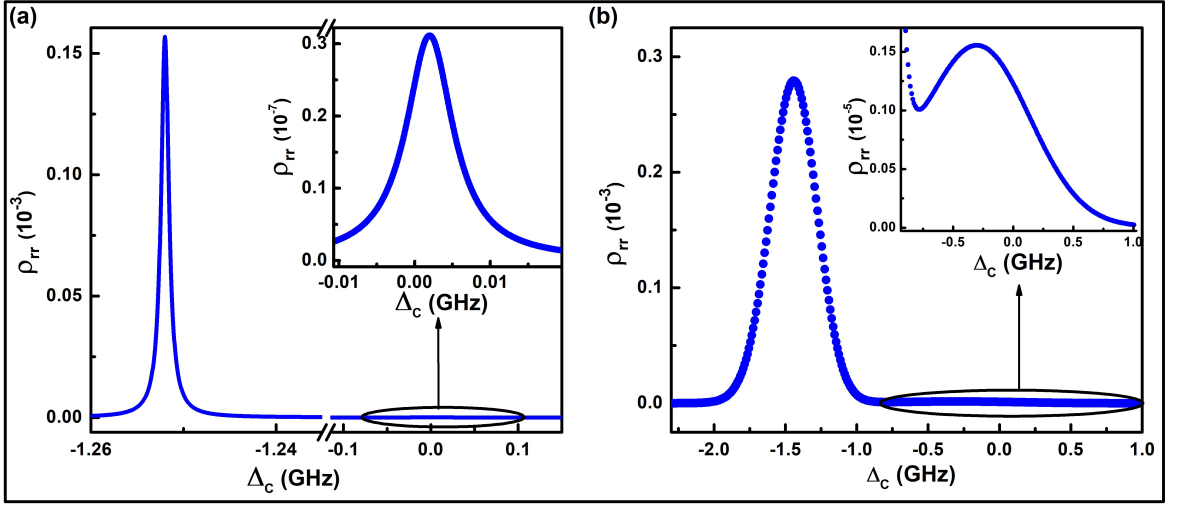


Figure 4.2: Population of the Rydberg state $|r\rangle$ i.e. ρ_{rr} as a function of Δ_C . The optical parameters used are $\Delta_P = 1250$ MHz and $\Omega_P = 400$ MHz and $\Omega_C = 10$ MHz. (a) For a cold atomic ensemble with the inset showing the magnified view of peak due to the transition $|g_1\rangle \rightarrow |r\rangle$. The main peak is due to $|g_2\rangle \rightarrow |r\rangle$. (b) For a thermal vapor ensemble where ρ_{rr} is Doppler averaged over the Maxwell-Boltzmann distribution. The inset shows the magnified view of peak due to $|g_1\rangle \rightarrow |r\rangle$.

Rydberg state population ρ_{rr} as a function of Δ_C is depicted in figure 4.2. For a cold atomic ensemble, as shown in figure 4.2(a), two peaks are observed for ρ_{rr} when Δ_C is scanned over the frequency span of the dressed states. These two peaks corresponds to the two dressed states. The separation between these two peak is $\simeq \Delta_P + (\Omega_P^2/(2\Delta_P))$. For the parameters specified in the figure 4.2, $\Delta_P \gg \Omega_P$. Thus, population of the state $|g_1\rangle$ is much smaller than $|g_2\rangle$. In this case, the peak corresponding to the transition $|g_2\rangle \rightarrow |r\rangle$ is of larger magnitude compared to the transition $|g_1\rangle \rightarrow |r\rangle$. The inset of the figure 4.2(a) shows the population of the dressed state $|g_1\rangle \rightarrow |r\rangle$. In a cold atomic ensemble, the atoms are considered to be frozen. Thus, the width of the peak corresponds to the natural line-width or the Rabi frequency. As presented in figure 4.2, the line-width of the peak due to the transition $|g_1\rangle \rightarrow |r\rangle$ is $\approx \Gamma_1$. Similarly, for $|g_2\rangle \rightarrow |r\rangle$ transition it is Ω_{eff} or Γ_2 whichever is dominating.

For a thermal vapor ensemble, the three-level system is Doppler averaged over the Maxwell Boltzmann distribution in order to include the effect of velocity of the atom. As shown in figure 4.2(b), ρ_{rr} as a function of Δ_C , also shows two peaks due to both these dressed states. Similar to the cold atom ensemble, the two peaks have different magnitude for thermal vapor

system as well. The peak corresponding to $|g_1\rangle \rightarrow |r\rangle$ transition have a detuning of Δ_C and for $|g_2\rangle \rightarrow |r\rangle$ it is $\Delta_P + \Delta_C$. Thus, after Doppler averaging the width of the peak due to $|g_1\rangle \rightarrow |r\rangle$ is $\approx k_C v_p$ and for $|g_2\rangle \rightarrow |r\rangle$ it is $\approx (k_C - k_P)v_p$, where k_P and k_C are the wave vector due to the probe and coupling beam respectively and v_p represents the most probable speed. The inset of the figure 4.2(b) corresponds to the transition $|g_1\rangle \rightarrow |r\rangle$. The line-width of this peak is observed to be larger than that of the transition $|g_2\rangle \rightarrow |r\rangle$.

For thermal atomic vapor the peak due to the transition $|g_1\rangle \rightarrow |r\rangle$ is observed to be red shifted unlike the cold-atom case. This is arising due to the population normalization factor corresponding to the state $|g_1\rangle$. As explained in section 2.3.2, for cold atom ensemble this is $\simeq \frac{\Omega_P^4}{16\Delta_P^4}$. However, for thermal atom this population is given by $\simeq \frac{\Omega_P^4}{16(\Delta_P + \vec{k}_P \cdot \vec{v})^4}$, which is dependent on the velocity of the atom \vec{v} and the wave vector \vec{k}_P . On the red detuned side factor $\vec{k}_P \cdot \vec{v} < 0$. Since, we have considered Δ_P is positive, the quantity $\Delta_P + \vec{k}_P \cdot \vec{v}$ reduces on the red detuned side. Thus, the Rydberg population increases which shifts the population maxima to the red detuned side of the spectrum.

4.1.2 Two-atom model

Let us consider a system of two interacting atoms. The energy level diagram for the individual atom is shown in figure 4.3(a). The energy difference between the two dressed states $|g_1\rangle$ and $|g_2\rangle$ is $\delta = \Delta_P + \frac{\Omega_P^2}{2\Delta_P}$. Thus, as shown in figure 4.3(a), when the applied laser has a detuning of Δ_C from the transition $|g_1\rangle \rightarrow |r\rangle$, the detuning from $|g_2\rangle \rightarrow |r\rangle$ is $\Delta_C + \delta$. The coupling laser satisfies the dipole allowed transition from the state $|e\rangle \rightarrow |r\rangle$.

The composite two-atom system has eight-levels as shown in figure 4.3 (b). $|g_1g_1\rangle$ ($|g_2g_2\rangle$) represents energy level where both the atoms are in $|g_1\rangle$ ($|g_2\rangle$) state. $|g_1g_2\rangle$ and $|g_2g_1\rangle$ represent levels with one atom in $|g_1\rangle$ state and the other atom in $|g_2\rangle$ state. When one atom is in $|g_2\rangle$ ($|g_1\rangle$) and the other atom is in the Rydberg state $|r\rangle$, it is represented by the level $|rg_2\rangle$ ($|g_1r\rangle$). $|rr\rangle$ represents level with both the atoms in the Rydberg state.

Let us consider that the laser is resonant to the transition $|g_1\rangle \rightarrow |r\rangle$. Then, the transition

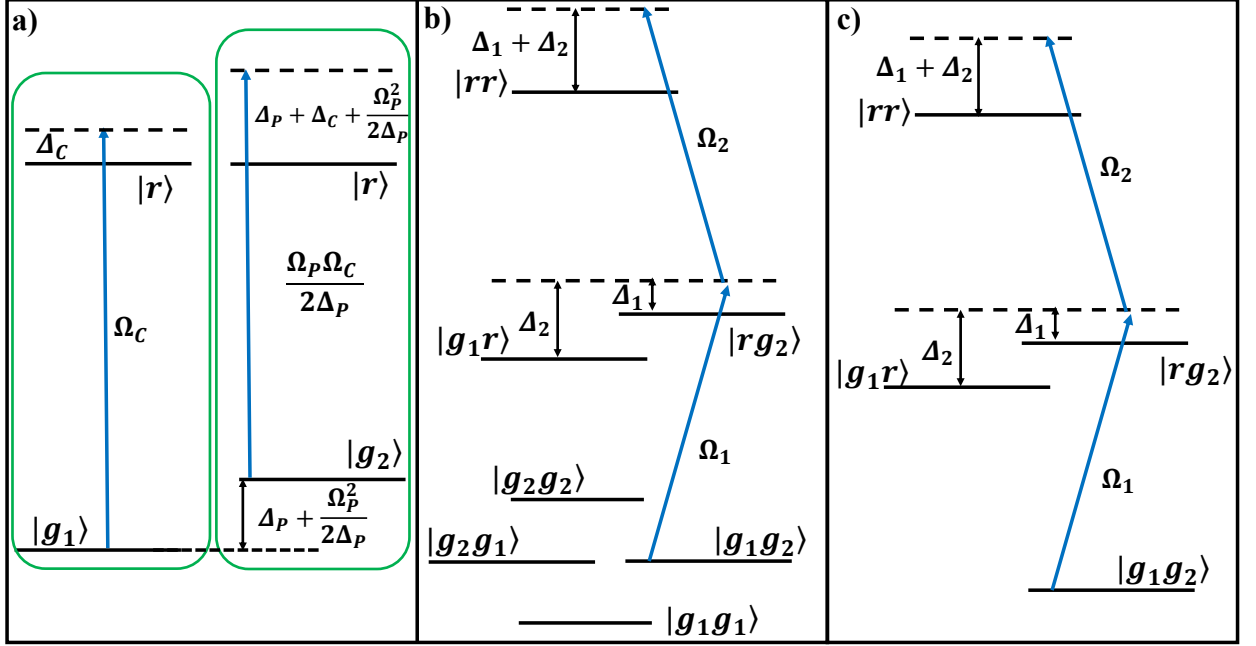


Figure 4.3: (a) Energy level diagram for single atom with $\delta = \Delta_P + \frac{\Omega_P^2}{2\Delta_P}$ representing the energy difference between the states $|g_1\rangle$ and $|g_2\rangle$. The laser is detuned by Δ_C to the transition $|g_2\rangle \rightarrow |r\rangle$. (b) Composite two-atom model with laser close to the resonance of the transition $|g_1\rangle \rightarrow |r\rangle$. $\Omega_1 = \Omega_C$ and $\Omega_2 = \frac{\Omega_P\Omega_C}{2\Delta_P}$ are the Rabi frequencies for the transitions $|g_1\rangle \rightarrow |r\rangle$ and $|g_2\rangle \rightarrow |r\rangle$ respectively. (c) Simplified two-atom model by eliminating the states not contributing to the Rydberg excitation processes.

$|g_2\rangle \rightarrow |r\rangle$ is out of resonance to the applied laser. Thus, the state $|g_2g_2\rangle$ does not contribute to the Rydberg excitation. As presented in chapter-2, the population of the state $|g_1\rangle$ is $\frac{\Omega_P^4}{16\Delta_P^4}$. Thus, the population of the state $|g_1g_1\rangle$ is $\left(\frac{\Omega_P^4}{16\Delta_P^4}\right)^2$. This population is negligibly small compared to other states. Therefore, excitation from $|g_1g_1\rangle$ to the Rydberg state can be neglected. Since $\Omega_C \ll \Gamma_{eg}$, the coupling laser cannot build coherence between the two dressed states. Also, the state $|g_1g_2\rangle$ and $|g_2g_1\rangle$ are degenerate with equal populations. Thus, we consider any one of them in the model by suitably normalizing the population. Using all these conditions the two-atom model is reduced to a four level system as shown in figure 4.3(c), when it is resonant to the transition $|g_1\rangle \rightarrow |r\rangle$.

The laser frequency is scanned further in order to satisfy resonance to the transition $|g_2\rangle \rightarrow |r\rangle$ as shown in figure 4.4(a). Just like the previous case, any one of the states $|g_1g_2\rangle$ or $|g_2g_1\rangle$ is

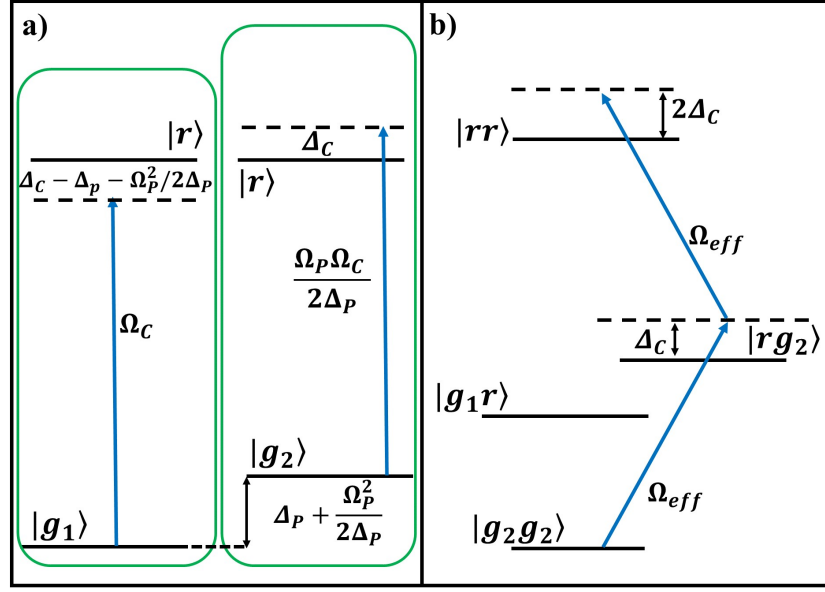


Figure 4.4: (a) Energy level diagram for single atom with $\delta = \Delta_P + \frac{\Omega_P^2}{2\Delta_P}$ representing the energy difference between the states $|g_1\rangle$ and $|g_2\rangle$. The laser is detuned by Δ_C to the transition $|g_2\rangle \rightarrow |r\rangle$. (b) Composite two-atom model with laser close to the resonance of the transition $|g_2\rangle \rightarrow |r\rangle$. $\Omega_{eff} = \frac{\Omega_P\Omega_C}{2\Delta_P}$ is the Rabi frequency for the transitions $|g_2\rangle \rightarrow |r\rangle$ respectively.

considered by suitably normalizing the population. The coupling laser satisfies resonance to the transition $|g_1g_2\rangle \rightarrow |g_1r\rangle$. Apart from that, $|g_2g_2\rangle \rightarrow |rg_2\rangle$ transition will also satisfy resonance as shown in figure 4.4(b). Hence, the state $|g_2g_2\rangle$ contributes to the Rydberg excitation unlike the previous case. Since, the population of the state $|g_2\rangle \simeq 1$, the population of $|g_2g_2\rangle \simeq 1$. This population is much larger than that of state $|g_1g_2\rangle$. Therefore, the contribution of the transition $|g_2g_2\rangle \rightarrow |rg_2\rangle$ is much larger than that of $|g_1g_2\rangle \rightarrow |g_1r\rangle$ to the Rydberg excitation. This $|g_2g_2\rangle \rightarrow |g_2r\rangle$ transition is equivalent to an effective two level system with $|g\rangle \rightarrow |r\rangle$ by adiabatically eliminating the intermediate state $|e\rangle$ of a three level system.

In an effective two level system, the population transfer to the Rydberg state due to the transition $|g_1\rangle \rightarrow |r\rangle$ is neglected. However, this population is observed to be enhancing due to Rydberg-Rydberg interaction. This enhancement can be explained by the exact two-atom calculation considering each atom as a three level system. However, as discussed above, for given laser parameters using the dressed state picture, the Hilbert space is simplified which is

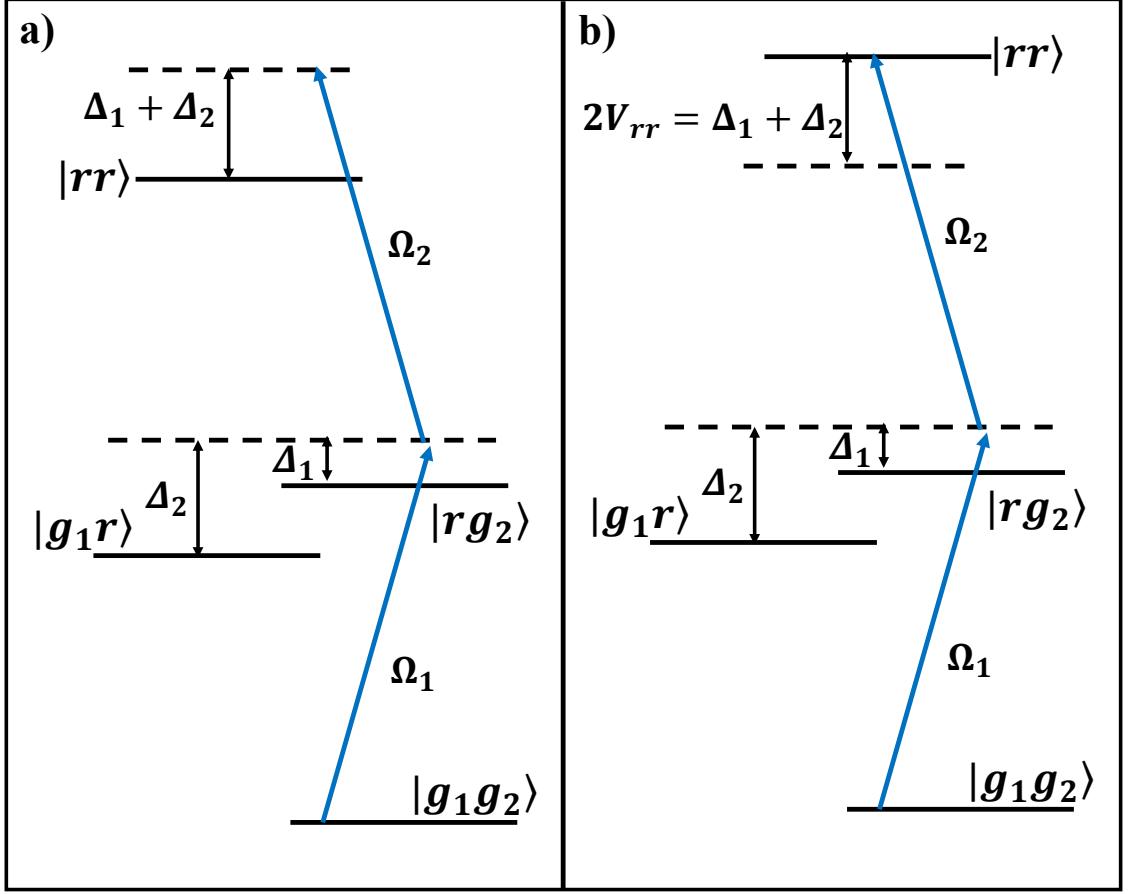


Figure 4.5: Energy level diagram of the two-atom system with laser satisfying resonance condition to $|g_1\rangle \rightarrow |r\rangle$ when (a) the atoms are not-interacting and (b) for interacting system with $2V_{rr} = \Delta_1 + \Delta_2$ i.e. the anti-blockade condition when the system satisfies the resonance $|rg_2\rangle \rightarrow |rr\rangle$. The states are $|1\rangle \equiv |g_1g_2\rangle$, $|2\rangle \equiv |rg_2\rangle$, $|3\rangle \equiv |g_1r\rangle$ and $|4\rangle \equiv |rr\rangle$. The Rabi frequencies are $\Omega_1 = \Omega_C$, $\Omega_2 = \Omega_{eff}$ and interaction $V_{rr} = \frac{C_6}{r^6}$.

used to model the population enhancement.

The energy level diagram for the two-atom system when the laser is resonant to the transition $|g_1\rangle \rightarrow |r\rangle$ is shown in figure 4.5(a). The Hamiltonian for the system is given by

$$H = H^{(1)} \otimes \mathbf{I} + \mathbf{I} \otimes H^{(2)} + 2V_{rr} |r\rangle \langle r|. \quad (4.1)$$

Here, V_{rr} represents the strength of Van der Waals interaction between the two atoms in Rydberg state and \mathbf{I} is a two dimensional identity matrix. $H^{(1)}$ and $H^{(2)}$ represent the Hamiltonians

of atom 1 and atom 2 respectively which are given by

$$H^{(1)} = \frac{-\hbar}{2} \begin{pmatrix} 0 & \Omega_1 \\ \Omega_1 & 2\Delta_1 \end{pmatrix}, H^{(2)} = \frac{-\hbar}{2} \begin{pmatrix} 2\delta & \Omega_2 \\ \Omega_2 & 2\Delta_2 \end{pmatrix}.$$

Since, atom 2 is excited from $|g_2\rangle$ to $|r\rangle$, the Rabi frequency $\Omega_2 = \Omega_{eff}$. Similarly for atom 1 the Rabi frequency is $\Omega_1 = \Omega_C$. Δ_1 and Δ_2 are the laser detunings of atom 1 and atom 2 respectively. δ is the energy difference between the two ground states $|g_1\rangle$ and $|g_2\rangle$. Thus, the Hamiltonian for the two-atom system depicted in figure 4.5(a) is calculated to be

$$H = \frac{-\hbar}{2} \begin{pmatrix} 2\delta & \Omega_1 & \Omega_2 & 0 \\ \Omega_1 & 2(\Delta_1 + \delta) & 0 & \Omega_2 \\ \Omega_2 & 0 & 2\Delta_2 & \Omega_1 \\ 0 & \Omega_2 & \Omega_1 & 2(\Delta_1 + \Delta_2) \end{pmatrix}. \quad (4.2)$$

The decay and decoherence in the system is incorporated by the Lindblad operator. There are four elements in the Lindblad matrix of the two-atomic system. The population decay of both the atoms from Rydberg state to their respective ground states. These are represented by the diagonal elements. The off-diagonal terms represent the dipole dephasing rate. Since, the two dressed states are linear combination of bare atomic states, the dipole dephasing rate of each atom depends on the dephasing between the bare atomic states. The L_D matrix for atom 1 is $L_{D1} = \begin{pmatrix} \Gamma_1 \rho_{22} & \frac{-\Gamma_2 \rho_{g_1 r}}{2} \\ \frac{-\Gamma_{rr} \rho_{r g_1 1}}{2} & -\Gamma_1 \rho_{rr} \end{pmatrix}$ and the for atom 2 it is $L_{D2} = \begin{pmatrix} \Gamma_3 \rho_{rr} & \frac{-\Gamma_4 \rho_{g_2 r}}{2} \\ \frac{-\Gamma_4 \rho_{r g_2}}{2} & -\Gamma_3 \rho_{rr} \end{pmatrix}$. These dephasing terms are mapped to a three-level system in order to calculate their corresponding values. For $|g_1\rangle \rightarrow |r\rangle$ transition, $\Gamma_1 = \Gamma_{re}$ and $\Gamma_2 = \Gamma_{re} + \Gamma_{eg}$. Similarly for $|g_2\rangle \rightarrow |r\rangle$ transition, $\Gamma_3 = \Gamma_{rg}$ and $\Gamma_4 = \Gamma_{rg} + \Gamma_{eg}(\Omega_P/2\Delta_P)$. The composite L_D matrix for the diatomic system is calculated as⁵⁸

$$L_D = L_{D1} \otimes \rho^{(2)} + \rho^{(1)} \otimes L_{D2}. \quad (4.3)$$

Here, $\rho^{(1)}$ and $\rho^{(2)}$ represent the density matrix of atom 1 and 2 respectively. In order to

map the individual atoms to the composite two-atom model the density matrix is mapped as $\rho = \rho^{(1)} \otimes \rho^{(2)}$. For the two-atom system the density matrix is given by

$$\rho = \begin{pmatrix} \rho_{11} & \rho_{12} & \rho_{13} & \rho_{14} \\ \rho_{21} & \rho_{22} & \rho_{33} & \rho_{24} \\ \rho_{31} & \rho_{32} & \rho_{33} & \rho_{34} \\ \rho_{41} & \rho_{42} & \rho_{43} & \rho_{44} \end{pmatrix} \quad (4.4)$$

Thus, the L_D matrix of the two-atom system is calculated to be

$$L_D = \begin{pmatrix} \Gamma_1 \rho_{22} + \Gamma_3 \rho_{33} & \Gamma_3 \rho_{34} - \frac{\Gamma_2 \rho_{12}}{2} & \Gamma_1 \rho_{24} - \frac{\Gamma_4 \rho_{13}}{2} & -(\Gamma_2 + \Gamma_4) \frac{\rho_{14}}{2} \\ \Gamma_3 \rho_{43} - \frac{\Gamma_2 \rho_{21}}{2} & \Gamma_3 \rho_{44} - \Gamma_1 \rho_{22} & -(\Gamma_2 + \Gamma_4) \frac{\rho_{23}}{2} & -\frac{\Gamma_4 \rho_{24}}{2} - \Gamma_1 \rho_{24} \\ \Gamma_1 \rho_{42} - \frac{\Gamma_4 \rho_{31}}{2} & -(\Gamma_2 + \Gamma_4) \frac{\rho_{32}}{2} & -\Gamma_3 \rho_{33} + \Gamma_1 \rho_{44} & -\frac{\Gamma_2 \rho_{34}}{2} - \Gamma_3 \rho_{34} \\ -(\Gamma_2 + \Gamma_4) \frac{\rho_{41}}{2} & -\frac{\Gamma_4 \rho_{42}}{2} - \Gamma_1 \rho_{42} & -\frac{\Gamma_2 \rho_{43}}{2} - \Gamma_3 \rho_{43} & -\Gamma_1 \rho_{44} - \Gamma_3 \rho_{44} \end{pmatrix} \quad (4.5)$$

The dynamics of the system is studied using the optical Bloch equations (OBE) $\dot{\rho} = \frac{1}{i\hbar} [H, \rho] + L_D$. Using the steady state condition i.e. $\dot{\rho} = 0$ the OBEs for the system are found to be

$$\Omega_1(1 - 2\rho_{22} - \rho_{33} - \rho_{44}) + \Omega_2(\rho_{14} - \rho_{32}) + 2\Delta_1\rho_{12} + 2i\Gamma_3\rho_{34} - i\Gamma_2\rho_{12} = 0. \quad (4.6)$$

$$\Omega_1(\rho_{14} - \rho_{23}) + \Omega_2(1 - \rho_{22} - 2\rho_{33} - \rho_{44}) + 2(\Delta_2 - \delta)\rho_{13} + 2i\Gamma_1\rho_{24} - i\Gamma_4\rho_{13} = 0. \quad (4.7)$$

$$\Omega_1(\rho_{13} - \rho_{24}) + \Omega_2(\rho_{12} - \rho_{34}) + 2(\Delta_1 + \Delta_2 - \delta + 2V)\rho_{14} - i(\Gamma_2 + \Gamma_4)\rho_{14} = 0. \quad (4.8)$$

$$\Omega_1(\rho_{21} - \rho_{12}) + \Omega_2(\rho_{24} - \rho_{42}) + 2i\Gamma_3\rho_{44} - 2i\Gamma_1\rho_{22} = 0. \quad (4.9)$$

$$\Omega_1(\rho_{24} - \rho_{13}) + \Omega_2(\rho_{21} - \rho_{43}) - 2(\Delta_2 - \delta - \Delta_1)\rho_{23} - i(\Gamma_2 + \Gamma_4)\rho_{23} = 0. \quad (4.10)$$

$$\Omega_1(\rho_{23} - \rho_{14}) + \Omega_2(\rho_{22} - \rho_{44}) + 2(\Delta_2 - \delta + 2V)\rho_{24} - 2i(\Gamma_1 + \Gamma_4/2)\rho_{24} = 0. \quad (4.11)$$

$$\Omega_1(\rho_{34} - \rho_{43}) + \Omega_2(\rho_{31} - \rho_{13}) + 2i(\Gamma_1\rho_{44} - \Gamma_3\rho_{33}) = 0. \quad (4.12)$$

$$\Omega_1(\rho_{33} - \rho_{44}) + \Omega_2(\rho_{32} - \rho_{14}) + 2(\Delta_1 + 2V)\rho_{34} - 2i(\Gamma_3 + \Gamma_2/2)\rho_{34} = 0. \quad (4.13)$$

$$\Omega_1(\rho_{43} - \rho_{34}) + \Omega_2(\rho_{42} - \rho_{24}) - 2i(\Gamma_1 + \Gamma_3)\rho_{44} = 0. \quad (4.14)$$

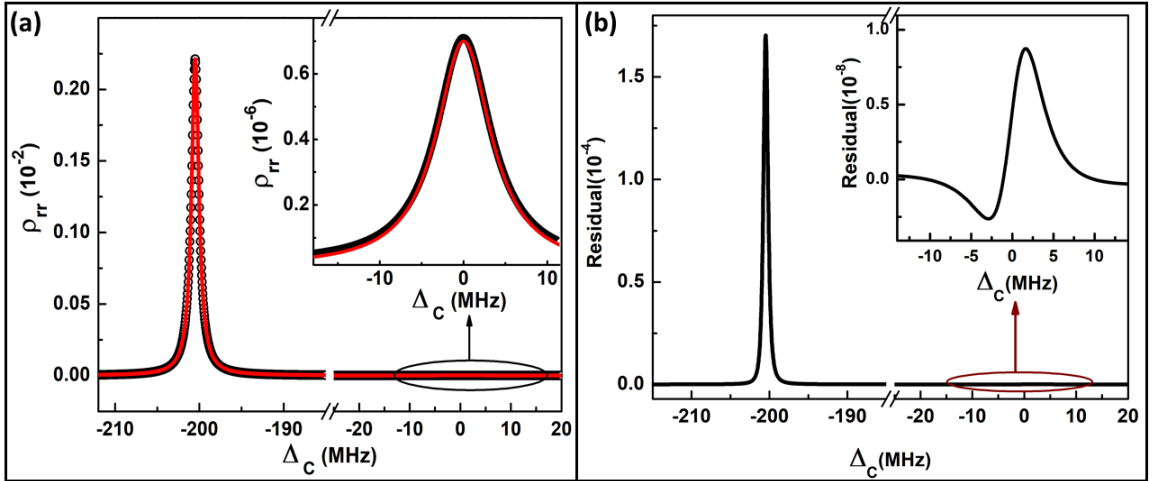


Figure 4.6: (a) Rydberg population ρ_{rr} as a function of Δ_C for non-interacting two-atomic system (\circ) and for a single atom three-level exact calculation (—) in a cold atomic ensemble. The parameters used are $\Omega_P = 20$ MHz, $\Delta_P = 200$ MHz and $\Omega_C = 1$ MHz. The inset shows the magnified view of the peak corresponding to the transition $|g_1\rangle \rightarrow |r\rangle$ at $\Delta_C = 0$. (b) The residual plot of the non-interacting two-atom model and the three-level system with the variation of Δ_C . The inset shows the magnified view of the residual plot of the peak corresponding to the transition $|g_1\rangle \rightarrow |r\rangle$ at $\Delta_C = 0$.

These time-independent OBEs are solved numerically to calculate the population of the Rydberg state for applied laser satisfying the resonance $|g_1\rangle \rightarrow |r\rangle$ which is denoted as $\rho_{rr}^{(1)}$ and

is given by

$$\rho_{rr}^{(1)} = \left(\frac{(\rho_{22} + \rho_{33})}{2} + \rho_{44} \right) \left(\frac{\Omega_P^4}{8\Delta_P^4} \right). \quad (4.15)$$

The factor $\frac{\Omega_P^4}{8\Delta_P^4}$ represents the population of the state $|g_1g_2\rangle$ including the normalization factor for the population of $|g_2g_1\rangle$. The coupling laser is scanned further to satisfy the resonance $|g_2\rangle \rightarrow |r\rangle$ as shown in figure 4.4. In this case the laser satisfies resonance to the transition $|g_2g_2\rangle \rightarrow |rg_2\rangle$. Rydberg state population for this transition is equivalent to that of an effective two level system with adiabatically eliminating the intermediate state. Using the energy level diagram presented in figure 4.4, Rydberg population when the laser satisfy resonance to the transition $|g_2\rangle \rightarrow |r\rangle$ which is denoted as $\rho_{rr}^{(2)}$ and is given by

$$\rho_{rr}^{(2)} = \left(\frac{(\rho_{33} + \rho_{44})}{2} \right) \quad (4.16)$$

Thus, the population of the Rydberg state over the whole scan of the coupling laser is given by

$$\rho_{rr} = \rho_{rr}^{(1)} + \rho_{rr}^{(2)} \quad (4.17)$$

This Rydberg state population as a function of Δ_C is depicted in figure 4.6 (a). When the atoms are not interacting i.e. $V_{rr} = 0$, the two-atom model will be equivalent to a three-level system. As shown in the figure 4.6 (a) the Rydberg population calculated using the two-atom model matches to that of a three-level system for a cold atomic ensemble. The inset of the figure 4.6 represents the peak corresponding to the transition $|g_1\rangle \rightarrow |r\rangle$. The residual plot of both the system are depicted in figure 4.6 (b). For both the peaks the residuals are found to be two-order of magnitude smaller than the maximum peak values. Thus, for both the peaks a good agreement is observed between the two-atom model and the three-level system. This also verifies that the calculation does not have any numerical errors.

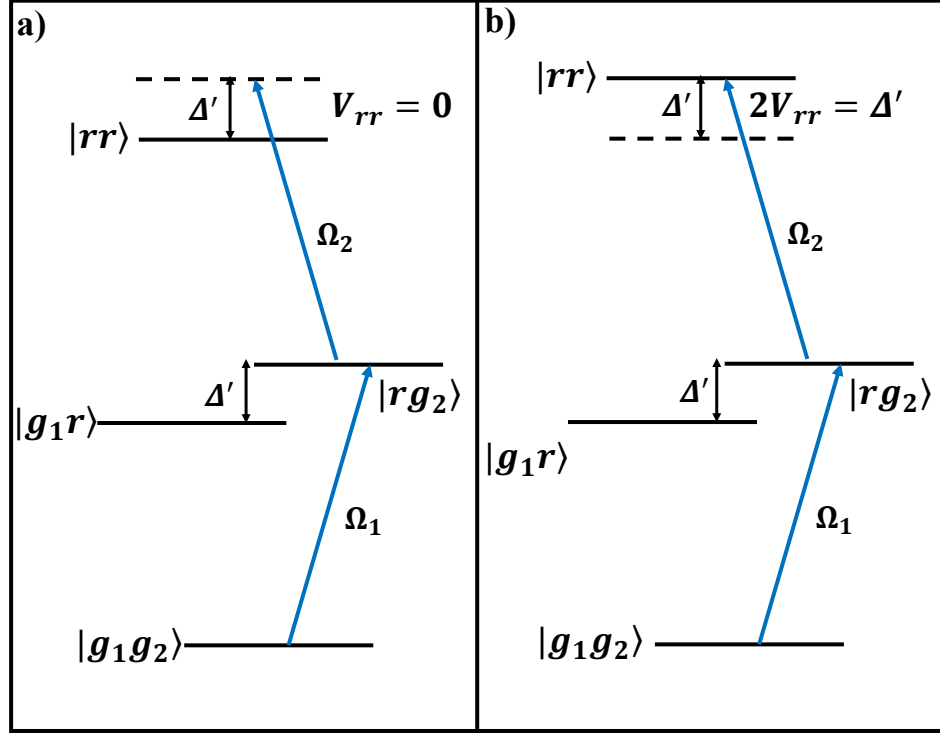


Figure 4.7: Energy level diagram of the two-atom system with laser satisfying resonance condition to $|g_1\rangle \rightarrow |r\rangle$ when (a) the atoms are not-interacting and (b) the atoms are interacting such that the energy level shift due to interaction satisfies $2V_{rr} = \Delta'$ i.e. the anti-blockade condition where the system satisfies the resonance $|rg_2\rangle \rightarrow |rr\rangle$. The states are $|1\rangle \equiv |g_1g_2\rangle$, $|2\rangle \equiv |rg_2\rangle$, $|3\rangle \equiv |g_1r\rangle$ and $|4\rangle \equiv |rr\rangle$. The Rabi frequencies are $\Omega_1 = \Omega_C$, $\Omega_2 = \Omega_{eff}$.

4.1.3 Interaction induced enhanced excitation

Let us consider the two-atom system such that the laser is resonant to the transition $|g_1g_2\rangle \rightarrow |rg_2\rangle$ i.e. $\Delta_1 = 0$. Thus, the applied laser is off resonant to the transition $|g_1g_2\rangle \rightarrow |g_1r\rangle$ by Δ' . The energy level diagram for the system is shown in figure 4.7(a). When the atoms are not interacting the applied laser does not satisfy resonance to the state $|rr\rangle$. Therefore, the atom in the state $|g_2\rangle$ cannot be excited to the Rydberg state. The atoms are considered to be interacting via Van der Waals interaction which is included as a shift in the energy level of the state $|rr\rangle$. The inter-atomic separation is considered such that the interaction strength $V_{rr} = \Delta'$. Thus, the transition $|rg_2\rangle \rightarrow |rr\rangle$ satisfies resonance unlike the non-interacting system as shown in figure 4.7(b). Thus, atoms in the state $|g_2\rangle$ are also excited to the Rydberg state. Therefore, the Rydberg population enhances for the system due to interaction compared to a non-interacting

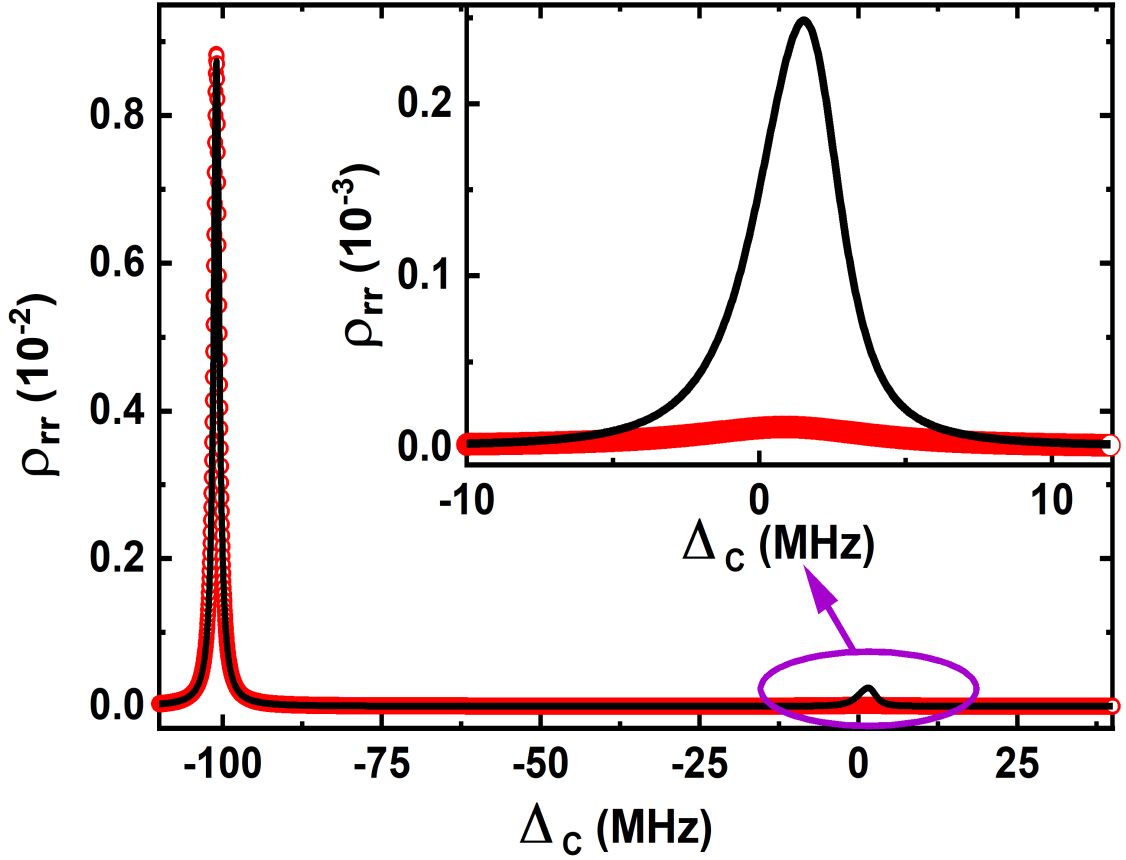


Figure 4.8: Rydberg population of the two-atomic system ρ_{rr} as a function of Δ_C for an ultra-cold atomic ensemble for a non-interacting two-atom system (\circ) and two-atom system satisfying the anti-blockade condition $2V_{rr} = \Delta'$ is presented by ($_$). The inset shows the magnified peak corresponding to $\Delta_C = 0$. The parameters used are $\Delta_P = 100$ MHz, $\Omega_P = 20$ MHz and $\Omega_C = 1$ MHz.

system. This phenomenon is known as Rydberg anti-blockade and the condition satisfied by the interaction ($2V_{rr} = \Delta'$) is known as Rydberg anti-blockade condition.

ρ_{rr} as a function of Δ_C for the two-atom system in a cold atomic ensemble is depicted in figure 4.8. The red circle represents ρ_{rr} with $V_{rr} = 0$ and the black line represents ρ_{rr} satisfying $2V_{rr} = \Delta'$. The peak at $\Delta_C = -100$ MHz corresponds to the usual two photon transition $g_2 \rightarrow |r\rangle$. The peak near $\Delta_C = 0$ corresponding to the transition $|g_1\rangle \rightarrow |r\rangle$ is known as the anti-blockade peak. The inset of the figure 4.8 corresponds to the anti-blockade peak at $\Delta_C = 0$. A significant enhancement in the Rydberg population is observed due to Rydberg anti-blockade effect as compared to the non-interacting system. This enhancement

signifies that the population is transferred from $|g_2\rangle \rightarrow |r\rangle$ which is facilitated due to presence of interaction. The population enhancement factor for the parameters presented in fig 4.8 is 4.2×10^3 for the cold atomic ensemble.

4.1.4 Non-interacting two-atom model for thermal vapor

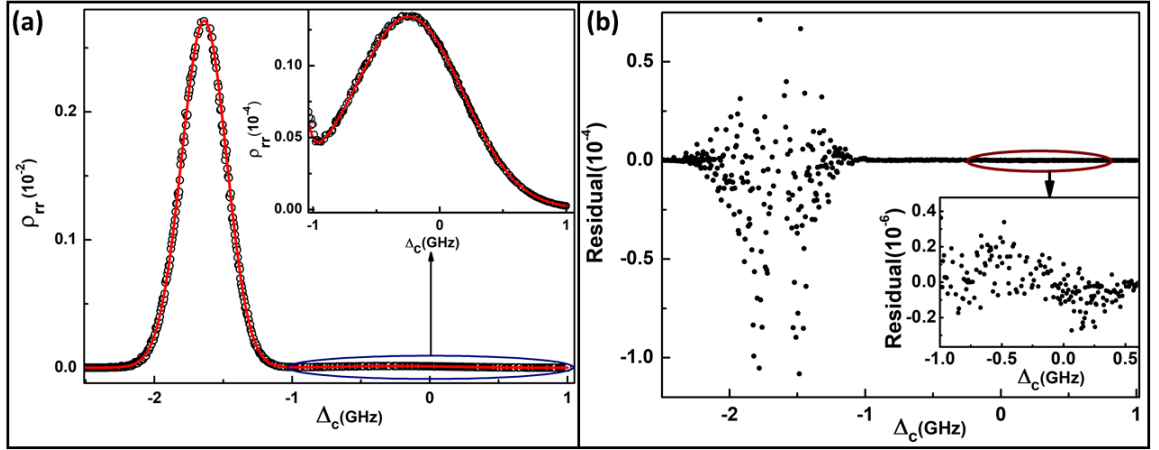


Figure 4.9: (a) Rydberg population calculated using exact three-level single atomic system (—) and two-atoms non-interacting model (o) for a thermal atomic ensemble. Inset shows the magnified view of the peak near $\Delta_C = 0$. Laser parameters used in the calculation are $\Omega_P = 400$ MHz, $\Omega_C = 5$ MHz and $\Delta_P = 1.5$ GHz. (b) The residual plot of the non-interacting two-atom model and the three-level system with the variation of Δ_C . The inset shows the magnified view of the residual plot of the peak corresponding to the transition $|g_1\rangle \rightarrow |r\rangle$ at $\Delta_C = 0$.

Let us consider the two-atom system in a thermal vapor ensemble where the atoms move with a broad range of velocities. Thus, the system is Doppler averaged over all possible velocities using Maxwell-Boltzmann distribution. Let us consider atom 1 and atom 2 are moving with velocities v_1 and v_2 respectively. The probe and the coupling lasers are considered in a counter-propagating configuration with wave vectors k_P and k_C respectively. Thus, the probe and coupling laser detunings for the thermal ensemble are given by $\Delta_P^{(i)} = \Delta_P - k_P v_i$ and $\Delta_C^{(i)} = \Delta_C + k_C v_i$ respectively. Here $i = 1$ and 2 for atom 1 and atom 2 respectively. The two photon detunings for atom 1 and atom 2 is thus given by $\Delta_1 = \Delta_C + k_C v_1 - \frac{\Omega_P^2}{4(\Delta_P - k_P v_1)}$ and $\Delta_2 = \Delta_P + \Delta_C - (k_P - k_C)v_2 + \frac{\Omega_P^2}{4(\Delta_P - k_P v_2)}$ respectively. The population of the states $|g_1 g_2\rangle$

and $|g_2g_1\rangle$ is given by $\frac{\Omega_P^4}{16(\Delta_P - k_P v_1)^4}$ and $\frac{\Omega_P^4}{16(\Delta_P - k_P v_2)^4}$. Thus, the Rydberg population when the laser satisfies the resonance to the transition $|g_1\rangle \rightarrow |r\rangle$ is found to be

$$\begin{aligned} \rho_{rr}^{(1)} = & \frac{1}{\sqrt{\pi}v_p} \int_{-\infty}^{\infty} \frac{\rho_{22}(v_1) + \rho_{44}(v_1)}{2} \frac{\Omega_P^4}{16(4\Delta_P - k_P v_1)^4} \exp\left(\frac{-v_1^2}{v_p^2}\right) dv_1 \\ & + \frac{1}{\sqrt{\pi}v_p} \int_{-\infty}^{\infty} \frac{\rho_{33}(v_2) + \rho_{44}(v_2)}{2} \frac{\Omega_P^4}{16(4\Delta_P - k_P v_2)^4} \exp\left(\frac{-v_2^2}{v_p^2}\right) dv_2. \end{aligned} \quad (4.18)$$

Here, v_p represents the most probable speed of the atom. Monte-Carlo technique is used to evaluate the integral which is explained in appendix A. Similarly when the laser satisfies the resonance $|g_2\rangle \rightarrow |r\rangle$ the Rydberg state population is given by

$$\rho_{rr}^{(2)} = \frac{1}{\sqrt{\pi}v_p} \int_{-\infty}^{\infty} \frac{\rho_{33}(v_2) + \rho_{44}(v_2)}{2} \exp\left(\frac{-v_2^2}{v_p^2}\right) dv_2. \quad (4.19)$$

Therefore, the Rydberg population over the whole scan of Δ_C is $\rho_{rr} = \rho_{rr}^{(1)} + \rho_{rr}^{(2)}$. ρ_{rr} as a function of Δ_C is depicted in figure 4.9(a). The inset of figure 4.9(a) represents the peak corresponding to the transition $|g_1\rangle \rightarrow |r\rangle$. Just like the cold atom system for $V_{rr} = 0$, ρ_{rr} for two-atom model is compared to Doppler averaged Rydberg state population of a three-level system. A good agreement is observed between both the models as depicted in figure 4.9(b). For both the peaks the residuals are found to be two orders of magnitude smaller than the maximum peak values. The width of the peak corresponding to the transition $|g_1\rangle \rightarrow |r\rangle$ is nearly $k_C v_p$ and for the transition $|g_2\rangle \rightarrow |r\rangle$ it is $\sim \Delta k v_p$ as explained in the section 4.1.

4.1.5 Interacting two-atom model for thermal vapor

Now let us consider two atoms in thermal vapor ensemble are interacting with each other. The laser detunings of atom 1 and atom 2 are given by Δ_1 and $\Delta_2 = \Delta_1 + \Delta'$ respectively. The corresponding energy level diagram is shown in figure 4.10(a). The atoms are considered to be interacting via Van der Waal's interaction with strength V_{rr} . Since the atoms move randomly in the system, it is Doppler averaged over the whole velocity class using Maxwell-Boltzmann

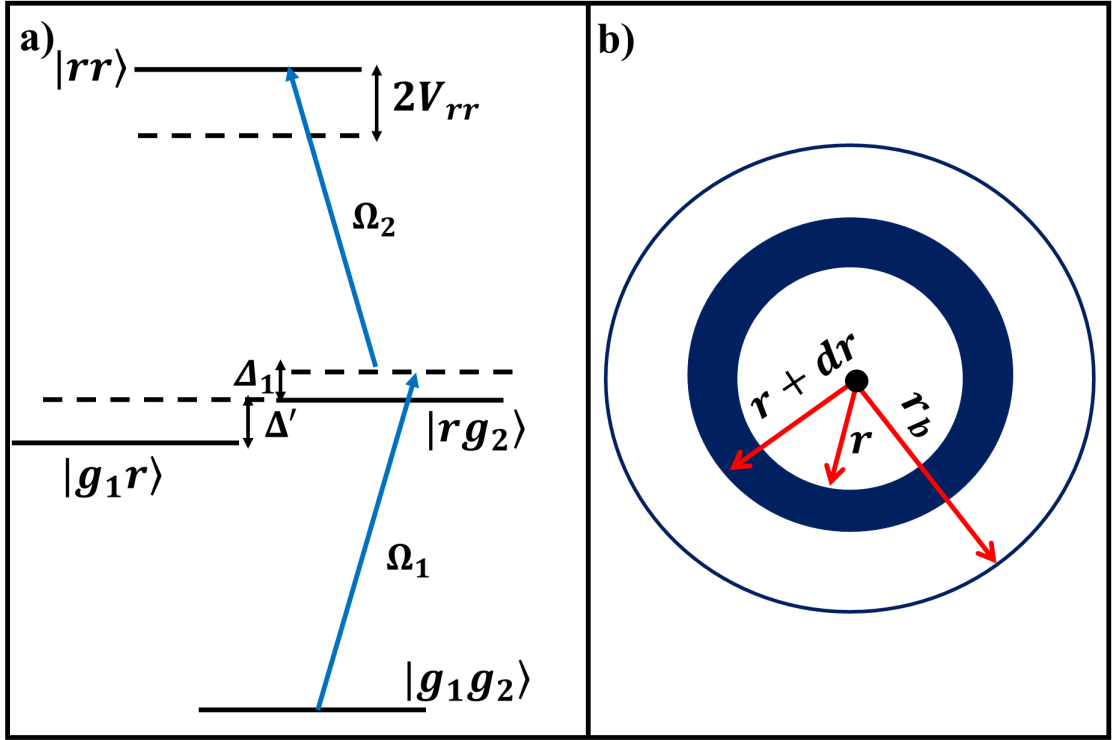


Figure 4.10: (a) Energy level diagram to model Rydberg anti-blockade. Δ_1 and $\Delta_2 (= \Delta_1 + \Delta')$ are the coupling laser detuning of atom 1 and 2 respectively. (b) Schematic of the interaction sphere of radius r_b . The atom in the dressed state $|g_2\rangle$ is placed at the centre of the sphere. The atoms in the spherical shell of radius r and thickness dr can compensate for the two-photon resonance to the $|rr\rangle$ state due to van der Waals type Rydberg-Rydberg interaction ($V_{rr} = C_6/r^6$) with the atom at the center.

distribution.

Let us consider an interaction sphere of radius r_b as shown in the figure 4.10 (b). $r_b = \sqrt[6]{\frac{C_6}{\hbar\Omega_2}}$ is the blockade radius. The volume of the interaction sphere is $V = \frac{4\pi r_b^3}{3}$. Suppose the total number of atoms inside the interaction sphere is N . The vapor density of the atoms inside the sphere is $n = \frac{3N}{4\pi r_b^3}$. We consider that the atom satisfying resonance to the coupling laser $|g_1\rangle \rightarrow |r\rangle$ is at the center of the sphere and has a velocity of v_1 . Not all the atoms inside the interaction sphere but only certain atoms moving with specific velocity class satisfying the anti-blockade condition due to its inter-atomic separation from atom 1 will contribute to this effect.

To calculate the effective number of atoms contributing to the anti-blockade process, let us choose an annular region of radius 'r' and width 'dr'. The volume enclosed by this annular

region is $dV = 4\pi r^2 dr$. The total no of atoms present in that annular region is given by,

$$n_b = n4\pi r^2 dr. \quad (4.20)$$

These atoms are considered to be in the state $|g_2\rangle$. For a particular Rydberg state r_b is constant and thus the atomic density n is also constant. Out of these n_b atoms, only atoms with specific velocity satisfy anti-blockade condition and are excited to the $|rr\rangle$ state. Suppose the atoms moving with velocity v_2 within the velocity window dv are only contributing to the anti-blockade effect. So, the number of atoms in the annular region moving with velocity v_2 is found as

$$N'_b = n_b f(v_2) dv_2 \Rightarrow N'_b = \frac{n_b}{\sqrt{\pi} v_p} e^{-\frac{v_2^2}{v_p^2}} dv_2. \quad (4.21)$$

The velocity width dv_2 is calculated using the line-width of the state $|g_1r\rangle$. The velocity is related to the Rabi frequency Ω_2 as $dv_2 = \frac{\Omega_2}{\Delta k}$, where $\Delta k = k_C - k_P$ is the wave vector mismatch between the probe and the coupling laser. Substituting the value of n from equation 4.18 and Δk in the equation 4.21, the number of atoms in the annular region satisfying the enhanced excitation condition is calculated as

$$N'_b = \frac{4\pi r^2 n}{\sqrt{\pi} v_p} e^{-\frac{v_2^2}{v_p^2}} \frac{\Omega_2}{\Delta k} dr. \quad (4.22)$$

The velocity v_2 is calculated using the anti-blockade condition. As mentioned earlier, the atom at the center of the interaction sphere is moving with velocity v_1 . Thus, the laser detunings of both the atoms are found to be $\Delta_1 = \Delta_C + k_C v_1 - \frac{\Omega_P^2}{4(\Delta_P - k_P v_1)}$ and $\Delta_2 = \Delta_P + \Delta_C - (k_P - k_C)v_2 + \frac{\Omega_P^2}{4(\Delta_P - k_P v_2)}$. The anti-blockade condition constrains the velocity of the second atom to depend on the velocity of the first atom and their inter-particle separation. The resonance condition for the system is given by

$$2V_{rr} = \Delta_1 + \Delta_2. \quad (4.23)$$

$$\begin{aligned}
\Rightarrow 2V_{rr} &= \Delta_P + \Delta_C - (k_P - k_C)v_2 + \frac{\Omega_P^2}{4(\Delta_P - k_P v_2)} + \Delta_C + k_C v_1 - \frac{\Omega_P^2}{4(\Delta_P - k_P v_1)} \\
&= \Delta_P + \Delta_{LS_{v_2}} + 2\Delta_C - (k_P - k_C)v_2 - \Delta_{LS_{v_1}} + k_C v_1.
\end{aligned} \tag{4.24}$$

where the light shift factors are

$$\Delta_{LS_{v_1}} = \frac{\Omega_P^2}{4(\Delta_P - k_P v_1)}$$

and

$$\Delta_{LS_{v_2}} = \frac{\Omega_P^2}{4(\Delta_P - k_P v_2)}.$$

The laser parameters are considered such that the laser detuning is larger than the Doppler width i.e. $\Delta_P \gg k_P v_1, k_P v_2$. Thus, the above two light shift factors are expanded using Taylor's series expansion and neglecting the second and higher order terms of $\frac{\Delta k v_1}{\Delta_P}$ and $\frac{\Delta k v_2}{\Delta_P}$ we get

$$\Delta_{LS_{v_1}} = \frac{\Omega_P^2}{4\Delta_P} \left(1 + \frac{k_P v_1}{\Delta_P}\right)$$

and

$$\Delta_{LS_{v_2}} = \frac{\Omega_P^2}{4\Delta_P} \left(1 + \frac{k_P v_2}{\Delta_P}\right).$$

Using these values of $\Delta_{LS_{v_1}}$ and $\Delta_{LS_{v_2}}$ in equation 4.24 we have

$$\Delta_P + \frac{\Omega_P^2}{4\Delta_P} \left(1 + \frac{k_P v_2}{\Delta_P}\right) + 2\Delta_C + k_C v_2 - k_P v_2 - \frac{\Omega_P^2}{4\Delta_P} \left(1 + \frac{k_P v_1}{\Delta_P}\right) + k_C v_1 = 2\frac{C_6}{r^6} \tag{4.25}$$

$$\Rightarrow v_2 = A \left(2\frac{C_6}{r^6} - \Delta'_{v_1}\right) \tag{4.26}$$

where $\Delta'_{v_1} = \Delta_P + 2\Delta_C + \left(k_C - \frac{\Omega_P^2 k_P}{4\Delta_P^2}\right) v_1$ and $\frac{1}{A} = k_C - k_P + \frac{\Omega_P^2 k_P}{4\Delta_P^2}$. Thus, v_2 is derived as a function of the velocity of the central atom v_1 and the inter-particle separation r . Substituting the value of v_2 in equation 4.20, the number of contributing atoms in the annular region is found

to be

$$N'_b = \frac{4\pi r^2 n}{\sqrt{\pi} v_p} e^{-\left([A(2\frac{C_6}{r^6} - \Delta'_{v_1})]^2 / v_p^2\right)} \frac{\Omega_2}{\Delta k} dr. \quad (4.27)$$

The total no of atoms in the interaction sphere which contribute to the anti-blockade phenomenon is then calculated by integrating N'_b given in equation 4.27 over the radius of the interaction sphere r_b which is given by

$$N_b = \frac{1}{\sqrt{\pi} v_p} \int_0^{r_b} 4\pi r^2 n e^{-\left([A(2\frac{C_6}{r^6} - \Delta'_{v_1})]^2 / v_p^2\right)} \frac{\Omega_2}{\Delta k} dr \quad (4.28)$$

To simplify the integral let us define $x = 2\frac{C_6}{r^6} - \Delta'_{v_1}$ which can be used to calculate

$$r^3 = \frac{\sqrt{2C_6}}{(\Delta'_{v_1} + x)^{\frac{1}{2}}}$$

$$\Rightarrow r^2 dr = -\frac{\sqrt{2C_6}}{6} \frac{dx}{(\Delta'_{v_1} + x)^{\frac{3}{2}}}$$

The integral limit will also change due to change of variables. For $r \rightarrow 0$, $x \rightarrow \infty$ and for $r \rightarrow r_b$, $x \rightarrow 2\frac{C_6}{r_b^6} - \Delta'_{v_1}$. The first factor $\frac{C_6}{r_b^6}$ is the blockade condition and is $\simeq \Omega_2$. The second factor Δ'_{v_1} depends on the velocity of the central atom v_1 and the laser detunings Δ_P and Δ_C . For zero velocity class of atoms i.e. $v_1 = 0$, $\Delta'_{v_1} \simeq \Delta_P$ which is $\gg \Omega_2$. For blue detuned side $v_1 > 0$, thus $\left(k_C - \frac{\Omega_P^2 k_P}{4\Delta_P^2}\right) v_1 > 0$. Therefore, the factor $\Delta'_{v_1} > \Delta_P$ and thus it is $\gg \Omega_2$. For red detuned side with $v_1 < 0$, thus $\left(k_C - \frac{\Omega_P^2 k_P}{4\Delta_P^2}\right) v_1 < 0$. For smaller value of v_1 , $\Delta_P \gg \left(k_C - \frac{\Omega_P^2 k_P}{4\Delta_P^2}\right) v_1$ in this region also $\Delta'_{v_1} \gg \Omega_2$. However, for large value of v_1 , $\Delta'_{v_1} \simeq \Omega_2$. Therefore for a major part of the velocity spectrum of v_1 , $\Delta'_{v_1} \gg 2\frac{C_6}{r_b^6}$. Hence, for $r \rightarrow r_b$, $x \rightarrow -\infty$ will be valid for this region. Substituting r and dr in terms of x on equation 4.28 we have

$$N_b = \frac{2\pi n \Omega_2 \sqrt{2C_6}}{3\sqrt{\pi} v_p \Delta k} \int_{-\infty}^{\infty} \frac{e^{-\frac{A^2 x^2}{v_p^2}}}{(\Delta'_{v_1} + x)^{\frac{3}{2}}} dx \quad (4.29)$$

In the velocity spectrum mentioned previously $\Delta'_{v_1} \gg x$. Thus, the numerator of the above

equation is expanded using a binomial expansion

$$\frac{1}{(\Delta'_{v_1} + x)^{\frac{3}{2}}} = \frac{1}{\Delta'_{v_1}} \left(1 - \frac{3}{2} \frac{x}{\Delta'_{v_1}} + \frac{15}{8} \left(\frac{x}{\Delta'_{v_1}} \right)^2 - \dots \right)$$

Since the integral presented in equation 4.29 is even, all the terms with odd power of x will be integrated to zero. Compared to first term, the contribution of the rest of the terms with even power of x is very small and hence are neglected in the integral. Therefore, the integral in equation 4.29 gives

$$N_b = \frac{2\pi n \Omega_2 \sqrt{2C_6}}{3\sqrt{\pi} v_p \Delta k (\Delta'_{v_1})^{3/2}} \int_{-\infty}^{\infty} e^{-\frac{A^2 x^2}{v_p^2}} dx \quad (4.30)$$

This equation is solved using the gamma function which gives

$$N_b = \frac{\pi n \Omega_2 \sqrt{8C_6}}{3A \Delta k (\Delta'_{v_1})^{\frac{3}{2}}} \quad (4.31)$$

Substituting the values of A and Δ'_{v_1} in the above equation gives

$$N_b = \frac{\pi n \Omega_2 \sqrt{8C_6} (k_C - k_P + \frac{\Omega_P^2 k_P}{4\Delta_P^2})}{\Delta k \left[\Delta_P + 2\Delta_C + k_C v_1 - \frac{\Omega_P^2 k_P v_1}{4\Delta_P^2} \right]^{\frac{3}{2}}} \quad (4.32)$$

The atom at the center of the interaction sphere can move with all possible velocity range. Thus, the total Rydberg population is calculated by Doppler averaging N_b over the velocity v_1 using Maxwell-Boltzmann distribution which is given by

$$\rho_{rr} = \frac{1}{\sqrt{\pi} v_p} \int_{-\infty}^{\infty} N_b \rho_{rr}(v_1) e^{-v_1^2/v_p^2} dv_1$$

The real part of susceptibility in the regime $\Omega_P \gg \Omega_C$ is related to the population of the Rydberg state as¹²⁷

$$Re(\chi_{3L}) = \frac{n |\mu_{eg}|^2}{\epsilon_0 \hbar \Delta_P} \rho_{rr}$$

$$\Rightarrow \text{Re}(\chi_{3L}) = \frac{\Omega_2 \sqrt{8\pi C_6} |\mu_{eg}|^2 (\Delta k + \frac{\Omega_P^2 k_P}{4\Delta_P^2})}{\epsilon_0 \hbar v_p \Delta k} n^2 \int_{-\infty}^{\infty} \frac{\rho_{rr}(v_1) e^{(-v_1^2/v_p^2)}}{(\Delta_P - k_P v_1) (\Delta'_{v_1})^{\frac{3}{2}}} dv_1 \quad (4.33)$$

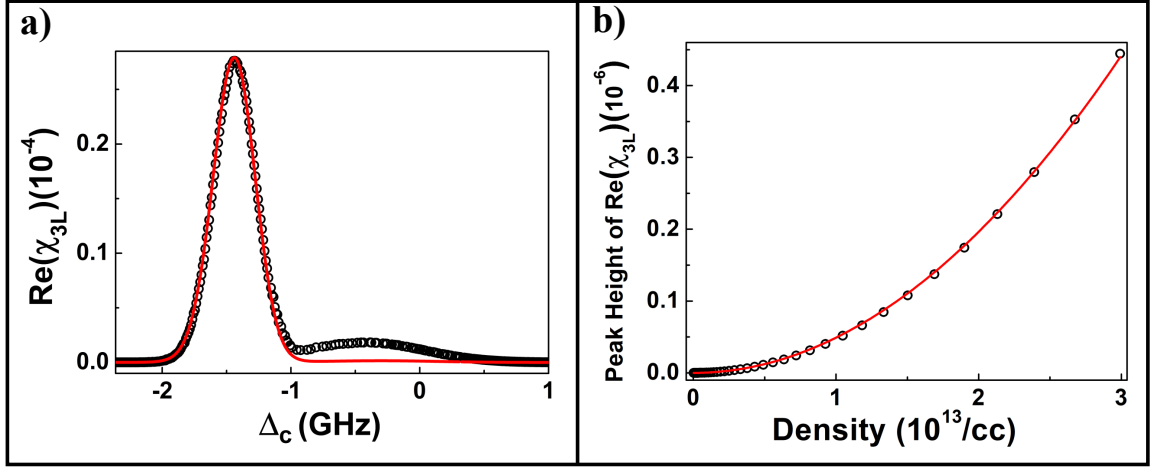


Figure 4.11: (a) Dispersion spectrum of the probe laser calculated using non-interacting model (solid line) and two-atom interacting model (\circ). (b) Calculated dispersion peak height of the anti-blockade peak using two-atom interacting model (\circ) showing the quadratic dependence (solid line) on density.

The dispersion of the probe beam $\text{Re}(\chi_{3L})$ as a function of Δ_C is shown in figure 4.11(a). This model presented above describes the anti-blockade peak corresponding to the transition $|g_1 g_2\rangle \rightarrow |rr\rangle$. The usual two photon peak is studied by using the transition $|g_2 g_2\rangle \rightarrow |r g_2\rangle$. For comparison, a non-interacting two-atom model is also depicted in the figure 4.11(a). A significant enhancement in the anti-blockade peak is observed for the interacting system as compared to the non-interacting one. The population enhancement is observed to be nearly ten times compare to a non-interacting system as presented in figure 4.11(a). This enhancement depends on the interaction strength C_6 . Thus, this phenomenon depends strongly on the principal quantum number of the Rydberg state. Apart from that, it also depends on the density of the atomic vapor. Peak height of the anti-blockade peak in the plot of $\text{Re}(\chi_{3L})$ as a function of the density is also depicted in figure 4.11(b). A quadratic dependence of the anti-blockade peak height is observed with n . Thus, the results provide theoretical prediction of the existence of Rydberg anti-blockade phenomenon in a thermal vapor ensemble.

4.2 Experimental observation

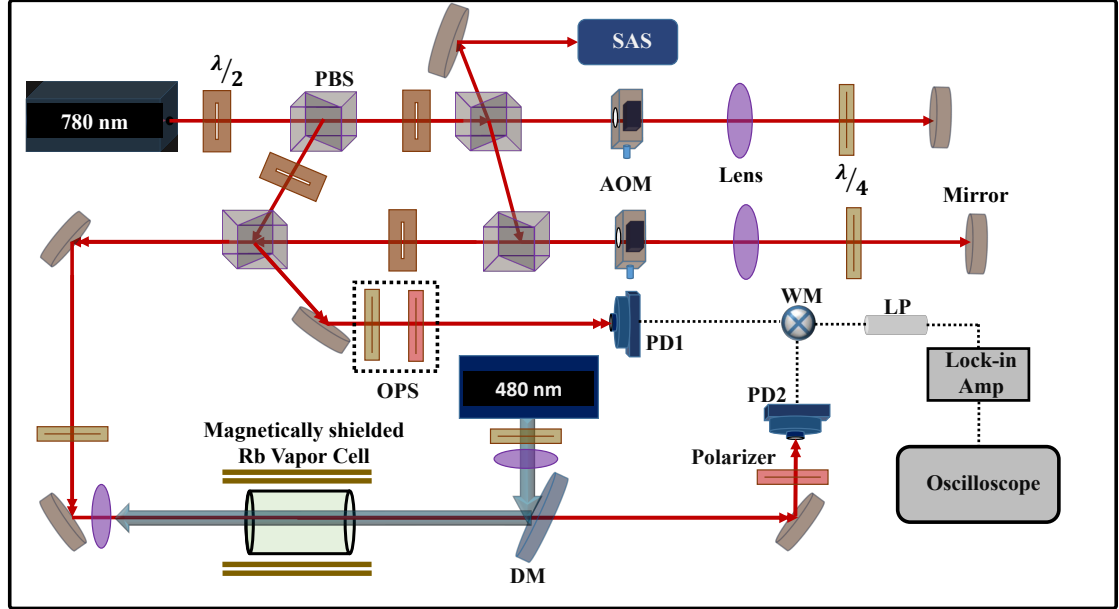


Figure 4.12: *Experimental Set-up to measure the dispersion of the probe beam using OHDT due to the two photon excitation to the Rydberg state.* $\lambda/2$: Half wave plate, $\lambda/4$: Quarter wave plate, PBS: Polarizing beam splitter, AOM: Acousto-optic modulator, DM: Dichroic mirror, PD: Photo detector, WM: Waveform mixer, OPS: Optical phase shifter, SAS: saturated absorption spectroscopy and LP: Low pass filter.

An experiment is performed in thermal atomic vapor to observe the Rydberg anti-blockade effect. The schematic of the experimental set up is depicted in figure. 4.12. The atoms are excited to the Rydberg state using a two photon excitation scheme. Optical heterodyne detection technique (OHDT)^{126,128} is used to measure the dispersion of the probe beam propagating through a magnetically shielded rubidium vapor cell. The details of the OHDT and the theoretical model for relating the dispersion of the probe beam with Rydberg population is presented in the reference.^{128,165} The probe beam is blue detuned from the atomic resonance of the transition $^{85}\text{Rb } 5S_{1/2}F = 3 \rightarrow 5P_{3/2}$ by 1.25 GHz which is well outside the Doppler linewidth. The frequency offset of 800 MHz is generated between the probe beams using AOMs. Both the beams are derived from an external cavity diode laser operating at 780 nm. The coupling laser operating in the range of 478 to 482 nm satisfying two photon transition to the Rydberg state

counter-propagates the probe beams through the vapor cell. The density of the atomic vapor is varied by changing the temperature of the cell using a heating arrangement and the temperature is controlled using a PID controller. The non-linear phase shift of the probe laser ($Re(\chi_{3L})$) due to two-photon excitation to the Rydberg state in the presence of the coupling laser is measured using the OHDT.

The corresponding energy level diagram associated with the experiment is depicted in figure 4.13(a). A typical dispersion spectrum of the probe beam observed in the experiment during excitation to a Rydberg state of $33S_{1/2}$ by scanning the coupling beam is presented in the figure. 4.13(b). Four different peaks are observed in the spectrum of $Re(\chi_{3L})$ when Δ_C is scanned by few GHz. Out of the four peaks, three of them correspond to the hyperfine ground state of rubidium. Two of them are for $^{85}\text{Rb } 5S_{1/2}F = 2$ and $F = 3$ to the Rydberg state and the other one corresponds to $^{87}\text{Rb } 5S_{1/2}F = 2 \rightarrow |r\rangle$ transition. The probe beam blue detuned to the transition $^{85}\text{Rb } 5S_{1/2}F = 3 \rightarrow 5P_{3/2}$ by 1.25 GHz. Thus, the peak at $\Delta_C \simeq -1.25$ GHz, corresponds to the two photon excitation peak. This peak is used to study the blockade phenomenon.¹²⁷ However, a fourth peak at $\Delta_C = 0$ that does not satisfy any resonant two-photon atomic transitions is also observed. The existence of this peak can only be explained using the phenomenon of Rydberg anti-blockade. This peak is used to study the Rydberg anti-blockade effect. The experiment is performed for the Rydberg states $35S_{1/2}$, $40S_{1/2}$, $45S_{1/2}$ and $53S_{1/2}$. The beam waist (Rayleigh range) of the probe and the coupling laser was $95 \mu\text{m}$ (36.33 mm) and $80 \mu\text{m}$ (41.86 mm). The probe laser power is kept fixed at 4 mW which corresponds to a Rabi frequency of 400 MHz. The coupling laser power is varied by following $n^{3/2}$ law to keep the coupling Rabi frequency fixed at 4 MHz. By varying the density of the rubidium vapor the variation in the dispersion of the probe beam is measured using OHDT with $\Delta_P = 1.25$ GHz. All the laser parameters including the gain in lock-in amplifier are kept fixed throughout the experiment for all the Rydberg states.

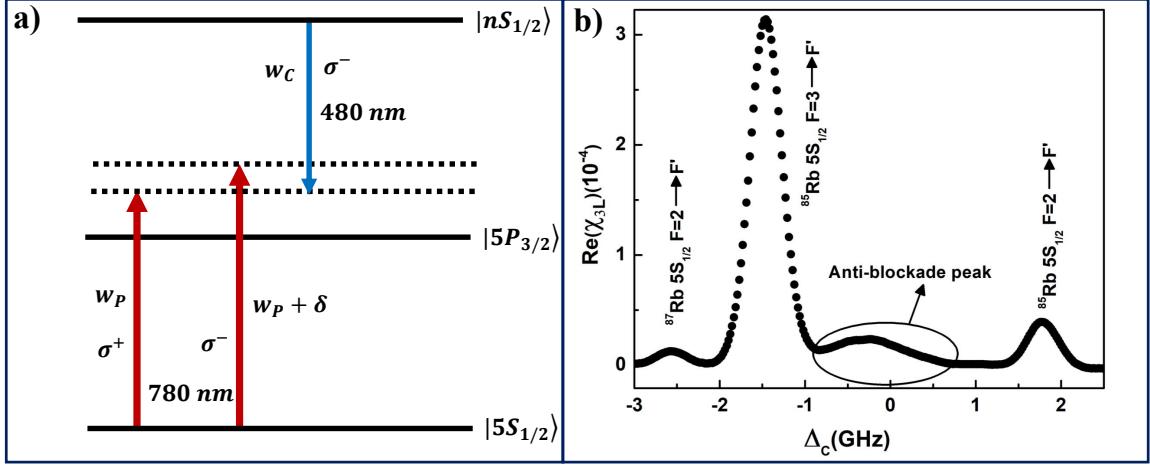


Figure 4.13: (a) Energy level diagram of the two-photon atomic excitation to the Rydberg state. (b) Observed dispersion signal of the probe beam while scanning the coupling laser frequency Δ_c .

4.3 Analysis

As predicted in the theoretical model, two peaks are observed in the experiment that corresponds to the two dressed states. One of them is the usual two photon resonant peak that arises in a three level system. The other one is the anti-blockade peak arising due to Rydberg-Rydberg interaction. The inter-atomic interaction is repulsive for $nS_{1/2}$ Rydberg state. Therefore, the anti-blockade peak is anticipated to be observed on the blue detuned side of the dispersion spectrum. For Rydberg states with lower principal quantum number, the interaction is weak and becomes significant only at very high atomic density. However, with increase in Rydberg state principal quantum number, the interaction becomes significant and the anti-blockade peak is observed even at lower densities. The usual two photon resonant peak has a width of nearly $\Delta k v_p$ as presented in the theoretical model. Similarly, for the anti-blockade peak the width is nearly $k_C v_p$. The width of the anti-blockade peak is observed to be larger than the two photon peak as presented in figure 4.14, which is in good agreement with the theory. For repulsive interaction, as shown in figure 4.10(a), the contribution of the off resonant atom to the Rydberg population is more in a blue detuned case as compared to a red detuned case. Referring to the two photon resonant peak presented in figure 4.14, the anti-blockade effect is larger on

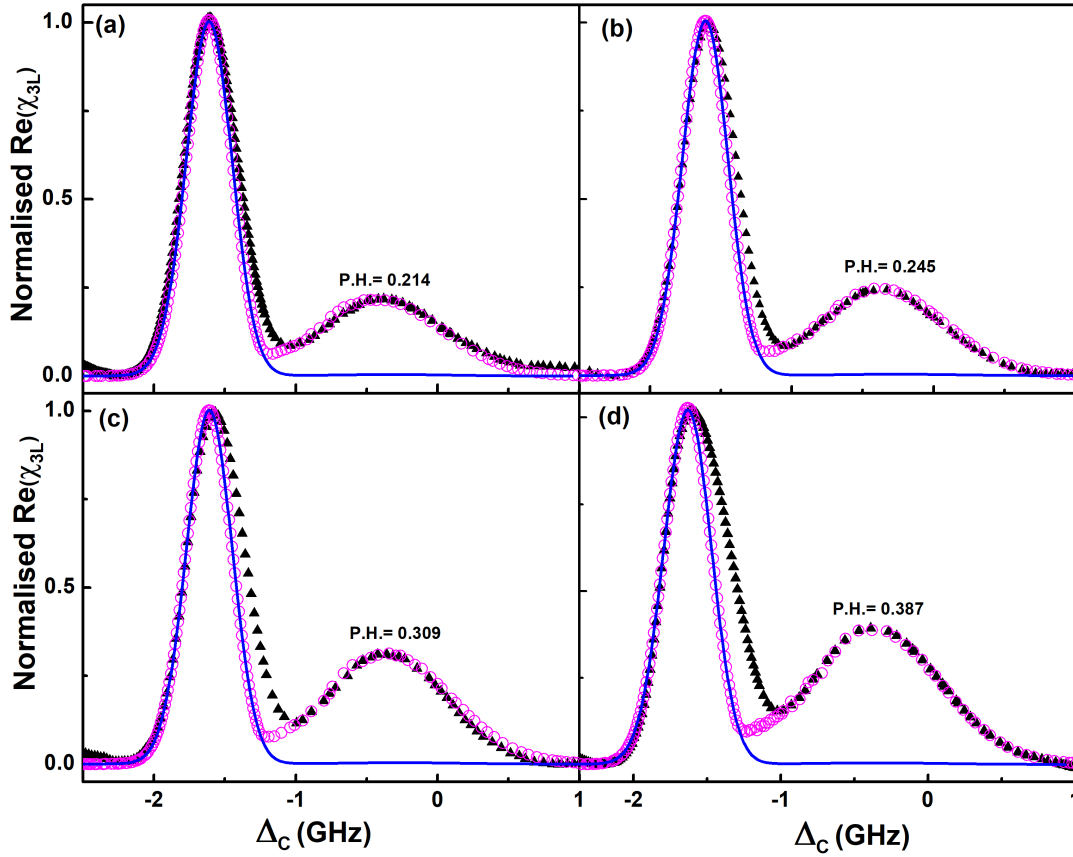


Figure 4.14: Dispersion spectrum measured from the experiment (black triangle) and calculated from the interacting two-atom model (\circ) for the Rydberg state with principal quantum numbers (a) $n = 35$ (b) $n = 40$ (c) $n = 45$ and (d) $n = 53$. For comparison, dispersion calculated from the non-interacting model is depicted as solid lines for all the n states. P.H. represents the Peak height of the anti-blockade peak.

the blue detuned side compared to the red detuned side while coupling to $nS_{1/2}$ state. Since, both blockade and anti-blockade effect is contained in the two photon resonant peak, it is difficult to model theoretically. However, this peak is compared to a non-interacting model in order to have a qualitative understanding. As shown in figure 4.14, with increase in principal quantum number a deviation is observed in the experimental data compared to the non interacting model. The deviation on the blue detuned side of the spectrum is an indication of the dominating anti-blockade effect.

The experiment is repeated for Rydberg states with $n = 35, 40, 45$ and $53 S_{1/2}$. The dispersion spectrum observed in the experiment is compared to the interacting two-atom model and is depicted in figure 4.14. Both the peak widths are found to be matching with the theoretical

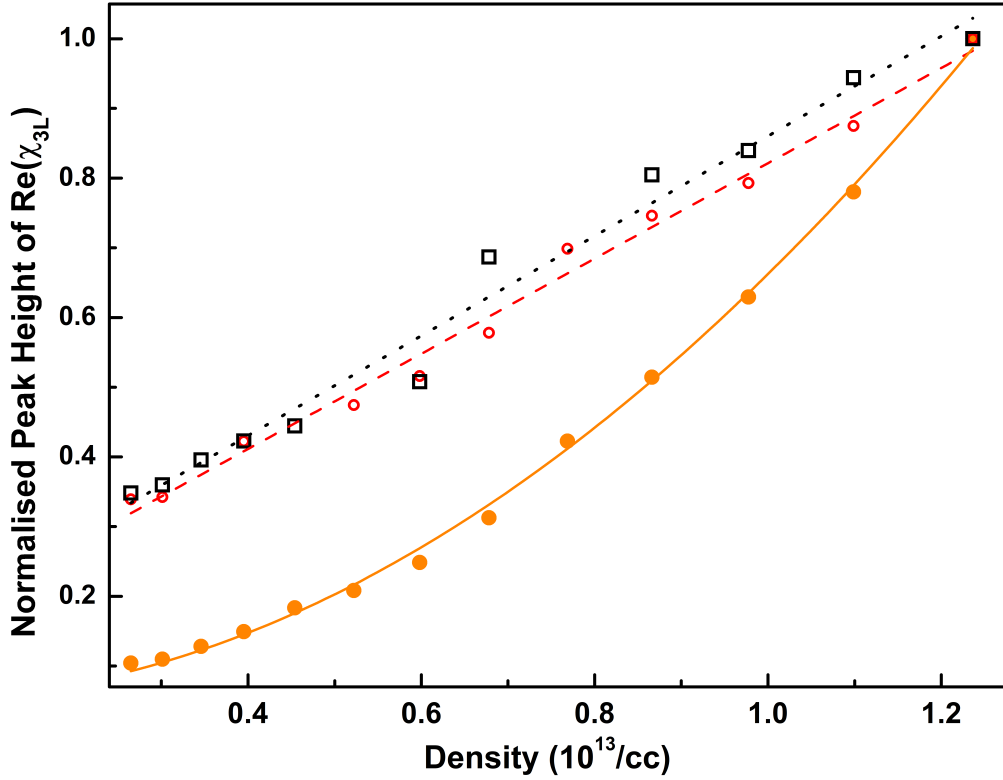


Figure 4.15: Anti-blockade peak height (●) and the usual two-photon resonant peak height for $^{85}\text{Rb } 5S_{1/2} F=3 \rightarrow nS_{1/2}$ (○) and $^{85}\text{Rb } 5S_{1/2} F=2 \rightarrow nS_{1/2}$ transition (◊) for $n = 35$ Rydberg state as a function of the density of the atomic vapor. The peak heights are normalized to the dispersion peak height corresponding to the highest density. Dotted lines are the straight line fitting of usual two-photon resonant peaks showing the linear dependence of density whereas the solid line is fitting of the anti-blockade peak height showing quadratic dependence of density.

model for all Rydberg states. Both peak heights are normalized to the height of the experimental peaks. $Re(\chi_{3L})$ calculated from a three-level system is also depicted in figure 4.14. A significant enhancement in the anti-blockade peak height is observed when the density of the atomic vapor is increased to have more than two-atom inside the interaction sphere.

With increase in principal quantum number of the Rydberg state, the anti-blockade peak height is observed to be increasing for fixed atomic density. This is arising as the anti-blockade peak height depends on the interaction strength C_6 as mentioned in the equation 4.33. However, the scaling of C_6 with the principal quantum number of the Rydberg state could not be observed using this peak. This is due to the fact that, when the number of atoms in the state $|g_2\rangle$ inside the interaction sphere is more than one, the blockade effect contributes. Along with

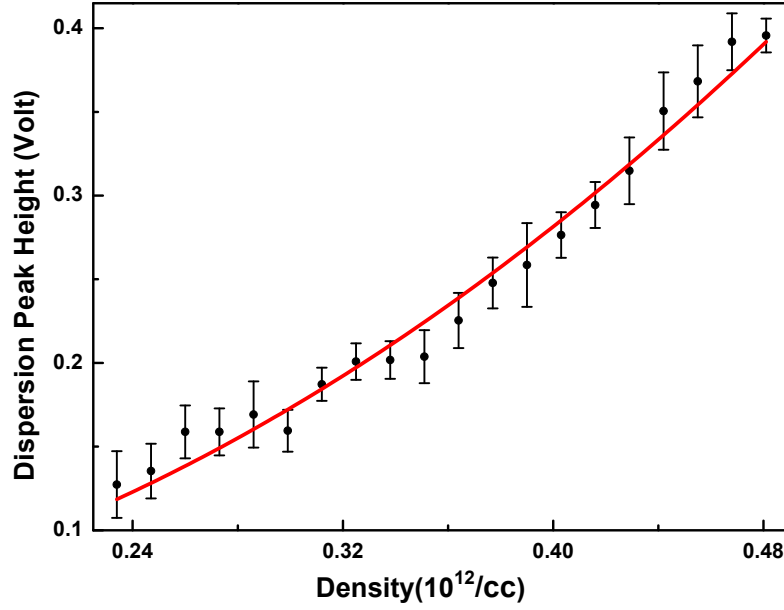


Figure 4.16: The dispersion peak height for anti-blockade peak as a function of the density of the atomic vapor. The dots are the experimental observation and red line represents the quadratic fitting.

that other cascaded processes involving more number of atoms also contribute to the Rydberg excitation. Therefore, it will be difficult to model theoretically. For a Rydberg state with $n=35$, the interaction is small and the number of atom in the state $|g_2\rangle$, $N_b \simeq 1$ with atomic density of $3.0 \times 10^{13}/\text{cc}$. Thus, the experimental data is expected to match with the two-atom model presented in the theory. The dispersion peak height for the anti-blockade peak is measured with the variation of density and is depicted in figure 4.15. For $35S_{1/2}$, a quadratic dependence of the anti-blockade peak height with the density of the atomic vapor is observed as predicted in the theoretical model. The height of the two photon resonant peaks corresponding to the transitions $^{85}\text{Rb } 5S_{1/2} F = 2 \rightarrow 35S_{1/2}$ and $^{85}\text{Rb } 5S_{1/2} F = 3 \rightarrow 35S_{1/2}$ is also measured by varying the atomic density. For these two peaks, the variation is observed to be linear. The peaks corresponding to the transition $^{85}\text{Rb } 5S_{1/2} F = 2 \rightarrow 35S_{1/2}$ is expected to be non-interacting as the applied laser is highly detuned from the atomic resonance. Therefore, a linear dependence of density is expected. For the two photon resonant peak corresponding to $^{85}\text{Rb } 5S_{1/2} F = 3 \rightarrow 35S_{1/2}$, both the blockade and anti-blockade effects are present which may be

compensating each other such that the variation with density is roughly linear. The dotted and dashed lines are the linear fittings and the solid line is the quadratic fit of the peak height data as shown in figure 4.15. The reduced χ^2 for the quadratic fit is found to be 1.4×10^{-4} . This is due to insufficient number of data in the experimental observation. Thus, the experiment is performed using the modified OHDT in order to have a higher number of data for better statistics.

In order to collect larger number of data for the anti-blockade peak, the modified OHDT is used. The experimental set-up for the modified OHDT is explained in details in chapter 3. The peak height of the anti-blockade peak in the dispersion spectrum of the probe beam is measured by varying the density of the atomic vapor. The density and the peak height data is collected simultaneously using LabVIEW program. The statistical error is then calculated for the anti-blockade peak height. The plot for the anti-blockade peak height with the density of the atomic vapor is depicted in figure 4.16. The red line represents the fitting with a quadratic function. The reduced χ^2 for the fitting is found to be 0.57, which indicates the fitting has improved due to higher number of data points.

4.4 Conclusion

We observe the interaction induced enhancement in Rydberg excitation or Rydberg anti-blockade using thermal rubidium vapor. Using the dressed state picture of the three-level atomic system, a two-atom interacting model is formulated to explain the anti-blockade effect. An experiment is performed in thermal rubidium vapor to observe the dispersion of the probe beam due to two photon excitation to the Rydberg state. The anti-blockade peak is observed in the experiment along with other resonant peaks. The population of the Rydberg state is observed to be enhancing quadratically with the density of the atomic vapor for $n=35$, as predicted in the theoretical model. The quadratic dependence of the anti-blockade peak with the density of the atomic vapor could not be observed for higher principal quantum number states as the number of atoms inside the interaction sphere will be larger than two. The deviation from the quadratic

behavior is arising due to the blockade effect and the cascaded processes on the anti-blockade peak having more than one atom in the $|g_2\rangle$ state inside the interaction sphere. In order to study the effect of higher number of atoms, the model for three atoms in the interaction sphere has to be formulated by suitably incorporating the blockade effect and other cascaded processes in the system. Incorporating all these effects in the model will be difficult. Therefore, the study presented here is limited to a two-atom model. Also, the scaling of the interaction strength with the principal quantum number of the Rydberg state could not be observed. However, the result presented here provides a clear indication of the existence of the Rydberg anti-blockade effect in thermal atomic vapor.

Chapter 5

Study of the effect of super-atom dephasing on Rydberg blockade in thermal vapor

Strong dipolar inter-atomic interactions of Rydberg atoms are considered to be a useful tool to study many co-operative phenomena such as Rydberg blockade and Rydberg anti-blockade. Rydberg blockade is a phenomenon where the energy of the Rydberg state shifts out of resonance to the applied laser by interacting with nearby atoms. It has a variety of applications as it generates a correlated atomic ensemble.⁴ The blockade phenomenon has been experimentally studied by various groups in ultra-cold atomic ensemble,⁴²⁻⁴⁷ single atom trap^{54,55} and Bose Einstein condensate.⁴⁸⁻⁵³ It was realized that a fully blocked ensemble of N atoms can be represented by a super-atom with dipole moment enhanced by a factor of \sqrt{N} . This leads the system to a many-body entangled state.^{56,57} This enhances the possibility of realization of non-classical sources of light.^{10,56,57,66} Optically driven Rydberg interaction induced many body effect due to the blockade phenomenon are also studied in a dissipative system theoretically⁷¹⁻⁷⁵ as well as experimentally in ultra-cold ensemble.⁷⁶

Thermal vapor ensemble has an advantage in terms of simplified experimental set-up compared to a cold atomic ensemble. Experimentally, it has been observed that Rydberg excitation

in thermal vapor in the mean field regime shows non-equilibrium phase transition.^{101,118,176,177} Study of non-equilibrium dynamics in a driven dissipative thermal ensemble is reported recently using Rydberg interaction.¹²¹ Similarly, partial suppression in the Rydberg excitation has also been observed when the atom is excited using a pulsed laser.¹⁷⁸ Using Rabi oscillation in nano-second time scale, existence of Van der Waals interaction between Rydberg atoms has been reported.²¹ Using two photon excitation to Rydberg state, observation of blockade¹⁵⁸ and anti-blockade¹³¹ effects are reported in thermal atomic vapor. A single photon source based on strongly interacting Rydberg atoms has also been reported in thermal atomic vapor.¹²⁹

For cold atomic ensemble, the atoms are considered to be frozen. Thus, the dephasing in the system is mostly due to the population decay and the laser frequency noise. However, for thermal vapor ensemble the velocity of the atoms contribute significantly to the dephasing rate. The population decay is dominated by transit time dephasing which arises mostly due to the transverse movement of the atoms through the beam profile. Also, the super-atom dephasing, arising due to transverse velocity of the atoms inside the blockade sphere becomes significant for a thermal vapor system.

In this chapter, we have presented an approximate model for N-interacting atoms inside the blockade sphere for cold as well as thermal vapor ensemble. The exact numerical calculation for two, three and four atoms inside the blockade sphere are presented. Using suitable approximations due to strong Rydberg-Rydberg interaction and symmetry in the system, the optical Bloch equations are simplified which leads to an approximate model with a set of four independent equations irrespective of the number of atoms in the blockade sphere. Using the two, three and four-atom calculations, the OBEs of the approximate model are extrapolated for N-atoms inside the blockade sphere using the method of induction. Due to the phenomena of blockade, atoms present inside the blockade sphere combinely behave as a super-atom as presented in section 2.8.3. Using this super-atom picture, an empirical formula is also derived for N-interacting atoms inside the blockade sphere for a cold atomic ensemble. The effect of different dephasing mechanisms in the blockade phenomenon is also studied in details.

5.1 Two-atom model

5.1.1 Two-atom system in thermal vapor

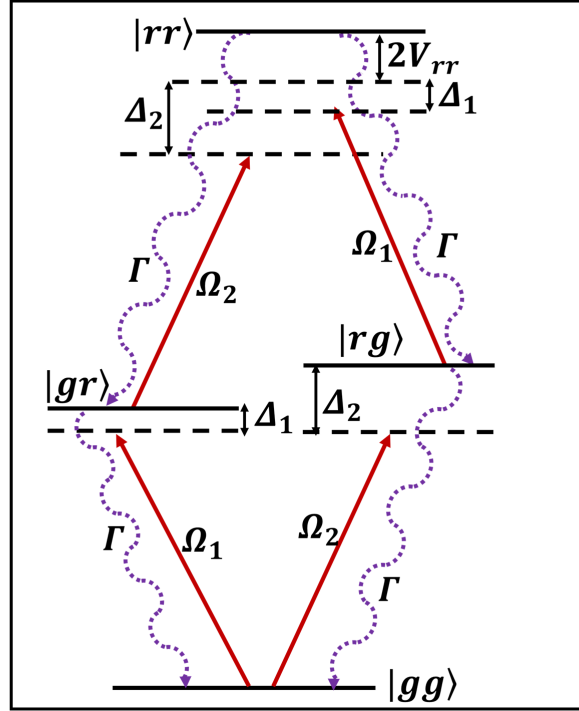


Figure 5.1: (a) The energy level diagram of the two-atom system with levels $|1\rangle \equiv |gg\rangle$, $|2\rangle \equiv |gr\rangle$, $|3\rangle \equiv |rg\rangle$ and $|4\rangle \equiv |rr\rangle$. The applied laser is detuned by Δ_1 from one atomic resonance and Δ_2 from the other atomic resonance and the Rabi frequencies are Ω_1 and Ω_2 .

Consider a simple case of two atoms each of them having two energy levels, a ground state $|g\rangle$ and an excited state $|r\rangle$ coupled by an applied laser. In a thermal vapor ensemble, the atoms move randomly and the Doppler effect due to the velocity of the atoms is significant enough to take into consideration. Both the atoms are considered to be moving with different velocities. Let us consider the velocity of atom 1 and atom 2 are \vec{v}_1 and \vec{v}_2 respectively. So the laser detunings are given by $\Delta_1 = \Delta - \vec{k} \cdot \vec{v}_1$ for atom 1 and $\Delta_2 = \Delta - \vec{k} \cdot \vec{v}_2$ for atom 2, where Δ is the laser detuning with respect to the atoms at rest and \vec{k} is the wave vector of the applied laser. The Rabi frequencies of atom 1 and atom 2 are considered to be Ω_1 and Ω_2 respectively. Figure 5.1 represents the energy level diagram for the two-atom system. $|1\rangle$ corresponds to the level where both the atoms are in the ground state, $|2\rangle$ and $|3\rangle$ correspond to levels with one

atom in the ground state and the other one in the Rydberg state and when both the atoms are in the Rydberg state, it is represented with level $|4\rangle$. The Hamiltonian for the composite two-atom system is given by

$$H = H^{(1)} \otimes \mathbf{I} + \mathbf{I} \otimes H^{(2)} + 2V_{rr} |4\rangle \langle 4|. \quad (5.1)$$

Here $H^{(1)} = \frac{-\hbar}{2} \begin{bmatrix} 0 & \Omega_1 \\ \Omega_1 & 2\Delta_1 \end{bmatrix}$ and $H^{(2)} = \frac{-\hbar}{2} \begin{bmatrix} 0 & \Omega_2 \\ \Omega_2 & 2\Delta_2 \end{bmatrix}$ represent the Hamiltonians of atom 1 and atom 2 respectively calculated using the rotating wave approximation and $\mathbf{I} = \begin{bmatrix} 1 & 0 \\ 0 & 1 \end{bmatrix}$ is a 2 dimensional identity matrix. The two atoms are considered to be interacting via Van der Waals interaction. As presented in chapter 2 section 2.1.2, the interaction potential is $V_{rr} = \frac{C_6}{r^6}$. This interaction is significant when both the atoms are in the Rydberg state and hence it is included as a shift in energy of the state $|4\rangle$. Using equation 5.1 the Hamiltonian for the two-atom system is calculated to be

$$H = \frac{-\hbar}{2} \begin{bmatrix} 0 & \Omega_1 & \Omega_2 & 0 \\ \Omega_1 & 2\Delta_1 & 0 & \Omega_2 \\ \Omega_2 & 0 & 2\Delta_2 & \Omega_1 \\ 0 & \Omega_2 & \Omega_1 & 2(\Delta_1 + \Delta_2) + 2V_{rr} \end{bmatrix}. \quad (5.2)$$

The decay and decoherences of the system are incorporated in the model using the Lindblad matrix. The dephasing mechanisms in the system are described below.

Dephasing mechanisms in the system

There are two significant dephasing mechanisms present in this system.

1. Population decay

The first dephasing mechanism is the population decay, that comprises of the rate of population transfer from the excited state to the ground state. The population decay in ultra-cold atom is mostly due to the spontaneous emission due to finite lifetime of the excited state. However,

for thermal ensemble, the finite transit time of the atom moving transverse to the beam profile dominates. Due to the motion of the atoms, when a Rydberg excited atom moves out of the beam profile and a ground state atom comes in, it can be considered as a population decay from Rydberg state to the ground state.

2. Laser frequency noise

The second dephasing mechanism is the laser frequency noise limited by the source. The output of the ECDL is not ideally monochromatic but it exhibits some fluctuation of the optical phase. Thus, when the laser field is applied for atomic excitation, it introduces a decoherence between the states.

The Lindblad matrix for the two-atom system where these dephasing mechanisms are suitably incorporated is given by⁵⁸

$$L_D = L_D^{(1)} \otimes \rho^{(2)} + \rho^{(1)} \otimes L_D^{(2)}. \quad (5.3)$$

$\rho^{(i)}$ and $L_D^{(i)}$ represent the density matrix and Lindblad matrix for the i th atom. For an individual atom these are given by

$$L_D^{(i)} = \begin{bmatrix} \Gamma \rho_{22}^{(i)} & -\gamma \rho_{12}^{(i)} \\ -\gamma \rho_{21}^{(i)} & -\Gamma \rho_{22}^{(i)} \end{bmatrix}, \rho^{(i)} = \begin{bmatrix} \rho_{11}^{(i)} & \rho_{12}^{(i)} \\ \rho_{21}^{(i)} & \rho_{22}^{(i)} \end{bmatrix}. \quad (5.4)$$

where Γ is the population decay rate and $\gamma = \frac{\Gamma}{2} + \gamma_{rel}$ is the dipole dephasing rate, where γ_{rel} is the laser frequency noise. To calculate the L_D matrix for the two-atom system the density matrix is mapped to a four-level system using $\rho = \rho^{(1)} \otimes \rho^{(2)}$. The L_D matrix for the two-atom model is given by,

$$L_D = \begin{bmatrix} \Gamma(\rho_{22} + \rho_{33}) & \Gamma\rho_{34} - \gamma\rho_{12} & \Gamma\rho_{24} - \gamma\rho_{13} & -2\gamma\rho_{14} \\ \Gamma\rho_{43} - \gamma\rho_{21} & \Gamma(\rho_{44} - \rho_{22}) & -(2\gamma)\rho_{23} & (\Gamma + \gamma)\rho_{24} \\ \Gamma\rho_{42} - \gamma\rho_{31} & -(2\gamma)\rho_{32} & \Gamma(\rho_{44} - \rho_{33}) & (\Gamma + \gamma)\rho_{34} \\ -2\gamma\rho_{41} & (\Gamma + \gamma)\rho_{42} & (\Gamma + \gamma)\rho_{43} & -2\Gamma\rho_{44} \end{bmatrix}. \quad (5.5)$$

The dynamics of the system is studied using the Optical Bloch equations (OBEs) which is given by

$$\frac{d\rho}{dt} = \frac{1}{i\hbar}[H, \rho] + L_D. \quad (5.6)$$

Using the steady state condition i.e. $\frac{d\rho}{dt} = 0$, the OBEs for the two atom system are found to be

$$\Omega_1(1 - 2\rho_{22} - \rho_{33} - \rho_{44}) + \Omega_2(\rho_{14} - \rho_{32}) + 2\Delta_1\rho_{12} + 2i(\Gamma\rho_{34} - \gamma\rho_{12}) = 0. \quad (5.7)$$

$$\Omega_1(\rho_{14} - \rho_{23}) + \Omega_2(1 - \rho_{22} - 2\rho_{33} - \rho_{44}) + 2\Delta_2\rho_{13} + 2i(\Gamma\rho_{24} - \gamma\rho_{13}) = 0. \quad (5.8)$$

$$\Omega_1(\rho_{13} - \rho_{24}) + \Omega_2(\rho_{12} - \rho_{34}) + 2(\Delta_1 + \Delta_2 + 2V)\rho_{14} - 4i\gamma(\rho_{14}) = 0. \quad (5.9)$$

$$\Omega_1(\rho_{21} - \rho_{12}) + \Omega_2(\rho_{24} - \rho_{42}) + 2i\Gamma(\rho_{44} - \rho_{22}) = 0. \quad (5.10)$$

$$\Omega_1(\rho_{24} - \rho_{13}) + \Omega_2(\rho_{21} - \rho_{43}) + 2(\Delta_2 - \Delta_1)\rho_{23} - 4i\gamma(\rho_{23}) = 0. \quad (5.11)$$

$$\Omega_1(\rho_{23} - \rho_{14}) + \Omega_2(\rho_{22} - \rho_{44}) + 2(\Delta_2 + 2V)\rho_{24} - 2i(\Gamma + \gamma)\rho_{24} = 0. \quad (5.12)$$

$$\Omega_1(\rho_{34} - \rho_{43}) + \Omega_2(\rho_{31} - \rho_{13}) + 2i\Gamma(\rho_{44} - \rho_{33}) = 0. \quad (5.13)$$

$$\Omega_1(\rho_{33} - \rho_{44}) + \Omega_2(\rho_{32} - \rho_{14}) + 2(\Delta_1 + 2V)\rho_{34} - 2i(\Gamma + \gamma)\rho_{34} = 0. \quad (5.14)$$

$$\Omega_1(\rho_{43} - \rho_{34}) + \Omega_2(\rho_{42} - \rho_{24}) - 4i\Gamma(\rho_{44}) = 0. \quad (5.15)$$

These equations are solved numerically using singular value decomposition¹⁸⁵ in fortran to calculate the population of the Rydberg state. The states $|2\rangle$ and $|3\rangle$ have half of the population in the Rydberg state with the other half in the ground state. Thus, the Rydberg state population of the two-atom system is given by $\rho_{rr} = \frac{(\rho_{22} + \rho_{33})}{2} + \rho_{44}$. Rydberg population is plotted as a function of Δ_1 and is shown in figure 5.2 with $\Omega_1 = \Omega_2$ and $\gamma_{rel} = 0$ for both interacting and non-interacting systems. The interaction strength is considered such that it satisfies the

blockade condition. As shown in figure 5.2 (a), for $\Delta_1 - \Delta_2 = 0$, where both the atoms are moving with the same velocity, a significant suppression in population due to Rydberg interaction is observed as compared to the non-interacting system. This suppression is due to the blockade effect arising as a result of strong inter-atomic interaction. However, when the velocity of the two atoms are different satisfying $\Delta_1 - \Delta_2 = \Omega$, a very small deviation is observed between the interacting and the non-interacting system as depicted in figure 5.2(b). This also signifies that the blockade phenomenon reduces when the velocity difference between the atoms is increasing. In addition to that, as shown in figure 5.2(c) when $\Delta_1 - \Delta_2 = 3\Omega$, the interacting system behaves similar to a non-interacting one. Thus, from this observation it can be anticipated that, when the atoms are moving with the same longitudinal velocity or within the velocity range such that $\Delta_1 - \Delta_2 \leq \Omega$ they interact with each other and can participate in the blockade process. If the velocities are very different such that $\Delta_1 - \Delta_2 > \Omega$, they behave like non-interacting.

Therefore, the blockade phenomenon for a system in thermal atomic vapor is explained by solving its OBEs for an atomic system moving with same longitudinal velocity. Thereafter, it can be Doppler averaged over the whole velocity class to include the effect of thermal motion of the atoms. In the next section, we discuss the simplified two-atom model by considering equal detunings for both the atoms.

5.1.2 Simplified two-atom system with super-atom dephasing

Let us consider a two-level atomic system as shown in figure 5.3 (a). It has two energy levels, a ground state $|g\rangle$ and an excited state $|r\rangle$. A laser with Rabi frequency Ω is applied to excite the atom from $|g\rangle \rightarrow |r\rangle$ which has a frequency detuning of Δ from the atomic resonance. Two such identical interacting atoms are considered in an ultra-cold atomic ensemble where they are considered to be frozen. The energy level diagram for the composite two-atom system is shown in figure 5.3 (b). Using the similar approach as presented in equation 5.1, the Hamiltonian for the two-atom system is written as,

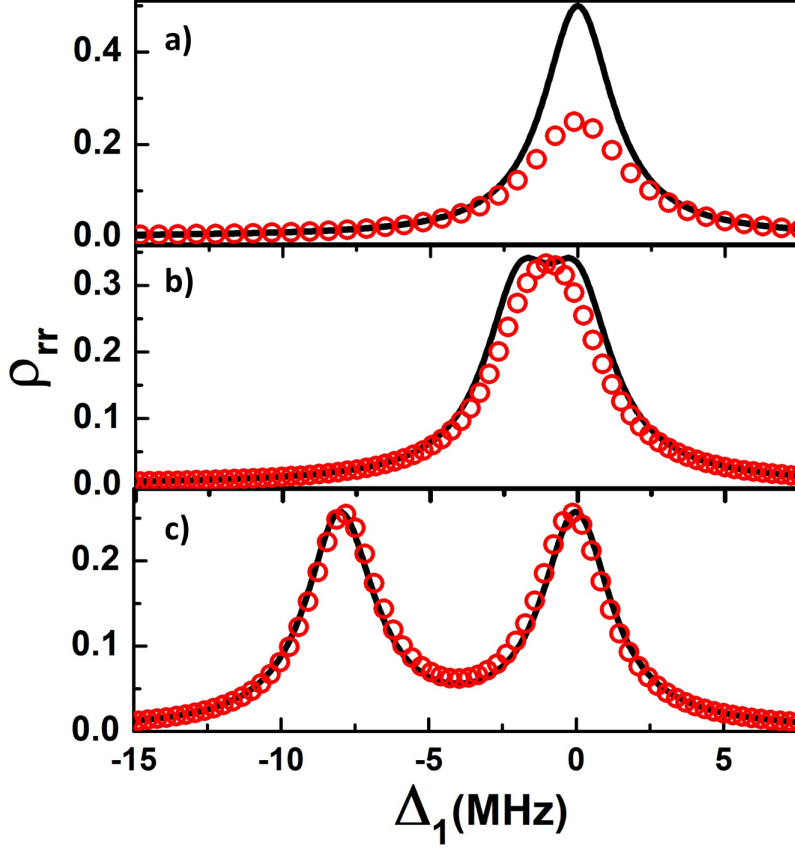


Figure 5.2: Rydberg state population as a function of Δ_1 for non-interacting (—) and interacting (\circ) two-atom system with (a) $\Delta_1 - \Delta_2 = 0$, (b) $\Delta_1 - \Delta_2 = \Omega$ and (c) $\Delta_1 - \Delta_2 = 3\Omega$. The parameters used for these plots are $\Omega_1 = \Omega_2 = 2$ MHz, $\Gamma = 0.1$ MHz, $\gamma_{rel} = 0$ and $V_{rr} = 10$ MHz.

$$H = \frac{-\hbar}{2} \begin{bmatrix} 0 & \Omega & \Omega & 0 \\ \Omega & 2\Delta & 0 & \Omega \\ \Omega & 0 & 2\Delta & \Omega \\ 0 & \Omega & \Omega & 4(\Delta + V_{rr}) \end{bmatrix}. \quad (5.16)$$

Similarly, the L_D matrix for the system is calculated using the equation 5.3 to incorporate the effects of decoherence mechanisms. The population decay and the dephasing due to the laser frequency noise is included in the L_D matrix of individual atoms. However, a third dephasing also arises in the thermal atomic system called a the super-atom dephasing.

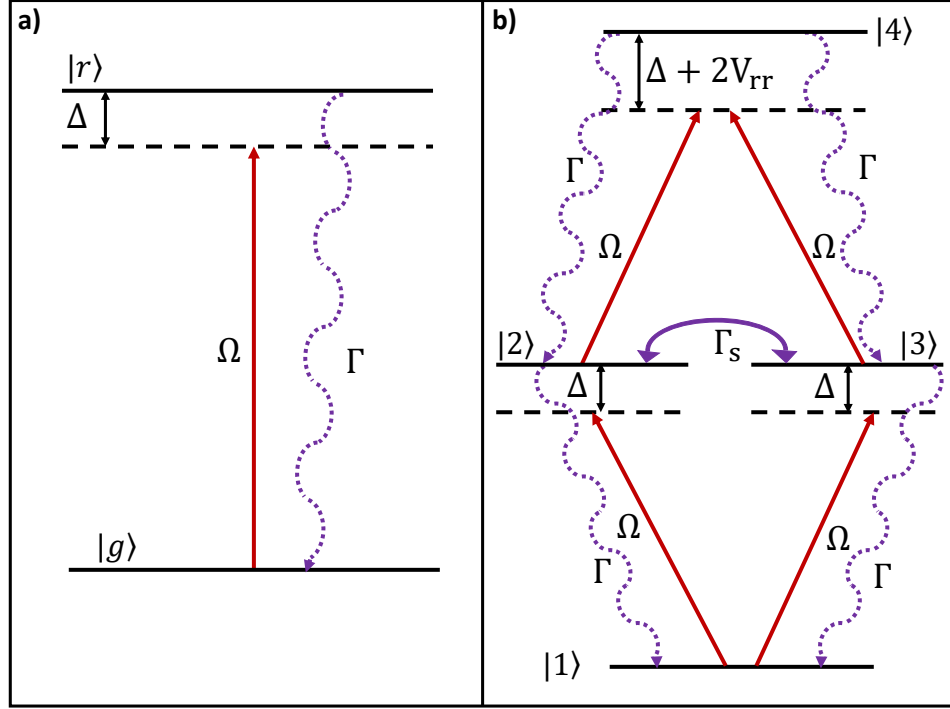


Figure 5.3: (a) A two-level atomic system with ground state $|g\rangle$ and Rydberg state $|r\rangle$. Ω (Δ) is the Rabi frequency (laser detuning) of the applied laser and Γ is the population decay rate. (b) The energy level diagram of an identical two-atom system with levels $|1\rangle \equiv |gg\rangle$, $|2\rangle \equiv |gr\rangle$, $|3\rangle \equiv |rg\rangle$ and $|4\rangle \equiv |rr\rangle$. Γ_S is the super-atom dephasing introduced between the states $|2\rangle$ and $|3\rangle$.

Super-atom dephasing

Although it has been observed in the previous section that atoms with same longitudinal velocity only participate in the blockade phenomenon, the transverse velocity of the atom may move it out of the blockade sphere. This introduces a dephasing between the atoms contributing to the blockade phenomenon. This dephasing is called as the super-atom dephasing (Γ_S). To understand about this dephasing, let us consider a hypothetical situation where two atoms moving with same longitudinal velocity and the transverse velocity component is zero. In this condition the relative distance between the atoms remains constant. The composite two-atom system can be explained using the basis state $|gg\rangle$, $|+\rangle = \frac{1}{\sqrt{2}}(|gr\rangle + e^{-i\phi}|rg\rangle)$, $|-\rangle = \frac{1}{\sqrt{2}}(|gr\rangle - e^{-i\phi}|rg\rangle)$ and $|rr\rangle$. Here, the phase difference $\phi = \vec{k} \cdot (\vec{r}_1 - \vec{r}_2)$ with \vec{k} representing the wave vector of the applied laser and \vec{r}_1 and \vec{r}_2 represent the positions of both the atoms. In an ultra-cold

atomic ensemble where the atoms are frozen the blockade sphere can be imagined to be fixed in space. For an ensemble where the atoms are moving with same longitudinal velocities and the transverse velocities are zero, the system can be imagined as if the blockade sphere is co-propagating with the participating atoms along the propagation direction of the laser beam. In both these cases, the phase ϕ between the state $|gr\rangle$ and $|rg\rangle$ remains constant. However, for a thermal atomic ensemble, the atoms participating in the blockade process may move out of the blockade sphere due to their transverse velocities and new atoms can enter inside the same blockade sphere. The relative positions of the new atoms could be different than the previous atoms which would lead to the dephasing of the coherence between the states $|gr\rangle$ and $|rg\rangle$. This dephasing is called as the super-atom dephasing and is denoted as Γ_S . Crudely speaking, the super-atom dephasing would depend on the size of the blockade sphere and average velocity of the atoms (v_{avg}) in thermal vapor as $\Gamma_S = v_{avg}/2r_b$, where r_b is the blockade radius. If the blockade radius is taken to be $5 \mu\text{m}$ then $\Gamma_S = 50 \text{ MHz}$ for the thermal ensemble at room temperature. In our model, we study the effect of super-atom dephasing in the system by varying it from zero to 60 MHz.

Thus, the L_D matrix for the two-atom system including the super-atom dephasing along with the population decay and laser frequency noise is given by,

$$L_D = \begin{pmatrix} \Gamma(\rho_{22} + \rho_{33}) & \Gamma\rho_{34} - \gamma\rho_{12} & \Gamma\rho_{24} - \gamma\rho_{13} & -2\gamma\rho_{14} \\ \Gamma\rho_{43} - \gamma\rho_{21} & \Gamma(\rho_{44} - \rho_{22}) & -(2\gamma + \Gamma_S)\rho_{23} & (\Gamma + \gamma)\rho_{24} \\ \Gamma\rho_{42} - \gamma\rho_{31} & -(2\gamma + \Gamma_S)\rho_{32} & \Gamma(\rho_{44} - \rho_{33}) & (\Gamma + \gamma)\rho_{34} \\ -2\gamma\rho_{41} & (\Gamma + \gamma)\rho_{42} & (\Gamma + \gamma)\rho_{43} & -2\Gamma\rho_{44} \end{pmatrix}. \quad (5.17)$$

The OBEs for this system is calculated using equation 5.6 in steady state which are given

by

$$\Omega(1 - 2\rho_{22} - \rho_{33} - \rho_{44}) + \Omega(\rho_{14} - \rho_{32}) + 2\Delta\rho_{12} + 2i(\Gamma\rho_{34} - \gamma\rho_{12}) = 0. \quad (5.18)$$

$$\Omega(\rho_{14} - \rho_{23}) + \Omega(1 - \rho_{22} - 2\rho_{33} - \rho_{44}) + 2\Delta\rho_{13} + 2i(\Gamma\rho_{24} - \gamma\rho_{13}) = 0. \quad (5.19)$$

$$\Omega(\rho_{13} - \rho_{24}) + \Omega(\rho_{12} - \rho_{34}) + 2(2\Delta + 2V)\rho_{14} - 4i\gamma(\rho_{14}) = 0. \quad (5.20)$$

$$\Omega(\rho_{21} - \rho_{12}) + \Omega(\rho_{24} - \rho_{42}) + 2i\Gamma(\rho_{44} - \rho_{22}) = 0. \quad (5.21)$$

$$\Omega(\rho_{24} - \rho_{13}) + \Omega(\rho_{21} - \rho_{43}) - 4i\gamma(\rho_{23}) - 2i\Gamma_S\rho_{23} = 0. \quad (5.22)$$

$$\Omega(\rho_{23} - \rho_{14}) + \Omega(\rho_{22} - \rho_{44}) + 2(\Delta + 2V)\rho_{24} - 2i(\Gamma + \gamma)\rho_{24} = 0. \quad (5.23)$$

$$\Omega(\rho_{34} - \rho_{43}) + \Omega(\rho_{31} - \rho_{13}) + 2i\Gamma(\rho_{44} - \rho_{33}) = 0. \quad (5.24)$$

$$\Omega(\rho_{33} - \rho_{44}) + \Omega(\rho_{32} - \rho_{14}) + 2(\Delta + 2V)\rho_{34} - 2i(\Gamma + \gamma)\rho_{34} = 0. \quad (5.25)$$

$$\Omega(\rho_{43} - \rho_{34}) + \Omega(\rho_{42} - \rho_{24}) - 4i\Gamma(\rho_{44}) = 0. \quad (5.26)$$

These equations are solved numerically using same technique mentioned above to calculate the Rydberg state population of the composite system which is given by $\rho_{rr} = \rho_{44} + (\rho_{22} + \rho_{33})/2$. ρ_{rr} as a function of Δ is depicted in figure 5.4 (a) for $V_{rr} = 0$. Although the two-atom model can be solved exactly due to less complexity in mathematical formulation, with the same technique it becomes difficult to solve the system exactly when the number of atoms in the interaction sphere is large. In the next section we discuss a simplified two-atom model in order to reduce the mathematical complexity.

5.1.3 Approximate two-atom model

The two-atom model presented in the previous section assumes the atoms are indistinguishable. This introduces a symmetry in the system which is used to simplify the OBEs of the two-atom exact numerical calculations. The parameters of the laser coupling of the states $|1\rangle$ and $|4\rangle$ to the states $|2\rangle$ and $|3\rangle$ are the same. Hence, the population and the coherence terms connecting these states are also the same, i.e. $\rho_{22} = \rho_{33}$, $\rho_{12} = \rho_{13}$ and $\rho_{24} = \rho_{34}$. Apart from that, the system is considered to be strongly interacting such that it satisfies the blockade condition.

Thus, the doubly Rydberg excited state $|4\rangle$ shifts out of resonance to the applied laser and is not populated i.e. $\rho_{44} = 0$. These conditions are used in the OBEs of the two-atom exact calculation which gives $Im(\rho_{24}) = 0$ and $\rho_{23} = \frac{\Gamma}{2\gamma + \Gamma_S} \rho_{22}$. From this equation it can be noted that, for $\gamma_{rel} = \Gamma_S = 0$, $\rho_{23} = \rho_{22}$. This is due to the fact that, in absence of dephasing mechanisms the coherence between the two atoms will be maximum. Using the approximations the exact two-atom numerical calculation in steady state simplifies to a set of four OBEs as presented in equation 5.27. This simplified OBEs for the system is called as the approximate two-atom model.

$$\begin{aligned}
\Omega(1 - (3 + \frac{\Gamma}{2\gamma + \Gamma_S})\rho_{22} + \rho_{14}) + 2\Delta\rho_{12} + 2i\Gamma(\rho_{24}) - 2i\gamma\rho_{12} &= 0 \\
2\Omega(\rho_{12} - \rho_{24}) + 2(2\Delta + 2V)\rho_{14} - 4i\gamma\rho_{14} &= 0 \\
\Omega(Im(\rho_{12})) + \Gamma\rho_{22} &= 0 \\
\Omega((1 + \frac{\Gamma}{2\gamma + \Gamma_S})\rho_{22} - \rho_{14}) + 2(\Delta + 2V)(\rho_{24}) - 2i(\Gamma + \gamma)(\rho_{24}) &= 0
\end{aligned} \tag{5.27}$$

These equations are solved to evaluate the matrix element ρ_{22} which gives the Rydberg population due to the blockade process for the approximate two-atom model.

5.1.4 Empirical formula based on the super-atom model

As presented in section 2.1, the population of the Rydberg state using a two-level system is given by

$$\rho_{rr} = \frac{\Omega^2}{2\Omega^2 + 4\Delta^2(\Gamma/(2\gamma)) + 2\gamma\Gamma}. \tag{5.28}$$

Similarly the coherence between the two states is given by

$$Re(\rho_{gr}) = \frac{\Omega\Delta\Gamma/\gamma}{\Omega^2 + 4\Delta^2(\Gamma/2\gamma) + 2\Gamma\gamma}. \tag{5.29}$$

Consider the case where both the atoms are moving with same longitudinal velocity and the transverse velocity is zero. The composite two-atom system can be explained using the basis

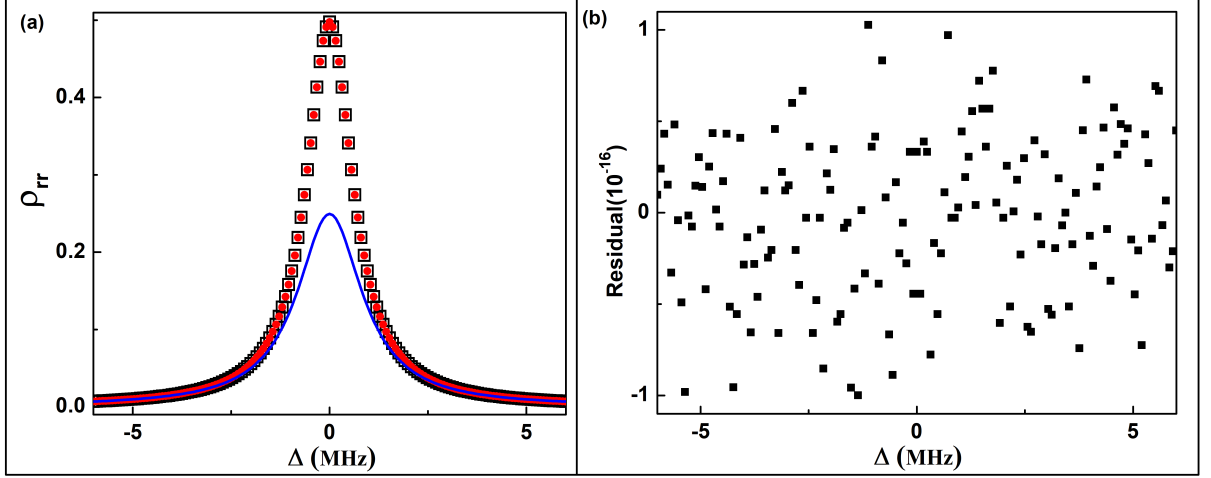


Figure 5.4: (a) The population of the Rydberg state as a function of Δ with $\Omega = 1$ MHz, $\Gamma = 0.1$ MHz, $\gamma_{rel} = 0$ and $\Gamma_S = 0$ for the single atom two-level system (●) and exact two-atom calculation with $V_{rr} = 0$ (□) and with $V_{rr} = 20$ MHz (—). (b) The residual plot of the exact two-atom calculation with $V_{rr} = 0$ and the single atom two-level system.

state $|gg\rangle, |+\rangle = \frac{1}{\sqrt{2}}(|gr\rangle + e^{-i\phi}|rg\rangle)$, $|-\rangle = \frac{1}{\sqrt{2}}(|gr\rangle - e^{-i\phi}|rg\rangle)$ and $|rr\rangle$, where $\phi = \vec{k} \cdot (\vec{r}_1 - \vec{r}_2)$ and remains constant during the excitation process since the relative position of the atoms is constant. Such a system can be considered as frozen during the Rydberg excitation process. System being frozen during the excitation process is an important aspect of the study which is achieved in the experiments with ultra-cold atoms. It can be shown that the Rabi coupling of the transition $|gg\rangle \rightarrow |+\rangle$ is $\sqrt{2}\Omega$ and for the transition $|gg\rangle \rightarrow |-\rangle$ it is 0. Similarly, the Rabi coupling of the transition $|+\rangle \rightarrow |rr\rangle$ is $\sqrt{2}\Omega$ and for $|-\rangle \rightarrow |rr\rangle$ it is 0. The energy shift of the $|rr\rangle$ state due to strong Rydberg-Rydberg interaction makes it out of resonance from the driving laser and hence the population of the $|rr\rangle$ state is assumed to be 0. Such a system can be reduced to an effective two-level system with energy levels $|gg\rangle$ and $|+\rangle$ with the coupling Rabi frequency to be $\sqrt{2}\Omega$. Also, the effective Rydberg population of the state $|+\rangle$ is reduced by a factor of 2. The population decay rate from $|+\rangle$ to $|gg\rangle$ is the same as Γ due to the compensation between the factors of enhanced Rabi frequency and reduced population. Considering it as an effective two-level system, we derive the empirical formula to find the

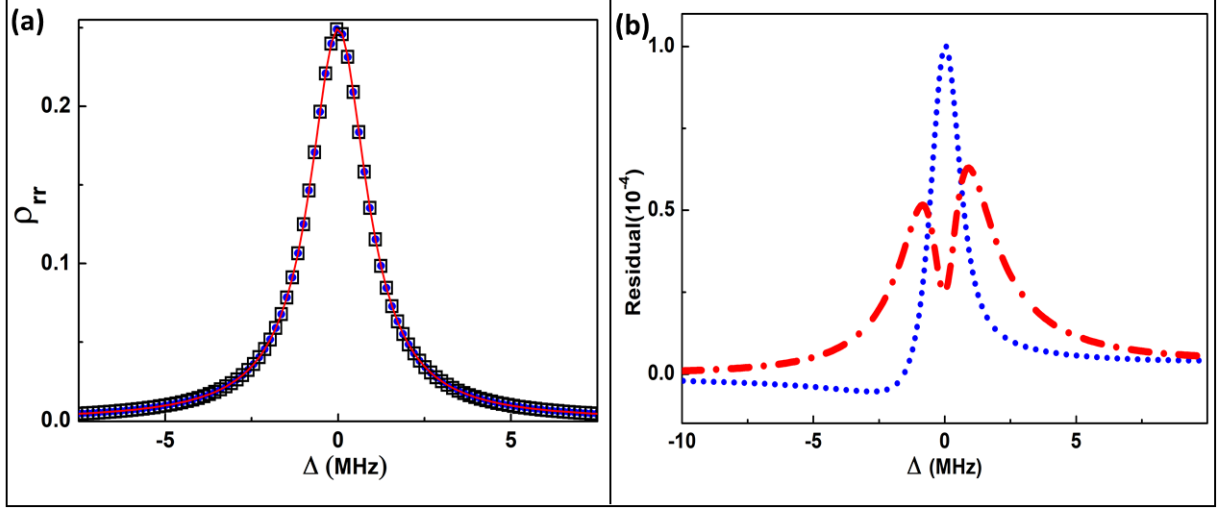


Figure 5.5: (a) ρ_{rr} as a function of Δ for two-atom exact numerical calculation (\square) and approximate model (\bullet) with $V_{rr} = 20$ MHz and for the empirical formula (---). (b) The residual plot of empirical formula (blue dotted line) and approximate model (red dashed line) with the exact numerical calculation.

effective Rydberg population of the composite two-atom system which is given by,

$$\rho_{rr} = \frac{\Omega^2}{4\Omega^2 + 4\Delta^2(\Gamma/(2\gamma)) + 2\gamma\Gamma}. \quad (5.30)$$

Using similar approach, an empirical formula is derived for the coherence term $Re(\rho_{gr})$ using the super-atom picture. Due to the blockade process in a two-atom system, the coherence between the ground state $|gg\rangle$ and the entangled state $\frac{1}{\sqrt{2}}(|gr\rangle + |rg\rangle)$ reduces by a factor of $1/\sqrt{2}$. Using this condition, the empirical formula for the coherence between $|g\rangle$ and $|r\rangle$ for two-atom system is given by

$$Re(\rho_{gr}) = \frac{(\sqrt{2}\Omega)\Delta\Gamma/\gamma}{\sqrt{2}((\sqrt{2}\Omega)^2 + 4\Delta^2(\Gamma/2\gamma) + 2\Gamma\gamma)}. \quad (5.31)$$

Rydberg population as a function of the laser detuning for the exact numerical calculation is presented in figure 5.4(a) using $V_{rr} = 0$. When the atoms are non-interacting, the two-atom system will be equivalent to a single atom picture i.e. a two-level system. Rydberg population calculated using the two-level system presented in equation 5.28 is also depicted in

figure 5.4(a). The residual plot of the non-interacting two-atom calculation and the single atom picture is depicted in figure 5.4 (b). They are found to be in good agreement with each other with residual 15 order of magnitude smaller than the maximum peak height. This also verifies that the calculation does not have any numerical errors. Now the interaction is included such that it satisfies the blockade condition i.e. $2V_{rr} > \Omega$. This is the case where any one out of the two atoms is excited to the Rydberg state. Therefore, the population of the Rydberg state reduces approximately by a factor of 2 in the two-atom model compared to the non-interacting system as presented in figure 5.4 (a).

For the two-atom system satisfying the blockade phenomena, Rydberg population is calculated using the empirical formula presented in equation 5.30 and is depicted in figure 5.5 (a). The Rydberg population calculated from the exact numerical calculation and the empirical formula matches to each other as shown in the figure 5.5 (a), where γ_{rel} and Γ_S is considered to be zero. The residual plot between them (blue dotted line) is depicted in 5.5 (b). The residuals are found to be nearly 3 orders of magnitude smaller than the maximum peak value. Although for finite γ_{rel} and Γ_S a significant deviation is observed between them which is explained in details later in this chapter. However, the empirical formula is sufficient to explain the blockade phenomenon for the system with $\Gamma_S = 0$ and $\gamma_{rel} = 0$.

Rydberg population calculated using the approximate model is also depicted in figure 5.5 (a). It is observed that the approximate model matches to the exact numerical calculation for $V_{rr} > \sqrt{2}\Omega$, with residuals 3 orders of magnitude smaller than the maximum peak value as shown in figure 5.5 (b). However, for $V_{rr} \leq \sqrt{2}\Omega$ a significant deviation of the approximate model is observed compared to the exact calculation. This is due to the fact that, for $V_{rr} \leq \Omega$, the exact calculation satisfies the anti blockade condition along with the blockade process when the applied laser is frequency scanned. However, in the approximate calculation the system is assumed to be strongly interacting. Thus, it can explain the blockade process only.

Similarly, the coherence between the state $|g\rangle$ and $|r\rangle$ is also studied for the two-atom model. The dispersion of the laser beam due to single photon excitation to the Rydberg state

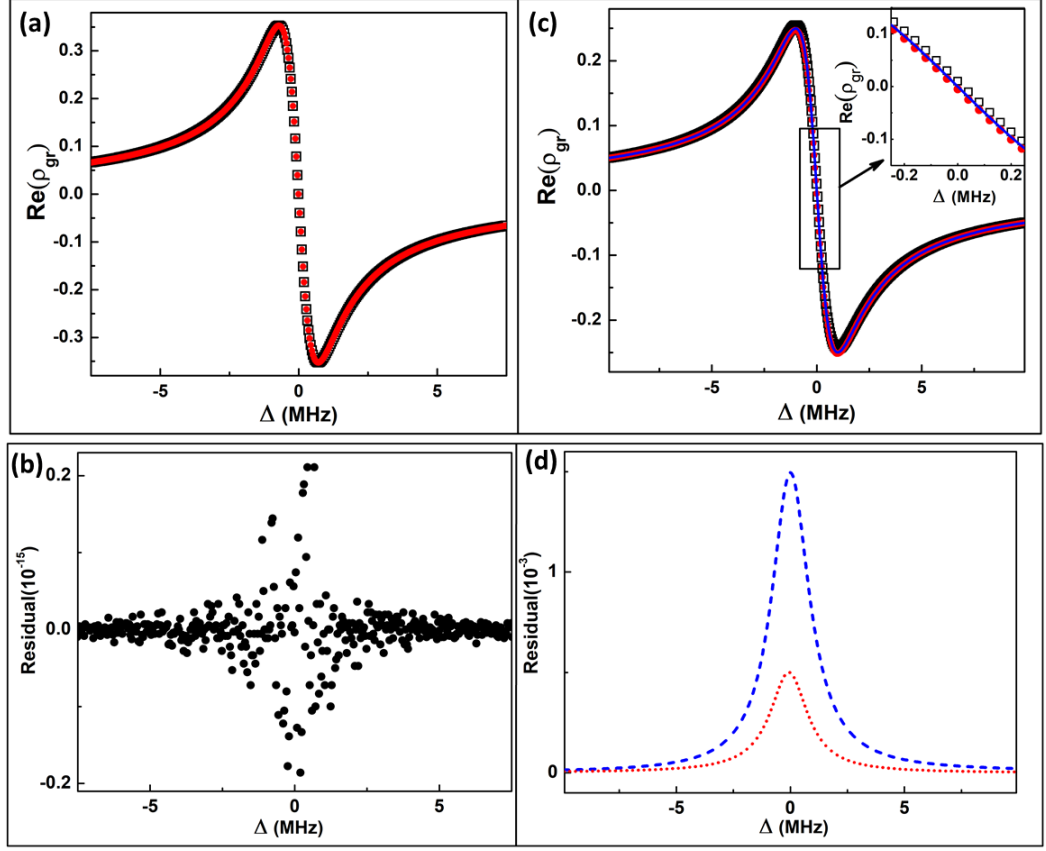


Figure 5.6: Dispersion of the probe beam due to single photon excitation to the Rydberg state as a function of Δ with $\Omega = 1$ MHz and $\Gamma = 0.1$ MHz for (a) exact two-atom calculation (\square) with $V_{rr} = 0$ and for single atom picture (\bullet). (b) The residual plot for the non-interacting two-atom model and the single atom calculation. (c) ρ_{rr} as a function of Δ for empirical formula (—), approximate model (\bullet) and exact calculation (\square) with $V_{rr} = 20$ MHz. The inset of the figure represents a magnified view of a small section of the graph. (d) the residual plot for empirical formula (blue dashed line) and approximate calculation (red dotted line) with the exact calculation.

for the two-atom system is represented by the quantity

$$Re(\rho_{gr}) = \frac{Re(\rho_{12}) + Re(\rho_{13}) + Re(\rho_{24}) + Re(\rho_{34})}{2}.$$

$Re(\rho_{gr})$ is plotted as a function of Δ for the exact numerical calculation as depicted in figure 5.6 (a). When the system is non-interacting, this is compared to $Re(\rho_{gr})$ calculated using equation 5.29 and is also depicted in the same figure. They are found to be in good agreement with residual 14 orders of magnitude smaller than the maximum peak value as depicted in figure 5.6

(b). When the interaction is included such that the system satisfies the blockade condition, $Re(\rho_{gr})$ is found to be deviating from $Re(\rho_{gr})$ calculated using a single atom picture. This is due to the presence of the blockade effect that shifts the $|rr\rangle$ state out of resonance to the applied laser. For a two-atom system, the empirical formula for the single photon dispersion is presented in equation 5.31. $Re(\rho_{gr})$ as a function of Δ , calculated using the empirical formula is plotted in figure 5.6 (c). It is found to be in good agreement with the exact calculation with residual less than 2×10^{-3} as shown in figure 5.6 (d), which is 3 orders of magnitude smaller than the maximum peak height. Probe dispersion due to single photon excitation for the approximate two-atom model presented in equation 5.27, is given by $Re(\rho_{12})$. This is compared to $Re(\rho_{gr})$ calculated from the exact numerical calculation and is depicted in figure 5.6 (c). In presence of the strong interaction, a good agreement is observed between them with residual (red dotted line) less than 5×10^{-4} as shown in figure 5.6 (d), which is 3 orders of magnitude smaller than the maximum peak value.

Therefore, we present three different approaches to study the blockade effect for a two-atom system, the exact numerical calculation, approximate model and the empirical formula. For atomic system with $\Gamma_S = \gamma_{rel} = 0$, a good agreement is observed between them. However, for thermal vapor ensemble, these dephasing mechanisms are significant. Therefore, in the next section the effect of these dephasing mechanisms in the blockade phenomenon are studied.

5.1.5 Effect of dephasing mechanisms in the two-atom model

For a thermal ensemble of atoms, there are three major dephasing mechanisms in the system. Two of them are the population decay and the super-atom dephasing arising due to thermal motion of the atom. The third one is the dephasing due to laser frequency noise.

Population decay

For thermal vapor ensemble, the population decay is dominated by the finite transit time of the atom as explained in section 5.1.1. For a beam size of $100\mu m$ and the thermal atoms at temperature 400 K, $\Gamma \simeq 1.5$ MHz, which is the typical value of population decay rate in thermal atomic

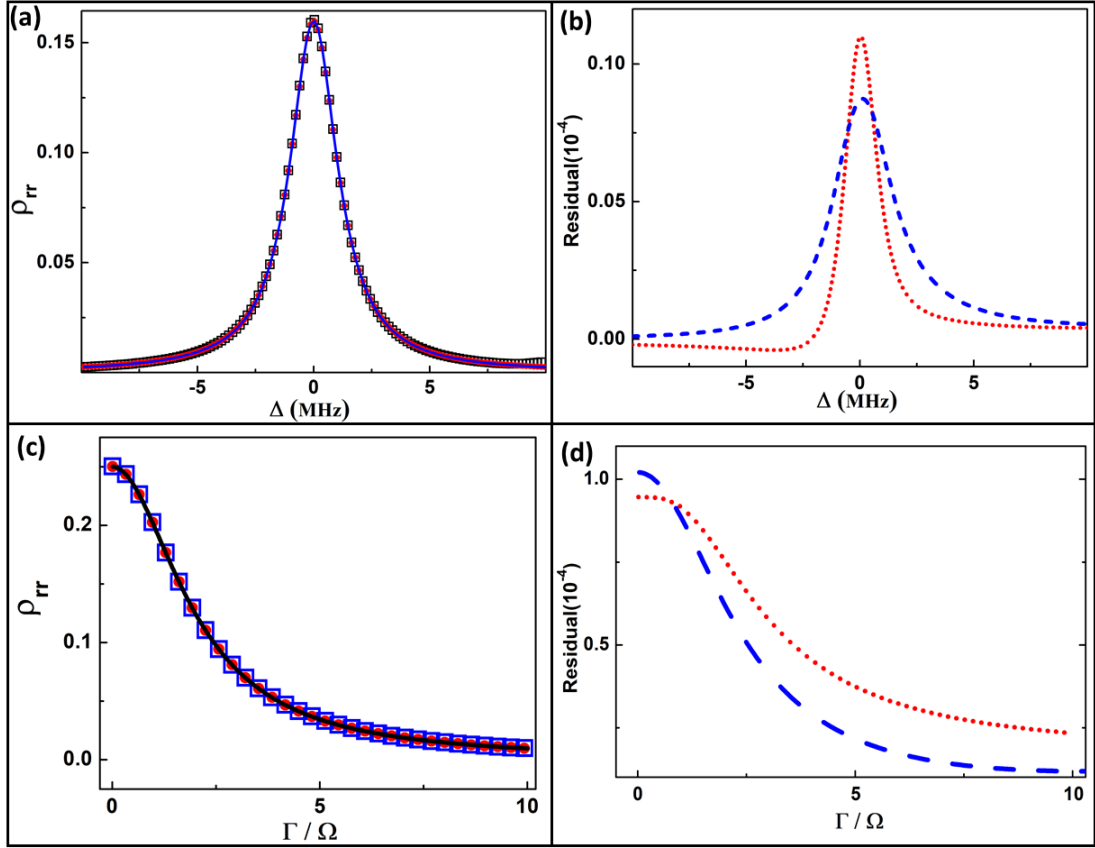


Figure 5.7: (a) Rydberg population with the variation of Δ using $\Gamma = 1.5$ MHz for exact numerical calculation (\square), approximate two-atom model (\bullet) and the empirical formula (---). (b) The residual plot of the empirical formula (red dotted line) and approximate model (blue dashed line) with the exact calculation with the variation of Δ . (c) ρ_{rr} as a function of Γ at $\Delta = 0$ for exact numerical calculation (\square), approximate two-atom model (\bullet) and the empirical formula (---). (d) The residual plot of the empirical formula (red dotted line) and approximate model (blue dashed line) with the exact calculation by varying Γ . In both the plots $\Omega = 1$ MHz, $\gamma_{rel} = 0$ and $\Gamma_S = 0$.

vapor. For cold atomic ensemble, this decay rate is ~ 100 KHz. As shown in figure 5.7 (a), Rydberg population calculated using the exact numerical calculation, the approximate model and the empirical formula match to each other for $\Gamma = 1.5$ MHz with $\gamma_{rel} = 0$ and $\Gamma_S = 0$. The residuals of the approximate model (blue dashed line) and the empirical formula (red dotted line) with the exact numerical calculation are depicted in figure 5.7 (b). The residuals are found to be four order of magnitude smaller than the maximum peak value. Similarly the population of the Rydberg state at $\Delta = 0$ with the variation of Γ using $\gamma_{rel} = 0$ and $\Gamma_S = 0$ is also depicted in figure 5.7 (c). For any variation of Γ , a good agreement is observed between

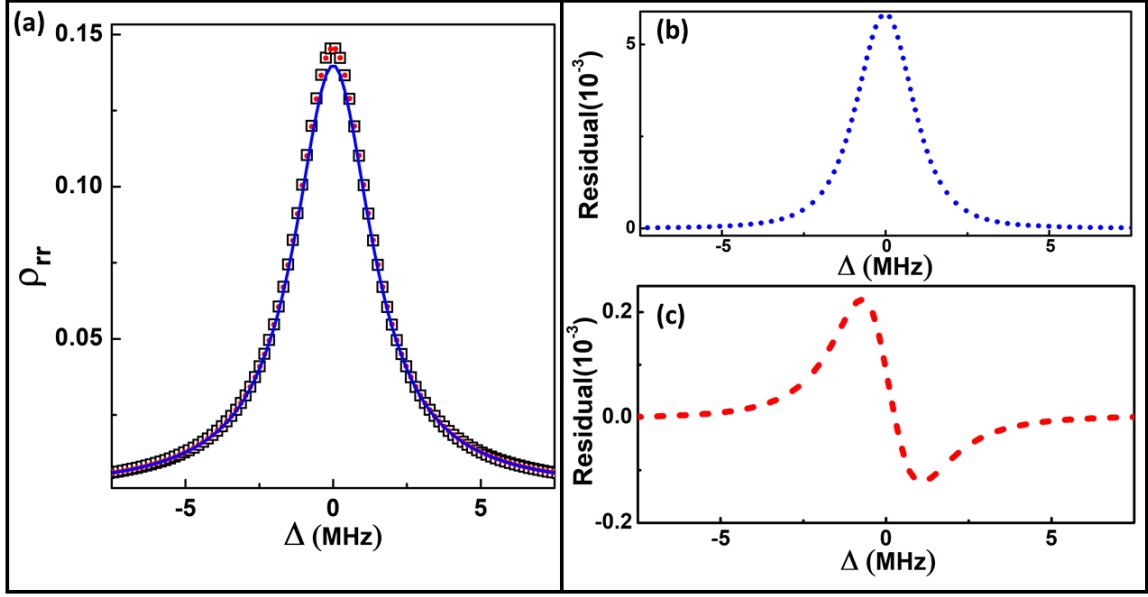


Figure 5.8: (a) Rydberg population as a function of Δ with $\Gamma = 1.5$ MHz, $\gamma_{rel} = 0.3$ MHz and $\Gamma_S = 0$ for exact numerical calculation (\square), approximate model (\bullet) and the empirical formula (—). The residual plot of exact numerical calculation with the (b) empirical formula (blue dotted line) and (c) the approximate calculation (red dashed line) with the variation of frequency.

them with residual three order of magnitude smaller than the maximum peak value as shown in figure 5.7(d).

Laser frequency noise

The typical laser frequency noise for an experiment mentioned in reference¹⁵⁸ is around 300 KHz which can't be neglected while compared to the population decay rate of the Rydberg state which is around 1.5 MHz. For a two-atom system, as shown in figure 5.8 (a), the Rydberg population calculated using the exact numerical calculation and the empirical formula does not match to each other with $\gamma_{rel} = 300$ KHz. The residuals are depicted in figure 5.8(b) which is only a order of magnitude smaller than the maximum peak value. For a cold atomic ensemble, the population decay rate is $\simeq 100$ KHz. Thus, γ_{rel} is significant compared to Γ in this case. Therefore, the disagreement observed between the exact numerical calculation and the empirical formula would be larger. However, the approximate model is found to have a good agreement with the exact numerical calculation as presented in figure 5.8 (a). The

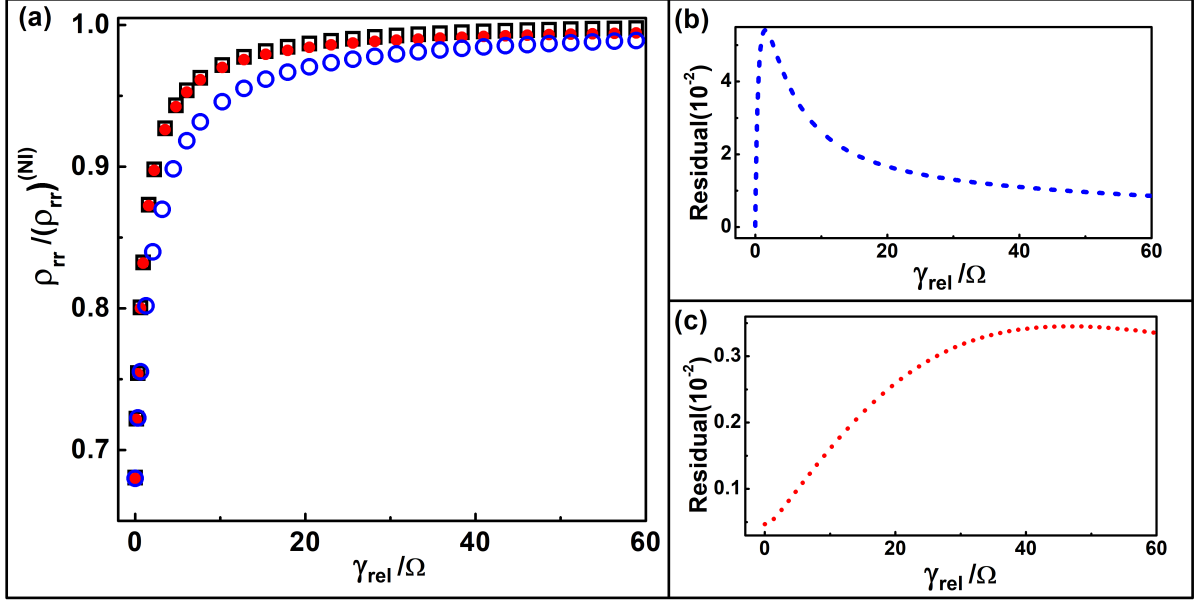


Figure 5.9: (a) $\rho_{rr}^{(b)}$ as a function of γ_{rel}/Ω at $\Delta = 0$ with $\Gamma = 1.5$ MHz for exact numerical calculation (\square), approximate model (\bullet) and the empirical formula (\circ). The residual plot of the exact numerical calculation with (b) the empirical formula (blue dashed line) and (c) the approximate calculation (red dotted line) with the variation of γ_{rel} .

residual plot is depicted in figure 5.8 (c), which is nearly three orders of magnitude smaller than the maximum peak value.

To analyze it further, let us define a quantity $\rho_{rr}^{(b)} = \frac{\rho_{rr}}{\rho_{rr}^{(NI)}}$ called as the normalized Rydberg blockaded population, where ρ_{rr} and $\rho_{rr}^{(NI)}$ are the Rydberg population for an interacting and non-interacting system respectively. For $\rho_{rr}^{(b)} = 1$, the system behaves as non-interacting and for interacting system $\rho_{rr}^{(b)} < 1$. The variation of $\rho_{rr}^{(b)}$ as a function of γ_{rel} is shown in figure. 5.9 (a). The blockade effect is found to be reducing with increase in γ_{rel} as expected and then the system becomes non-interacting at very high γ_{rel} . A clear deviation is observed between the empirical formula and the exact numerical calculation as presented in 5.9 (b) with residuals only an order of magnitude smaller than the maximum peak value. However, the approximate model is found to be in good agreement with the exact numerical calculation. For any variation of γ_{rel} , the residuals as depicted in figure 5.9(c) are found to be nearly three orders of magnitude smaller than the maximum peak value.

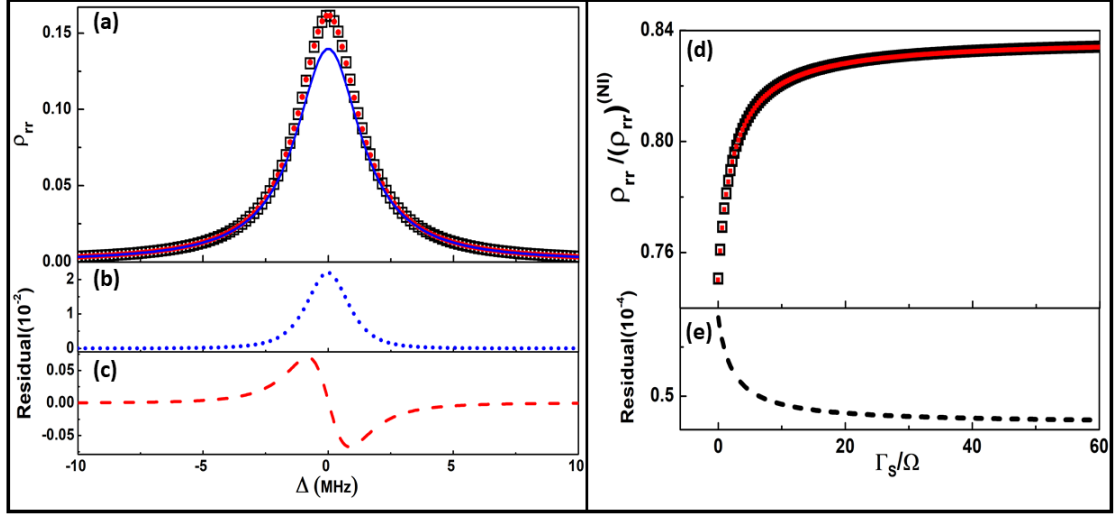


Figure 5.10: (a) ρ_{rr} as a function of Δ with $\Gamma_S = 50$ MHz for exact numerical calculation (\square), approximate model (\bullet) and the empirical formula (---). The residual plot of the exact calculation with (b) the empirical formula (blue dotted line) and (c) the approximate calculation (red dashed line) with the variation of frequency. (d) ρ_{rr}^b at $\Delta = 0$ with Γ_S / Ω using $\gamma_{rel} = 0.3$ MHz for exact numerical calculation (\square) and for the approximate model (---). $\Gamma = 1.5$ MHz and $\gamma_{rel} = 0.3$ MHz are used for both the plots. (e) Residual plot of the approximate model and the empirical formula with the variation of Γ_S .

Super-atom dephasing

As mentioned in the section 5.1.1, the transverse velocity of the atoms participating in the blockade process introduce a significant dephasing in the system called as the super-atom dephasing. For a Rydberg state with $n=50$, the blockade radius $r_b \simeq 5\mu m$. Atoms in thermal vapor at temperature 400 K, have an average velocity of $v \simeq 400$ m/s. Therefore, $\Gamma_S = \frac{v}{2r_b} \simeq 50$ MHz will be the super-atom dephasing rate in the system. For a two-atom system, the Rydberg population as a function of Δ is shown in figure 5.10 (a) with $\Gamma_S = 50$ MHz, $\Gamma = 1.5$ MHz and $\gamma_{rel} = 300$ KHz. The figure also represents the variation of ρ_{rr} using the empirical formula. Since the super-atom dephasing cannot be included in the empirical formula, it is found to be deviating from both the exact calculation. The residual plot is depicted in figure 5.10 (b) which is an order of magnitude smaller than the maximum peak value of ρ_{rr} . However, the approximate model and exact calculation are found to be in good agreement with each other. Their residual plot is depicted in figure 5.10(c). The residual is found to be 3 orders of mag-

nitude smaller than the maximum peak value. The variation of normalized Rydberg blocked population $\rho_{rr}^{(b)}$ at $\Delta = 0$ with Γ_S is depicted in figure 5.10 (d). With increase in Γ_S , $\rho_{rr}^{(b)}$ is observed to be increasing and then saturates after certain value of Γ_S . This explains that the blockade effect reduces due to the increase in Γ_S . However, for any variation of Γ_S , as depicted in figure 5.10 (d), $\rho_{rr}^{(b)} < 1$. This explains that the system does not reach to a non-interacting regime. The approximate model and the exact calculation are found to be in good agreement with each other with residuals as depicted in figure 5.10 (e), which is 3 orders of magnitude smaller than the maximum peak value. Thus, Γ_S has a significant contribution in the Rydberg blockade phenomenon in thermal vapor and its effect has to be included during the calculation. This observation also signifies that Rydberg blockade can still be observed in thermal vapor ensemble where Γ_S is significantly large.

5.2 Three-atom model

Now consider a system with three interacting identical atoms, each having two energy levels, a ground state $|g\rangle$ and an excited state $|r\rangle$ coupled by an applied laser with Rabi frequency Ω . The energy level diagram of the composite system is depicted in figure 5.11 (a). $|1\rangle$ corresponds to the level where all the atoms are in the ground state. $|2\rangle$, $|3\rangle$ and $|5\rangle$ represent levels with any one atom in Rydberg state and the other two in the ground state. $|4\rangle$, $|6\rangle$ and $|7\rangle$ represent the levels with two-atoms in the Rydberg state and one atom in the ground state and $|8\rangle$ represents the level with all the atoms in the Rydberg state. The time independent Hamiltonian for the three-atom system is given by

$$H = H^{(1)} \otimes \mathbf{I} \otimes \mathbf{I} + \mathbf{I} \otimes H^{(2)} \otimes \mathbf{I} + \mathbf{I} \otimes \mathbf{I} \otimes H^{(3)} \quad (5.32)$$

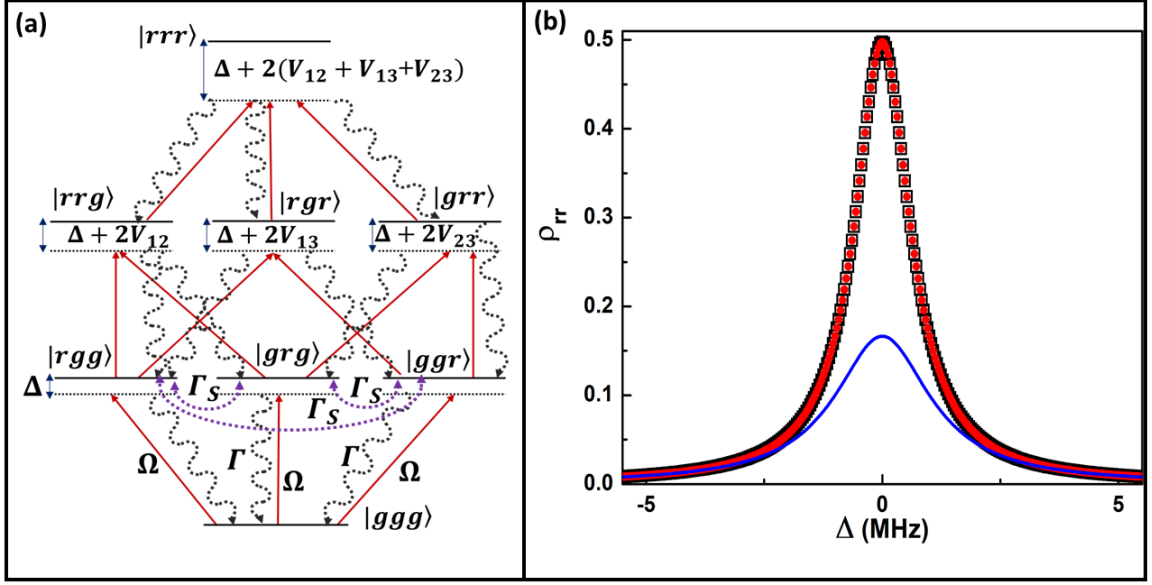


Figure 5.11: (a) The energy level diagram for three interacting atoms. The applied laser is detuned by Δ from the atomic resonance and Rabi frequency of the transition is Ω . $|ggg\rangle \equiv |1\rangle$, $|rgg\rangle \equiv |2\rangle$, $|rgr\rangle \equiv |3\rangle$, $|grr\rangle \equiv |5\rangle$, $|rrg\rangle \equiv |4\rangle$, $|rgr\rangle \equiv |6\rangle$, $|grr\rangle \equiv |7\rangle$ and $|rrr\rangle \equiv |8\rangle$. (b) ρ_{rr} as a function of Δ for non-interacting three-atom calculation (\square), two-level system (\bullet) and interacting three-atom model (—).

$$\Rightarrow H = -\frac{\hbar}{2} \begin{pmatrix} 0 & \Omega_1 & \Omega_2 & 0 & \Omega_3 & 0 & 0 & 0 \\ \Omega_1 & 2\Delta_1 & 0 & \Omega_2 & 0 & \Omega_3 & 0 & 0 \\ \Omega_2 & 0 & 2\Delta_2 & \Omega_1 & 0 & 0 & \Omega_3 & 0 \\ 0 & \Omega_2 & \Omega_1 & 2(\delta_{12} + V) & 0 & 0 & 0 & \Omega_3 \\ \Omega_3 & 0 & 0 & 0 & 2\Delta_3 & \Omega_1 & \Omega_2 & 0 \\ 0 & \Omega_3 & 0 & 0 & \Omega_1 & 2(\delta_{13} + V) & 0 & \Omega_2 \\ 0 & 0 & \Omega_3 & 0 & \Omega_2 & 0 & 2(\delta_{23} + V) & \Omega_1 \\ 0 & 0 & 0 & \Omega_3 & 0 & \Omega_2 & \Omega_1 & 2(\delta + 3V) \end{pmatrix}. \quad (5.33)$$

Here, $\delta_{12} = \Delta_1 + \Delta_2$, $\delta_{13} = \Delta_1 + \Delta_3$, $\delta_{23} = \Delta_2 + \Delta_3$ and $\delta = \Delta_1 + \Delta_2 + \Delta_3$. Similarly, the Lindblad matrix for the system is calculated to be

$$L_D = L_D^{(1)} \otimes \rho^{(2)} \otimes \rho^{(3)} + \rho^{(1)} \otimes L_D^{(2)} \otimes \rho^{(3)} + \rho^{(1)} \otimes \rho^{(2)} \otimes L_D^{(3)} \quad (5.34)$$

The Lindblad matrix and the density matrix for i^{th} atom is given by

$$L_D^{(i)} = \begin{bmatrix} \Gamma \rho_{22}^{(i)} & -\gamma \rho_{12}^{(i)} \\ -\gamma \rho_{21}^{(i)} & -\Gamma \rho_{22}^{(i)} \end{bmatrix}, \rho^{(i)} = \begin{bmatrix} \rho_{11}^{(i)} & \rho_{12}^{(i)} \\ \rho_{21}^{(i)} & \rho_{22}^{(i)} \end{bmatrix}. \quad (5.35)$$

Density matrix of the individual atoms are mapped to the three-atom model using $\rho = \rho^{(1)} \otimes \rho^{(2)} \otimes \rho^{(3)}$. Γ_S is included in the composite Lindblad matrix of the three-atom system between the states $|2\rangle$, $|3\rangle$ and $|5\rangle$. The OBEs of the system are solved numerically in steady state to calculate the Rydberg population which is given by

$$\rho_{rr} = \frac{1}{3}(\rho_{22} + \rho_{33} + \rho_{55}) + \frac{2}{3}(\rho_{44} + \rho_{66} + \rho_{77}) + \rho_{88}.$$

The population of the Rydberg state as a function of laser detuning for the exact numerical calculation is depicted in figure 5.11 (b). When the atoms are considered non-interacting, it is found to be matching with a single atom two-level system as presented in the same figure. A significant suppression in the Rydberg population is observed when the system is strongly interacting satisfying the blockade condition compare to a non-interacting system as depicted in figure 5.11 (b).

Using the similar approach as the two-atom model, the OBEs of this system is also simplified further using the available symmetry and suitable approximations due to strong Rydberg-Rydberg interaction. We ignore the inhomogeneous light shift of the single Rydberg excited states which introduces the dephasing in many-body Rabi oscillation.⁵⁶ Since, the atoms are identical and indistinguishable, coupling of the states $|1\rangle$, $|4\rangle$, $|6\rangle$, $|7\rangle$ and $|8\rangle$ to the states $|2\rangle$, $|3\rangle$ and $|5\rangle$ are considered to be the same. Hence, the population of these states and the corresponding coherence terms are also the same, i.e. $\rho_{12} = \rho_{13} = \rho_{15}$, $\rho_{22} = \rho_{33} = \rho_{55}$, $\rho_{24} = \rho_{26} = \rho_{34} = \rho_{37} = \rho_{56} = \rho_{57}$, $\rho_{28} = \rho_{38} = \rho_{58}$ and $\rho_{27} = \rho_{36} = \rho_{54}$ and $\rho_{16} = \rho_{14} = \rho_{17}$. The states $|4\rangle$, $|6\rangle$, $|7\rangle$ and $|8\rangle$ contains two or more atoms in the Rydberg state. Thus, the energy level shift of these states are large due to strong interaction between the atoms. Therefore, the applied laser becomes out of resonance to these states and hence the

populations $\rho_{44} = \rho_{66} = \rho_{77} = \rho_{88} = 0$. Thus, there won't be any coherence between these states i.e. $\rho_{48} = \rho_{68} = \rho_{78} = \rho_{46} = \rho_{47} = \rho_{67} = 0$. Using all these approximations, we get $\rho_{23} = \frac{\Gamma}{2\gamma + \Gamma_S} \rho_{22}$ and $\rho_{24} = \frac{3\gamma}{\Gamma + \gamma} \rho_{27}$. Further simplifications of the exact numerical OBEs in steady state reduced to a set of four independent equation which are given by

$$\begin{aligned}
\Omega(1 - (4 + 2(\frac{\Gamma}{2\gamma + \Gamma_S}))\rho_{22} + 2\rho_{14}) + 2\Delta\rho_{12} + 4i\Gamma\rho_{24} - 2i\gamma\rho_{12} &= 0 \\
2\Omega(\rho_{12}) + 2(2\Delta + 2V)\rho_{14} - 4i\gamma\rho_{14} &= 0 \\
\Omega Im(\rho_{12}) + \Gamma\rho_{22} &= 0 \\
\Omega((1 + \frac{\Gamma}{2\gamma + \Gamma_S})\rho_{22} - \rho_{14}) + 2(\Delta + 2V)(\rho_{24}) - 2i(\Gamma + \gamma)\rho_{24} &= 0
\end{aligned} \tag{5.36}$$

These equations are solved to calculate the matrix element ρ_{22} which is the Rydberg population for the approximate three-atom model. This is compared to the Rydberg population calculated from the exact numerical calculations and is depicted in figure. 5.12 (a). A good agreement is observed between them for strongly interacting regime for $V_{rr} > \sqrt{3}\Omega$ with residual less than 10^{-5} as presented in figure 5.12(b). The residuals are four orders of magnitude smaller than the maximum peak value. However, with an interaction strength $V_{rr} \leq \sqrt{3}\Omega$ the approximate model significantly deviates from the exact calculation.

To derive the empirical formula we can choose the basis states for the composite three-atom system. The states with two or more atoms excited to the Rydberg state are shifted out of resonance to the exciting laser due to strong interaction and hence are not populated during the excitation process. Neglecting these states, the basis states of the reduced Hilbert space can be chosen as $|ggg\rangle$, $|a\rangle = (|ggr\rangle + |grg\rangle + |rgg\rangle)/\sqrt{3}$, $|b\rangle = (e^{i\pi/3}|ggr\rangle + e^{-i\pi/3}|grg\rangle - |rgg\rangle)/\sqrt{3}$ and $|c\rangle = (e^{-i\pi/3}|ggr\rangle + e^{i\pi/3}|grg\rangle - |rgg\rangle)/\sqrt{3}$. The Rabi coupling of the transition $|ggg\rangle \rightarrow |a\rangle$ is $\sqrt{3}\Omega$ and for the transitions $|ggg\rangle \rightarrow |b\rangle$ and $|ggg\rangle \rightarrow |c\rangle$ are 0. Also, the effective Rydberg population of the state $|a\rangle$ is reduced by a factor of 3. The population decay rate from $|a\rangle$ to $|ggg\rangle$ is same as Γ due to the compensation between the factors enhancing the Rabi frequency and reducing the Rydberg population. Thus, the

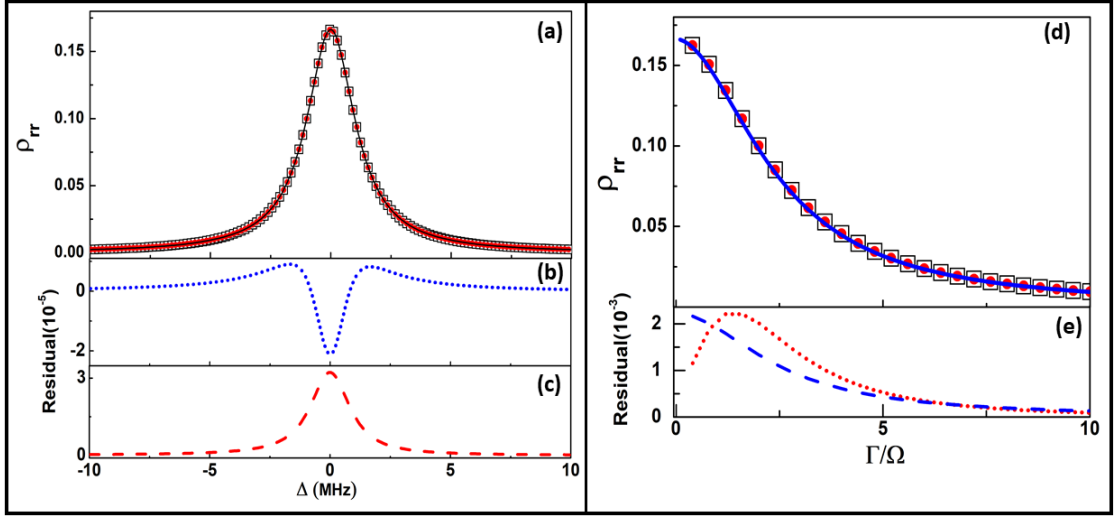


Figure 5.12: (a) The population of the Rydberg state as a function of Δ with $\Omega = 1$ MHz, $\Gamma = 0.1$ MHz and $V_{rr} = 50$ MHz for exact three-atom calculation (\square), approximate model (\bullet) and for empirical formula (—). The residual plot of (b) approximate model (blue dotted line) and (c) empirical formula (red dashed line) with exact calculation. (d) ρ_{rr} at $\Delta = 0$ is plotted as a function of Γ for exact calculation (\square), empirical formula (—) and approximate model (\bullet). (e) The residual plot of empirical formula (red dotted line) and approximate model (blue dashed line) with exact calculation by varying Γ .

composite three-atom system can be reduced to an effective two-level system with levels $|ggg\rangle$ and $|a\rangle$ with coupling Rabi frequency $\sqrt{3}\Omega$. The empirical formula for the Rydberg population of the three-atom system is given by

$$\rho_{rr} = \frac{\Omega^2}{6\Omega^2 + 4\Delta^2(\Gamma/2\gamma) + 2\Gamma\gamma}. \quad (5.37)$$

Rydberg population calculated using the empirical formula is also depicted in figure 5.12 (a). The residual plot with the exact calculation is depicted in figure 5.12 (c). The empirical formula is found to be in good agreement with the exact numerical calculation having residuals 3 orders of magnitude smaller than the maximum peak value. In all these plots $\gamma_{rel} = 0$, $\Gamma_S = 0$ and the interaction strength $V_{rr} > \sqrt{3}\Omega$. Similar to the two-atom model, ρ_{rr} at $\Delta = 0$ with the variation of Γ is depicted in the figure 5.12 (d). For any variation of Γ , the residuals of the approximate model and the empirical formula with the exact numerical calculation are found to be 2 orders of magnitude smaller than the maximum peak value as depicted in the inset of

figure 5.12 (e). This indicates they are in good agreement with each other for any variation of Γ .

5.2.1 Effect of dephasing mechanisms in three-atom model

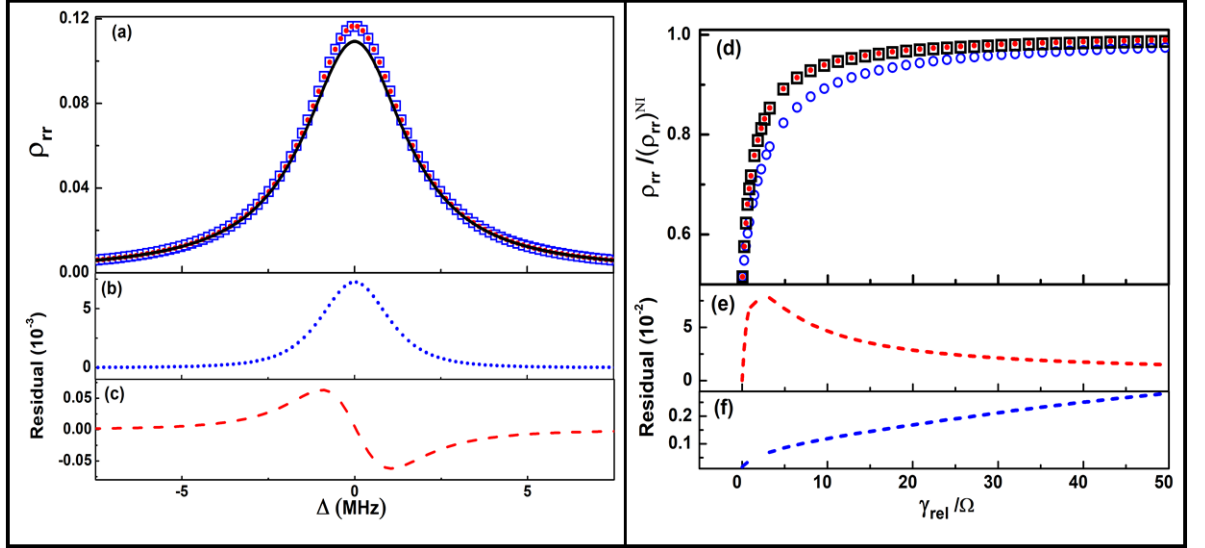


Figure 5.13: (a) Rydberg population as a function of Δ with $\Gamma = 1.5$ MHz, $\gamma_{rel} = 0.3$ MHz and $\Gamma_S = 0$ for exact numerical calculation (\square), approximate model (\bullet) and the empirical formula (---). The residual plot of (b) the empirical formula (blue dotted line) and (c) approximate model (red dashed line) with the exact calculation by varying Δ . (d) ρ_{rr}^b as a function of γ_{rel}/Ω at $\Delta = 0$ with $\Gamma = 1.5$ MHz for approximate model (\square), the exact numerical calculation (\bullet) and empirical formula (\circ). The residual plot of (e) the empirical formula (red dashed line) and (f) approximate model (blue dotted line) with the exact calculation by varying γ_{rel} .

Just like the two-atom model, the effect of γ_{rel} and Γ_S on the blockade processes has also been studied here. As shown in figure 5.13 (a), when $\gamma_{rel} = 0.3$ MHz, a clear deviation is observed between the exact calculation and the empirical formula as depicted in figure 5.13 (b). The residual is only an order of magnitude smaller than the maximum peak value. Also, the variation of the normalized Rydberg blocked population with γ_{rel} is depicted in figure 5.13 (d). With increase in γ_{rel} the empirical formula is found to be deviating from the exact calculation. This is due to the fact that, during the consideration of the empirical formula, the system is considered to be coherent. Thus, the dephasing introduced in the system due to γ_{rel} is not being taken care in the formula. The residual plot of the empirical formula with the exact nu-

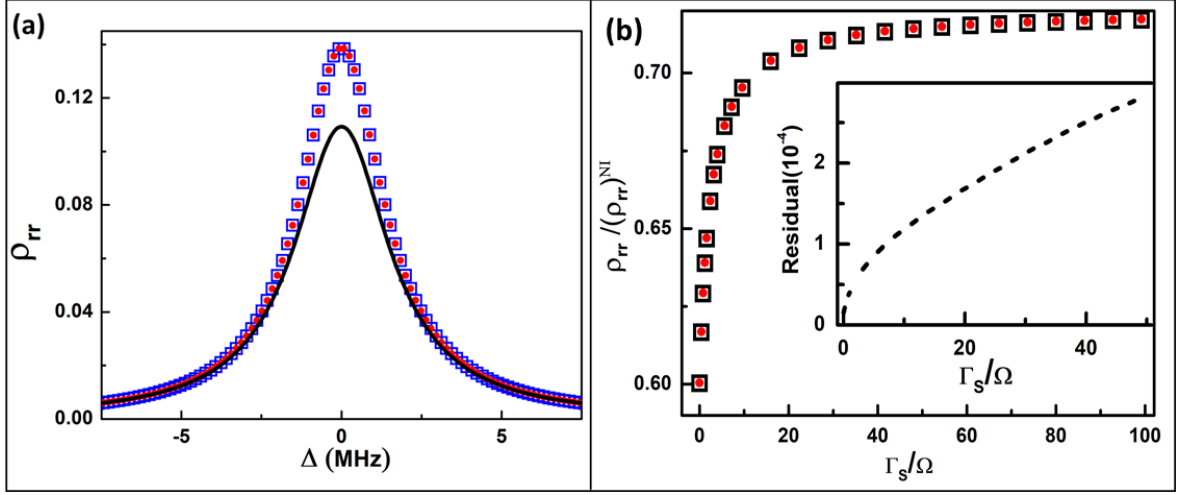


Figure 5.14: (a) ρ_{rr} as a function of Δ with $\Gamma_S = 50$ MHz, $\gamma_{rel} = 0.3$ MHz and $\Gamma_S = 1.5$ MHz for exact three-atom calculation (\square), approximate model (\bullet) and the empirical formula (—). (b) ρ_{rr}^b at $\Delta = 0$ with Γ_S / Ω for approximate model (\bullet) and the exact calculation (\square). The inset shows the residual plot of the graph.

merical calculation is depicted in figure 5.13(e). The residuals are found to be only an order of magnitude smaller than the maximum peak value. Thus, a significant deviation is observed between them. However, the approximate model is found to be in good agreement with the exact calculation as depicted in figure 5.13(c) with residual 3 orders of magnitude smaller compared to the maximum peak value. Also with the variation of γ_{rel} , residuals of the empirical formula with the exact calculation is depicted in figure 5.13(d). The residuals are found to be 2 orders of magnitude smaller than the maximum peak value with the variation of γ_{rel} indicating a good agreement between them.

Similarly the effect of Γ_S on the Rydberg population is also studied for the three-atom system. Rydberg population with the variation of Δ for $\Gamma_S = 50$ MHz is depicted in figure 5.14(a). The approximate model and the exact calculation are found to be producing similar result with the variation of Δ . However, the super-atom dephasing cannot be introduced in the empirical formula and hence it deviates from the exact calculations as well as the approximate model. $\rho_{rr}^{(b)}$ at $\Delta = 0$ with the variation of Γ_S is depicted in figure 5.14 (b). The approximate model and the exact calculation are found to be in good agreement with each other with residual less than 3×10^{-4} as shown in the inset of figure 5.14 (b), which is 3 orders of magnitude smaller

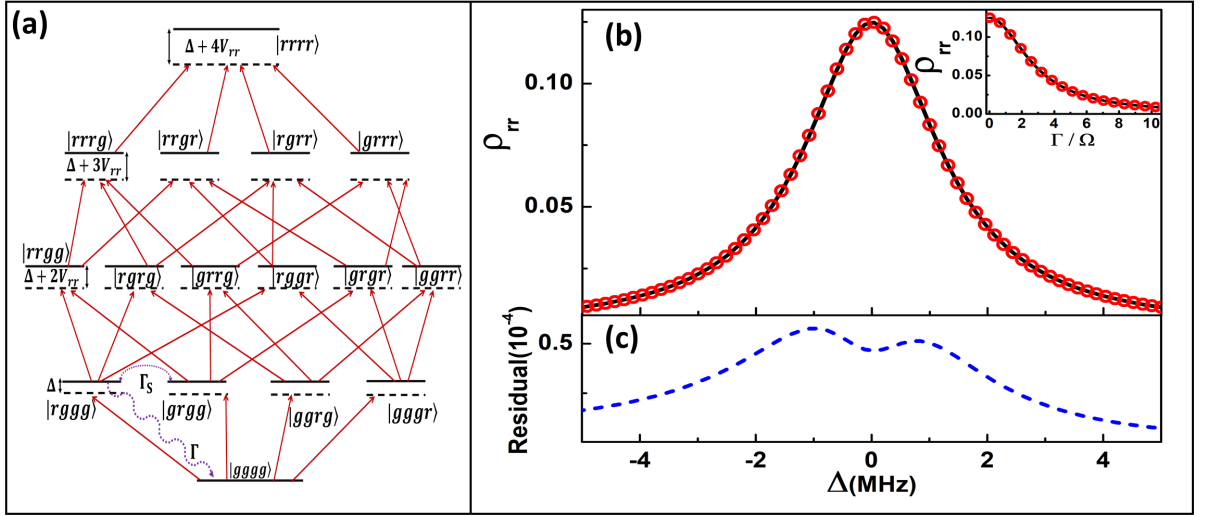


Figure 5.15: (a) The energy level diagram for 4 interacting atoms with states $|1\rangle = |gggg\rangle$, $|2\rangle = |rggg\rangle$ and $|4\rangle = |rrgg\rangle$. (b) The population of the Rydberg state as a function of laser detuning Δ with $\Omega = 1$ MHz, $\Gamma = 0.1$ MHz and $V_{rr} = 200$ MHz for the empirical formula (\circ) and the approximate model (—). The inset shows the variation of ρ_{rr} as a function of Γ/Ω . (c) The residual plot of the approximate model and the empirical formula with the variation of frequency.

than the maximum peak value. It can also be observed that the blockade effect reduces with increase in Γ_S . However, after a certain value of Γ_S , a saturation in $\rho_{rr}^{(b)}$ is observed. $\rho_{rr}^{(b)} < 1$ explains that the system does not reach a non-interacting regime even for larger value of Γ_S . Therefore, this signifies that the blockade phenomenon can be observed for a thermal ensemble of atoms where Γ_S is large.

5.3 Four-atom model

To extend the study further, let us consider a system of four identical atoms each with two energy levels $|g\rangle$ and $|r\rangle$. The energy level diagram for the system is depicted in figure 5.15(a). The energy level $|1\rangle \equiv |gggg\rangle$ represents all the atoms in the ground state. $|2\rangle \equiv |rggg\rangle$ and $|4\rangle \equiv |rrgg\rangle$ represent levels with one and two atoms in the Rydberg state respectively with rest of the atoms in the ground state. Using the similar approach as the two and three-atom model, the Hamiltonian and Lindblad operator for the system is written as

$$H = \sum_{i=1}^4 \mathbf{I}^{i-1} \otimes H^{(i)} \otimes \mathbf{I}^{4-i} + \sum_{i<j}^4 V_{ij} |r\rangle_i \langle r|_j \langle r|_i \langle r|_j. \quad (5.38)$$

$$L_D = \sum_i^4 \prod_{\substack{k=1 \\ i>1}}^{i-1} \rho^{(k)} \otimes L_D^{(i)} \otimes \prod_{\substack{j=i+1 \\ j\leq 4}}^4 \rho^{(j)}. \quad (5.39)$$

Γ_S is included in the composite L_D matrix between the states having one Rydberg excited atom. The OBEs in a steady state are calculated using 5.6. Using the available symmetry in the system, the four-atom model is simplified just like the two and three-atom model. The atoms are considered to be strongly interacting such that states having two or more Rydberg excited atoms will not be populated due to the blockade phenomenon. Using all these approximations the OBEs of the system are simplified to a set of four independent equations which are given by

$$\begin{aligned} \Omega(1 - (5 + 3(\frac{\Gamma}{2\gamma + \Gamma_S}))\rho_{22} + 3\rho_{14}) + 2\Delta\rho_{12} + 6i\Gamma\rho_{24} - 2i\gamma\rho_{12} &= 0. \\ 2\Omega(\rho_{12} + \rho_{24}) + 2(2\Delta + 2V)\rho_{14} - 4i\gamma\rho_{14} &= 0. \\ \Omega(Im\rho_{12}) + \Gamma\rho_{22} &= 0. \\ \Omega((1 + \frac{\Gamma}{2\gamma + \Gamma_S})\rho_{22} - \rho_{14}) + 2(\Delta + 2V)(\rho_{24}) - 2i(\Gamma + \gamma)\rho_{24} &= 0. \end{aligned} \quad (5.40)$$

These equations are solved to calculate the population of the Rydberg state ρ_{22} for the approximate four-atom model. The plot for the population of the Rydberg state with Δ is presented in figure 5.15 (b) where, $\gamma_{rel} = \Gamma_S = 0$. An empirical formula for the Rydberg population is also formulated for the four-atom model using using similar approach as the two and three-atom system which is given by

$$\rho_{rr} = \frac{\Omega^2}{8\Omega^2 + 4\Delta^2(\Gamma/2\gamma) + 2\Gamma\gamma}. \quad (5.41)$$

ρ_{rr} calculated using the empirical formula is also depicted in figure 5.15 (b). The residuals

of the plot are presented in figure 5.15 (c). A good agreement is observed between the approximate model and the empirical formula with residual 3 orders of magnitude smaller than the maximum peak value. The Rydberg state population with the variation of Γ is depicted in the inset of the figure 5.15 (b). For any variation of Γ the approximate model and the empirical formula are found to be in good agreement with each other for $\gamma_{rel} = \Gamma_S = 0$.

Similar studies as the two and three-atom system have been performed for the four-atom system in order to observe the effect of γ_{rel} and Γ_S on the blockade phenomenon. Similar to the previous cases, a clear deviation is observed between the empirical formula and the approximate model for $\gamma_{rel} = 0.3$ MHz and $\Gamma_S = 50$ MHz. However, a good agreement is always observed between the exact calculation and the approximate model in the regime $V_{rr} > \Omega$ as explained in the two and three-atom model. Therefore, from the above observations it can be anticipated that a system having finite Γ_S and γ_{rel} , the empirical formula is not sufficient to explain the blockade phenomena. However, the approximate model is useful for these cases.

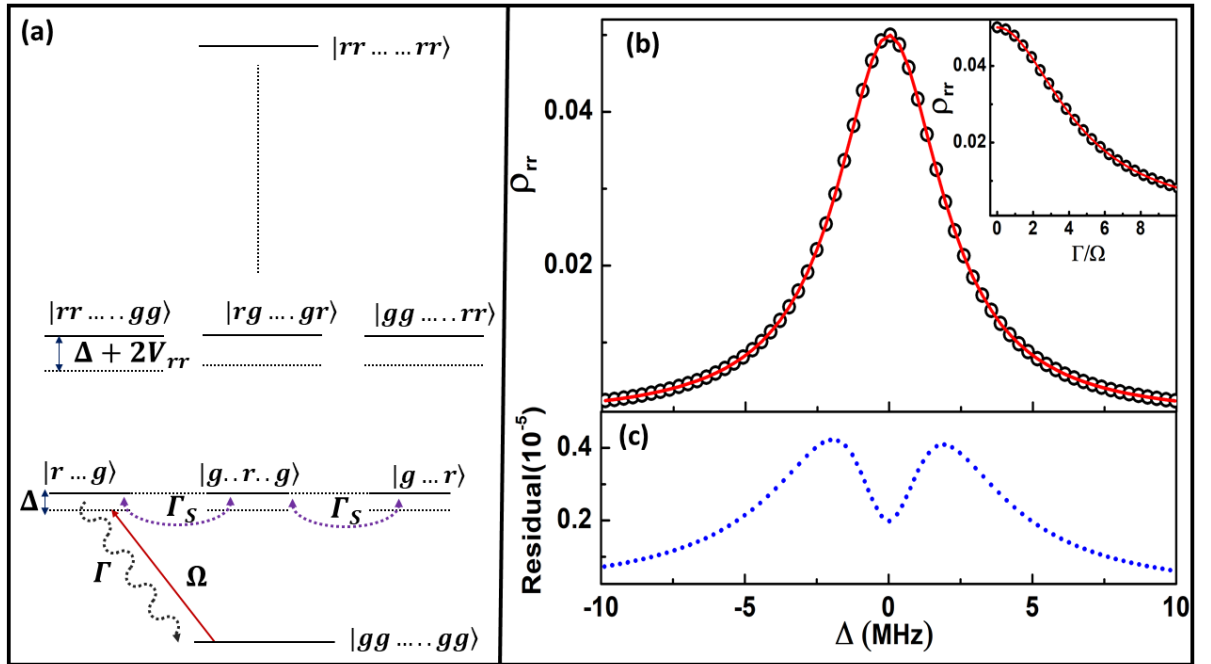


Figure 5.16: (a) The energy level diagram for N interacting atoms with states $|1\rangle \equiv |ggg \dots g\rangle$, $|2\rangle \equiv |rgg \dots g\rangle$ and $|3\rangle \equiv |rrg \dots g\rangle$. (b) The population of the Rydberg state as a function of laser detuning Δ with $\Omega = 1$ MHz, $\Gamma = 0.1$ MHz and $V_{rr} = 200$ MHz for approximate model (\circ) and for the empirical formula (—). The inset shows the variation of Rydberg population as a function of Γ/Ω .

5.4 N-atom model

Consider a system of N interacting identical atoms each having two energy levels, a ground state $|g\rangle$ and an excited state $|r\rangle$, coupled by an applied laser with Rabi frequency Ω and laser detuning Δ . The energy level diagram of the system is depicted in figure. 5.16(a). The Hamiltonian for the system is represented by,

$$H = \sum_{i=1}^N \mathbf{I}^{i-1} \otimes H^{(i)} \otimes \mathbf{I}^{N-i} + \sum_{i<j}^N V_{ij} |r\rangle_i |r\rangle_j \langle r|_i \langle r|_j \quad (5.42)$$

Where, V_{ij} represents the strength of the Van der Waal's interaction between atom i and atom j . Similarly, the Lindblad matrix for N -interacting atoms is given by,

$$L_D = \sum_i^N \prod_{\substack{k=1 \\ i>1}}^{i-1} \rho^{(k)} \otimes L_D^{(i)} \otimes \prod_{\substack{j=i+1 \\ j\leq N}}^N \rho^{(j)} \quad (5.43)$$

where $\rho^{(i)}$ and $L_D^{(i)}$ represents the density matrix and the lindblad matrix for the i th atom respectively. Γ_S is introduced between the Rydberg states in the composite Lindblad operator of the multi-atom system. However, solving the OBEs for a system with large number of atoms is a difficult task. But as observed from the approximate model of two, three and four-atom systems presented above, the OBEs is reduced to a set of four independent equations, which gives similar observations to that of the exact numerical calculations. These three sets of OBEs are extrapolated for N interacting atoms inside the blockade sphere using the method of induction which is given in equation 5.44.

$$\begin{aligned}
\Omega(1 - ((N + 1) + (N - 1)\frac{\Gamma}{2\gamma + \Gamma_S})\rho_{22} + (N - 1)\rho_{13}) + 2\Delta\rho_{12} + 2(N - 1)i\Gamma\rho_{23} - 2i\gamma\rho_{12} &= 0. \\
2\Omega(\rho_{12}) + 2\Omega(N - 3)\rho_{23} + 2((2\Delta + 2V)\rho_{13} - 4i\gamma\rho_{13}) &= 0. \\
\Omega(\text{Im}(\rho_{12})) + \Gamma\rho_{22} &= 0. \\
\Omega((1 + \frac{\Gamma}{2\gamma + \Gamma_S})\rho_{22} - \rho_{13}) + 2(\Delta + 2V)\rho_{23} - 2i(\Gamma + \gamma)\rho_{23} &= 0.
\end{aligned} \tag{5.44}$$

The population of the Rydberg state from equation 5.44 is given by ρ_{22} . The population as a function of laser detuning is depicted in figure 5.16 (b) for 10 atoms inside the blockade sphere. Using the similar approach as the two and three-atom model, the N-atom system can be reduced to an effective two-level system with levels $|gg \cdots g \cdots g\rangle$ and $|+\rangle = 1/\sqrt{N}(|rg \cdots g \cdots g\rangle + \cdots + |gg \cdots r \cdots g\rangle + \cdots + |gg \cdots g \cdots r\rangle)$. The coupling Rabi frequency of the transition $|gg \cdots g \cdots g\rangle \rightarrow |+\rangle$ is $\sqrt{N}\Omega$ and the total Rydberg population reduces by a factor of N. These factors compensate each other to give the population decay rate of $|+\rangle$ as Γ . Using this condition the empirical formula of Rydberg population with N atoms in the blockade sphere is given by

$$\rho_{rr} = \frac{\Omega^2}{2N\Omega^2 + 4\Delta^2(\Gamma/2\gamma) + 2\Gamma\gamma}.$$

Rydberg population calculated from the empirical formula for 10 atoms inside the blockade sphere is also depicted in figure 5.16(b). A good agreement is observed with the approximate model for $\Gamma = 0.1$ MHz, $\gamma_{rel} = 0$ and $\Gamma_S = 0$ with residuals four orders of magnitude smaller than the maximum peak value as depicted in figure 5.16 (c). Also, Rydberg state population with the variation of Γ is depicted in the inset of figure 5.16 (b). A good agreement is observed between the empirical formula and the approximate model with variation of Γ .

Similarly, the coherence between the state $|g\rangle$ and $|r\rangle$ is studied using the approximate model which is given by the quantity $Re(\rho_{12})$. An empirical formula is also derived for $Re(\rho_{gr})$

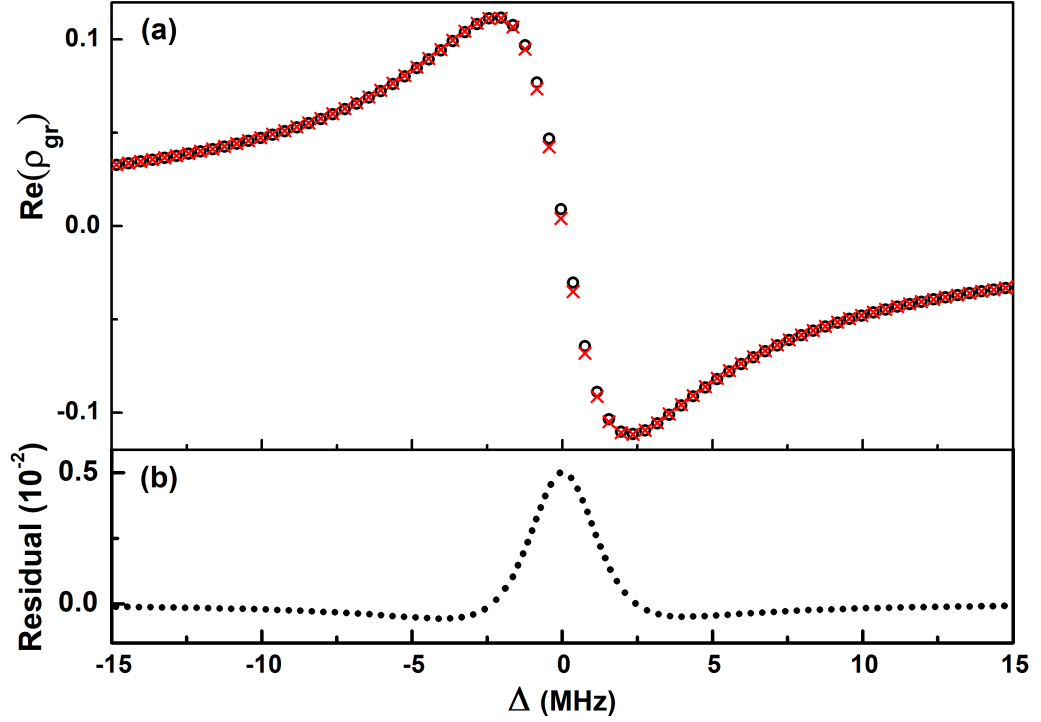


Figure 5.17: $\rho_{rg}^{(re)}$ as a function of Δ for the approximate model (\circ) and the empirical formula (\times) with $\Omega = 1$ MHz and $\Gamma = 0.1$ MHz and $\Gamma_S = \gamma_{rel} = 0$.

using the super-atom picture. for N atoms it is given by

$$Re(\rho_{gr}) = \frac{\Delta\Omega\Gamma/\gamma}{2N\Omega^2 + 4\Delta^2(\Gamma/2\gamma) + 2\Gamma\gamma} \quad (5.45)$$

$Re(\rho_{gr})$ calculated using the empirical formula is compared to $Re(\rho_{12})$ of the approximate model. As shown in figure 5.17 (a), a good agreement is observed between them for 10 atoms in the strongly interacting regime. The residuals are depicted in the figure 5.17 (b), which are an order of magnitude smaller than the maximum peak value.

5.4.1 Effect of laser frequency noise and super-atom dephasing in the model

The effect of γ_{rel} and Γ_S on the blockade phenomenon is studied. The variation of $\rho_{rr}^{(b)}$ with γ_{rel}/Ω is depicted in figure 5.18(a). Just like the two and three-atom model, as shown in

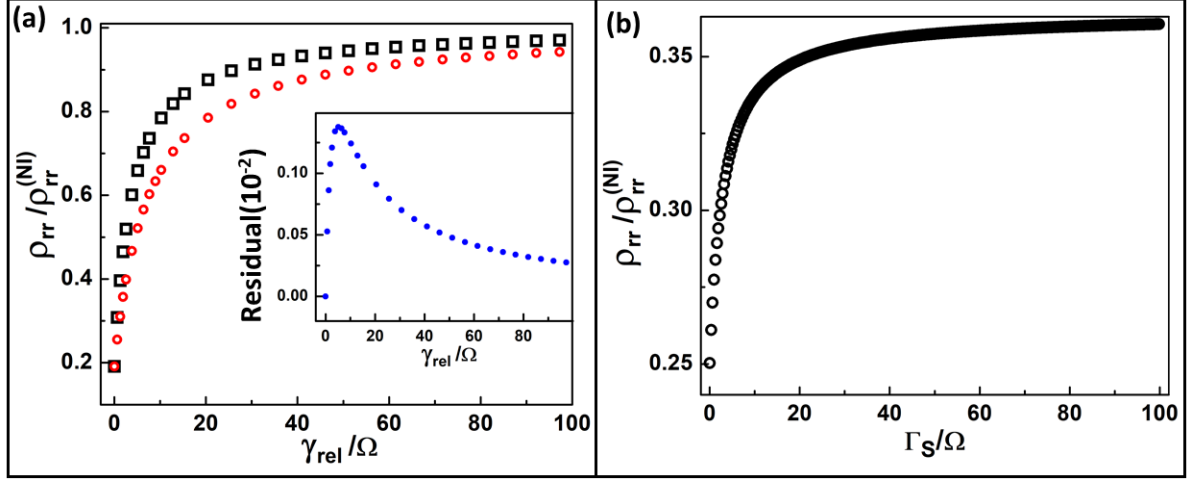


Figure 5.18: Normalized Rydberg blockaded population as a function of (a) γ_{rel}/Ω for the approximate model (\square) and the empirical formula (\circ) and (b) Γ_S/Ω for approximate model (\circ) for 10 interacting atoms with $\Delta = 0$, $\Gamma = 1.5$ MHz. The inset of (a) represents the residual plot of the empirical formula and the approximate model with the variation of γ_{rel} .

figure 5.18(a), for 10 atoms inside the blockade sphere, a deviation is observed between the approximate model and the empirical formula with increase in γ_{rel} . The normalized Rydberg blockaded population with increase in Γ_S , at $\Delta=0$ is depicted in figure 5.18(b). $\rho_{rr}^{(b)}$ is found to be increasing with increase in Γ_S indicating the blockade effect is reducing. However, the system does not reach a non-interacting regime even for higher Γ_S . This signifies the existence of blockade effect in thermal vapor ensemble. Γ_S cannot be included in the empirical formula and thus it deviates from the approximate model for finite Γ_S . Thus, for system with finite Γ_S and γ_{rel} , the empirical formula will not be sufficient to explain the blockade phenomenon. Thus, in that cases the approximate model with four OBEs presented here will be useful, where the mathematical complexity due to exact numerical calculation for higher number of atoms can be avoided.

5.5 Conclusion

The theoretical study presented here suggest that Rydberg blockade in an ensemble consisting of large number of atoms inside the blockade sphere with $\Gamma_S = \gamma_{rel} = 0$ can be modeled

using the simple empirical formula. However, the empirical formula is not sufficient to explain the blockade phenomena for significant dephasing due to laser frequency noise and relative motion of the atoms. Here, we have presented a model for Rydberg blockade with large number of atoms with suitably incorporating the super-atom dephasing and dephasing due to laser frequency noise. The exact optical Bloch equations for N -interacting atoms in the strong blockade regime are simplified using suitable approximations which gives only four independent OBEs. The approximate model is useful to explain the blockade phenomena for large number of atoms inside the blockade sphere for cold atomic ensemble where γ_{rel} is significant. This model is also useful for thermal vapor ensemble where Γ_S is large due to thermal motion of the atoms. We show that Rydberg blockade does not vanish with significant super-atom dephasing suggesting the possibility of observation of Rydberg blockade in thermal atomic vapor.

An experiment has been performed by our group in order to observe the blockade effect in thermal atomic vapor. The details regarding the experimental technique and the observations can be found in the reference.^{127,165} OHDT has been used to measure the dispersion of the probe beam due to two-photon excitation to the Rydberg state. The blockade effect has been observed on the red detuned side of the two-photon resonance peak for the transition $^{85}\text{Rb } F = 3 \rightarrow nS_{1/2}$, where the anti-blockade phenomena has negligible effect. However, the non-linearity is observed to be small as the spectrum is Doppler broadened due to significant residual wave vector mismatch. Therefore, a four-photon excitation scheme is proposed where the residual wave vector mismatch can be minimized to zero by suitable beam geometry. Thus, the thermal vapor ensemble will behave like a cold atom system leading to a strong optical non-linearity in the Rydberg blockade regime. This can lead to application of thermal vapor in quantum information processing.

Chapter 6

Theoretical study of Rydberg blockade using four-photon excitation

Rydberg blockade phenomenon that arises due to strong dipolar interactions between Rydberg atoms has a variety of applications.⁴ The blockade phenomenon has been experimentally studied by various groups in ultra-cold atomic ensemble⁴²⁻⁴⁷ as well as in thermal atomic vapor.¹²⁷ In most of the experiments, a two-photon scheme is used for Rydberg excitation. For rubidium vapor, a probe at 780 nm excite the atoms from $5S_{1/2}$ to $5P_{3/2}$ and the coupling laser at 480 nm excite the atoms from $5P_{3/2}$ to the Rydberg state. The residual wave vector between the two lasers in the counter-propagating configuration is given by $\Delta k = k_P - k_C \simeq 0.8 \times 10^6 m^{-1}$. Here, k_P and k_C are the wave vectors of the probe and the coupling laser respectively. In cold atomic ensemble as well as in thermal atomic vapor, this wave vector mismatch introduces a dephasing due to the velocity of the atom. For thermal atomic vapor at 300 K, the most probable velocity $v_p \simeq 240$ m/s. Thus, the Doppler broadening due to the residual wave vector mismatch $\Delta kv \simeq 200$ MHz. Similarly, in cold atomic ensemble, the average velocity of the atoms within the trap $\simeq 10$ cm/s. Thus, the dephasing introduced in the system due to wave vector mismatch is $\Delta kv \simeq 100$ KHz. A study reported Doppler free Rydberg excitation in Rubidium atom using three-photon excitation scheme.¹⁸² EIT has also been studied experimentally using three-photon Rydberg excitation in atomic vapor.¹⁸³ Analytical calculation of

four-photon Rydberg excitation using adiabatic elimination has also been reported using Cs vapor.¹⁸⁴

In this chapter, we propose a four-photon excitation scheme for rubidium atomic vapor where the residual wave vector mismatch can be minimized. Due to very small residual wave vector mismatch, the system in thermal atomic vapor will behave similar to a cold atom ensemble. A five-level excitation scheme is used to study the dynamics of the single atom system. The blockade phenomenon is studied using a two-atom model by simplifying the five-level system of individual atom to an effective two-level system with suitable approximations. The effect of super-atom dephasing on the blockade phenomenon is also studied using this model. The experimental proposal in thermal and cold atomic ensemble is also presented.

6.1 Five-level system

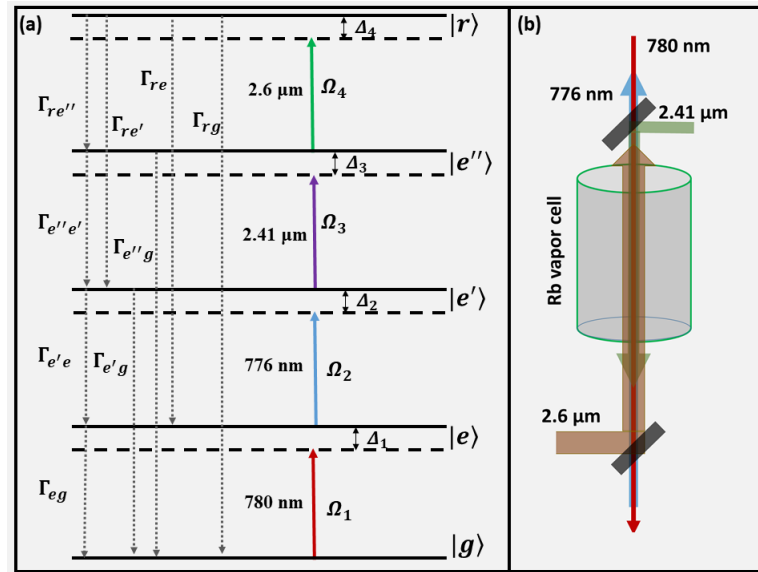


Figure 6.1: (a) Five-level atomic system with levels $|g\rangle$, $|e\rangle$, $|e'\rangle$, $|e''\rangle$ and $|r\rangle$ coupled by four laser sources with Rabi frequencies (laser detunings) Ω_1 (Δ_1), Ω_2 (Δ_2), Ω_3 (Δ_3) and Ω_4 (Δ_4). Γ_{if} is the population decay rate from initial state $|i\rangle$ to $|f\rangle$. (b) Four-photon excitation to the Rydberg state with beams in counter-propagating configuration.

Let us consider a five-level atomic system coupled by four laser sources. The energy level diagram for the system is depicted in figure 6.1 (a). The level $|g\rangle$ represents the ground state,

levels $|e\rangle$, $|e'\rangle$ and $|e''\rangle$ represent the intermediate excited states and $|r\rangle$ represents the Rydberg state. Applied lasers with Rabi frequencies (laser detunings) Ω_1 (Δ_1), Ω_2 (Δ_2), Ω_3 (Δ_3) and Ω_4 (Δ_4) couple the transitions $|g\rangle \rightarrow |e\rangle$, $|e\rangle \rightarrow |e'\rangle$, $|e'\rangle \rightarrow |e''\rangle$ and $|e''\rangle \rightarrow |r\rangle$ respectively. The time independent Hamiltonian for the five-level system using the rotating wave approximations is given by

$$H = -\frac{\hbar}{2} \begin{bmatrix} 0 & \Omega_1 & 0 & 0 & 0 \\ \Omega_1 & 2\Delta_1 & \Omega_2 & 0 & 0 \\ 0 & \Omega_2 & 2(\Delta_1 + \Delta_2) & \Omega_3 & 0 \\ 0 & 0 & \Omega_3 & 2(\Delta_1 + \Delta_2 + \Delta_3) & \Omega_4 \\ 0 & 0 & 0 & \Omega_4 & 2(\Delta_1 + \Delta_2 + \Delta_3 + \Delta_4) \end{bmatrix}. \quad (6.1)$$

The density matrix for the five-level system is given by

$$\rho = \begin{bmatrix} \rho_{gg} & \rho_{ge} & \rho_{ge'} & \rho_{ge''} & \rho_{gr} \\ \rho_{eg} & \rho_{ee} & \rho_{ee'} & \rho_{ee''} & \rho_{er} \\ \rho_{e'g} & \rho_{e'e} & \rho_{e'e'} & \rho_{e'e''} & \rho_{e'r} \\ \rho_{e''g} & \rho_{e''e} & \rho_{e''e'} & \rho_{e''e''} & \rho_{e''r} \\ \rho_{rg} & \rho_{re} & \rho_{re'} & \rho_{re''} & \rho_{rr} \end{bmatrix}. \quad (6.2)$$

The decay and decoherence is incorporated in the system using the Lindblad matrix which is given by

$$L(\rho) = -\frac{1}{2} \sum_m (C_m^\dagger C_m \rho + \rho C_m^\dagger C_m) + \sum_m C_m \rho C_m^\dagger. \quad (6.3)$$

Here, summation index m represents all possible decay channels of the system and $C_m = C_{if} = \sqrt{\Gamma_{if}} |f\rangle \langle i|$, with $|i\rangle$ and $|f\rangle$ denoting the initial state and final state respectively and Γ_{ij} represents the population decay rate from $|i\rangle$ to $|f\rangle$. The dipole allowed decays that arises due to process of spontaneous emission are given by $\Gamma_{re''}$, $\Gamma_{e''e'}$, $\Gamma_{e'e}$, Γ_{eg} and Γ_{re} . However, the system have few indirect decays that arises due to the finite transit time of the atoms through

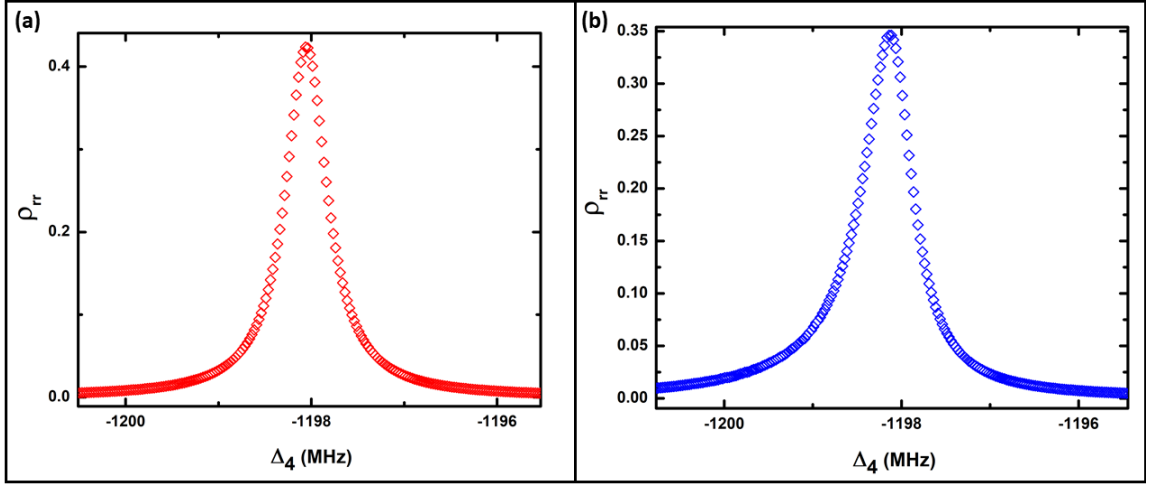


Figure 6.2: Rydberg population as a function of Δ_4 with $\Omega_1 = 150$ MHz, $\Omega_2 = 300$ MHz, $\Omega_3 = 180$ MHz, $\Omega_4 = 180$ MHz, $\Delta_1 = 1200$ MHz, $\Delta_2 = -800$ MHz and $\Delta_3 = 800$ MHz for (a) cold atom and (b) thermal vapor. The decay terms are $\Gamma_{re''} = 0.01$ MHz, $\Gamma_{e''e'} = 0.1$ MHz, $\Gamma_{e'e} = 1$ MHz, $\Gamma_{eg} = 6$ MHz, $\Gamma_{re} = 0.01$ MHz, $\Gamma_{rg} = \Gamma_{e''g} = \Gamma_{e'g} = 0.1$ MHz.

the beam profile. These decays are represented by Γ_{rg} , $\Gamma_{e''g}$ and $\Gamma_{e'g}$ as depicted in figure 6.1 (a). The different physical quantities associated with the system are calculated using the OBEs given by

$$\dot{\rho} = \frac{1}{i\hbar}[H, \rho] + L_D.$$

These equations are solved in steady state condition where $\dot{\rho} = 0$. The quantity ρ_{rr} is calculated which gives population of the Rydberg state. ρ_{rr} as a function of Δ_4 for the cold atom system is depicted in figure 6.2(a). The FWHM of the peak is found to be 0.54 MHz for the parameters $\Omega_1 = 150$ MHz, $\Omega_2 = 300$ MHz, $\Omega_3 = 180$ MHz, $\Omega_4 = 180$ MHz, $\Delta_1 = 1200$ MHz, $\Delta_2 = -800$ MHz and $\Delta_3 = 800$ MHz. The parameters are chosen such that the population get transfer from the ground state to the Rydberg state without populating the intermediate states. Thus, any laser parameter satisfying the conditions $\Delta_i \gg \Omega_i$, where $i = 1, 2$ and 3 can be used for the Rydberg excitation.

6.1.1 Doppler averaging

In order to extend the system for thermal atomic vapor, the effect of velocity is considered in the model. In a thermal vapor ensemble, the atoms can move with broad range of velocities. Thus, the Doppler's effect comes into the picture. In order to minimize the effect of velocity, we propose a Rydberg excitation scheme for rubidium atom exciting to $70S_{1/2}$. Details regarding the excitation scheme is presented in section 6.4. The laser beams are considered in a counter-propagating configuration as presented in figure 6.1 (b), in order to reduce the wave vector mismatch. The beams with Rabi frequencies Ω_1 and Ω_3 counter-propagate the beams with Rabi frequencies Ω_2 and Ω_4 . The single photon laser detunings will vary due to Doppler effect. For an atom moving with velocity v , the detunings are given by $\Delta'_1 = \Delta_1 - k_1v$, $\Delta'_2 = \Delta_2 + k_2v$, $\Delta'_3 = \Delta_3 - k_3v$, $\Delta'_4 = \Delta_4 + k_4v$. Here $k_i, i \in \{1, 2, 3, 4\}$ are the wave-vector corresponding to each laser. The \pm sign corresponds to the direction of propagation of the applied laser. Thus, the four-photon detuning of the excitation process is given by $\delta_4 = \Delta'_1 + \Delta'_2 + \Delta'_3 + \Delta'_4 = \Delta_1 + \Delta_2 + \Delta_3 + \Delta_4 - ((k_1 - k_2) - (k_4 - k_3))v$. The residual wave vector mismatch is defined as $\Delta k = \Delta k_1 - \Delta k_2$, where $\Delta k_1 = k_1 - k_2$ and $\Delta k_2 = k_4 - k_3$. The wave vectors for the laser configuration presented in figure 6.1 (b) are $k_1 = 1.282 \times 10^6 \text{ cm}^{-1}$, $k_2 = 1.289 \times 10^6 \text{ cm}^{-1}$, $k_3 = 0.414 \times 10^6 \text{ cm}^{-1}$ and $k_4 = 0.384 \times 10^6 \text{ cm}^{-1}$. The configuration is used such that Δk becomes minimum. Thus, the effect of Doppler broadening can be minimized. The beams are considered in the counter-propagating configuration as presented in figure 6.1 where the residual wave vector mismatch is found to be $\Delta k \simeq 0.023 \times 10^6 \text{ m}^{-1}$. Using these values of k , the system is Doppler averaged over the whole velocity class using a Maxwell-Boltzmann distribution. Rydberg population ρ_{rr} is calculated for the thermal vapor ensemble by solving the OBEs.

ρ_{rr} as a function of Δ_4 is depicted in figure 6.2(b). The FWHM of the peak is found to be 0.7 MHz. This width is comparable to that of the cold atomic ensemble. This is arising as Δk is very small for this system unlike the two-photon Rydberg excitation scheme. Therefore, the Doppler width $\Delta k v_p$ becomes smaller for the system, where v_p is the most probable speed of the atom. Thus, using a four-photon excitation scheme, the residual wave vector mismatch is

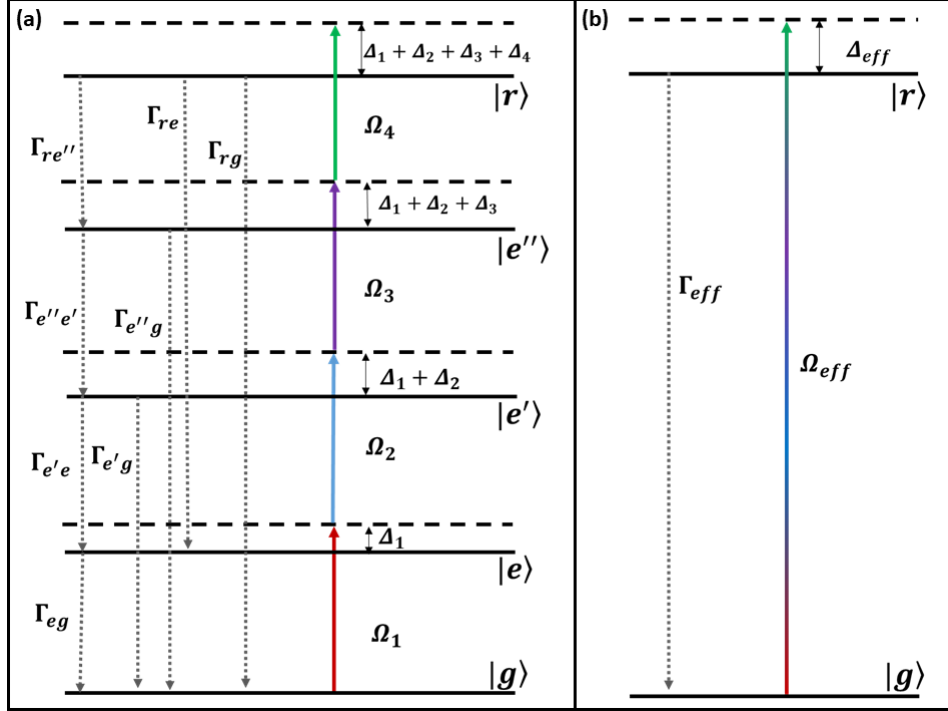


Figure 6.3: (a) Five-level atomic system $|g\rangle$, $|e\rangle$, $|e'\rangle$, $|e''\rangle$ and $|r\rangle$ coupled by four laser sources with Rabi frequencies (laser detunings) Ω_1 (Δ_1), Ω_2 (Δ_2), Ω_3 (Δ_3) and Ω_4 (Δ_4). Γ_{if} is the population decay rate from initial state $|i\rangle$ to $|f\rangle$. (b) Effective two-level system by adiabatically eliminating the intermediate state with levels $|g\rangle$ and $|r\rangle$ coupled by lasers with effective Rabi frequency Ω_{eff} , effective detuning Δ_{eff} and effective decay rate Γ_{eff} .

reduced which ultimately reduces the Doppler broadening and the system behaves similar to a cold atomic ensemble. Therefore, using a four-photon excitation process, the Rydberg blockade phenomenon can be studied in thermal vapor ensemble where the system will produce similar result like the cold atom.

6.2 Effective two-level system using adiabatic elimination

In order to study the blockade phenomenon in thermal atomic vapor using the four-photon excitation, a multi-atom system is considered. However, the mathematical complexity comes in even with two interacting atoms which will have 25 energy levels. Thus, solving the OBEs require large computation. Thus, the five-level system is simplified to an effective two-level system using the adiabatic elimination condition which is described here.

The Hamiltonian of the five-level system is given by,

$$H = -\frac{\hbar}{2} \begin{bmatrix} 0 & \Omega_1 & 0 & 0 & 0 \\ \Omega_1 & 2\Delta_1 & \Omega_2 & 0 & 0 \\ 0 & \Omega_2 & 2\delta_2 & \Omega_3 & 0 \\ 0 & 0 & \Omega_3 & 2\delta_3 & \Omega_4 \\ 0 & 0 & 0 & \Omega_4 & 2\delta_4 \end{bmatrix}.$$

Where $\delta_2 = \Delta_1 + \Delta_2$, $\delta_3 = \Delta_1 + \Delta_2 + \Delta_3$ and $\delta_4 = \Delta_1 + \Delta_2 + \Delta_3 + \Delta_4$. In order to simplify the system the Hamiltonian is modified which is given by

$$H' = H + \frac{\hbar}{2} \delta_4 I_{5 \times 5} \quad (6.4)$$

$$\Rightarrow H' = -\frac{\hbar}{2} \begin{bmatrix} -\delta_4 & \Omega_1 & 0 & 0 & 0 \\ \Omega_1 & 2\Delta_1 - \delta_4 & \Omega_2 & 0 & 0 \\ 0 & \Omega_2 & 2\delta_2 - \delta_4 & \Omega_3 & 0 \\ 0 & 0 & \Omega_3 & 2\delta_3 - \delta_4 & \Omega_4 \\ 0 & 0 & 0 & \Omega_4 & \delta_4 \end{bmatrix}$$

The time evolution of the system is studied using the time dependent Schrodinger's equation.

$$i\hbar\dot{\psi} = \hat{H}'\psi \quad (6.5)$$

Here ψ represents a 5×1 column vector with elements $\{C_g(t), C_e(t), C_{e'}(t), C_{e''}(t), C_r(t)\}$. Here, $|C_i(t)|^2$ represents the probability amplitude of the state $|i\rangle$. Substituting ψ in equation

6.5 we get

$$i\hbar\dot{C}_g = -\frac{\hbar}{2}(-\delta_4 C_g + \Omega_1 C_e) \quad (6.6)$$

$$i\hbar\dot{C}_e = -\frac{\hbar}{2}(\Omega_1 C_g + (2\Delta_1 - \delta_4)C_e + \Omega_2 C_{e'}) \quad (6.7)$$

$$i\hbar\dot{C}_{e'} = -\frac{\hbar}{2}(\Omega_2 C_e + (2\delta_2 - \delta_4)C_{e'} + \Omega_3 C_{e''}) \quad (6.8)$$

$$i\hbar\dot{C}_{e''} = -\frac{\hbar}{2}(\Omega_3 C_{e'} + (2\delta_3 - \delta_4)C_{e''} + \Omega_4 C_r) \quad (6.9)$$

$$i\hbar\dot{C}_r = -\frac{\hbar}{2}(\Omega_4 C_{e''} + \delta_4 C_r) \quad (6.10)$$

Using the adiabatic elimination condition $\Delta_i \gg \Omega_i$, where $i = 2, 3, 4$, the population of the states $|e\rangle$, $|e'\rangle$ and $|e''\rangle$ are neglected. Thus, the quantities $C_e(t)$, $C_{e'}(t)$, $C_{e''}(t)$ will be time independent. The above equations are solved using this condition to calculate

$$C_e = \frac{C_g \Omega_1 + C_{e'} \Omega_2}{(\delta_4 - 2\Delta_1)} \quad (6.11)$$

$$C_{e'} = \frac{C_e \Omega_2 + C_{e''} \Omega_3}{(\delta_4 - 2\delta_2)} \quad (6.12)$$

$$C_{e''} = \frac{C_{e'} \Omega_3 + C_r \Omega_4}{(\delta_4 - 2\delta_3)} \quad (6.13)$$

The quantities C_e , $C_{e'}$, $C_{e''}$ are calculated in terms of C_g and C_r using the above equations. Substituting the values of C_e , $C_{e'}$, $C_{e''}$ in equation 6.6 and 6.10, the Hamiltonian reduces to an effective two-level one which is given by

$$H = -\frac{\hbar}{2} \begin{bmatrix} 0 & \Omega_{eff} \\ \Omega_{eff} & 2\Delta_{eff} \end{bmatrix}.$$

The parameter Ω_{eff} and δ_{eff} are given by

$$\Omega_{eff} = \frac{\Omega_1 \Omega_2 \Omega_3 \Omega_4}{(\delta_4 - 2\Delta_1)(\delta_4 - 2\delta_3)} \left(\frac{1}{\delta_4 - 2\delta_2 - \frac{(\Omega_2)^2}{\delta_4 - 2\Delta_1} - \frac{(\Omega_3)^2}{\delta_4 - 2\delta_3}} \right) \quad (6.14)$$

$$\Delta_{eff} = 2\delta_4 + \frac{(\Omega_4)^2}{\delta_4 - 2\delta_3} - \frac{(\Omega_1)^2}{\delta_4 - 2\Delta_1} + \left(\frac{1}{\delta_4 - 2\delta_2 - \frac{(\Omega_2)^2}{\delta_4 - 2\Delta_1} - \frac{(\Omega_3)^2}{\delta_4 - 2\delta_3}} \right) \left[\left(\frac{\Omega_4\Omega_3}{\delta_4 - 2\delta_3} \right)^2 - \left(\frac{\Omega_1\Omega_2}{\delta_4 - 2\Delta_1} \right)^2 \right] \quad (6.15)$$

Thus, with adiabatic elimination, the five-level system is reduced to an effective two-level system with states $|g\rangle$ and $|r\rangle$. Now the effective decay rate from $|r\rangle$ to $|g\rangle$ for the effective 2-level system is given by $\Gamma_{eff} = \Gamma_{rg} + \Gamma_{re} + \Gamma_{re''}$. The L_D matrix of the effective two-level system is calculated to be

$$L_D = \Gamma_{eff} \begin{bmatrix} \rho_{rr} & -\frac{\rho_{gr}}{2} \\ -\frac{\rho_{rg}}{2} & -\rho_{rr} \end{bmatrix}$$

The OBEs of the system is solved in steady state to calculate the density matrix element ρ_{rr} which gives the Rydberg population for the effective two-level system. This, Rydberg population is plotted as a function of Δ_4 and is depicted in figure 6.4 (a) and is compared to the Rydberg population calculated using the five-level system. A good agreement is observed between both the calculation with residual less than 10^{-2} as depicted in figure 6.4 (b), while the maximum peak value is $\simeq 0.35$. The parameters used in the plot are $\Omega_1 = 150$ MHz, $\Omega_2 = 300$ MHz, $\Omega_3 = 180$ MHz, $\Omega_4 = 180$ MHz, $\Delta_1 = 1200$ MHz, $\Delta_2 = -800$ MHz and $\Delta_3 = 800$ MHz. However, for any parameter satisfying the adiabatic elimination condition mentioned above in this section, the two models agree with each other. This indicates that with adiabatic elimination, the five-level system is reduced to a simple effective two-level system which is useful to study phenomena due to multiple atom system.

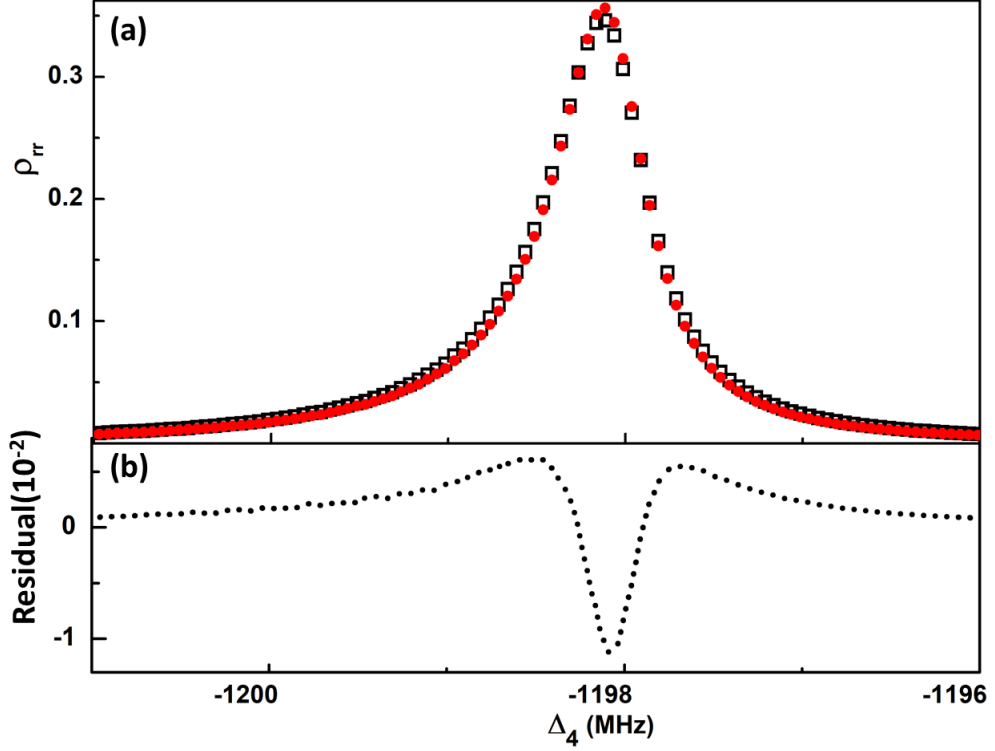


Figure 6.4: (a) Rydberg state population as a function of Δ_4 calculated using the five-level system (\square) and the effective two-level system (\bullet) for parameters $\Omega_1 = 150$ MHz, $\Omega_2 = 300$ MHz, $\Omega_3 = 180$ MHz, $\Omega_4 = 180$ MHz, $\Delta_1 = 1200$ MHz, $\Delta_2 = -800$ MHz and $\Delta_3 = 800$ MHz. The decay terms are $\Gamma_{re''} = 0.01$ MHz, $\Gamma_{e''e'} = 0.1$ MHz, $\Gamma_{e'e} = 1$ MHz, $\Gamma_{eg} = 6$ MHz, $\Gamma_{re} = 0.01$ MHz, $\Gamma_{rg} = \Gamma_{e''g} = \Gamma_{e'g} = 0.1$ MHz and $\Gamma_{eff} = 0.17$ MHz. (b) The residual plot with the variation of frequency.

6.3 Theory of Rydberg blockade using four-photon excitation

As presented in the previous section, the five-level system reduced to an effective two-level system with energy levels $|g\rangle$ and $|r\rangle$ as shown in figure 6.5 (a). Let us consider a system of two interacting atoms as shown in figure 6.5 (b). The level $|1\rangle \equiv |gg\rangle$ corresponds to both the atoms in the ground state, $|2\rangle \equiv |rg\rangle$ and $|3\rangle \equiv |gr\rangle$ correspond to the levels with one atom in the ground state and the other in the Rydberg state and $|4\rangle \equiv |rr\rangle$ corresponds to the level with both the atoms in the Rydberg state. The Hamiltonian of this system is given by

$$H = H^{(1)} \otimes I + I \otimes H^{(2)} + 2V_{rr} |4\rangle \langle 4|, \quad (6.16)$$

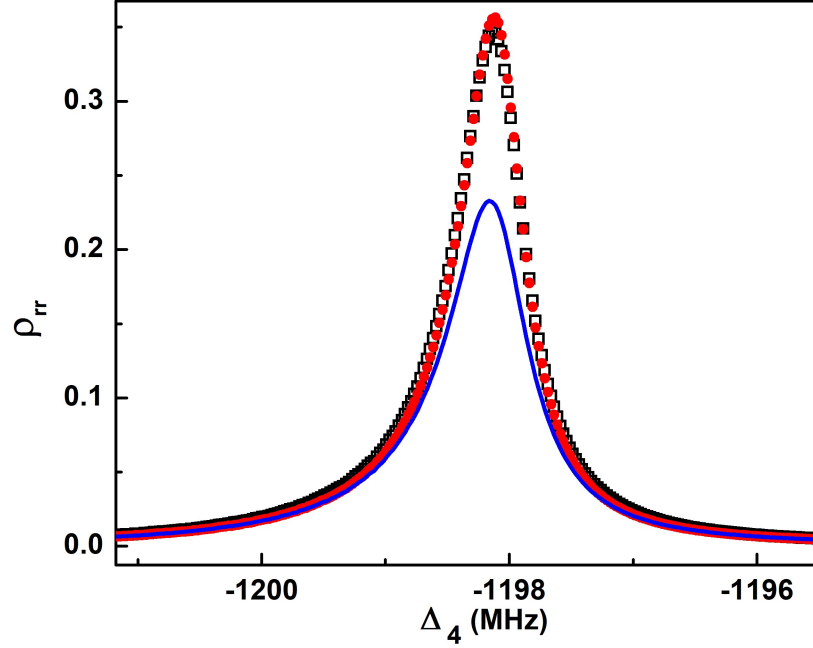


Figure 6.6: Rydberg state population as a function of Δ_4 for single atom five-level system (\bullet), two-atom system with $V_{rr} = 0$ (\square) and $V_{rr} = 20$ MHz (—). The parameters used are $\Omega_1 = 150$ MHz, $\Omega_2 = 300$ MHz, $\Omega_3 = 180$ MHz, $\Omega_4 = 180$ MHz, $\Delta_1 = 1200$ MHz, $\Delta_2 = -800$ MHz, $\Delta_3 = 800$ MHz, $\Gamma = 0.17$ MHz and $\Gamma_S = 0$.

The L_D matrix and the density matrix for the i th atom is given by

$$L_D = \Gamma \begin{bmatrix} \rho_{22}^{(i)} & -\frac{\rho_{12}^{(i)}}{2} \\ -\frac{\rho_{21}^{(i)}}{2} & -\rho_{22}^{(i)} \end{bmatrix}, \rho^{(i)} \begin{bmatrix} \rho_{11}^{(i)} & \rho_{12}^{(i)} \\ \rho_{21}^{(i)} & \rho_{22}^{(i)} \end{bmatrix}$$

We have explained in the previous chapter that, the transverse velocity of the atoms participating in the blockade process introduces a dephasing in the system known as the super-atom dephasing (Γ_S). This dephasing arises between the state $|gr\rangle$ and $|rg\rangle$ due to the variation of relative position of the atoms. Thus, this dephasing is included between the states $|2\rangle$ and $|3\rangle$ phenomenologically in the composite L_D matrix of the two-atom system. Thus, the L_D matrix for the system is calculated as

$$L_D = -\Gamma \begin{bmatrix} \rho_{22} + \rho_{33} & -\frac{\rho_{12}}{2} + \rho_{34} & -\frac{\rho_{13}}{2} + \rho_{24} & -\rho_{14} \\ -\frac{\rho_{21}}{2} + \rho_{43} & -\rho_{22} + \rho_{44} & -\rho_{23}(1 + \Gamma_S/\Gamma) & -\frac{3\rho_{24}}{2} \\ -\frac{\rho_{31}}{2} + \rho_{42} & -\rho_{32}(1 + \Gamma_S/\Gamma) & -\rho_{33} + \rho_{44} & -\frac{3\rho_{34}}{2} \\ -\rho_{41} & -\frac{3\rho_{42}}{2} & -\frac{3\rho_{43}}{2} & -2\rho_{44} \end{bmatrix} \quad (6.17)$$

The dynamics of the system is studied using OBEs which is given by

$$\dot{\rho} = \frac{1}{i\hbar} [H, \rho] + L_D \quad (6.18)$$

The OBEs of the system are solved in a steady state $\dot{\rho} = 0$. The population of the Rydberg state for the two-atom system is calculated to be

$$\rho_{rr} = \frac{(\rho_{22} + \rho_{33})}{2} + \rho_{44}. \quad (6.19)$$

In a cold atomic ensemble the atoms are considered to be frozen. However, in thermal vapor ensemble, they move with a broad range of velocities. In order to extend the blockade theory of four-photon excitation for thermal atomic vapor, the atoms are considered to be moving with different velocities. Consider the velocity of atom 1 and atom 2 are v_1 and v_2 respectively. Thus, the laser detunings are given by $\Delta'_1 = \Delta_1 - \Delta k v_1$ and $\Delta'_2 = \Delta_2 - \Delta k v_2$. Here, Δk is the residual wave vector mismatch. Using Monte-Carlo technique the system is Doppler averaged over these velocities using the Maxwell-Boltzmann distribution. The Rydberg population for thermal vapor is given by

$$\rho_{rr} = \int_{-\infty}^{\infty} \int_{-\infty}^{\infty} \rho_{rr}(v_1, v_2) e^{-v_1^2/v_p^2} e^{-v_2^2/v_p^2} dv_1 dv_2. \quad (6.20)$$

Rydberg population for the thermal vapor two-atom system is plotted as a function of Δ_4 in figure 6.6. When the system is non-interacting, this population is expected to be same as that of the single atom picture. As depicted in figure 6.6, they are found to be in good agreement

with each other. When, the interaction is included the population is observed to be suppressed significantly compare to the non-interacting system. This is due to the blockade effect arising for interaction between the atoms.

Using the similar approach as mentioned in chapter 5, the exact OBEs of the system can be simplified to have the approximate model with 4 independent equations. Extending the study for three and four-atom system, the model can be extended for N atoms inside the blockade sphere.

6.3.1 Effect of Super atom dephasing

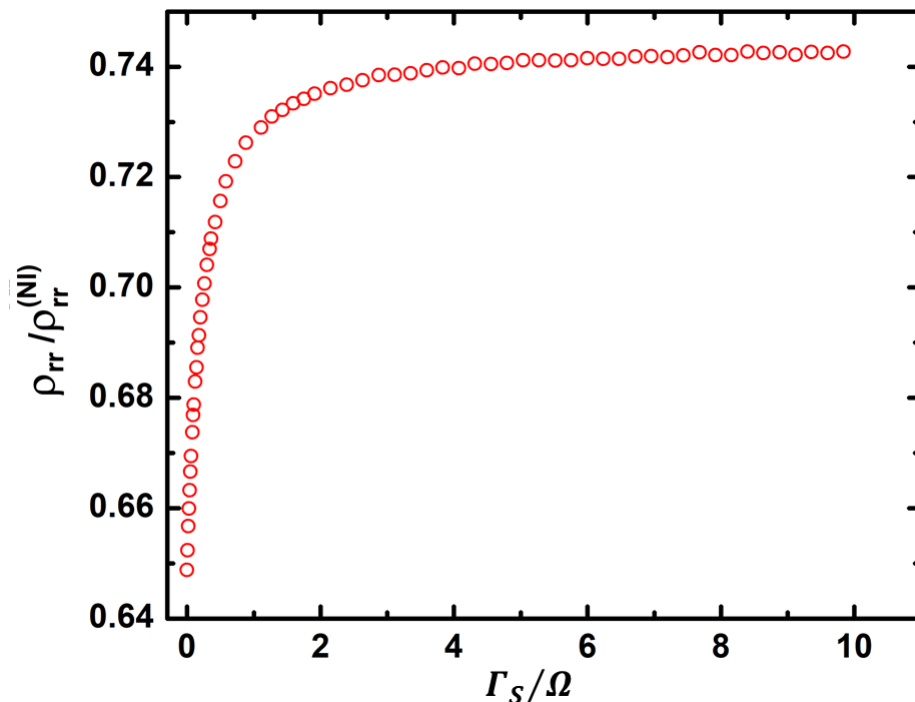


Figure 6.7: Normalized Rydberg blocked population as a function of Γ_S / Ω for the two-atom interacting system.

The effect of the super-atom dephasing is also studied in the system. The super-atom dephasing for a thermal vapor ensemble at temperature 400 K, is calculated to be 50 MHz. It was observed that the blockade effect reduces when Γ_S increases. The normalized Rydberg blocked population is defined as $\rho_{rr}^{(b)} = \rho_{rr} / \rho_{rr}^{(NI)}$ is calculated, where ρ_{rr} and $\rho_{rr}^{(NI)}$ represents the Rydberg population for the interacting and non-interacting two-atom model. $\rho_{rr}^{(b)}$ as a function

of the Γ_S is depicted in figure 6.7. With increase in Γ_S , the blockade effect is observed to be reducing. However, even for large value of Γ_S , $\rho_{rr}^{(b)} < 1$, which indicates that the system does not reach to a non-interacting regime. This observation indicates that the blockade effect can be observed in thermal atomic vapor.

6.4 Experimental proposal using four-photon excitation

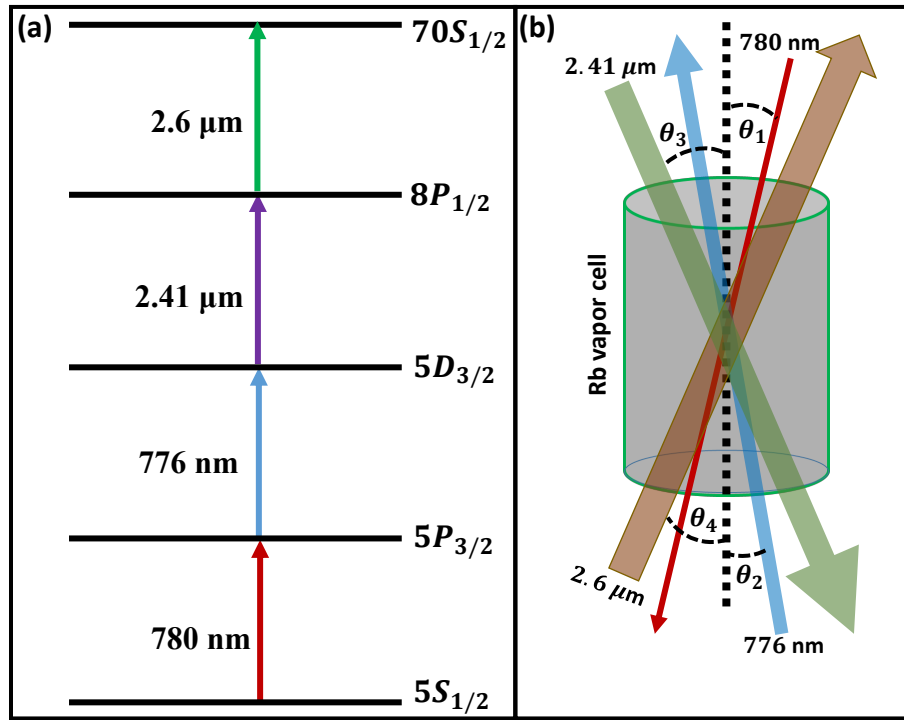


Figure 6.8: *Experimental proposal for four-photon excitation. (a) The energy level diagram for rubidium atom excited to a Rydberg state $70S_{1/2}$ by four photon excitation. (b) Experimental set-up with suitable geometry such that residual wave vector $\Delta k = 0$.*

The experiment in thermal atomic vapor can be performed using four-photon excitation. The corresponding energy level diagram for the excitation is presented in figure 6.8 (a). The transitions are chosen to minimize the residual wave vector mismatch. Diode lasers can be used for the wavelengths 780 nm and 776 nm. Fiber coupled high power diode laser are required for the wavelengths 2.41 μm and 2.6 μm with power nearly 1 watt. When the atoms are in counter-propagating configuration as shown in figure 6.1(b), the residual wave vector is

$\Delta k \simeq 0.023 \times 10^6 \text{ m}^{-1}$. However, the beam geometry can be changed as shown in figure 6.8 (b) such that the residual wave vector can be reduced to zero. One such configuration is $\theta_1 = 6^\circ$, $\theta_2 = 6^\circ$, $\theta_3 = 2.67^\circ$ and $\theta_4 = 2.93^\circ$ for which $\Delta k = 0$. In this configuration the thermal vapor system will behave similar to a cold atomic ensemble. The Rydberg excitation with four-photon can also be performed in cold atom ensemble. The average velocity of the atoms in an ultra-cold atomic ensemble $\simeq 10 \text{ cm/s}$. Thus, during the two-photon excitation with 780 and 480 nm laser, the dephasing due to residual wave-vector mismatch becomes $\simeq 100 \text{ KHz}$. However, in an experiment with four-photon excitation, this dephasing can be reduced to zero by suitable alignment of beam angle.

6.5 Conclusion

We have studied the blockade phenomenon in thermal atomic vapor using four-photon excitation. Using the adiabatic elimination the five-level system is reduced to an effective two-level system. The blockade phenomenon is studied using a two-atom model. The effect of super-atom dephasing in the blockade phenomenon is also studied. It is observed that unlike the single photon or two-photon case, atoms with different velocity also participate in the blockade process. Also, for thermal atomic vapor where the super-atom dephasing will be large the blockade phenomenon does not vanish which indicate the existence of Rydberg blockade in thermal atomic vapor.

The experiment can be performed in thermal atomic vapor with rubidium atom as explained in the section 6.4. The advantage of the system over the usual two-photon excitation scheme is the residual wave vector mismatch which can be reduced to zero with suitable beam geometry. Thus, the system in thermal atomic vapor will produce similar result to that of a cold atomic ensemble. This also opens up the possibility of the application of thermal atomic vapor in quantum information processing.

Chapter 7

Summary and Future plans

We have demonstrated the phenomenon of Rydberg anti-blockade in thermal atomic vapor using the OHDT. A two-atom model using the dressed state picture of the three level system is presented to explain the experimental observation. The observations are verified for multiple Rydberg states where a good qualitative agreement between the theory and the experiment indicates the existence of the anti-blockade phenomena in thermal atomic vapor. This is the first ever observation of Rydberg anti-blockade phenomenon reported in a thermal vapor ensemble. The scaling of the interaction strength with the principal quantum number of the Rydberg state could not be observed in the experiment. This is due to the presence of blockade and other cascading processes involving three or more atoms which could not be determined with our simple theoretical model. The experiment can be performed in a cold atomic ensemble where the atoms are frozen and the anti-blockade effect can be studied there to observe the scaling of interaction strength.

The theoretical study of the Rydberg blockade phenomenon using an interacting model of N atoms inside the blockade sphere is also presented in this thesis. Exact calculation of two, three and four-atom model with suitable approximations are extrapolated to formulate an approximate model for N atoms. Also, an empirical formula is derived for N atoms using the super-atom picture. In a cold atomic ensemble where dephasing due to laser frequency noise can't be neglected, the empirical formula is not sufficient to explain the blockade phenomenon.

Thus, the approximate model for N atoms presented here is more appropriate to study the phenomenon of blockade in ultra-cold atomic ensemble with large laser frequency noise. The study also indicates the existence of the blockade phenomenon in thermal atomic vapor where the super-atom dephasing is very large. An experiment can be performed in thermal atomic vapor to observe the blockade effect. The blockade phenomenon can be studied at the red detuned side of the two-photon excitation peak where the anti-blockade effect is negligible.

The Rydberg blockade phenomenon is also studied theoretically using a four-photon excitation scheme. The advantage in this process is the residual wave vector mismatch which is much smaller compared to a two-photon process. The blockade phenomenon is studied theoretically using the two-atom model by suitably reducing individual atom to an effective two-level system using adiabatic elimination. It is observed that although atoms are moving with different velocity in thermal vapor, they participate in the blockade process unlike the single-photon or two-photon excitation scheme.

The experiment in thermal atomic vapor can be performed using four photon excitation. With a two-photon Rydberg excitation with 780 nm and 480 nm laser, the wave vector mismatch is larger. This leads to the Doppler broadening of $\simeq 250$ MHz of the transition lines in thermal atomic vapor at room temperature. However, using four-photon excitation process, the transitions can be chosen such that the wave vector mismatch can be minimized. Four-photon excitation scheme to the Rydberg state $70S_{1/2}$ in rubidium vapor is proposed. By suitable alignment of beam geometry the residual wave-vector mismatch can be reduced to zero. In this situation, the thermal vapor system behaves equivalent to a cold atomic ensemble. The blockade effect can be observed using the four-photon excitation process, where the dominating dephasing mechanism is the super-atom dephasing. The Rydberg excitation with four-photon can also be performed in cold atom ensemble. The average velocity of the atoms in an ultra-cold atomic ensemble $\simeq 10$ cm/s. Thus, during the two photon excitation to the Rydberg state, the dephasing due to residual wave-vector mismatch becomes $\simeq 100$ KHz. However, in an experiment with four-photon Rydberg excitation, this dephasing can be reduced to zero by suitable alignment of beam angle.

SUMMARY

In this thesis, a theoretical study of Rydberg blockade as well as theoretical and experimental study of Rydberg anti-blockade effects are presented with emphasis on thermal atomic vapor. Using optical heterodyne detection technique, dispersion of the probe beam is observed due to two-photon excitation to the Rydberg state in thermal atomic vapor. The phenomena of interaction induced enhancement in Rydberg excitation or Rydberg anti-blockade is demonstrated in the system. A model involving two interacting atoms is formulated using the dressed state picture of the three-level atomic system to explain the experimental observations. A non-linear dependence of the peak height on the atomic vapor density is observed for the anti-blockade peak arising in the dispersion spectrum of the probe laser. The peak height also increases with increase in principal quantum number of the Rydberg state. A good agreement is found between the experimental observations and the proposed interacting model for different Rydberg states indicating the existence of Rydberg anti-blockade in thermal vapor.

A theoretical model that explains the possibility of Rydberg blockade for an ensemble of N -atoms in thermal atomic vapor is also presented. Starting from a two atom model, the blockade theory is extended to three and four atoms inside the blockade sphere. An effective model is formulated for N atoms using the method of induction. Also, the effect of different dephasing mechanisms on the blockade process, arising due to the velocity of the atoms in thermal vapor ensemble are studied. The existence of blockade effect in thermal atomic vapor is observed in the theory where the dephasing due to relative motion of the atoms is large. In addition to this, a theoretical model for Rydberg blockade in thermal atomic vapor is proposed using four-photon excitation scheme. The advantage of using this scheme is the residual wave vector mismatch which is much smaller compared to a two-photon process. The blockade phenomenon is studied theoretically with the two-atom model by suitably reducing the individual atomic system to an effective two-level system using adiabatic elimination. It is observed that although atoms are moving with different velocity in thermal vapor, they participate in the blockade process unlike the single-photon or two-photon excitation scheme.

Bibliography

- ¹ R. W. Boyd, *Nonlinear Optics*, London: Academic Press, ISBN:978-0-12-369470-6, (2015).
- ² W. Nie, Optical Nonlinearity: Phenomena, applications and materials, *Adv. Mater.* **5**, 520-545 (1993).
- ³ S. Wabnitz, B. J. Eggleton, Springer International Publishing, ISBN 978-3-319-14992-9 (2015).
- ⁴ M. Safman, T. G. Walker, K. Mølmer, *Rev. Mod. Phys.*, **82**, 2313–2363, (2010).
- ⁵ I. Friedler, D. Petrosyan, M. Fleischhauer, G. Kurizki, *Phys. Rev. A* **72**, 043803 (2005).
- ⁶ S. Sevincli, N. Hankel, C. Ates, T. Pohl, *Phys. Rev. Lett.* **107**, 153001 (2011).
- ⁷ A. V. Gorshkov, J. Otterbach, M. Fleischhauer, T. Pohl, M. D. Lukin, *Phys. Rev. Lett.* **107**, 133602 (2011).
- ⁸ J. D. Pritchard, D. Maxwell, A. Gauguier, K. J. Weatherill, M. P. A. Jones, C. S. Adams, *Phys. Rev. Lett.* **105**, 193603 (2010).
- ⁹ V. Parigi *et al.*, *Phys. Rev. Lett.* **109**, 233602 (2012).
- ¹⁰ T. Peyronel *et al.*, *Nature* **488**, 57 (2012).
- ¹¹ O. Firstenberg, T. Peyronel, Qi-Yu Liang, A. V. Gorshkov, M. D. Lukin, V. Vuletić, *Nature* **502**, 71 (2013).
- ¹² S. Baur, D. Tiarks, G. Rempe, S. Dürr, *Phys. Rev. Lett.* **112**, 073901 (2014).

- ¹³ C. Ates, S. Sevincli, T. Pohl, *Phys. Rev. A* **83**, 041802(R) (2011).
- ¹⁴ K. J. Weatherill *et al.* *J. Phys. B: At. Mol. Opt. Phys.* **41**, 201002 (2008).
- ¹⁵ A. K. Mohapatra, M. G. Bason, B. Butscher, K. J. Weatherill, C. S. Adams, *Nature Phys.* **4**, 890 (2008).
- ¹⁶ A. K. Mohapatra, T. R. Jackson, C. S. Adams, *Phys. Rev. Lett.* **98**, 113003 (2007).
- ¹⁷ H. Gorniaczyk *et al.*, *Phys. Rev. Lett.* **113**, 053601 (2014).
- ¹⁸ M. Khazali, K. Heshami, C. Simon, *Phys. Rev. A* **91**, 030301(R) (2015).
- ¹⁹ Y.M. Liu *et al.*, *Phys. Rev. A* **89**, 033839 (2014).
- ²⁰ C. S. Hofmann *et al.*, *Phys. Rev. Lett.* **110**, 203601 (2013).
- ²¹ T. Baluktsian, B. Huber, R. Löw, T. Pfau, *Phys. Rev. Lett.* **110**, 123001 (2013).
- ²² J. Han *et al.*, *Phys. Rev. A* **92**, 063824 (2015).
- ²³ H. Schmidt, A. Imamoglu, *Opt. Lett.* **21**, 1936 (1996).
- ²⁴ H. Wang, D. Goorskey, M. Xiao, *Phys. Rev. Lett.* **87**, 073601 (2001).
- ²⁵ H. Chang, H. Wu, C. Xie, H. Wang, *Phys. Rev. Lett.* **93**, 213901 (2004).
- ²⁶ S. Li, X. Yang, X. Cao, C. Zhang, C. Xie, H. Wang, *Phys. Rev. Lett.* **101**, 073602 (2008).
- ²⁷ H. Kang, Y. Zhu, *Phys. Rev. Lett.* **91**, 093601 (2003).
- ²⁸ H. Lo, P. Su, Y. Chen, *Phys. Rev. A* **81**, 053829 (2010).
- ²⁹ W. Chen *et al.*, *Science* **341**, 768 (2013).
- ³⁰ A. Ashkin, *Phys. Rev. Lett.* **40**, 729 (1978).
- ³¹ E. L. Raabet *et al.*, *Phys. Rev. Lett.* **59**, 2631 (1987).

- ³² W.D. Phillips, H.J. Metcalf, *Scientific American*, March 1987, 36 (1987).
- ³³ C.N. Cohen-Tannoudji, W.D. Phillips, *Physics Today*, October 1990, 33 (1990).
- ³⁴ S. Chu, *Scientific American*, February 1992, 71 (1992).
- ³⁵ G.B. Lubkin, *Physics Today*, January 1996, 22 (1996).
- ³⁶ C. N. C. Tannoudji, *Rev. of Mod. Phys.* **70**, 707 (1998).
- ³⁷ M. H. Anderson *et al.*, *Science* **269**, 198 (1995).
- ³⁸ K. B. Davis *et al.*, *Phys. Rev. Lett.* **75**, 3969 (1995).
- ³⁹ C. C. Bradley *et al.*, *Phys. Rev. Lett.* **75**, 1687 (1995).
- ⁴⁰ B. DeMarco and D. S. Jin, *Science* **285**, 1703 (1999).
- ⁴¹ R. H. Dicke, *Phys. Rev.* **93**, 99 (1954).
- ⁴² D. Tong *et al.*, *Phys. Rev. Lett.*, **93**, 063001 (2004).
- ⁴³ K. Singer *et al.*, *Phys. Rev. Lett.*, **93**, 163001 (2004).
- ⁴⁴ T. C. Liebisch, A. Reinhard, P. R. Berman, G. Raithel, *Phys. Rev. Lett.*, **95**, 253002 (2005)
- ⁴⁵ T. Vogt *et al.*, *Phys. Rev. Lett.*, **97**, 083003 (2006).
- ⁴⁶ R. Heidemann *et al.*, *Phys. Rev. Lett.*, **99**, 163601 (2007).
- ⁴⁷ U. Raitzsch *et al.*, *Phys. Rev. Lett.*, **100**, 013002 (2008).
- ⁴⁸ N. Malossi *et al.*, *J. of Phys.: Conference Series* **594**, 012041 (2015).
- ⁴⁹ R. Heidemann *et al.*, *Phys. Rev. Lett.*, **100**, 033601 (2008).
- ⁵⁰ J. Wang, M. Gacesa, R. Côté, *Phys. Rev. Lett.* **114**, 243003 (2015).
- ⁵¹ T. Karpiuk *et al.*, *N. J. Phys.*, **17**, 053046 (2015).

- ⁵² N. Henkel, R. Nath, T. Pohl, *Phys. Rev. Lett.* **104**, 195302 (2010).
- ⁵³ M. Viteau *et al.*, *Phys. Rev. Lett.* **107**, 060402 (2011).
- ⁵⁴ E. Urban *et al.*, *Nature Phys.*, **5**, 110-114 (2009).
- ⁵⁵ A. Gaëtan *et al.*, *Nature Phys.*, **5**, 115-118 (2009).
- ⁵⁶ Y. O. Dudin, A. Kuzmich *Science*, **336**, 887 (2012).
- ⁵⁷ T. M. Weber *et al.*, *Nature Phys.*, **11**, 157-161 (2015).
- ⁵⁸ L. Béguin *et al.*, *Phys. Rev. Lett.* **110**, 263201 (2013).
- ⁵⁹ P. Bachor , T. Feldker , J. Walz and F. Schmidt-Kaler, *J. Phys. B: At. Mol. Opt. Phys.* **49**, 154004 (2016).
- ⁶⁰ Y Chougale and R. Nath, *J. Phys. B: At. Mol. Opt. Phys.* **49**, 144005 (2016).
- ⁶¹ M. Brune *et al.*, *Phys. Rev. Lett.* **65**, 976 (1990).
- ⁶² M. Brune, S. Haroche, J. M. Raimond, *Phys. Rev. A* **45**, 5193 (1992).
- ⁶³ C. Guerlin *et al.*, *Nature* **448**, 889 (2007).
- ⁶⁴ M. Brune *et al.*, *Phys. Rev. Lett.* **101**, 240402 (2008).
- ⁶⁵ S. Gleyzes *et al.*, *Nature* **446**, 297 (2007).
- ⁶⁶ D. Maxwell *et al.*, *Phys. Rev. Lett.*, **110**, 103001 (2013).
- ⁶⁷ H. Weim *et al.*, *Nature Phys.* **6**, 382 (2010).
- ⁶⁸ D. Tiarks, S. Schmidt, G. Rempe, S. Dürr, *Science Advances* **2**, 1600036 (2016).
- ⁶⁹ D. E. Chang, V. Vuletić, M. D. Lukin, *Nature Photonics* **8**, 685 (2014).
- ⁷⁰ H. Busche *et al.*, *Nature Physics* **13**, 655 (2017).

- ⁷¹ J. T. Young *et al.*, *Phys. Rev. A* **97**, 023424 (2018).
- ⁷² A. W. Glaetzle *et al.*, *Phys. Rev. A* **86**, 043403 (2012).
- ⁷³ D. Petrosyan, M. Höning, M. Fleischhauer, *Phys. Rev. A*, **87**, 053414 (2013).
- ⁷⁴ D. W. Schönleber, M. Gärttner, J. Evers, *Phys. Rev. A*, **89**, 033421 (2014).
- ⁷⁵ E. Levi, R. Gutiérrez, I. Lesanovsky, *J. Phys. B: At. Mol. Opt. Phys.* **49**, 184003 (2016).
- ⁷⁶ N. Malossi *et al.*, *Phys. Rev. Lett.* **113**, 023006 (2014).
- ⁷⁷ M. D. Lukin *et al.*, *Phys. Rev. Lett.* **87**, 037901 (2001).
- ⁷⁸ J. H. Shapiro, *Phys. Rev. A* **73**, 062305 (2006).
- ⁷⁹ A. Aspuru-Guzik, and P. Walther, *Nature Phys.* **8**, 285 (2012).
- ⁸⁰ I. M. Georgescu, S. Ashhab, F. Nori, *Rev. of Mod. Phys.* **86**,153 (2014).
- ⁸¹ D. Jaksch *et al.*, *Phys. Rev. Lett.* **85**, 2208 (2000).
- ⁸² B. He *et al.*, *Phys. Rev. Lett.* **112**, 133606 (2014).
- ⁸³ D. Paredes-Barato, C. S. Adams, *Phys. Rev. Lett.* **112**, 040501 (2014).
- ⁸⁴ M. Saffman, T. G. Walker, *Phys. Rev. A* **66**, 065403 (2002).
- ⁸⁵ M. Saffman, T. G. Walker, *Phys. Rev. A* **72**, 042302 (2005).
- ⁸⁶ E. Brion, A. S. Mouritzen, K. Mølmer, *Phys. Rev. A* **76**, 022334 (2007).
- ⁸⁷ E. Brion, K. Mølmer, M. Saffman, *Phys. Rev. Lett.* **99**, 260501 (2007).
- ⁸⁸ L. Isenhower *et al.*, *Phys. Rev. Lett.* **104**, 010503 (2010).
- ⁸⁹ T. Wilk *et al.*, *Phys. Rev. Lett.* **104**, 010502 (2010).
- ⁹⁰ C. Ates, T. Pohl, T. Pattard, J. M. Rost, *Phys. Rev. Lett.* **98**, 023002 (2007).

- ⁹¹ T. Amthor, C. Giese, C. S. Hofmann, M. Weidmuller, *Phys. Rev. Lett.* **104**, 013001 (2010).
- ⁹² T. Pohl and P. R. Berman, *Phys. Rev. Lett.* **102**, 013004 (2009)
- ⁹³ J. Qian *et al.*, *Phys. Rev. A* **80**, 053413 (2009).
- ⁹⁴ Z. C. Zuo, K. Nakagawa, *Phys. Rev. A* **82**, 062328 (2010).
- ⁹⁵ T. E. Lee, H. Häffner, M. C. Cross, *Phys. Rev. Lett.* **108**, 023602 (2012).
- ⁹⁶ S. Basak, Y. Chougale, R. Nath, *Phys. Rev. Lett* **120**, 123204 (2018).
- ⁹⁷ X Q Shao, J B You , T Y Zheng, C H Oh, S Zhang, *Phys. Rev. A* **89** 052313 (2014).
- ⁹⁸ S L Su, Q Guo, H F Wang, S Zhang, *Phys. Rev. A* **92**, 022328 (2015).
- ⁹⁹ D X Li, X Q Shao, *Phys. Rev. A* **98**, 062338 (2018).
- ¹⁰⁰ S L Su , arXiv:1901.04267 (2019).
- ¹⁰¹ A. W. Carr, M. Saffman, *Phys. Rev. Lett.* **111**, 033607 (2013).
- ¹⁰² A. D. Bounds *et al.*, *New J. Phys.* **21** 053026 (2019).
- ¹⁰³ L. Sárkány, J. Fortágh, D. Petrosyan, *Phys. Rev. A* **92**, 030303(R) (2015).
- ¹⁰⁴ S. L. Su *et al.*, *Phys. Rev. A* **93**, 012306 (2016)
- ¹⁰⁵ S-L Su, Ya Gao, Erjun Liang, Shou Zhang, *Phys. Rev. A* **95**, 022319 (2017).
- ¹⁰⁶ S-L Su *et al.*, *Phys. Rev. A* **96**, 042335 (2017).
- ¹⁰⁷ C. Wang *et al.* *Laser Phys.* **30** 045201, (2020).
- ¹⁰⁸ X Tan *et al.*, *Chin. Phys. B* **27** 100307(2018).
- ¹⁰⁹ J L Wu, J Song, S-L. Su, *Phys. Lett. A* **384** 126039 (2020).
- ¹¹⁰ E. F. Worden, J G Conway, J A Paisner, *Opt. Lett.* **3** 156–8 (1978).

- ¹¹¹ J P Hermann, J J Wynne, *Opt. Lett.* **5** 236–8 (1980).
- ¹¹² S. Mauger, J Millen, M P A Jones, *J. Phys. B: At. Mol. Opt. Phys.* **40**, 319 (2007).
- ¹¹³ X. Zhang, F. B. Dunning, S. Yoshida, J. Burgdörfer, *Phys. Rev. A* **92** 051402 (2015).
- ¹¹⁴ B. Huber *et al.*, *Phys. Rev. Lett.* **107**, 243001 (2011).
- ¹¹⁵ A. K. Kölle *et al.*, *Phys. Rev. A* **85**, 063821 (2012).
- ¹¹⁶ J. M. Kondo *et al.*, *Optics Lett.* **40**, 5570 (2015).
- ¹¹⁷ M. Marcuzzi, E. Levi, S. Diehl, J. P. Garrahan, I. Lesanovsky, *Phys. Rev. Lett.* **113**, 210401 (2014).
- ¹¹⁸ N. Šibalić *et al.*, *Phys. Rev. A* **94**, 011401(R) (2016).
- ¹¹⁹ N. R. de Melo *et al.*, *Phys. Rev. A* **93**, 063863 (2016).
- ¹²⁰ D. Weller, A. Urvoy, A. Rico, R. Löw, and H. Kübler, *Phys. Rev. A* **94**, 063820 (2016).
- ¹²¹ D-S Ding *et al.*, *Phys. Rev. X* **10**, 021023 (2020).
- ¹²² C G Wade *et al.*, *Nat. Photon.* **11** 40–3 (2016).
- ¹²³ C. Carr *et al.*, *Phys. Rev. Lett.* **111**, 113901 (2013).
- ¹²⁴ D. Weller *et al.*, *Phys. Rev. A* **99**, 043418 (2019)
- ¹²⁵ D Barredo, H Kübler, R Daschner, R Löw, T Pfau, *Phys. Rev. Lett.* **110** 123002 (2013).
- ¹²⁶ A. Bhowmick, S. S. Sahoo, A. K. Mohapatra, *Phys. Rev. A* **94**, 023839 (2016).
- ¹²⁷ A. Bhowmick, D. Kara, A. K. Mohapatra, *arXiv:1802.06599* (2018).
- ¹²⁸ A. Bhowmick, D. Kara, A. K. Mohapatra, *Pramana J. Phys.* **92**, 76 (2019).
- ¹²⁹ Fabian Ripka, Harald Kübler, Robert Löw, Tilman Pfau, *Science* **362**, 446–449 (2018).

- ¹³⁰ D. Kara, T. Firdoshi, A. K. Mohapatra, Manuscript under preparation.
- ¹³¹ D. Kara, A. Bhowmick, A. K. Mohapatra, *Scientific Reports* **8**, 5256 (2018).
- ¹³² D. Kara, A. K. Mohapatra, Manuscript under preparation.
- ¹³³ V. Gupta *et. al.*, Manuscript under preparation
- ¹³⁴ J. R. Rydberg, *Phil. Mag. 5th Ser*, **29**,331 (1890).
- ¹³⁵ N. Bohr, *Phil. Mag.* **26**, 1, 476 (1913)
- ¹³⁶ H. E. White, Introduction to atomic spectra, McGraw-Hill, New York, (1934).
- ¹³⁷ Thomas F. Gallagher, Cambridge University Press. ISBN 0-521-02166-9 (1994).
- ¹³⁸ A.C. Ipsen, K. Splittorff, arXiv:1401.8141v2 (2014)
- ¹³⁹ E. Schrödinger, **Physical Review** **28**, number 6 (1926).
- ¹⁴⁰ E. Almadi, E. Segre, *Nuovo Cimento* **11**, 145 (1934).
- ¹⁴¹ E. Fermi, *Nuovo Cimento***11**, 157 (1934).
- ¹⁴² F.A. Jenkins, E. Segre *Nuovo Cimento* **55**, 59 (1939).
- ¹⁴³ T. F. Gallagher, *Rep. Prog. Phys.* **51**, 143 (1988).
- ¹⁴⁴ H. J. Korsh, R. Möhlenkamp, *Z. Phys. A-Atom and Nuclei* **314**, 267 (1983).
- ¹⁴⁵ B. C. Yang, F. Robicheaux, *Physical Review A* **91**,043407 (2015).
- ¹⁴⁶ A. J. McCulloch *et al.*, *Physical Review A* **95**,063845 (2017).
- ¹⁴⁷ S. E. Anderson, G. Raithe, *Nature Comm.* **4**, 2967 (2013).
- ¹⁴⁸ Jonathan D. Pitchard, PhD Thesis, Durham University, 2011.
- ¹⁴⁹ D. Comparat, P. Pillet, *Journal of the Optical Society of America B*, **27**, A208 (2010).

- ¹⁵⁰ M. Zwiernik and P. Kok, *Phys. Rev. A* **79**, 022304 (2009).
- ¹⁵¹ J. Gillet, G. S. Agarwal, T. Bastin, *Phys. Rev. A* **81**, 013837 (2010).
- ¹⁵² J. Schmiedmayer, R. Folman, T. Calarco, *Journal of Modern Optics* **49**, 1375 (2010).
- ¹⁵³ P. S. Jessen, I. H. Deutsch, R. Stock, *Quantum Information Processing* **3**, 91 (2004).
- ¹⁵⁴ X. L. Zhang, L. Isenhower, A. T. Gill, T. G. Walker, M. Saffman, *Phys. Rev. A* **82**, 030306(R) (2010).
- ¹⁵⁵ K. S. Kleinbach *et al.*, *Phys. Rev. Lett.* **118**, 223001 (2017).
- ¹⁵⁶ N. R. de Melo *et al.*, *Phys. Rev. A* **93**, 063863 (2016).
- ¹⁵⁷ H. Kibler *et al.*, *Nature Phot.* **4**, 112 (2010).
- ¹⁵⁸ A. Bhowmick, D. Kara and A. K. Mohapatra *arXiv:1802.06599* (2018).
- ¹⁵⁹ F. Letscher *et al.*, *Phys. Rev. A* **95**, 023410, (2017).
- ¹⁶⁰ P. Meystre, M. Sargent, *Element of quantum optics* (1990).
- ¹⁶¹ D. Z. Chruściński, S. Pascazio, <https://arxiv.org/abs/1710.05993v2> (2017).
- ¹⁶² M. Fleischhauer, A. Imamoglu, J. P. Marangos, *Rev. Mod. Phys.* **77**, 633 (2005).
- ¹⁶³ R. Han, H. K. Ng, B-G Englert, *J. of Mod. Opt.*, **60**, 255 (2013).
- ¹⁶⁴ Phd Thesis, Sushree S Sahoo, NISER Bhubaneswar (2020).
- ¹⁶⁵ PhD thesis, Arup Bhowmick, NISER Bhubaneswar (2019).
- ¹⁶⁶ D. A. Steck, Rubidium 85 d line data, <http://steck.us/alkalidata>
- ¹⁶⁷ D. A. Steck, Rubidium 87 d line data, <http://steck.us/alkalidata>
- ¹⁶⁸ E. A. Goldschmidt *et. al.* *Phys. Rev. Lett.* **116**, 013001 (2016)

- ¹⁶⁹ Andrei Derevianko *et. al.* *Phys. Rev. A* **92**, 063419 (2015)
- ¹⁷⁰ F. Karlewski, M. Mack, J. Grimm, N. Sàdor, J. Fortàgh, *Phys. Rev. A.*, **91**, 043422 (2015).
- ¹⁷¹ M. M. Valado *et al.*, *Phys. Rev. A* **88**, 045401 (2013).
- ¹⁷² H. kang, Y. Zhu *Phys. Rev. Lett.* **91**, 093601 (2003)
- ¹⁷³ G. Müller, A. Witch, R. Rinkleff, K. Danzmann *Opt. Comm.* **127**, 37 (1996)
- ¹⁷⁴ A. M. Akulshin, S. Barreiro, A. Lezama *Phys. Rev. Lett.* **83**, 4277 (1999)
- ¹⁷⁵ A. M. Akulshin, A. I. Sidorov, R. J. McLean, P. Hannaford *J. Opt. B:Quantum Semiclass. Opt* **6**, 491 (2004).
- ¹⁷⁶ F. Letscher, O. Thomas, T. Niederprüm, M. Fleischhauer, H. Ott, *Phys. Rev. X* **7**, 021020 (2017).
- ¹⁷⁷ N. R. de Melo *et al.*, *Phys. Rev. A* **93**, 063863 (2016).
- ¹⁷⁸ S. Yoshida, J. Burgdörfer, X. Zhang, F. B. Dunning, *Phys. Rev. A* **95**, 042705 (2017).
- ¹⁷⁹ A. Reiserer, G. Rempe, *Rev. Mod. Phys.* **87**, 1379 (2015).
- ¹⁸⁰ C. S. Adams, *Review of Scientific Instruments* **71**, 59 (2000).
- ¹⁸¹ K. Singer, S. Jochim, M. Mudrich, A. Mosk, M. Weidemüller, *Review of Scientific Instruments* **73**, 4402 (2002)
- ¹⁸² I. I. Ryabtsev *et. al.*, *Phys. Rev. A* **84** 053409 (2011).
- ¹⁸³ C. Carr *et. al.* , *Optics Lett.* **37**, 18, (2012).
- ¹⁸⁴ E.A. Gazazyan , G.G. Grigoryan, D.N. Khachatryan, *J. Contemp. Phys.* **53**, 293–300 (2018).
- ¹⁸⁵ H. M. Antia, Numerical methods for scientiests and engineers, ISBN: 978-9380250-40-3 (2012).

¹⁸⁶ C. J. Hawthorn, K. P. Weber and R. E. Scholten, *Rev. of Sci. inst.*, **72**, 4477 (2001).

¹⁸⁷ R. W. P. Drever *et. al.*, *Appl. Phys. B* **31**, 97-105 (1983).

Appendix A

Data table

Sl. No.	Quantity	Symbol	Value
1	Speed of light in free space	c	$2.998 \times 10^8 \text{ ms}^{-1}$
2	Permeability of free space	μ_0	$4\pi \times 10^{-7} \text{ Hm}^{-1}$
3	Permittivity of free space	ϵ_0	$8.854 \times 10^{-12} \text{ Fm}^{-1}$
4	planck's constant	h	$6.625 \times 10^{-34} \text{ Js}$
5	Boltzmann's constant	k_B	$1.381 \times 10^{-23} \text{ JK}^{-1}$
6	Elementary charge	e	$1.602 \times 10^{-19} \text{ C}$
7	Bohr Magneton	μ_B	$9.274 \times 10^{-23} \text{ Am}^2$
8	Electron mass	m_e	$9.109 \times 10^{-31} \text{ Kg}$

Table A.1: Fundamental physical constants used in this thesis.

Adapted from: <http://physics.nist.gov/cuu/Constants>.

Sl. No.	Quantity	Symbol	Value
1	atomic number	Z	37
2	Relative natural abundance	$\eta(^{85}\text{Rb})$	72.17 %
3	Atomic mass	m	1.41×10^{-25} Kg
4	Nuclear spin	I	5/2
5	Vapor pressure at 25 ⁰ C	P_v	3.92×10^{-7} Torr
6	Electron spin g-factor	g_S	2.002319
7	Electron orbital g-factor	g_L	0.999993
8	Fine structure Lande's g-factor	$g_J(5^2S_{1/2})$	2.00233
9	Nuclear g-factor	g_I	-0.000294
10	D2 ($5^2S_{1/2} \rightarrow 5^2P_{3/2}$) wavelength vacuum	λ	780.2414 nm
11	D2 lifetime	τ	26.63 ns
12	D2 Natural linewidth	Γ	$2\pi \times 6.07$ MHz
13	D2 Transition dipole matrix element	$\langle J = 1/2 \hat{\mu} J' = 3/2 \rangle$	3.58×10^{-29} Cm
14	Saturation intensity ($F = 3 \rightarrow F' = 4$)	I_{sat}	3.89 mW/cm ²

Table A.2: Properties of ⁸⁵Rb

Appendix B

Monte-Carlo simulation

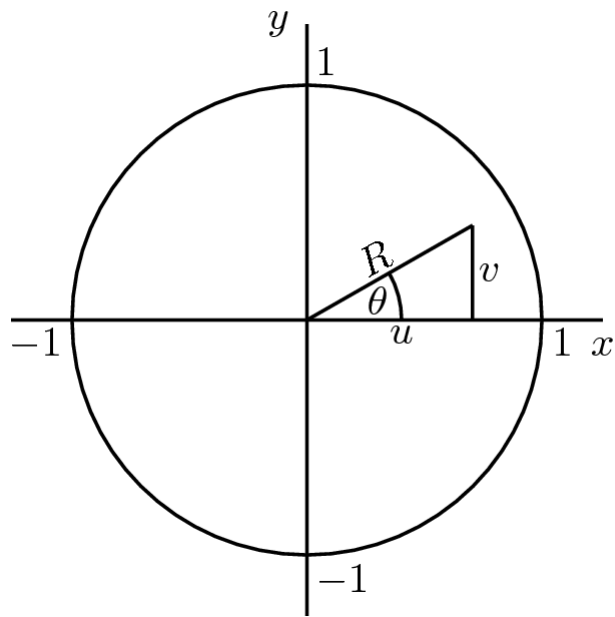


Figure B.1: *The Cartesian and polar co-ordinates relation in the unit circle.*

The Monte Carlo simulation is used in the work presented in this thesis to doppler-average the two-atom system each moving with different velocities. The Box-Muller transformation has been used to generate uniformly distributed random numbers. The Box-Muller transform is commonly expressed in two forms. The basic form which takes two randomly generated samples with uniform distribution on the interval $[0,1]$ and map them to two standard normally distributed samples. The other one is the polar form which takes two samples from a different

interval $[-1,1]$, and map them to two normally distributed sample without the use of sine and cosine functions. The polar form is relatively faster than the basic form and hence we have used it here.

Box-muller algorithm here is based on representing the joint distribution of two independent standard normal random Cartesian variable set to polar co-ordinates. Let us consider an integral in the cartesian co-ordinates given by

$$f(x, y) = \int \int \frac{1}{2\pi} \exp(-(x^2 + y^2)/2) dx dy$$

Directly solving it in the basic form is more time taking and computationally difficult. Thus using the relation between polar and Cartesian co-ordinates we can transform the integral to polar co-ordinates.

$$f(r, \theta) = \frac{1}{2\pi} \int_0^{2\pi} d\theta \int_0^R r e^{-(r^2/2)} dr$$

Which can be solved using the monte-carlo simulation by generating random numbers. Consider two random numbers set u and v in the closed interval $[-1,1]$. Now let us calculate $s = R^2 = u^2 + v^2$, where, s is always a positive number. We include only those values of s which lies in the open interval $(0,1)$ and discard all other values of u and v . Thus s will have a uniform distribution over a unit circle.

As shown in fig 5.1 we can relate the Cartesian variable u and v to polar variable r and θ . Thus we have $\cos(\theta) = u/r = u/\sqrt{s}$ and $\sin(\theta) = v/r = v/\sqrt{s}$. Thus we can define two variables $x = u\sqrt{\frac{-2\ln(s)}{s}}$ and $y = v\sqrt{\frac{-2\ln(s)}{s}}$. These two random numbers are similar to the cartesian variables having a gaussian distribution. However the width of the distribution can be changed depending on the requirement. This factor can be multiplied with the defined variables. Each of the variable can be considered as the velocity of an atom. Then the doppler averaging over the both the velocity can be performed using the algorithm.

B.1 Fortran code for monte carlo simulation

```

implicit real*8(a-h,o-z)
dimension a(20,20),v(20,20),b(20),si(20),e(20)
dimension a1(20,20)
open(1,file='rydpop',status='unknown')
open(2,file='twolevel',status='unknown')
C common dkp,dkc,vp,g2,dc,dp,fp,fc,grr,omega,delta,goff
C common dnb,q2
pi=3.141592654 !Value of Pi
dkp=1.2816549 !Probe wave vector
dkc=2.083 !Coupling wave vector
T=347.d0 !Temperature in Kelvin
dl=0.05 !Cell length in meter
C Rubidium partial pressure in Pascal (Liquid phase)
pv=133.32*10**(2.881+4.312-4040.0/T)
C Rubidium partial pressure in Pascal (Solid phase)
C pv=133.32*10**(2.881+4.857-4215.0/T)
C print *,'Vapor pressure in Pascal',pv
C Number of atoms per meter cube scaled by 1e16
dn=pv/(1.38e-7*T)
print *,'Atom Density X 1.0e16/meter cube',dn
C Most probable speed 2*kb*T/dm
vp=sqrt(1.38e2*T/1.445)
print *,'Average velocity in meter',vp
q2=1.0/(vp*dsqrt(2.d0*pi)) !Normalization factor
dpp=1575.d0
rbp=450.d0 !Probe detuning
rb1=10.d0 !Rydberg to ground state decay rate
dc1=1.0

```

```

dc2=1.0
dc3=1.0
dc4=8.2  !Rydberg–Rydberg interactions in MHz
dp1min=-2500
dp1max=1000
np=701  !Number data points
jmax=100000  !Number of random numbers generated
do i=1,np
  dp1=dp1min+(i-1)*(dp1max-dp1min)/(np-1)
  pop=0.d0
  j1=0
10  x1=2.d0*rand()-1.d0
    y1=2.d0*rand()-1.d0
    rsq=x1*x1+y1*y1
    if(rsq.ge.1.d0.or.rsq.eq.0.d0) goto 10
    j1=j1+1
    fac=dsqrt(-2.d0*dlog(rsq)/rsq)
    v1=fac*x1*vp
    v2=fac*y1*vp
    dppv1=dpp-dkp*v1
    dppv2=dpp-dkp*v2
    dp1v1=dp1+dkc*v1
    dp1v2=dp1+dkc*v2
    ls1=rbp**2/(4*(dppv1))
    ls2=rbp**2/(4*(dppv2))
C   Effective two photon Rabifrequency
    rb2=rb1*(rbp/(2*dppv2))

```

```

n=15
do i1=1,n
  do i2=1,n
    a(i1,i2)=0.d0
  end do
end do
a(1,2)=dc4
a(1,5)=rb2
a(1,7)=-2*rb1
a(1,8)=-rb2
a(1,12)=-rb1
a(1,14)=-2*dc1
a(1,15)=-rb1
a(2,1)=-dc4
a(2,6)=rb2
a(2,9)=rb2
a(2,13)=2*dc1
a(3,4)=dc2
a(3,5)=rb1
a(3,7)=-rb2
a(3,8)=-rb1
a(3,11)=-2*dc3
a(3,12)=-2*rb2
a(3,15)=-rb2
a(4,3)=-dc2
a(4,6)=rb1
a(4,9)=-rb1
a(4,10)=2*dc3

```

$$\begin{aligned}
a(5,1) &= rb2 \\
a(5,3) &= rb1 \\
a(5,6) &= dc2+dc4 \\
a(5,10) &= -rb1 \\
a(5,13) &= -rb2 \\
a(6,2) &= rb2 \\
a(6,4) &= rb1 \\
a(6,5) &= -(dc2+dc4) \\
a(6,11) &= -rb1 \\
a(6,14) &= -rb2 \\
a(7,2) &= -2*rb1 \\
a(7,7) &= -2*dc3 \\
a(7,11) &= 2*rb2 \\
a(7,15) &= 2*dc1 \\
a(8,1) &= rb2 \\
a(8,3) &= -rb1 \\
a(8,9) &= dc2+dc4 \\
a(8,10) &= rb1 \\
a(8,13) &= -rb2 \\
a(9,2) &= -rb2 \\
a(9,4) &= -rb1 \\
a(9,8) &= -(dc2+dc4) \\
a(9,11) &= rb1 \\
a(9,14) &= rb2 \\
a(10,5) &= -rb1 \\
a(10,7) &= rb2 \\
a(10,8) &= rb1 \\
a(10,11) &= 2*dc3+dc2
\end{aligned}$$

$$\begin{aligned}
a(10,15) &= -rb2 \\
a(11,6) &= -rb1 \\
a(11,9) &= rb1 \\
a(11,10) &= -(2*dc3+dc2) \\
a(12,4) &= -2*rb2 \\
a(12,12) &= -2*dc1 \\
a(12,14) &= 2*rb1 \\
a(12,15) &= 2*dc3 \\
a(13,5) &= -rb2 \\
a(13,8) &= rb2 \\
a(13,12) &= rb1 \\
a(13,14) &= 2*dc1+dc4 \\
a(13,15) &= -rb1 \\
a(14,6) &= -rb2 \\
a(14,9) &= -rb2 \\
a(14,13) &= -(2*dc1+dc4) \\
a(15,11) &= -2*rb2 \\
a(15,14) &= -2*rb1 \\
a(15,15) &= -2*(dc1+dc3) \\
a(1,1) &= 2*(dp1v1-ls1) \\
a(2,2) &= 2*(dp1v1-ls1) \\
a(3,3) &= 2*(dp1v2+dppv2+ls2) \\
a(4,4) &= 2*(dp1v2+dppv2+ls2) \\
a(5,5) &= 2*(dp1v1+dp1v2+dppv2+ls2-ls1)-4*u \\
a(6,6) &= 2*(dp1v1+dp1v2+dppv2+ls2-ls1)-4*u \\
a(8,8) &= -2*(dp1v1-dp1v2-dppv2-ls1-ls2) \\
a(9,9) &= -2*(dp1v1-dp1v2-dppv2-ls1-ls2) \\
a(10,10) &= 2*(dp1v2+dppv2+ls2)-4*u
\end{aligned}$$

```

a(11,11)=2*(dp1v2+dppv2+ls2)-4*u
a(14,14)=2*(dp1v1-ls1)-4*u
a(13,13)=2*(dp1v1-ls1)-4*u
*****
do i3=1,n
  b(i3)=0
enddo
b(1)=-rb1
b(3)=-rb2
*****
reps=1e-14
call svd(n,n,a,v,si,n,n,e,rep,ier)
C      print *, 'ier=',ier
C      if (ier.ne.0) go to 100
reps=1e-11
call svdevl(n,n,a,v,si,n,n,b,e,rep)
pop22=b(7)
pop44=b(15)
pop33=b(12)
pop1=((pop22+pop44))*((rb**4)/(16*((dppv1)**4)))
pop2=((pop33+pop44))*((rb**4)/(16*((dppv2)**4)))
pop=pop+pop1
if (j1.lt.jmax) goto 10
pop=(pop)/jmax
write(*,*) dp1,(pop)
write(1,*) dp1,pop
C      write(4,*) dp0,((rb)**2)/(4*(dp0**2)+2*((rb)**2)+(dc**2))
enddo

```

```

stop
end
*****
subroutine svd(n,m,a,v,sigma,la,lv,e,repr,ier)
implicit real*8(a-h,o-z)
parameter(itmax=30)
dimension a(20,20),v(20,20),sigma(20),e(20)

if(n.gt.m.or.n.le.0.or.m.le.0.or.m.gt.la.or.n.gt.lv) then
ier=111
return
endif
ier=0
g=0
rmax=0
do 3000 i=1,n
e(i)=g
s=0
do 1200 j=i,m
1200 s=s+a(j,i)**2
if(s.le.0.0) then
g=0
else
f=a(i,i)
g=sqrt(s)
if(f.ge.0.0) g=-g
h=f*g-s
a(i,i)=f-g

```

```

do 1800 j=i+1,n
s=0
do 1400 k=i ,m
1400   s=s+a(k,i)*a(k,j)
      f=s/h
      do 1600 k=i ,m
1600   a(k,j)=a(k,j)+f*a(k,i)
1800   continue
endif
sigma(i)=g
s=0
do 2000 j=i+1,n
2000   s=s+a(i,j)**2

if(s.le.0.0) then
g=0
else
f=a(i,i+1)
g=sqrt(s)
if(f.ge.0.0) g=-g
h=f*g-s
a(i,i+1)=f-g
do 2200 j=i+1,n
2200   e(j)=a(i,j)/h
do 2800 j=i+1,m
s=0
do 2400 k=i+1,n
2400   s=s+a(j,k)*a(i,k)

```

```

do 2600 k=i+1,n
2600     a(j,k)=a(j,k)+s*e(k)
2800     continue
endif
r1=abs(sigma(i))+abs(e(i))
if(r1.gt.rmax) rmax=r1
3000 continue
do 4000 i=n,1,-1
if(g.ne.0) then
h=a(i,i+1)*g
do 3200 j=i+1,n
3200     v(j,i)=a(i,j)/h

do 3800 j=i+1,n
s=0
do 3400 k=i+1,n
3400     s=s+a(i,k)*v(k,j)
do 3600 k=i+1,n
3600     v(k,j)=v(k,j)+s*v(k,i)
3800     continue
endif
do 3900 j=i+1,n
v(i,j)=0.0
v(j,i)=0.0
3900     continue
v(i,i)=1
g=e(i)
4000 continue

```

```

do 5000 i=n,1,-1
g=sigma(i)
do 4200 j=i+1,n
4200   a(i,j)=0
      if(g.ne.0.0) then
h=a(i,i)*g
do 4700 j=i+1,n
s=0
do 4400 k=i+1,m
4400   s=s+a(k,i)*a(k,j)
      f=s/h
do 4600 k=i,m
4600   a(k,j)=a(k,j)+f*a(k,i)
4700   continue
do 4800 j=i,m
4800   a(j,i)=a(j,i)/g
      else
do 4900 j=i,m
4900   a(j,i)=0.0
      endif
a(i,i)=a(i,i)+1
5000 continue

aeps=reps*rmax
do 8000 k=n,1,-1
do 7500 itr=1,itmax

do 5200 l=k,1,-1

```

```

        if (abs(e(1)).lt.aeps) go to 6000
        if (abs(sigma(1-1)).lt.aeps) go to 5400
5200    continue
5400    c=0.0
        s=1.0
        do 5800 i=1,k
            f=s*e(i)
            e(i)=c*e(i)
            if (abs(f).lt.aeps) go to 6000
            g=sigma(i)
            sigma(i)=sqrt(f*f+g*g)
            c=g/sigma(i)
            s=-f/sigma(i)
            do 5600 j=1,m
                r1=a(j,1-1)
                r2=a(j,i)
                a(j,1-1)=r1*c+r2*s
                a(j,i)=c*r2-s*r1
5600    continue
5800    continue

6000    z=sigma(k)
        if (1.eq.k) then
            if (z.lt.0.0) then
                sigma(k)=-z
            do 6200 j=1,n
6200    v(j,k)=-v(j,k)
        endif

```

```

go to 8000
endif

if( itr.eq.itmax) then
ier=11
go to 7500
endif

x=sigma(1)
y=sigma(k-1)
g=e(k-1)
h=e(k)
f=((y-z)*(y+z)+(g-h)*(g+h))/(2.*h*y)
g=sqrt(1.+f*f)
if(f.lt.0.0) g=-g
f=((x-z)*(x+z)+h*(y/(f+g)-h))/x

c=1.0
s=1.0
do 7000 i=1+1,k
g=e(i)
y=sigma(i)
h=s*g
g=c*g
e(i-1)=sqrt(f*f+h*h)
c=f/e(i-1)
s=h/e(i-1)
f=c*x+s*g

```

```

g=c*g-s*x
h=s*y
y=c*y

do 6400 j=1,n
x=v(j,i-1)
z=v(j,i)
v(j,i-1)=c*x+s*z
v(j,i)=c*z-s*x
6400    continue

sigma(i-1)=sqrt(f*f+h*h)
if(sigma(i-1).ne.0.0) then
c=f/sigma(i-1)
s=h/sigma(i-1)
endif

f=c*g+s*y
x=c*y-s*g
do 6600 j=1,m
y=a(j,i-1)
z=a(j,i)
a(j,i-1)=c*y+s*z
a(j,i)=c*z-s*y
6600    continue
7000    continue

e(1)=0
e(k)=f

```

```

        sigma(k)=x
7500    continue
8000    continue
end
*****
subroutine svdevl(n,m,u,v,sigma,lu,lv,b,wk, reps)
implicit real*8(a-h,o-z)
dimension u(20,20),v(20,20),sigma(20),b(20),wk(20)

smax=0.0
do 2000 i=1,n
    if(sigma(i).gt.smax) smax=sigma(i)
2000    continue

aeps=smax*reps
do 3000 i=1,n
    s=0.0
    if(sigma(i).gt.aeps) then
do 2400 j=1,m
2400        s=s+u(j,i)*b(j)
    s=s/sigma(i)
    endif
    wk(i)=s
3000    continue

do 4000 i=1,n
    s=0.0
    do 3400 j=1,n

```

```
3400     s=s+v(i ,j)*wk(j)
        b(i)=s
4000  continue
      end
```

Appendix C

LabVIEW Program for computer control

Laboratory Virtual Instrument Engineering Workbench (LabVIEW) is a system-design platform and development environment for a visual programming language from National Instruments. LabVIEW program is used in our experiments to interface the instruments with the computer to control it digitally as well as to collect and analyze the data. We collect data using a Tektronix oscilloscope DPO5034, for our experiment. The LabVIEW program to collect the data from multiple channels of the oscilloscope is presented in figure C.1. To record one set of data from 3 channels the program takes ~ 350 ms.

In some experiments the data has to be collected from multiple instruments simultaneously. In our experiment, the information about the temperature of the vapor cell, which ultimately measures the vapor density, is collected simultaneously with the experimental signal. Therefore, the program is modified for multiple instrument connection and is given in fig C.2. This program connects the DPO5034 oscilloscope to collect the data for experimental observations and the digital multimeter from Agilent to collect the resistance of the sensor for density measurement simultaneously. The observed signals collected in the LabVIEW program is also analyzed using the same formula and fitting windows. The initial data and the data after analysis are collected in the computer.

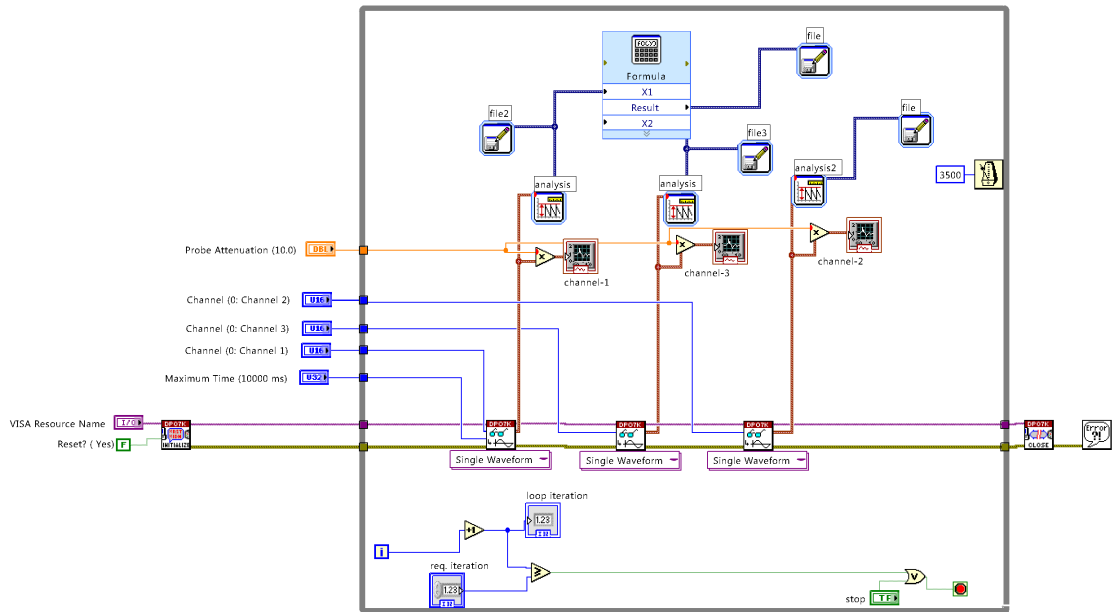


Figure C.1: Labview program for connecting the oscilloscope DPO5034 to the computer and transfer data.

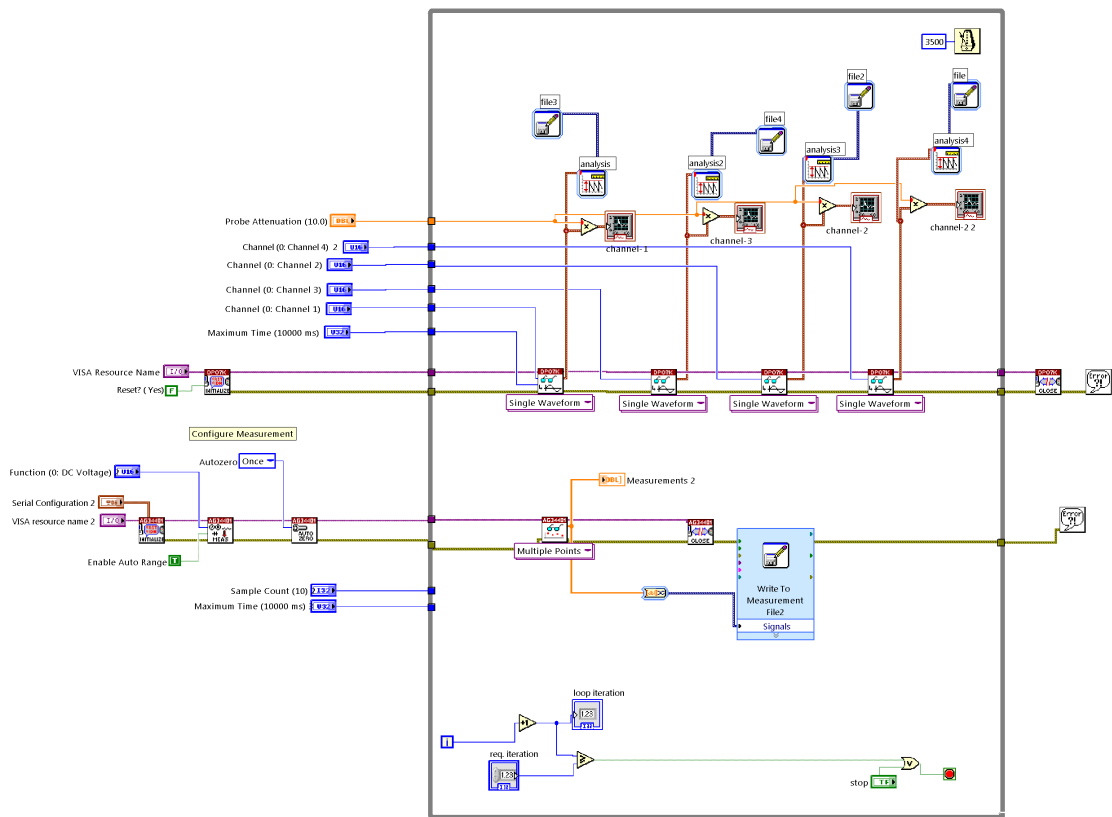


Figure C.2: LabVIEW program for connecting the oscilloscope DPO5034 and Agilent Digital multimeter to the computer and transfer data.

Appendix D

Cold atom set-up developments

D.1 Anti-helmholtz coil arrangements

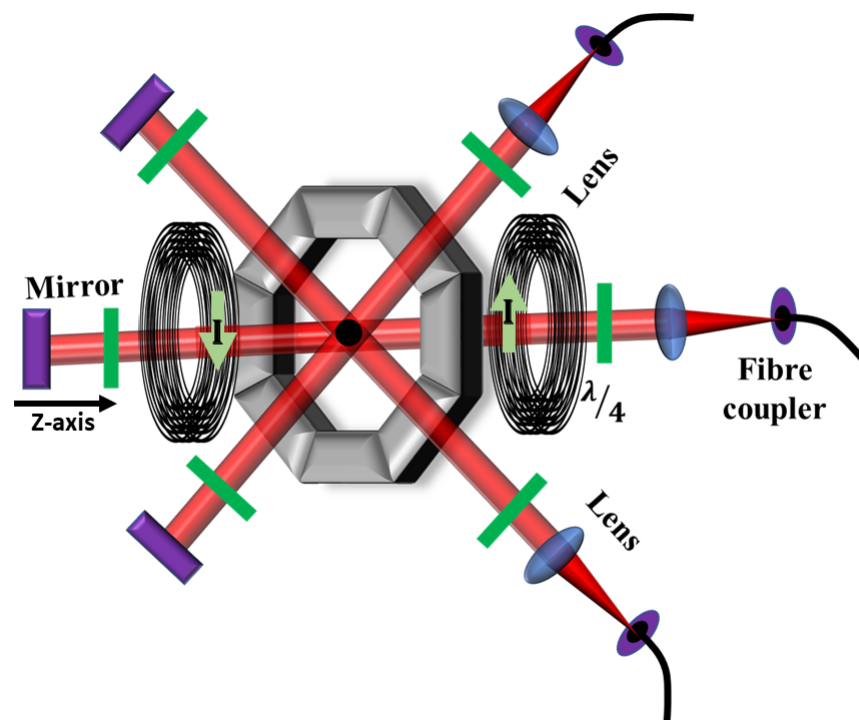


Figure D.1: MOT set-up for trapping atoms in a 3D trap. $\lambda/4$: quarter wave plate. I : current applied to the anti-Helmholtz coil.

A pair of magnetic coils in anti-Helmholtz configuration is required for the MOT set-up. This is needed to generate the magnetic field gradient in order to trap the atoms. For an anti-

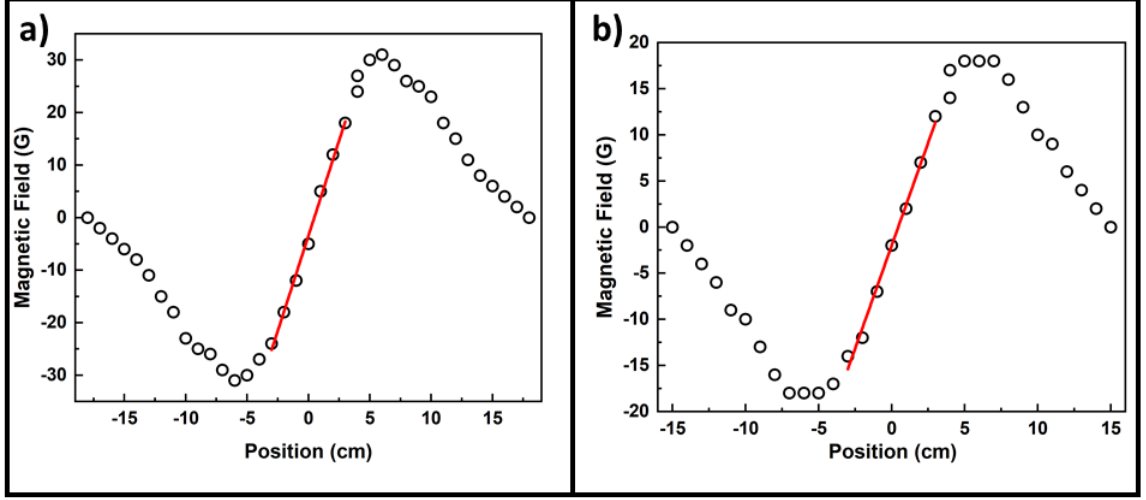


Figure D.2: Plot for magnetic field for current of (a) 5 amp and (b) 3 amp.

Helmholtz coil aligned in the z -axis having radius R and inter-coil separation d , the magnetic field gradient at any point in the axis is given by

$$\frac{dB}{dz} = \frac{3\mu_0 N I R^2}{2} \left(\frac{z + d/2}{(R^2 + (z - d/2)^2)^{5/2}} - \frac{z - d/2}{(R^2 + (z + d/2)^2)^{5/2}} \right) \quad (\text{D.1})$$

Here, μ_0 is the permeability, N is the number of turns of the coil and I is the current passing through it. The coils are placed on both side of the chamber as shown in figure D.1. Enameled copper wires of diameter 1.5mm are used to prepare the coil. The former for the coils are prepared in the mechanical workshop of NISER. The coils are having an inner diameter of 160 mm and total of 200 turns. A variable current source is used to apply current to the coils. The plot of the magnetic field due to the coils at various points in the axis is shown in figure D.2. For a current of 5 amp in each coil a field gradient of 7.5 G/cm is observed as shown in figure D.2(a). Similarly for 3 amp current as shown in D.2(b), a field gradient of 4.5 G/cm is observed. Since we are trapping Rb atoms, which requires a field gradient of $\simeq 4$ G/cm. Thus, a current of 3 amp is sufficient to generate the required field.

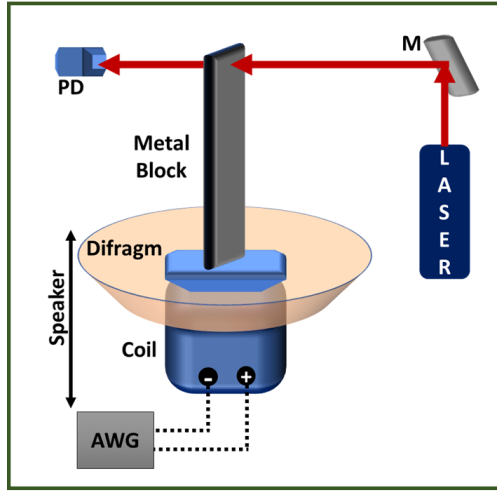


Figure D.3: *Optical setup to block the beam using mechanical shutter. M: Mirror, AWG: Arbitrary waveform generator and PD: Photo detector.*

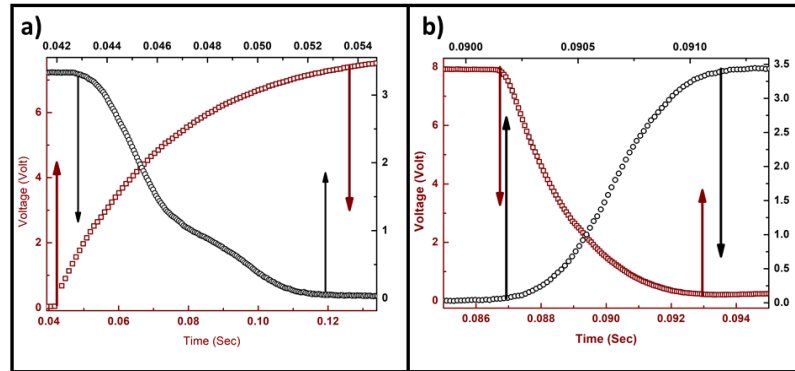


Figure D.4: *Rise time and fall time plot of the mechanical shutter and the detector signal. (a) Power supply switching on time (red) and detector switching off time (black) and (b) Power supply switching off time (red) and detector switching on time (black).*

D.2 Low cost mechanical shutter

In order to perform the experiment with MOT, the laser beams are applied to the trapped atoms. However, performing the experiment or measurements, the trapping as well as the re-pumper laser is switched off. This can be done using a mechanical shutter which can be controlled with an external waveform generator. Thus, we have prepared a mechanical shutter using a loudspeaker and a metal plate.^{180,181} The arrangement of the mechanical shutter is depicted in figure D.3. The diaphragm of the speaker is removed and the base is glued to a metal foil.

The speaker is connected to an arbitrary waveform generator. When the voltage is applied, due to electromagnetic induction the speaker base moves up and down depending on the applied voltage. This moves the metal foil up and down along with it.

When an oscillating signal is applied the speaker, the metal foil oscillates according to the signal. An experiment is performed in order to measure the response time of the mechanical shutter. A laser beam is applied from an ECDL which is passed through the foil. When the foil is down the beam will pass and will hit the photo-detector PD. When the foil is up the beam will be blocked and nothing will be seen in the PD. Thus due to the oscillating signal supplied to speaker, an oscillating output will be generated at the PD. The rise time and fall time of the generated signal is shown in figure D.4. When the power supply will be off the photo detector will be on and vice versa. As shown in figure D.4(a), the power supply switching on time $\simeq 100\text{ms}$ and the detector switching off time $\simeq 10\text{ms}$. Similarly, switching off time of the power supply is $\simeq 10\text{ms}$ and the detector on time is $\simeq 1\text{ms}$ as shown in figure D.4(b).

D.3 Computer Controlled AOM Driver

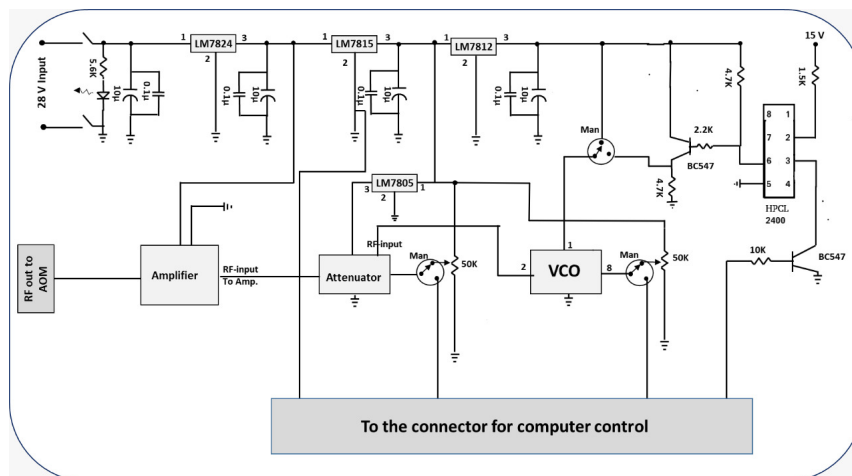


Figure D.5: *Electronic circuit for digitally controlled AOM driver.*

While performing the experiment, the MOT beams and the re-pumpers are switched off. However, after a short period of time again the beams are switched on and the experimental

beams are switched off. In order to do this, the AOMs are used in the path of the beam where a fast switching can be performed. When the AOM controllers are switched off, first order beam through the AOM will be blocked. However, this cannot be done with the mechanical shutter as the experimental time scales are of millisecond order. Thus, we need an AOM driver which can be controlled using digital signals.

The circuit diagram of the AOM driver is presented in appendix D. This AOM driver is used to frequency shift the MOT and the repumper beams. When the oscillating voltage is applied to the driver, the frequency shifted laser will be switched on and off in the same manner. An optocoupler and two transistors are used for fast switching. Switching time of $10 \mu\text{s}$ is achieved using this driver.

D.4 NI-DAQMx programming

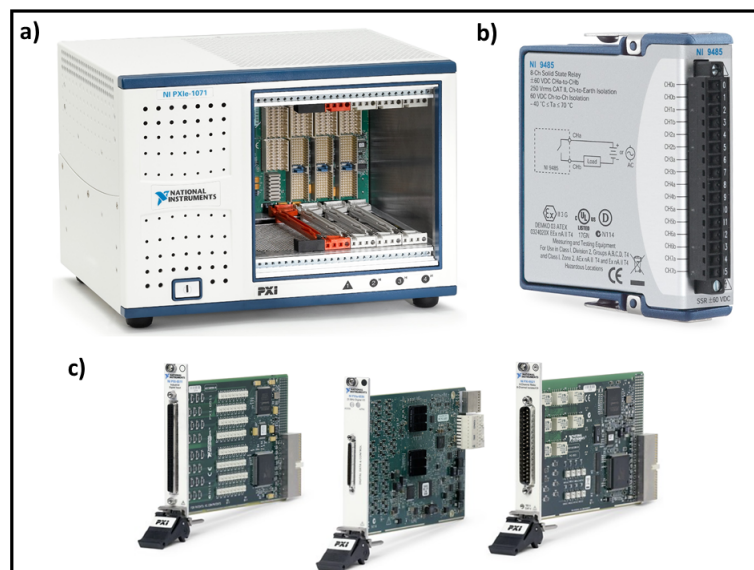


Figure D.6: NI PXIe system and DAQ card to generate digital output.

The MOT set-up requires the beams to be switched on and off in millisecond time scale. Therefore, the system has to be controlled using computer-program. For this we are using a NI-PXIe system and LabVIEW program. The PXIe system is a stand alone one which can be operated with windows. The LabVIEW is used to control hardwares and generate signals of

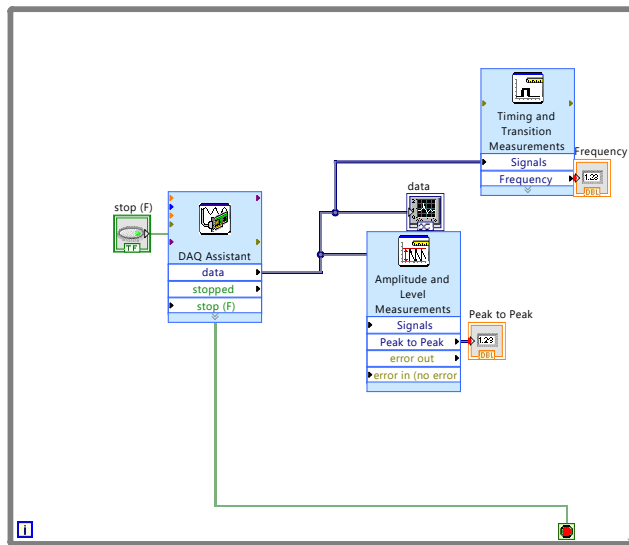


Figure D.7: NI-DAQmx program to acquire signal.

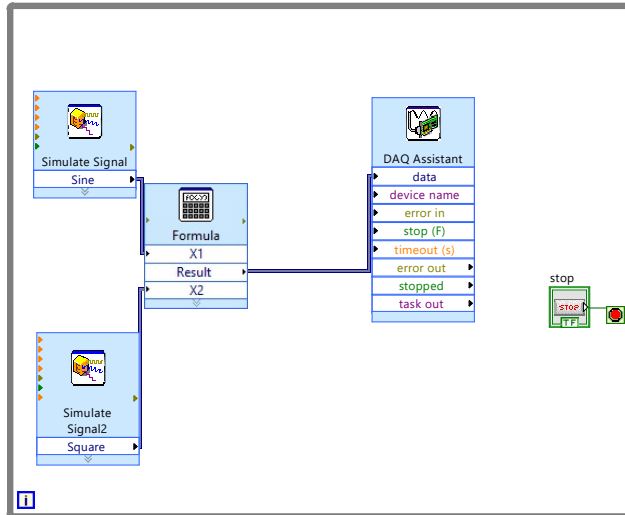


Figure D.8: NI-DAQmx program to generate signal.

required voltage and frequency through the DAQ card.

The PXIe system is shown in figure D.6 (a). This is connected to a monitor where the LabVIEW program can be written. In order to generate the digital signals, the PXIe system is connected to a DAQ card. The DAQ card is shown in figure D.6(b). In order to connect the DAQ card to the PXIe system, different modules are used which is shown in figure D.6(c). The DAQ card can generate digital and analog signals. The number of digital and analog output depends on the type of DAQ card. The DAQ card can be controlled with the LabVIEW program. Two LabVIEW programs are presented in figure D.7 and D.8 to acquire and generate signal.

Thesis Highlight

Name of the Student: Dushmanta Kara

Name of the CI/OCC: NISER Bhubaneswar

Enrolment No.: PHYS11201404002

Thesis Title: Study of Rydberg blockade and anti-blockade in rubidium atomic vapor

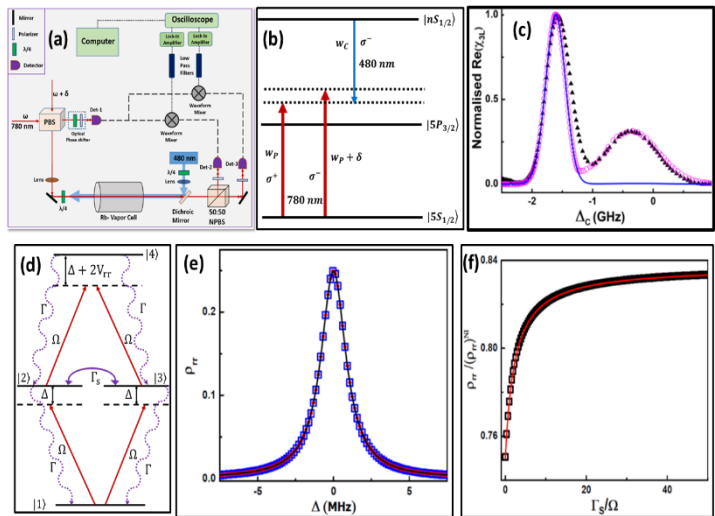
Discipline: Physical sciences

Sub-Area of Discipline: Quantum non-linear optics

Date of viva voce: 08-08-2021

In this thesis, a theoretical study of Rydberg blockade as well as theoretical and experimental study of Rydberg anti-blockade effects are presented with emphasis on thermal atomic vapor. Using optical heterodyne detection technique (fig.(a)), dispersion of the probe beam is observed due to two-photon excitation to the Rydberg state (fig.(b)) in thermal atomic vapor. The phenomena of interaction induced enhancement in Rydberg excitation or Rydberg anti-blockade is demonstrated in the system. A non-linear dependence of the peak height on the atomic vapor density is observed for the anti-blockade peak arising in the dispersion spectrum of the probe laser. The experimental observations is explained with a two-atom model using the dressed state picture of the three-level system. A good agreement is found between the experimental observations and the proposed interacting model indicating the existence of Rydberg anti-blockade in thermal vapor (fig.(c)).

A theoretical model that explains the possibility of Rydberg blockade for an ensemble of N-atoms in thermal atomic vapor is also presented. Using a two atom model (fig.(d)), the blockade process is studied using the exact calculation, an empirical formula and an approximate model. A good agreement is observed between them when the population is plotted as a function of laser detuning (fig.(e)). The theory is extended to three and four atoms inside the blockade sphere. An effective model is formulated for N atoms using the method of induction. Also, the effect of different dephasing mechanisms on the blockade process, arising due to the velocity of the atoms in thermal vapor ensemble are studied. In presence of large super-atom dephasing, the system does not reach to an non-interacting regime (fig.(f)), indicating the existence of Rydberg blockade in thermal atomic vapor. The existence of blockade effect in thermal atomic vapor is observed in the theory where the dephasing due to relative motion of the atoms is large. In addition to this, a theoretical model for Rydberg blockade in thermal atomic vapor is proposed using four-photon excitation scheme. The advantage of using this scheme is the residual wave vector mismatch which is much smaller compared to a two-photon process. The blockade phenomenon is studied theoretically with the two-atom model by suitably reducing the individual atomic system to an effective two-level system using adiabatic elimination.



(a) The experimental set-up of the optical heterodyne detection technique to measure the dispersion of the probe beam due to two-photon excitation to Rydberg state. (b) The energy level scheme of the two-photon excitation. (c) The matching of the theoretical model and the experimental observations for the anti-blockade peak. (d) Two-atom model to study the blockade phenomena. (e) Rydberg population as a function of laser detuning for the empirical formula, exact numerical calculation and the approximate model. (f) Normalized Rydberg blocked population with increase in super-atom dephasing.

In presence of large super-atom dephasing, the system does not reach to an non-interacting regime (fig.(f)), indicating the existence of Rydberg blockade in thermal atomic vapor. The existence of blockade effect in thermal atomic vapor is observed in the theory where the dephasing due to relative motion of the atoms is large. In addition to this, a theoretical model for Rydberg blockade in thermal atomic vapor is proposed using four-photon excitation scheme. The advantage of using this scheme is the residual wave vector mismatch which is much smaller compared to a two-photon process. The blockade phenomenon is studied theoretically with the two-atom model by suitably reducing the individual atomic system to an effective two-level system using adiabatic elimination.